Université de Liège

Faculté des Sciences
Département d'Astrophysique, Géophysique et Océanographie

Interactions in massive binaries: spectral modelling – CoMBiSpeC – and observational analyses

by

Matthieu Palate

Groupe d'Astrophysique des Hautes Energies

– Année académique 2013 - 2014 –

Supervisor:
Pr. Gregor Rauw

Dissertation présentée en vue de l'obtention du grade de Docteur en Sciences.

Supervisor – Pr. Gregor RAUW

Jury – Pr. Jean SURDEJ as President
Pr. Marc-Antoine DUPRET
Dr. Eric GOSSET
Pr. Gloria KOENIGSBERGER
Pr. Krešimir PAVLOVSKI
Pr. Gregor RAUW

Remerciements

Réaliser un doctorat est sans doute plus une question de passion que d'étude. Une passion pour l'astrophysique, pour la recherche, pour la connaissance. Cette thèse est l'aboutissement de ces quatre années de doctorat passées au sein du Groupe d'Astrophysique des Hautes Energies. Quatre années remplies de découvertes, de défis, d'interrogations, de voyages et de rencontres.

Mais tout ceci n'aurait pas été possible sans l'aide de mon promoteur le Pr. Gregor Rauw. Merci Gregor pour le temps que tu m'as consacré, pour ton aide de tous les jours, pour tes conseils non seulement pour les aspects scientifiques mais aussi pour des choses plus personnelles. Merci de m'avoir soutenu et fourni le financement sans lequel je n'aurais pas pu réaliser cette thèse. Merci enfin pour les (nombreuses) corrections de rapports, d'articles, de cette thèse, pour nos discussions et ta disponibilité.

Je voudrais ensuite remercier les membres du GAPHE et plus particulièrement le Pr. Jean-Pierre Swings et les Drs. Eric Gosset, Michaël De Becker, et Yaël Nazé pour leur accueil, leurs conseils et leur disponibilité. Merci au Pr. Jean-Pierre Swings et au Dr. Michaël De Becker pour leur relecture attentive de cette thèse. Merci enfin à Michaël d'avoir partagé son bureau avec moi pendant deux ans et demi (avant de me confier aux non moins sympathiques retraités du groupe).

I also want to thank Pr. Gloria Koenigsberger for giving me a warm welcome in her house in Cuernavaca, for her help in the understanding and use of her code, and for her support in the writing of several papers. Thank you very much Gloria.

I thank Pr. Jean Surdej who accepted to be President of the jury, along with Pr. Marc-Antoine Dupret, Dr. Eric Gosset, Pr. Gloria Koenigsberger, and Pr. Krešimir Pavlovski who agreed to be members of the jury.

Merci à ma femme, Marjorie, de m'avoir accompagné, soutenu et supporté durant cette thèse. Merci à mes parents, Michelle et Pierre, et à ma soeur, Mathilde de m'avoir écouté expliquer mes recherches sans (trop) se plaindre et d'avoir été là pour m'épauler et me conseiller. Merci enfin à ma famille et à mes amis, Bruno et Thomas, pour leur présence, leur soutien et l'intérêt qu'ils ont porté à mes recherches.

A toutes et à tous mille fois merci.

Abstract

Massive stars are very important to the life of the galaxies. They interact with their surrounding medium and can trigger the formation of new stars. They are also major contributors to the metal enhancement of the Universe. However, massive stars are rare and many open questions on their formation, evolution and characteristics remain. It also seems that at least 50 % of massive stars belong to a binary or multiple system (see Mahy et al. 2009, and Sana & Evans 2011) which represents a non-negligible part of these stars. One of the best ways to improve our knowledge on massive stars is to study massive binaries and their spectra. Spectral and atmosphere modelling of stars are very interesting tools that are now often used in spectral analyses. However, these models are designed for single spherical stars. In this context, we have developed a numerical code of spectral modelling of massive binary systems: CoMBiSpeC (code of massive binary spectral computation). In the case of circular synchronously rotating systems, our code computes the distorted stellar surface, the gravity distribution, and the temperature distribution accounting for gravity darkening, reflection effects, and radiation pressure effects. In the case of eccentric systems the TIDES (tidal interactions with dissipation of energy through shear) code (Moreno & Koenigsberger 1999, and Moreno et al. 2011) is used for the surface and velocity field computation. The spectral computation consists in summing the incremental contributions of each surface point. On each surface point, a local spectrum is computed from a spectral grid accounting for the local properties ($T_{\rm eff}$, $\log g$). These local spectra are Doppler shifted and multiplied by the area of the element projected along the line of sight towards the observer, and by a limb-darkening coefficient. The contribution is then summed to the total spectrum. This procedure is repeated for several orbital phases.

Our models, and the observational analyses of the four binary systems presented in the second part of this work, have allowed to explain several effects linked to binarity: luminosity class discrepancy, temperature distribution, Struve-Sahade effect, and line profile variations. We show that the classical luminosity class criteria are not well suited for binary systems. The different radial velocity semi-amplitudes for He I and He II lines can be explained by the temperature distribution at the stellar surface distorted by tidal interaction and radiation pressure effects. The variation of the relative line strength of one of

the component with respect to the other (Struve-Sahade effect) is due to intrinsic asymmetric line profiles that lead to wrong equivalent width measurement when Gaussian/Lorentzian profile are used for deblending the two components. Finally, certain kinds of line profile variations observed in eccentric or non-synchronously rotating systems, find their origin in tidal interactions that lead to surface oscillations. These oscillations produce migrating bumps in the line profiles that move from the blue to red wing.

Our last study concerns the multiplicity of the WR 138 system that was in debate for many years and for which we have concluded that it is composed of a Wolf-Rayet star and an O or B-type star on a wide orbit. This last study also shows the limitation of our code that cannot model the lines formed in the wind of a massive star and therefore cannot model a Wolf-Rayet star.

In conclusion, CoMBiSpeC is a first step in the spectral modelling of massive binary systems and several improvements (grid of spectra, reflection effect treatment, non-solar abundances, ...) are still needed to be able to study all massive binaries. Nevertheless, this model can explain and reproduce various observed phenomena which was the main goal of this thesis.

Résumé

Les étoiles massives sont très importantes pour la vie des galaxies. Elles interagissent avec le milieu environnant et peuvent déclencher la formation de nouvelles étoiles. Elles sont aussi des contributeurs majeurs à l'enrichissement en métaux de l'univers. Cependant, les étoiles massives sont rares et de nombreuses questions demeurent quant à leur formation, leur évolution ou leurs caractéristiques. Il semble également qu'au moins 50% des étoiles massives appartiennent à un système binaire ou multiple (voir Mahy et al. 2009 et Sana & Evans 2011) ce qui représente un part non négligeable de ces étoiles. Une des meilleures façons d'améliorer nos connaissances de ces étoiles est justement l'étude des systèmes binaires massifs et de leurs spectres.

La modélisation d'atmosphères et de spectres d'étoiles sont des outils très intéressants qui sont maintenant souvent utilisés dans l'analyse spectrale. Cependant, ces modèles ont été conçus pour des étoiles isolées et sphériques ce qui n'est pas le cas dans les systèmes binaires. Dans ce contexte, nous avons développé un code numérique de modélisation de spectres d'étoiles binaires massives : CoMBiSpeC (code of massive binary spectral computation). Dans le cas de systèmes circulaires en co-rotation synchrone, notre code calcule la surface des étoiles déformées par les interactions de marées. Il calcule ensuite les distributions de gravité et de température en tenant compte d'effets comme l'assombrissement gravitationnel, la réflexion et la pression de radiation. Dans le cas de systèmes excentriques, on utilise le code TIDES (tidal interactions with dissipation of energy through shear, Moreno & Koenigsberger 1999 et Moreno et al. 2011) pour calculer la surface et le champ de vitesse. Le calcul du spectre consiste quant à lui en la sommation des contributions incrémentales de chacun des points de la surface. En chacun de ces points, un spectre local est calculé à partir d'une grille de spectres et en tenant compte des propriétés locales ($T_{\rm eff}$, $\log g$). On applique ensuite un décalage Doppler à ces spectres et on les multiplie par la surface associée à l'élément et projetée le long de la ligne de visée vers l'observateur. Enfin, les spectres locaux sont multipliés par un coefficient d'assombrissement centre - bord et sommés pour obtenir le spectre total. Cette procédure est répétée pour plusieurs phases orbitales.

Nos modèles ainsi que les analyses observationnelles présentées dans la seconde partie de cette thèse, ont permis d'expliquer plusieurs effets liés à la

binarité : le problème de classe de luminosité, les effets de la distribution de température, l'effet Struve-Sahade et certaines variations de profil de raies. Nous avons montré que les critères classiques de classification de luminosité n'étaient pas adaptés aux systèmes binaires massifs. Les différences de demi-amplitudes de vitesse radiale entre les raies de He I et He II s'expliquent par la distribution de température à la surface des étoiles. Surfaces qui sont déformées par les interactions de marées et les effets de la pression de radiation. Les variations relatives de la profondeur des raies d'une étoile par rapport à l'autre au cours d'un cycle orbital (l'effet Struve-Sahade) sont dues à des profils de raies intrinsèquement asymétriques qui conduisent, lorsqu'on sépare les composantes et qu'on mesure leur largeur équivalente à l'aide d'un profil Gaussien/Lorentzien, à des valeurs incorrectes. Enfin, certaines variations de profil de raies observées dans des systèmes excentriques ou en co-rotation non synchrone, trouvent leur origine dans les interactions de marées qui conduisent à des oscillations à la surface des étoiles. Ces oscillations produisent des bosses dans le profil de raie. Ces bosses se déplacent de l'aile bleue à l'aile rouge de la raie durant le cycle orbital et sont donc responsables des variations de profils. Notre dernière étude concerne la multiplicité du système WR 138 qui était incertaine depuis de nombreuses années et pour lequel nous avons conclus qu'il s'agissait d'un système binaire composé d'une étoile de type Wolf-Rayet et d'une étoile de type O ou B en orbite large. Cette dernière étude montre aussi les limites de notre code qui ne permet pas de calculer les raies formées dans le vent stellaire et donc, ne permet pas de calculer le spectre d'une étoile Wolf-Rayet.

En conclusion, CoMBiSpeC est une première étape dans la modélisation spectrale de systèmes binaires massifs et plusieurs améliorations (grille de spectres, effet de réflexion, abondances non solaires, ...) sont encore nécessaires pour pouvoir étudier toutes les binaires massives. Néanmoins, ce modèle permet déjà d'expliquer et de reproduire divers phénomènes observés, ce qui était le but principal de cette thèse.

Contents

Introduction

Many people have forgotten that one of the most beautiful sights offered by nature lies in a starry night. How not to be puzzled and attracted by the mysteries of the infinite multitude of galaxies, stars, and planets ? The study of the Universe is also a way to answer the fundamental philosophical questions of the origin of the World and Life. This is probably why astronomy and astrophysics are so fascinating. Some of the most interesting objects are probably the massive stars. These stars are massive, rare, and luminous, they have a strong interaction with their surroundings, and their death in a supernova is one of the most powerful events of the Universe. The aim of this thesis is to study massive stars and more precisely massive binary systems and their spectra. Before developing this goal, we will briefly describe the main characteristics of the massive stars and their evolution (see e.g. the proceedings of the *39th Liège Astrophysical Colloquium*, Rauw et al. 2011).

Figure 1: Starry night at the ESO 3.6-metre telescope at La Silla. ©ESO/S. Brunier.

Definition

Massive stars are defined by a minimum initial mass of $8-10\ M_\odot$. This minimum mass is required for a star to reach the nuclear combustion of carbon in its core during its life (see e.g. Chiosi & Maeder 1986). In lower-mass stars, nuclear reactions come to an end before the ignition of carbon. The maximum mass is unknown but is often estimated to $\sim 150\ M_\odot$ (see e.g. Oey & Clarke 2005, and references therein), although in recent years the detection of stars as massive as $300\ M_\odot$ has been claimed (Crowther et al. 2010).

Characteristics

During their main-sequence lifetime, the spectral classification of massive stars is O or early B type. They lie in the upper left part of the Hertzsprung-Russell diagram. Therefore, they are very luminous with a luminosity that can reach $10^5 - 10^6\ L_\odot$, and very hot with an effective temperature higher than $15 - 20$ kK. According to Wien's law, the emission peak of massive stars lies in the UV and they are thus the main sources of ionization of the interstellar medium. They also have a high mass-loss rate that can reach $10^{-7} - 10^{-4}\ M_\odot\ \mathrm{yr}^{-1}$, and which is associated to strong stellar winds with terminal velocities of $1000-3000\ \mathrm{km\,s^{-1}}$. In comparison, the mass-loss rate of the Sun is $10^{-14}\ M_\odot\ \mathrm{yr}^{-1}$ with a terminal velocity of its wind of $400 - 700\ \mathrm{km\,s^{-1}}$. These wind and mass-loss lead the massive stars to further interact with the ambient interstellar medium. Massive stars can trigger the formation of new stars, and play a key role in the production and dissemination of various chemical elements. In conclusion, they can be considered as the engines of the galaxies. However, massive stars are rare, and represent a small fraction of the $\sim 10^{11}$ stars of our galaxy, the Milky Way. The reasons of this rarity have to be found in the low formation rate, and in the relatively short life-time. One can estimate that for one star with a mass of $60 - 120\ M_\odot$, about 250 stars of $1 - 2\ M_\odot$, and 640 of $0.5 - 1\ M_\odot$ are formed. The life time of an O-type star is about 10 Myrs which is 10^3 times shorter than the estimated life-time of the Sun (10 Gyrs). This short life-time is explained by the high mass of these stars that induces a high gravity compression. In order to support its own mass and remain in hydrostatic equilibrium, the star must have a high rate of nuclear reactions. Therefore, the more massive the star, the shorter is its life (see for instance Heger & Langer 2000, Nazé 2006).

Figure 2: Star formation region of the Tarantula Nebula (30 Doradus) in the Large Magellanic Cloud. The core of the nebula contains a dense star cluster (R136) where massive stars are formed. ©HST, NASA, ESA.

Evolution

The formation and evolution of massive stars are still open questions and subject to many debates. In a similar fashion to low-mass stars, everything likely starts with the collapse of a giant molecular cloud that forms proto-stars hidden to us by surrounding dust. The accretion of further material finally leads to the formation of the star. The big issue is to know how this accretion occurs. Indeed, in the case of massive stars, the high luminosity and radiation pressure should stop the accretion and prevent the formation of stars more massive than $\sim 10\,M_{\odot}$. In fact, it seems that the radiation field is not uniform and that it would be more intense in the polar regions than near the equator. Accretion could therefore continue through the equatorial region of the stars (see Yorke 2004). Once the star is formed, it spends the main part of its life in a core-hydrogen burning main-sequence phase. Its subsequent evolution depends on its initial mass and is summarized below. For single stars, the evolution is governed by the mass-loss through the stellar wind (see for example Vanbeveren 2009, Vink 2008), in the so-called Conti scenario: O $\rightarrow$ X $\rightarrow$ H-poor WN ($\rightarrow$ WC) $\rightarrow$ SN. The WN and WC are two types of Wolf Rayet stars rich in nitrogen or in carbon; X is a phase that depends on the initial mass of the star (see below).

Stars with an initial mass larger than 75 $M_\odot$ pass through a transition phase of N-type hydrogen-rich Wolf-Rayet stars, followed by a luminous blue variable (LBV) phase with eruptions that eject part of the envelope. These are the last stages in which the star burns hydrogen in its core. Stars less massive than 40 $M_\odot$ probably do not go through an LBV phase. They rather evolve towards a core-helium burning red (or yellow) supergiant (RSG or YSG) phase. In that stage, their core contracts and their envelope expands. The stars with a mass higher than 25 $M_\odot$ become classical Wolf-Rayet stars. Over most of the Wolf-Rayet phase, the star burns helium in its core. Towards the end of the evolution, it subsequently burns carbon, oxygen, neon, magnesium and silicon. The next stage would be the combustion of iron. However this reaction requires energy input and thus the nuclear reactions in the core stop. The core can no longer sustain the pressure from the layers above, and collapses. As a reaction, the outer layers are ejected and the star explodes as a supernova. The core itself becomes a neutron star or a black hole, depending on its mass. Some elements heavier than iron are synthesized during this extremely short collapse (less than 1 second) and released into the interstellar medium. The shock wave produced by the supernova can induce the collapse of a nearby molecular cloud triggering the formation of a new generation of stars (see for instance Machida et al. 2005, Leão et al. 2009, Nazé 2006, and references therein).

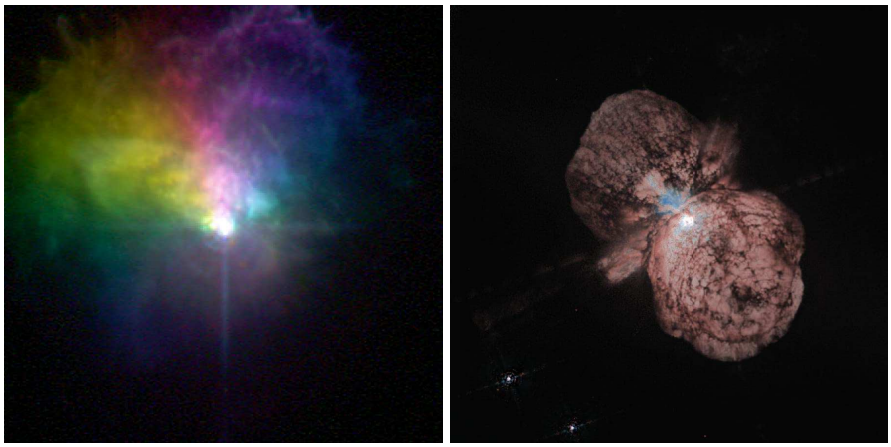

(a) RSG VY Canis Majoris (b) η Carinae

Figure 3: Illustration of an RSG (VY Canis Majoris) in polarized light (*left*) and of an LBV (η Carinae that underwent two eruptions in the 19th century, *right*). ©HST, NASA, ESA.

In summary, we thus expect that the evolution of single massive stars proceeds along the following lines:

O→WN (H-rich)→LBV→ WN (H-poor)→WC→SNIc	if $M \geq 75 M_{\odot}$.
O → LBV → WN (H-poor) → WC → SNIc	if $75 M_{\odot} > M \geq 40 M_{\odot}$.
O → RSG/YSG → WN (H-poor) → SNIb	if $40 M_{\odot} > M \geq 25 M_{\odot}$.
OB → RSG → WN → SNII	if $10 M_{\odot} \geq M > 25 M_{\odot}$.

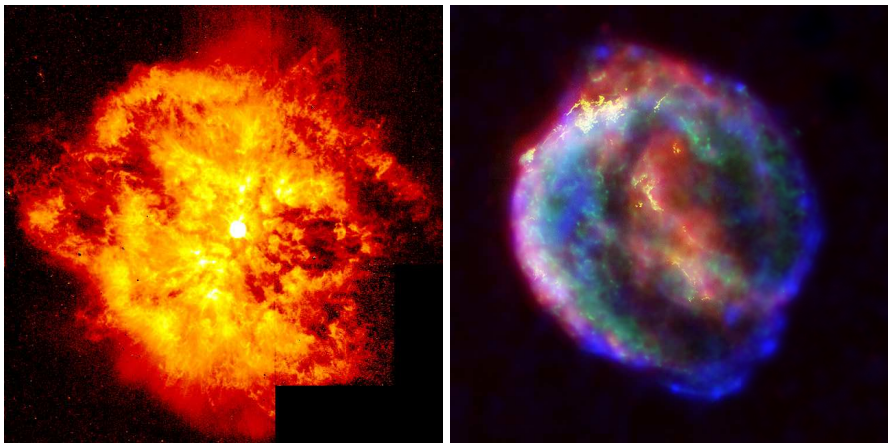

(a) WR 124 (b) Kepler's Supernova Remnant

Figure 4: *Left:* Wolf-Rayet star (WR 124) surrounded by matter ejected in previous evolutionary stages. *Right:* Kepler's supernova remnant in visible, X-ray and infrared light. ©HST, NASA, ESA.

Massive binaries

According to recent estimates, at least 50% of the massive stars belong to a binary or multiple system (see Mahy et al. 2009 and Sana & Evans 2011). A binary system is a couple of two stars orbiting around their common centre of mass. This definition can be extended to multiple systems in which the stars orbit around their centre of mass. A massive binary system is a binary system in which at least one star is a massive star. In this thesis, we will assume that the two stars are massive which is often the case (at least observationally). A star in a binary system suffers from the interactions with its companion that can, for example, modify the shape of the star and induce gravity darkening.

The formation and evolution of stars in binaries are also different due to these interactions. For example, mass transfers can occur when the star expands. These mass transfers called Roche lobe overflows modify the evolutionary track of the stars. Kinetic momentum transfer either during a Roche lobe overflow episode or through tidal interactions can also influence the rotational mixing and modify the surface abundances of the stars. Some other effects are also specific to massive binaries such as the Struve-Sahade effect (see for example Struve 1937, Sahade 1959, Howarth et al. 1997, Linder et al. 2007, Linder 2008, Mahy 2011).

Binary systems are therefore more complex than single stars. However, they also provide precious information. Photometric and spectral analyses allow to determine physical properties (such as masses, temperatures, and radii) of stars which is not possible (or very difficult) for single stars. In the case of eclipsing binaries, one can determine these parameters with a very high accuracy. Therefore a good understanding of binary systems, and especially massive binary systems, is very important to improve our knowledge on these stars. Moreover, as outlined above, massive stars are rare and a large fraction are in multiple systems, therefore the study of massive binaries represents an important field for the study of massive stars.

Spectral modelling

Spectra are the sources of a large part of our knowledge about the stars. Whilst classical tools have allowed to classify the stars, spectral modelling now helps us extracting more information from these spectra. State of the art model atmosphere codes allow for example to derive intrinsic properties such as the effective temperature, the mass-loss rate, the gravity, the chemical composition, the rotation, ... One can even, sometimes, estimate the radius and the distance of the star.

Spectral modelling of stars started relatively recently. One of the first spectral (continuum) modelling was performed by Williamson (1943) but the first complete atmosphere model is probably the model of Kurucz (1970). Since then, and thanks to the amazing progress of the computer power as well as the accurate determination of the atomic data, the number and quality of atmosphere models has increased. One can cite, for example, CMFGEN (Hillier & Miller 1998), FASTWIND (Santolaya-Rey et al. 1997), PoWR (Gräfener et al. 2002, Hamann & Gräfener 2003), PHOENIX (Hauschildt & Baron 1999), and TLUSTY (Hubeny & Lanz 1992). Some older models assumed plane-parallel, static atmospheres in local thermodynamic equilibrium (LTE), and composed only of hydrogen and helium. A mass discrepancy problem between the spectroscopic mass derived with these models and the one derived from

the evolutionary tracks rapidly occurred, and improved models were therefore developed to solve this issue. The new models are now non-LTE, non plane-parallel, include many chemical elements, and account for line-blanketing.

In massive stars, the radiation field is so strong that it dominates over the collisional processes in setting up the populations of atomic energy levels. Therefore, the LTE assumption breaks down and non-LTE models are needed. The radiation field is also responsible for the strong stellar wind as well as the large extension of the atmosphere of massive stars (depending on the wavelength, stellar winds can be optically thick out to tens or hundreds of stellar radii). In consequence, the plane-parallel approximation is no longer valid. Finally, metals in massive stars play an important role in the opacity computation. Due to the high temperature of massive stars, the metals are highly ionized and these ions efficiently absorb photons especially in the UV. Therefore, there is a blocking of the UV flux that leads to a heating of the inner atmosphere. This effect is accounted for in the so-called line-blanketing treatment. More information on stellar atmospheres can be found in Gray (2005).

Aims of the thesis

The atmosphere models are now well developed and can reproduce the main processes that act on the line formation and thus on the spectrum. As we mentioned before, these models are very important to better understand the stars and especially the massive stars. However, all these models are designed for single stars and do not account for tidal deformation and other interactions that modify (the shape of) the stars in a binary system. The aim of this thesis is to develop a spectral modelling tool for massive binary systems that accounts for various effects that affect these systems.

In chapter 1, we define in details massive binary systems. First, we recall some concepts on the orbits and we present the equation of the Roche potential which is the basis of the computation of the shape of tidally deformed stars. The radiative effects, reflection, radiation pressure, limb-darkening, and gravity darkening, that affect the stars are also discussed. The second point of this chapter concerns spectroscopy. We point out which is the information available in a spectrum and what are the problems linked to the binarity encountered in massive stars. Finally, we present, in a few words, other important techniques used to analyse the stars.

In chapter 2, we describe the model that we have developed: CoMBiSpeC. This acronym stands for “code of massive binary spectral computation”. The development of this code represents the heart of the thesis. We start the chapter by a technical description of the code; then, we explain the model itself.

CoMBiSpeC can be divided into two parts: the geometrical computation and the spectral computation.
The geometry depends on the orbit of the system: circular synchronous-rotation and eccentric or circular non-synchronous rotation systems. In the first case, we use the Roche potential to compute the shape of the stars. We have also developed a novel approach based on the work of Drechsel et al. (1995) and Howarth (1997) to treat the radiation pressure that modifies the Roche potential. The gravity distribution is computed according to the gradient of this potential. In the second case, the shape of the star is computed with the TIDES code (tidal interactions with dissipation of energy through shear, see Moreno & Koenigsberger 1999 and Moreno et al. 2011). Finally, the temperature distribution is computed accounting for the gravity darkening and reflection effects.
The spectral computation consists in summing the incremental contributions of each surface point. On each surface point, a local spectrum is computed from a spectral grid accounting for the local properties ($T_{\rm eff}$, $\log g$). These local spectra are Doppler shifted and multiplied by the area of the element projected along the line of sight towards the observer and by a limb-darkening coefficient. The contribution is then summed to the total spectrum. In the last point of this chapter, we give the limitations and the developments of the code.

In chapter 3, we present the observational analysis of four systems. The first two systems, LZ Cep and Spica, were analysed with CoMBiSpeC. In these studies, we searched for a best match between the observation and the model that helped us to refine the solutions previously determined. These studies also show strengths and weaknesses of our code. For example, the best matching solution of the spectra of Spica has shown that tidal interactions could be responsible of line profile variations. The third system, Plaskett's star, has been analysed in order to characterize the line profile variations. In this system, we have used CoMBiSpeC to show that, as in Spica, the tidal interactions could be responsible of the observed line profile variations. Unfortunately, due to the high number of free parameters, we could not find the best-matching parameters. The last system, WR 138, is composed of a WR star and its analysis with CoMBiSpeC is not possible. This last system is a good example of the improvements that remain to be done in order to completely reproduce an observed spectrum.

Finally, we present our conclusions and recall important results and perspectives in the last chapter of this thesis.

Chapter 1

Massive binary systems

In this chapter, we will define the concepts that are important in the study of binary systems: the elements of the orbit, the Roche potential, the radiative effects, and the darkening effects. Then, we will explain what spectroscopy is useful for, and what are the problems encountered in the analysis of binary systems. Finally, we will deal with photometry and other important techniques.

1.1 Definitions and Geometry

1.1.1 Orbits

The orbit is defined as the trajectory of a body around another one under the influence of gravitation. There exist two types of orbits: the open orbits and the closed ones. Only the latter are relevant for binary systems. Determining the type of the orbit is important when we deal with a binary system because it will influence the shape of the stars and the way they interact. In binary systems, the orbits are always closed orbits and are either circular or elliptical (improperly called eccentric). We will now briefly describe the orbits of the two centres of mass of the stars in a binary system. The equations presented here come from the courses of celestial mechanics and variable stars of G. Rauw (Rauw 2009b).

In terms of celestial mechanics, the motion of the centres of mass of the stars is a so-called two-body problem that describes the motion of two point-like masses m_1 and m_2 that interact gravitationally. If we write Newton's equations of m_2 with respect to m_1 we get

$$\ddot{\vec{r}} = -\mu \frac{\vec{r}}{r^3} = -\vec{\nabla}\left(-\frac{\mu}{r}\right) \tag{1.1}$$

where $\vec{r}$ is the vector joining the two masses, $\mu = G(m_1 + m_2)$, G is the gravitational constant ($G = 6.674\ 10^{-11}\ \mathrm{m^3\,kg^{-1}\,s^{-2}}$). This equation allows us to show that the motion occurs in a constant plane defined by $\vec{r} \wedge \vec{\dot{r}} = 0$ and we have $\left|\vec{r} \wedge \vec{\dot{r}}\right| = |\vec{h}| = \mathrm{Ctt}$ (Kelper's second law). From equation 1.1 we can derive the trajectory of the mass m_2 with respect to m_1 (in polar coordinates)

$$r = \frac{C}{1 + e\cos(\psi + \omega)} \tag{1.2}$$

where $C = \frac{h^2}{\mu}$, e is the eccentricity, ω the argument or longitude of periastron, and ψ the longitude angle. One can distinguish four trajectories depending on the eccentricity (see Fig. 1.1):

- $e = 0$: the trajectory is a circle (closed orbit),
- $0 < e < 1$: the trajectory is an ellipse (closed orbit),
- $e = 1$: the trajectory is a parabola (open orbit),
- $e > 1$: the trajectory is a hyperbola (open orbit).

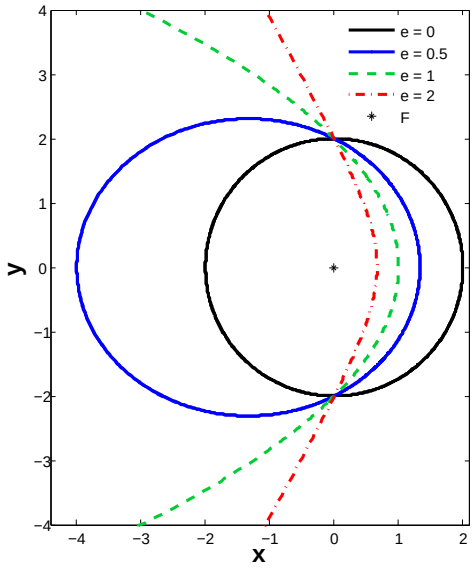

Figure 1.1: Orbit as a function of the eccentricity. The closed orbits (circle and ellipse) have $e < 1$ while open orbits (parabola and hyperbola) have $e \geq 1$. F is the focal point.

For binary systems, the first two cases are relevant[1].

The circular orbit is the simplest case because the radius is a constant and the true anomaly, $\phi = \psi - \omega$, is equal to the longitude angle, ψ, because the longitude of periastron is undefined.

For eccentric orbits, we can write the expression of the radius as a function of the semi-major axis a and the true anomaly. In this case, the true anomaly is the angle measured from periastron to the position of the star on its orbit relative to the centre of mass (i.e. one of the two focal points of the ellipse, see Fig. 1.2) and we have,

$$r = \frac{a(1 - e^2)}{1 + e\cos(\phi)} \tag{1.3}$$

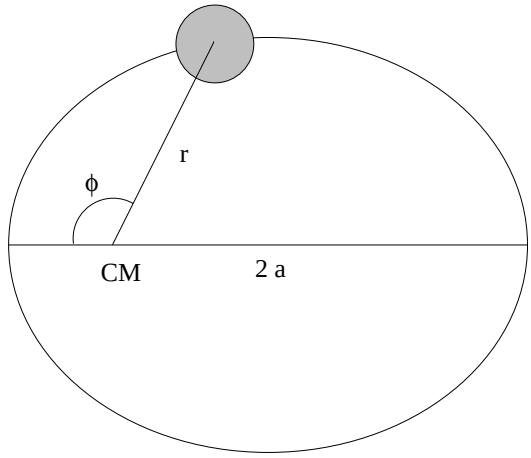

Figure 1.2: Relative motion of a star around the centre of mass (CM) of a binary system. Figure from Rauw (2009a).

The relation between the position of the mass on its orbit and the time, t, can be expressed through the eccentric anomaly, E : $\frac{a - r}{ae} = \cos E$ and Kepler's equation

$$E - e\sin E = M = \sqrt{\frac{\mu}{a^3}}(t - t_0) \tag{1.4}$$

[1]In the following, we will talk about eccentric orbits for the elliptical orbits.

where t_0 is the time of the periastron passage ($E = 0$) and M is the mean anomaly. Equivalently, we can link the true anomaly to the eccentric anomaly,

$$\cos\phi = \frac{\cos E - e}{1 - e\cos E} \tag{1.5}$$

These equations are used to switch from a time coordinate to an angular coordinate and to compute the orbital separation between the two stars during the orbital cycle. However, we also need other parameters to completely determine the orbit. These parameters are presented in the next section.

The elements of the orbit

To completely describe a Keplerian orbit we need 7 parameters. In the case of an eccentric orbit, (see Fig. 1.3) these parameters are $(\Omega, i, \omega, a, e, t_0, \mu)$.

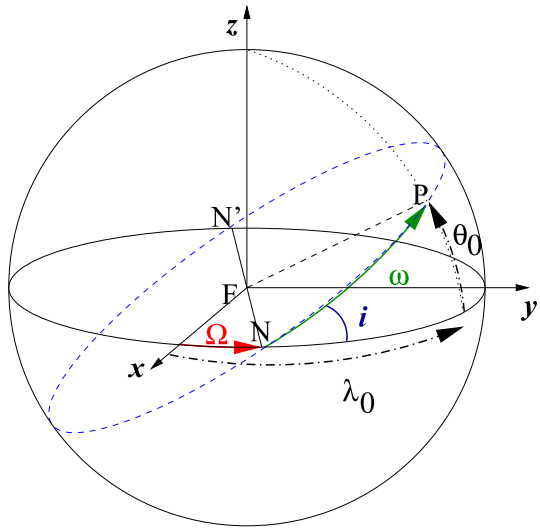

Figure 1.3: Definition of the angular elements of the orbit. P is the pericenter and its latitude and longitude are given by $\sin\theta_0 = \sin i \sin\omega$ and $\tan(\lambda_0 - \Omega) = \cos i \tan\omega$. F is the focal point. Figure from Rauw (2009b).

$\Omega_{\rm node}$ Longitude of the ascending node. The line of nodes NN' is the intersection between the orbital plane and the xy plane. The node where the mass crosses the xy plane from negative to positive latitude is the ascending node N (see Fig. 1.4).

i The inclination is the angle between the orbit and the xy plane, which is the plane of the sky (see Fig. 1.4).

ω Longitude of periastron (also called argument of periastron, see Fig. 1.4).

a Semi-major axis.

e Eccentricity.

t_0 Time of the periastron passage.

$\mu = G(m_1 + m_2)$.

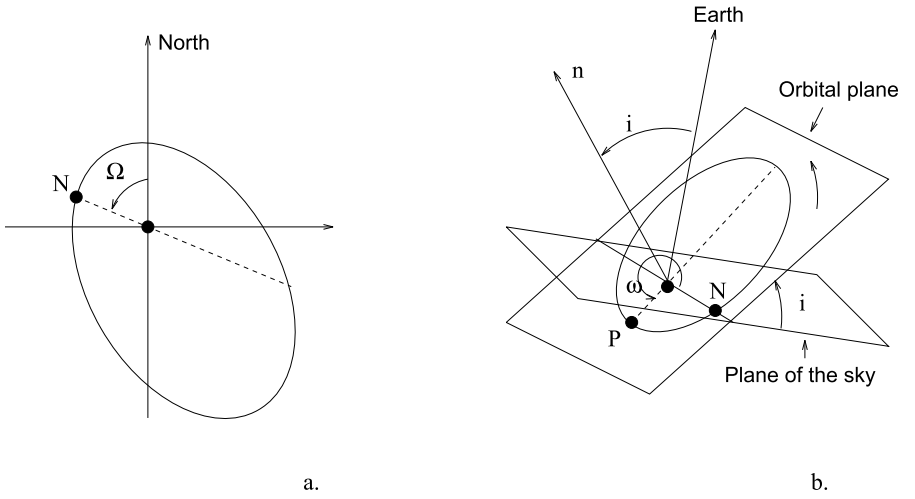

Figure 1.4: *a.* Apparent orbit with the reference node, N. The angle, Ω, indicates the line of nodes and is measured from the North direction in the trigonometric sense. *b.* Definition of the inclination and longitude of periastron. Figure adapted from Rauw (2009a).

In the case of a circular orbit, the parameters are the same but, because $e = 0$, some simplification occurs (ω is not defined for example).

The orbital phases and eclipses

We have shown above that we can use the time or an angle as independent parameter to describe the motion of the masses during the orbital cycle. In practice, the period and the time are usually known parameters. However, for numerical simulations that we will develop and/or analyses, it is more convenient to express the motion in terms of an angle rather than in terms of time. That is why we introduce the orbital phase, Φ, that is defined as

$$M = 2\pi\left(\Phi - \Phi_{\text{periastron}}\right), \tag{1.6}$$

and varies in the interval $[0, 1]$. The orbital phase is linked to the mean anomaly and is linearly dependent of the time. Phase zero is defined as the phase of conjunction (circular orbits) or the phase of periastron passage (eccentric orbits).

An eclipse occurs when a star comes in front of its companion. To observe an eclipse, the inclination of the system has to be more or less close to 90°, depending on the size and orbital separation of the stars. There are usually two eclipses during an orbital cycle: the eclipse of m_1 by m_2 and the eclipse of m_2 by m_1. For the circular orbit, the phase zero will be defined by the eclipse of m_1 by m_2 (or equivalently if there is no eclipses, the conjuction when m_2 is in front of m_1).

The equilibrium

A binary system can be said *in equilibrium* when its orbit is circular, the two stars are in synchronous co-rotation and the spin axes are perpendicular to the orbital plane. The synchronous co-rotation means that the orbital period and the stellar rotation period are equal. The systems in equilibrium can be described by the Roche potential approach (see sect. 1.1.2). The systems in non-equilibrium have to be described by a more complex model such as the TIDES[2] code (Moreno & Koenigsberger 1999, Moreno et al. 2005, Moreno et al. 2011, see sect. 2.3). According to Moreno & Koenigsberger (1999), the synchronicity can be described by the parameter $\beta = \dfrac{\omega_{\text{star}}}{\Omega_{\text{orbit}}}$ where ω_{star} and Ω_{orbit} are the angular stellar rotation velocity and the angular orbital velocity. In this dissertation we will assume that all spin axes are perpendicular to the orbital plane. Therefore, the equilibrium can be expressed by the β parameter. If $\beta = 1$ the system is in equilibrium, if $\beta \neq 1$ the system is not in equilibrium and tidally induced oscillations can be present.

[2]Tidal interactions with dissipation of energy through shear.

The radial velocities

The radial velocity (RV) is the projection of the velocity vector of the stars on the line of sight towards the observer. It is an important source of information. The RV can be measured from the Doppler shift of a spectrum:

$$\frac{\lambda - \lambda_0}{\lambda_0} = \frac{\mathrm{v_{rad}}}{c}, \tag{1.7}$$

where λ is the observed wavelength of a line, λ_0 is the wavelength of the line at rest, $\mathrm{v_{rad}}$ is the RV, and c the speed of light in empty space.

If we measure the RV at several orbital phases (or at different epochs), we can construct an RV curve (see Fig. 1.5[3] and 1.6).

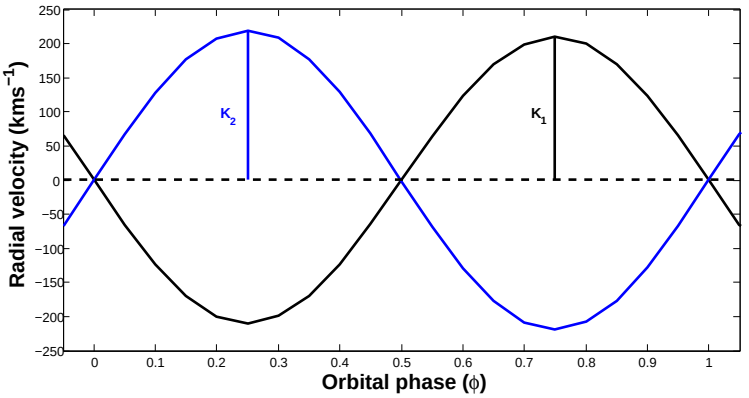

Figure 1.5: Example of a synthetic RV curve for model A (see appendix B.4 for the parameters). The system has a circular orbit and thus, the RV curve is a sine function (see also Palate et al. 2013b model 1 for more details). The semi-amplitudes are equal to: $K_1 = 209.8$ km s^{-1}and $K_2 = 218.9$ km s^{-1}.

RV depends on the time or equivalently on the true anomaly and can be expressed for a star with respect to the centre of mass of the system by

$$\mathrm{v_{rad}} = \mathrm{v_0} + \sin i \sqrt{\frac{\mu}{a\,(1-e^2)}}[\cos(\omega + \phi) + e\ \cos\omega], \tag{1.8}$$

where $\mathrm{v_0}$ is the radial velocity of the centre of mass of the system and $\mu = \frac{Gm_j^3}{(m_1+m_2)^2}$ with j equal to 1 for the RV of the mass m_2 (secondary) and equal to 2 for the RV of the mass m_1 (primary). This function is periodic of period P.

[3]The parameters of the models used in the figures are given in the appendix B.4.

The orbital period is therefore the first information that we can obtain with an RV curve. We can also obtain t_0 (the time of the periastron passage) because the extrema of the RV curve correspond to the nodes of the orbit. The eccentricity can generally be determined by a least-square numerical fitting. Finally, we can define the semi-amplitude K (see Fig. 1.5) of this RV curve

$$K = \sin i \sqrt{\frac{\mu}{a\,(1-e^2)}}. \tag{1.9}$$

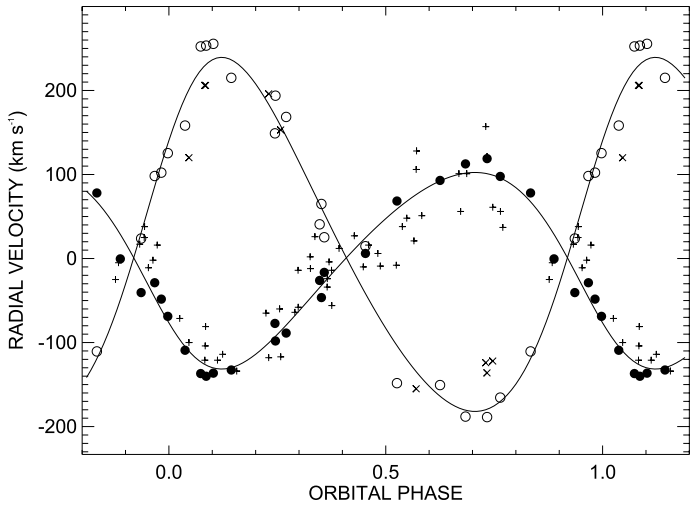

Figure 1.6: Example of the observed RV curve of the system HD 101131 (Gies et al. 2002). The semi-amplitudes are equal to: $K_1 = 117$ km s^{-1} and $K_2 = 211$ km s^{-1}. The parameters of the system are: $P = 9.64$ d, $e = 0.156$, $\omega = 122°$, $M_j \sin^3 i = 21.8$ and 12.1 $M_\odot$, $a_j \sin i = 22.0$ and 39.7 $R_\odot$ ($j = 1, 2$ for the primary and secondary).

If we use Kepler's third law, we can write that $a = (2\pi)^{-2/3}\mu^{1/3}\mathrm{P}^{2/3}$, and therefore we can express the mass function,

$$f(m) = \frac{m_j^3 \sin^3 i}{(m_1+m_2)^2} = \frac{K^3}{2\pi G}\mathrm{P}\left(1-e^2\right)^{3/2}, \tag{1.10}$$

where $j = 1$ or 2 for the secondary or primary. If we deal with a binary system where the spectral signatures of both stars can be seen (double-lined spectroscopic binary SB2) we can measure the semi-amplitude of the two stars,

and therefore, we have the mass ratio $q = m_2/m_1 = K_1/K_2$. We can also determine the minimum masses of the stars, $m_j \sin^3 i$. In the case of an SB1 system (only one star visible in the spectra) the problem is more difficult and requires assumptions on the mass ratio or on the mass of one of the stars.

1.1.2 The Roche potential

The Roche potential was introduced by the French astronomer Édouard Roche (1820-1883). It describes the gravitational and centrifugal potential created by two point-like masses m_1 and m_2 acting on a particle of mass m_3 negligible with respect to m_1 and m_2 ($m_3 <<< m_2 < m_1$). This potential can be used to describe the shape of the stars in a binary system under several assumptions:

- The system is in equilibrium, i.e. the orbit is circular and both stars co-rotate with the binary motion.
- The stars act like point-like masses, i.e., the main part of the stellar mass is in the core of the star and the envelope has no mass.
- The only acting force is gravity.

Under these assumptions, we can express the Roche potential (Φ) in an inertial frame of reference centred on the centre of the primary star (m_1) (see Fig. 1.7, and e.g. Kopal 1959)

$$\Phi = \frac{Gm_1}{r_1} + \frac{Gm_2}{r_2} + \frac{G(m_1+m_2)}{2a^3}(x^2+y^2) - \frac{Gm_2}{a^2}x \tag{1.11}$$

where $r_1 = \sqrt{x^2+y^2+z^2}$, $r_2 = \sqrt{(a-x)^2+y^2+z^2}$, x is the axis running from the centre of the primary towards the secondary, z the axis from the centre of the primary and perpendicular to the orbital plane, and y is perpendicular to x and z. The x, y, and z coordinates are expressed in length unit, m_1 and m_2 are respectively the masses of the primary and the secondary, a is the separation between the stars, and G is the gravitational constant. If we assume that the stars are in hydrostatic equilibrium, their surfaces follow an equipotential Φ_0 of the Roche potential.
For practical reasons (see chap. 2), we write the Roche potential in a dimensionless form:

$$\begin{aligned} \Omega &= \frac{a\Phi}{Gm_1} \\ &= \frac{1}{r'_1} + \frac{q}{r'_2} + \frac{q+1}{2}(x'^2+y'^2) - qx, \end{aligned} \tag{1.12}$$

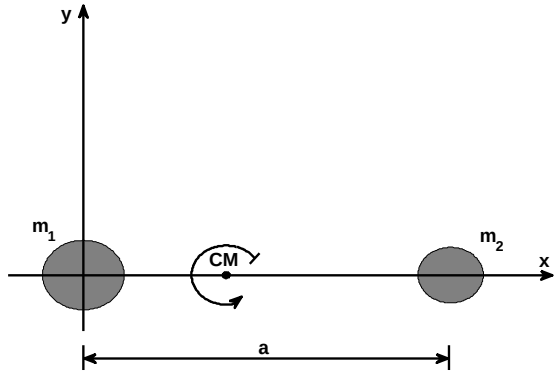

Figure 1.7: Inertial frame of reference centred on the centre of the primary star. The stars orbit around the centre of mass (CM).

where $r'_1 = \sqrt{x'^2 + y'^2 + z'^2}$, $r'_2 = \sqrt{(1-x')^2 + y'^2 + z'^2}$, $x' = \frac{x}{a}$, $y' = \frac{y}{a}$, $z' = \frac{z}{a}$, $q = \frac{m_2}{m_1} \leq 1$.
Finally, we use spherical coordinates and we have (for the primary, see Fig. 1.8):

$$\Omega_1 = \frac{1}{r} + \frac{q}{\sqrt{r^2 - 2r\cos\varphi\sin\theta + 1}} + \frac{q+1}{2}r^2\sin^2\theta - qr\cos\varphi\sin\theta \qquad (1.13)$$

where $r = \sqrt{x^2 + y^2 + z^2}$, $q = \frac{m_2}{m_1}$, $x = r\cos\varphi\sin\theta$, $y = r\sin\varphi\sin\theta$, and $z = r\cos\theta$. The θ and φ angles are the colatitude and longitude ($\varphi \in [0, 2\pi]$, $\theta \in [0, \pi]$). Notice that r' has been renamed r for readability.
For the computation, it is also more convenient to express the shape of the secondary in a system of axes centred on the centre of the secondary. Therefore, we can make a change of coordinates: $x \to (1 - x)$

$$\Omega_2 = \frac{q}{r} + \frac{1}{\sqrt{r^2 - 2r\cos\varphi\sin\theta + 1}} + \frac{q+1}{2}r^2\sin^2\theta - r\cos\varphi\sin\theta + \frac{1-q}{2} \qquad (1.14)$$

where $r = \sqrt{x^2 + y^2 + z^2}$, $q = \frac{m_2}{m_1}$, $x = r\cos\varphi\sin\theta$, $y = r\sin\varphi\sin\theta$, and $z = r\cos\theta$ and $\varphi \in [0, 2\pi]$, $\theta \in [0, \pi]$ and the x is now the axis running from the centre of the secondary towards the primary.

The norm of the gradient of the Roche potential (see below) sets the distribution of the local gravity at the stellar surface. This quantity is very important for the spectral computation and is not constant over the stellar surface. The potential is therefore constant at the stellar surface, but not its gradient.

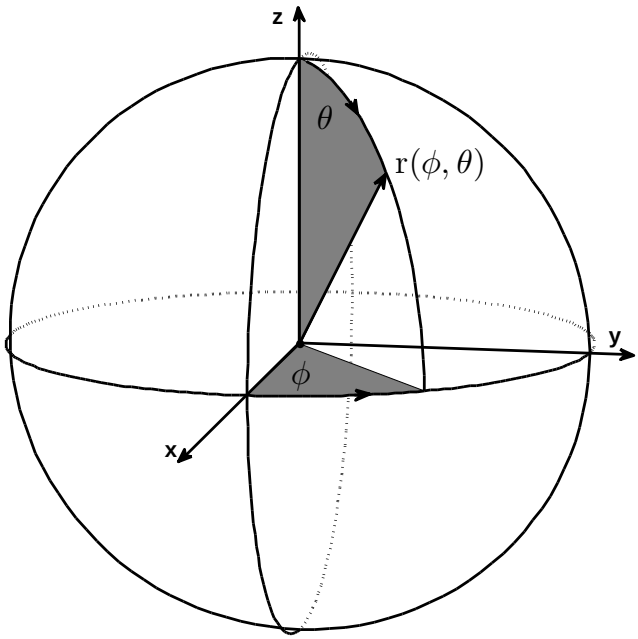

Figure 1.8: Spherical and Cartesian coordinate systems. Notice that θ is the colatitude and not the latitude.

The Roche lobe and the Lagrangian points

The Roche potential (see Fig. 1.9, and 1.10) has five points of equilibrium called the Lagrangian points. These Lagrangian points correspond to the zero value of the gradient of the Roche potential:

$$\vec{\nabla}\Omega = \begin{pmatrix} \partial_x\Omega \\ \partial_y\Omega \\ \partial_z\Omega \end{pmatrix} = \begin{pmatrix} -\dfrac{x}{r_1^3} + \dfrac{q\,(1-x)}{r_2^3} + (q+1)\,x - q \\ -\dfrac{y}{r_1^3} - \dfrac{qy}{r_2^3} + (q+1)\,y \\ -\dfrac{z}{r_1^3} - \dfrac{qz}{r_2^3} \end{pmatrix}, \tag{1.15}$$

where $r_1 = \sqrt{x^2+y^2+z^2}$ and $r_2 = \sqrt{(1-x)^2+y^2+z^2}$.

The first three points L_1, L_2, and L_3 are located on the x axis ($y = z = 0$) and are solutions of the equation: $\partial_x\Omega(x, y = z = 0) = 0$. The last two are

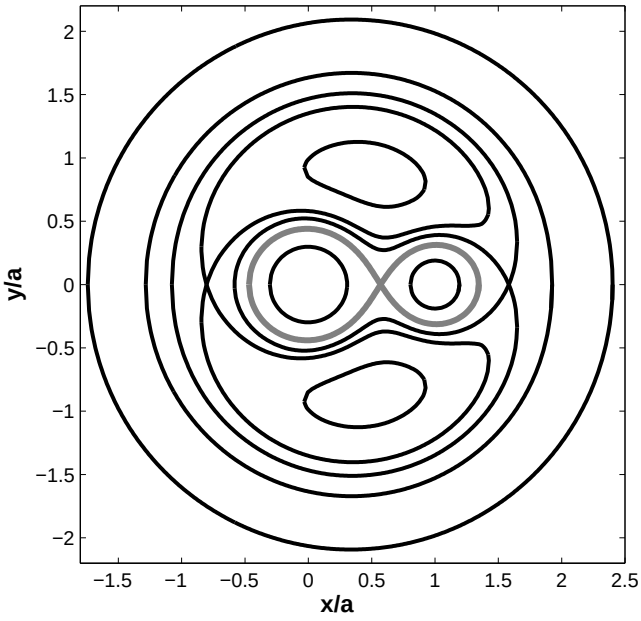

Figure 1.9: Example of Roche equipotentials projected in the *xy* plan for a mass ratio of $q = 0.5$. The Roche lobe is indicated in grey.

in the *xy* plane and are located at ($x = a/2$, $y = \pm a\sqrt{3}/2$, $z = 0$). The L_1 point is particularly interesting because it is the place where the two stars will get into contact when they expand. The equipotential passing through the L_1 point defines a volume called the Roche lobe. Once a star fills its Roche lobe, and continues expanding, it starts to lose material through this point. Then, the material will fall towards the companion thereby initiating a mass transfer. Once the stars are in over-contact, they have a common envelope and finally, they can get into contact with either the L_2 or L_3 point and lose material in a circumstellar envelope.

Eccentric systems

The treatment of the shape of the stars in an eccentric system is more complicated because the assumptions of the Roche potential break down. These systems are no longer in equilibrium. The first way to overcome this issue is to use an instantaneous Roche potential modified to account for the non-synchronicity of the stellar rotation (see e.g. Kopal 1959). However, eccentric systems often

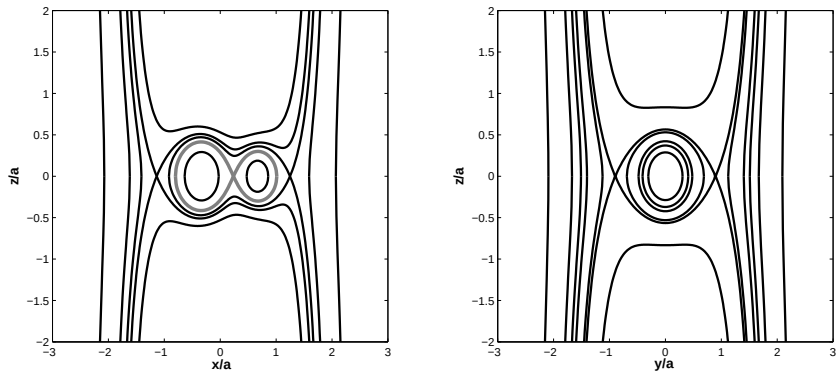

(a) *xz* projection (b) *yz* projection

Figure 1.10: Example of Roche equipotentials projected in the *xz* and *yz* planes for a mass ratio of $q = 0.5$. The Roche lobe is indicated in grey.

present line profile variability in their spectra (see e.g. Smith 1977, Vogt & Penrod 1983, Harrington et al. 2009, Palate et al. 2013b). The origins of these variabilities are large horizontal motions at the stellar surface called *tidal flows* (see Fig. 1.11). The tidal flows are not reproduced with an instantaneous Roche potential.

A more sophisticated approach has been proposed by Moreno & Koenigsberger (1999) and has been extended by Moreno et al. (2011). This model called TIDES (Tidal interactions with dissipation of energy through shear) code consists in solving the equations of motion of small surface elements. The TIDES model assumes that there exists a deformable and perturbed thin layer that lies on top of a rigid body in uniform rotation. Several forces are acting on the deformable layer: centrifugal and Coriolis forces, gas pressure, and viscous effects and obviously the gravitational potential of both stars. The TIDES code computes the stellar shape accounting for the energy dissipation through viscous effects and can reproduce quite well the tidal flows. This code also provides the local RV corrections with respect to a rigid body rotation, which is useful in the spectral computation. Finally, one can notice that the TIDES code could also be used for circular systems in asynchronous rotation. In such systems, tidal flows can also occur and the linear approximation of the Roche model is no longer valid because the viscous responses induce non-linear effects. The surface and velocity field computations obtained with the TIDES code are used in our model, CoMBiSpeC, to compute the spectra (see chap. 2).

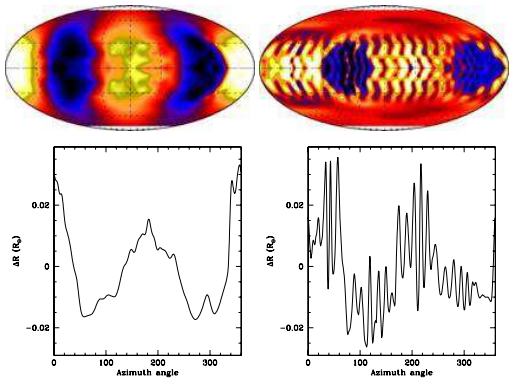

Figure 1.11: *Top*: maps of radius residuals ($r(\varphi) - R$) for $e = 0.8$, $P = 15$ d, $\beta_0 = 1.2$ at periastron (left) and 0.833 day later (right). The longitude $\varphi = 0$ is at the far left on each map and $\varphi = 180$ °is at the center. The sense of the stellar rotation is from left-to-right. White/black represents maximum/minimum residuals. *Bottom*: corresponding plots of the radius residuals along the equator. Figure from Moreno et al. (2011).

Classification of binaries

We can now introduce a classification of binary systems based on their shape: the detached, semi-detached, contact, and over-contact binaries.

- Detached binaries are systems in which the two stellar surfaces follow distinct equipotentials and none of the stars fills up its Roche lobe.

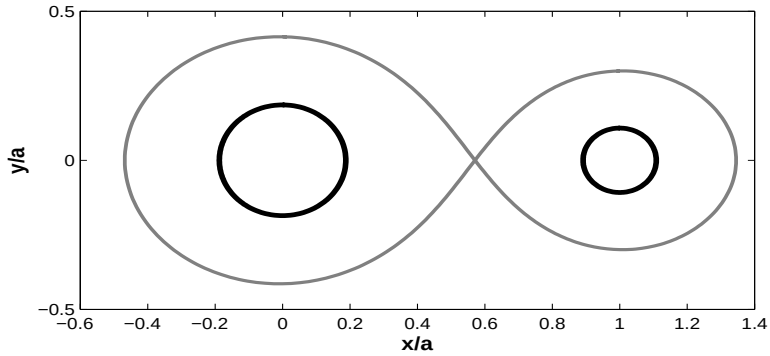

Figure 1.12: Detached binary in black. The Roche lobe is indicated in grey.

- Semi-detached binaries are systems in which the two stellar surfaces follow distinct equipotentials but one star fills its Roche lobe. Practically, the star that fills up its Roche lobe transfers mass to the companion. This situation is known as Roche lobe overflow (RLOF).

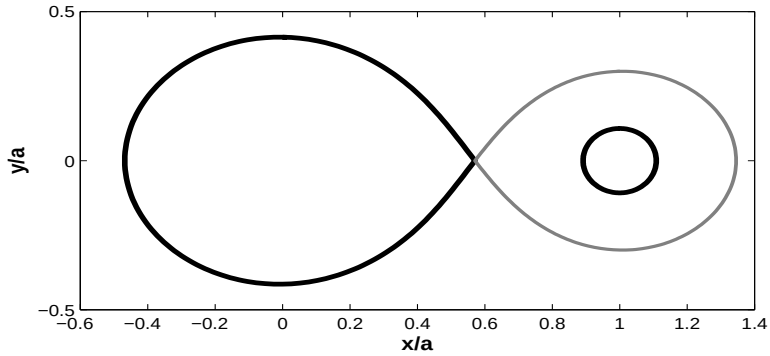

Figure 1.13: Semi-detached binary in black. The Roche lobe of the secondary is indicated in grey.

- Contact binaries are systems in which the two stars fill their Roche lobe. They are in contact at the L_1 point. In practice, this stage does not exist and the stars are in over-contact. Notice that our code, CoMBiSpeC, cannot model over-contact binaries and is limited to contact binaries.

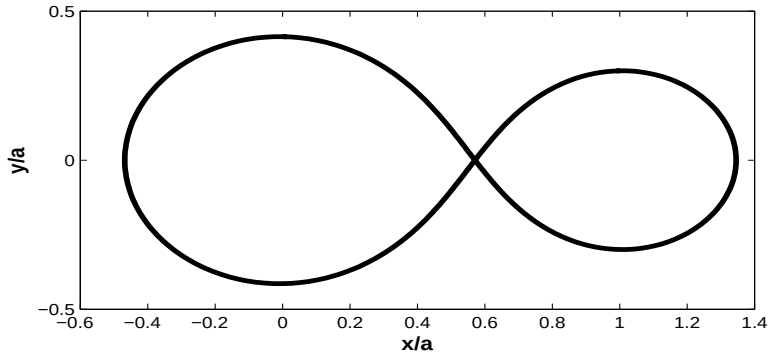

Figure 1.14: Contact binary. The two stars fill their Roche lobe.

- Over-contact binaries are systems in which a common envelope exists. It is the last stage where we can talk about two stars. Beyond this stage, the stars merge and form a new single star.

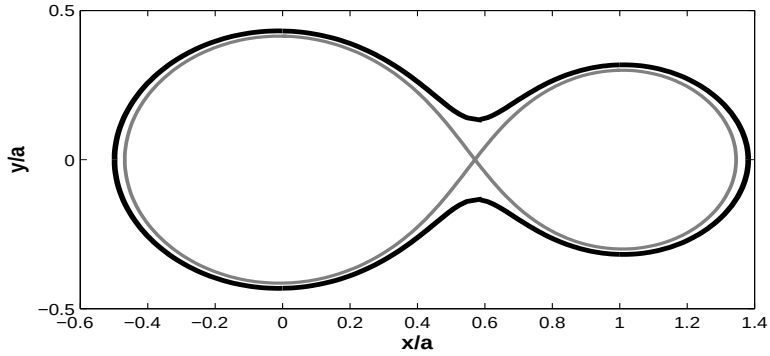

Figure 1.15: Over-contact binary in black. The Roche lobe is indicated in grey.

1.1.3 Darkening and radiative effects

The knowledge of the shape and gravity distribution at the stellar surface is not sufficient to compute a spectrum. The temperature distribution is also needed. However, several effects can affect this distribution. We present here three important effects: the limb-darkening, the gravity-darkening and the reflection effects. Finally, we will address the radiation pressure effects that act on the shape of the star and on its gravity and temperature distributions.

Limb-darkening effect

The limb-darkening is a well-known effect that refers to the decrease of the light intensity from the centre of the disk towards the edge (or limb). The limb-darkening is due to the increase of the optical depth along the line of sight towards the limb of the stellar disk. In other words, it reflects the dependence of the intensity (I) with the angle γ between the line of sight and the direction of the emergent flux. Milne (1921) introduced the first approximation of the limb-darkening. Several authors (see, for example, Al-Naimiy 1978, Diaz-Cordoves et al. 1995 and references therein, Claret & Bloemen 2011) have proposed other expressions to treat this effect. We have chosen the linear approximation which is the simplest formulation. According to Al-Naimiy (1978), we can write

$$I(\mu) = I(1)(1 - u + u\mu) \tag{1.16}$$

where $\mu = \cos\gamma$ and u is a scalar coefficient that depends on the temperature and the wavelength. We have used the tabulations of Al-Naimiy (1978) and Claret & Bloemen (2011) for the coefficient u. Even though this effect is important, its impact on the spectra of massive binaries is small. It is the main reason why we did not use a more sophisticated law for its treatment.

Gravity-darkening effect

The gravity-darkening consists in a variation of the temperature with gravity. This phenomenon has been first described by von Zeipel (1924) who showed that the radiative flux is proportional to the local gravity. This demonstration is known as von Zeipel's theorem

$$T_{\rm local} = T_{\rm pole}\left(\frac{\left\|\underline{\nabla}\Omega_{\rm local}\right\|}{\left\|\underline{\nabla}\Omega_{\rm pole}\right\|}\right)^{0.25p}, \tag{1.17}$$

where $p = 1$ in the case of massive stars. This phenomenon is very important and can lead to significant changes of temperature between the equator and the pole of the stars (see Fig. 1.16). In the case of contact binaries, the temperature drops theoretically to zero at the L_1 contact point. Practically, another effect (see next section) prevents this decrease of the temperature to zero. However, the difference between the polar and equatorial temperature can reach several thousand Kelvin, which is not negligible.

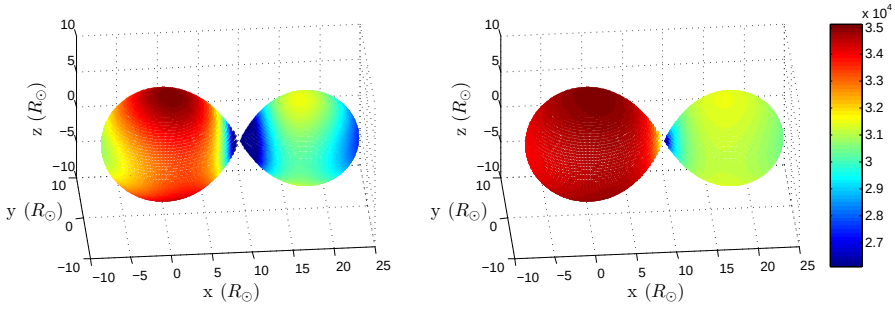

Figure 1.16: Example of temperature distribution affected by gravity darkening for model B (see appendix B.4 for the parameters). *Left:* the von Zeipel parameter, p, equals 1. *Right:* the von Zeipel parameter equals 0.25.

Recent studies (Espinosa Lara & Rieutord 2011 and references therein) proposed more complicated models to deal with gravity darkening. However, our computations have shown that the classical theorem is sufficient for the spectral computation. In the case of a contact binary, the effect of a change of the von Zeipel parameter, p, are small in a range of $p = 1 \pm 0.25$. The effect is moderate in a range of $p = 1 \pm 0.5$ and becomes important in the case of a change greater than 0.50. However, Espinosa Lara & Rieutord (2011) showed that their new formulation is equivalent to a change of the von Zeipel parameter in the range $[0.55, 1.12]$. In this range, the impact on the spectral computation is generally small and will often stand below the noise level (see Fig. 1.17).

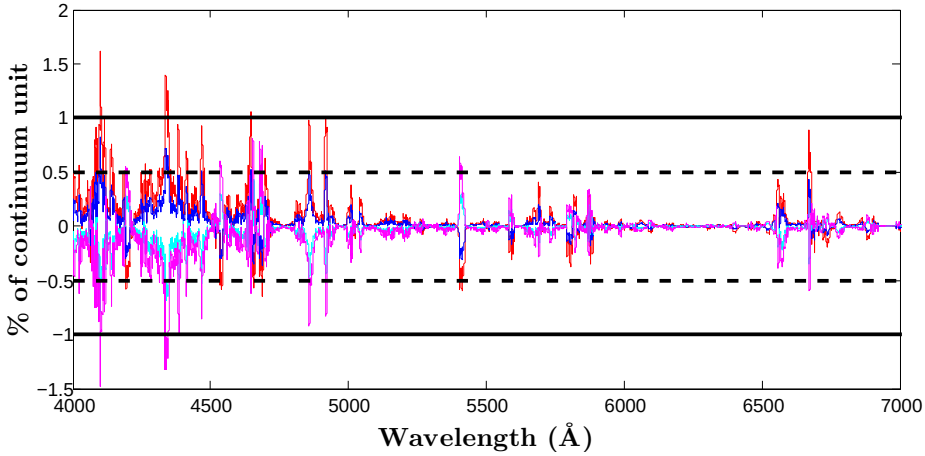

Figure 1.17: Relative difference between the spectra with a von Zeipel parameter $p = 0.5$ (*red*), 0.75 (*blue*), 1.25 (*ligth blue*), and 1.5 (*pink*) and the spectrum with $p = 1$ for the model based on the parameters of model B (see appendix B.4) at the orbital phase 0.25 where the lines of the two stars are the less blended. The horizontal lines display 0.5 (*dashed*) and 1% (*solid*) of relative difference.

Reflection effect

The reflection effect is the increase of the temperature of the facing part of the stars due to the mutual irradiation of each component by the other. The treatment of this effect is not straightforward and one of the most commonly adopted formalisms was proposed by Wilson (1990). In the case of circular (equilibrium) systems, the two stars always present the same face to each other and the solution of Wilson (1990) is completely valid. In the case of eccentric or

asynchronous binaries, the situation is different because the facing parts of the stars change during the orbital motion, thus, the solution is, strictly speaking, not valid. However, we will assume that, at each orbital phase, there exists an "instantaneous" reflection effect that heats the facing part of the stars for these systems. In other words, we will apply the solution of Wilson at each orbital phase. The impact of this assumption on the spectral computation is difficult to evaluate. One can notice that a recent work of Budaj (2011) suggests a new treatment of the reflection effect that would account for temperature redistribution at the stellar surface. This problem will be discussed in more details in the section 2.4.

The treatment proposed by Wilson (1990) consists in an iterative procedure in which we assume a radiative equilibrium at each point of the surface and calculate a coefficient of reflection. In each point of the primary (secondary), we compute the emitted and received bolometric flux. If we note $_1$ the quantities associated to the primary and $_2$ those of the secondary and if we consider two stellar surface elements ($dS_j = {r_j}^2 \sin\theta_j \Delta\theta\Delta\varphi / \cos\alpha_j$, see Fig. 1.18), we can write for the primary (resp. for the secondary with $_1 \longleftrightarrow {}_2$) that the received flux from the secondary is[4]

$$ {F_2}^{\text{received}} = A_1 \sum_{\varphi_{\text{vis}}} \sum_{\theta_{\text{vis}}} I_2 R_2 \cos\gamma_1 \cos\gamma_2 U(\gamma_2) \frac{{r_2}^2 \sin\theta_2 \Delta\theta\Delta\varphi}{\|\vec{s}\|^2 \cos\alpha_2} \tag{1.18} $$

where,

- A is the albedo defined by Wilson (1990) as the local ratio of the re-radiated energy to the irradiance energy ($A = 1$ in the case of local conservation of energy).
- θ and φ are the colatitude and longitude.
- R is the reflection factor. It is the ratio between the bolometric flux including reflection and the one without reflection.
- γ is the angle between the normal to the surface $\vec{e_n}$ and the vector between the two points $\vec{s}$.
- U is the linear limb-darkening correction (see sect.1.1.3).
- r is the radius of the star at the current position.

[4] ${F_j}^{\text{received/emitted}}$ has to be read: flux received/emitted from j.

- $\vec{s}$ is the vector between the two points.
- α is the angle between the normal to the surface $\vec{e_n}$ and the radial direction $\vec{e_r}$.
- I is the emitted flux and is equal to $I = \sigma_{SB} T^4$ with σ_{SB} the Stefan-Boltzmann constant and T the local effective temperature (i.e. accounting for gravity darkening).

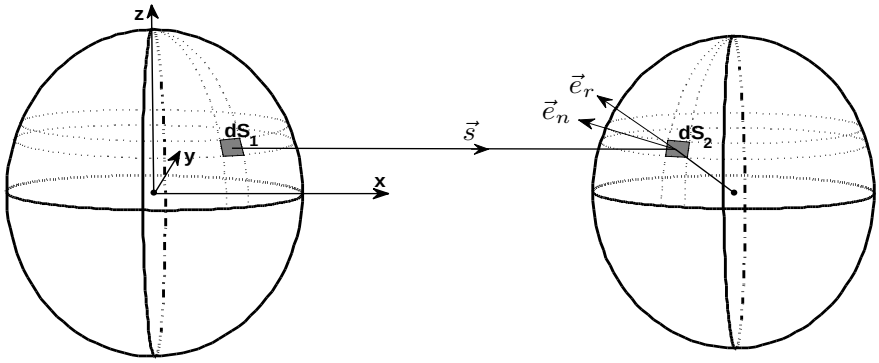

Figure 1.18: Geometrical elements for the reflection effect between the surface elements dS_1 and dS_2.

This equation is integrated numerically over all the surface elements of the secondary that "see" a surface element of the primary (two surface elements are visible one to another if $\cos\gamma_1 \geq 0$ and $\cos\gamma_2 \geq 0$). Then, we have to perform this integration for all the surface elements of the primary. In other words there are two numerical integrations. On the primary, the flux emitted by a surface element is

$$F_1{}^{\text{emitted}} = U(int) I_1 \tag{1.19}$$

where, $U(int)$ is the linear integrated limb-darkening correction $U(int) = \pi(1 - u/3)$ with u the linear coefficient of Claret & Bloemen (2011). The iteration is done on the reflection factor that can be expressed (Wilson 1990)

$$R_1 = 1 + \frac{F_2{}^{\text{received}}}{F_1{}^{\text{emitted}}} \tag{1.20}$$

Once we reach convergence (i.e. R does not vary anymore) the new temperatures are computed so that (see Fig. 1.19)

$$T_1{}^{\text{new}} = T_1{}^{\text{old}} R^{0.25} \tag{1.21}$$

The reflection effect is always included in the computation of CoMBiSpeC (see chap. 2).

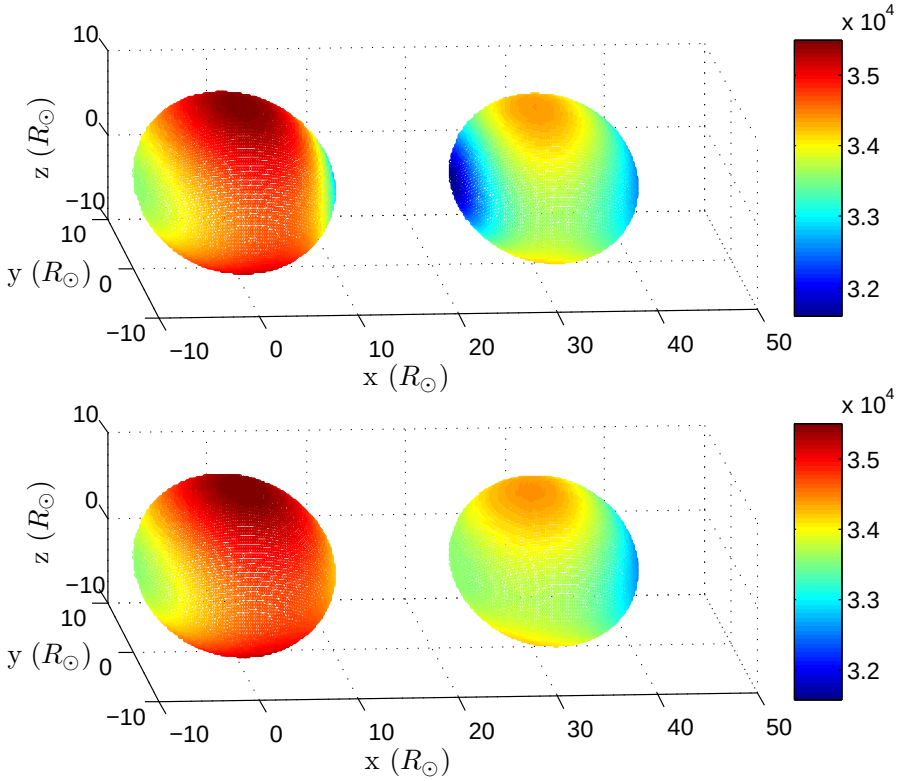

Figure 1.19: Example of temperature distribution for model C (see appendix B.4 for the parameters) without (*top*) and with (*bottom*) reflection effect. The lowest temperatures are not located at the parts of the stars which are facing each other when the reflection effect is accounted for.

Radiation pressure effects

The radiation pressure is an important issue in the computation of the stellar surface especially in the case of massive stars where this pressure can become high. A relatively rich literature (see for example Dermine et al. 2009, Howarth 1997, Schuerman 1972, Drechsel et al. 1995, and Phillips & Podsiadlowski 2002) is available on the treatment of the radiation pressure. On the basis of this literature, we have developed a new model for the radiation pressure (Palate et al. 2013b) that mixes the solutions of Howarth (1997), Drechsel et al. (1995) and Phillips & Podsiadlowski (2002). The radiation pressure can be divided in three parts (Dermine et al. 2009):

- Internal radiation pressure: the effect of the radiation pressure on each star's own surface.
- External radiation pressure: the impact of the radiation pressure of a star on the surface of its companion.
- Outer radiation pressure: the effect on the matter outside the binary orbit. This effect is not important in the computation of the stellar surfaces or in the spectral computation, that is why we do not consider it any further.

In our approach, the internal and external radiation pressures can be treated separately, which is one of the main advantages of the solution of Howarth (1997) with respect to the solution of other authors like Schuerman (1972). Another advantage is that the von Zeipel theorem remains valid. The difference between the two solutions is really important. In the Schuerman (1972) approach, the masses of the stars are scaled, while Howarth (1997) proposed to scale the entire Roche potential of the stars. *The latter approach is more physical (it is the potential, and not the actual mass of a star, which is diminished by radiation pressure), and leads to a simpler result (Howarth 1997).* This approach is more appropriate because the emitted bolometric flux and hence the radiation pressure scale with the local gradient of the potential (which also includes the attraction by the other star and the centrifugal forces). Therefore, according to Howarth (1997), the stellar topology is not affected by internal radiation pressure and the latter simply scales the local surface gravity (see Fig. 1.20). The Newtonian gravity is defined by

$$\vec{g} = \vec{\nabla}\phi, \tag{1.22}$$

where ϕ is a scalar gravity potential.

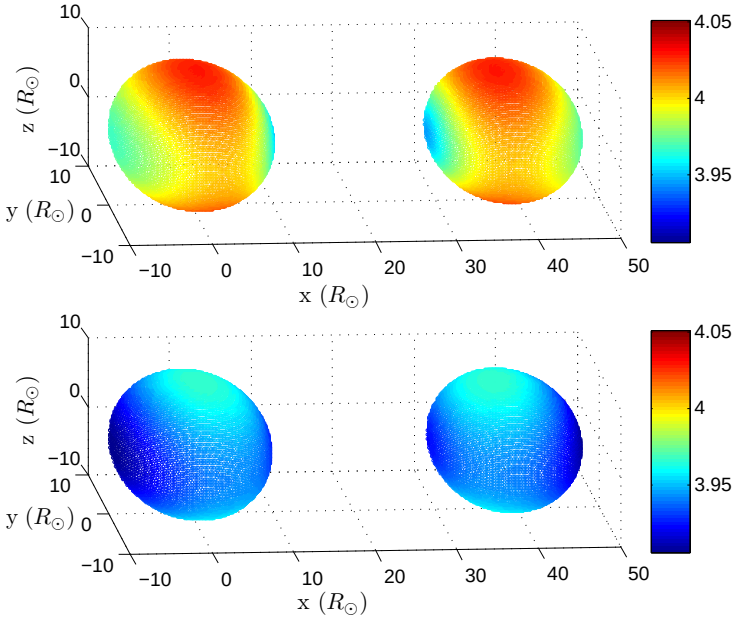

Figure 1.20: Example of gravity distribution for model A (see appendix B.4 for the parameters) without (*top*) and with (*bottom*) radiation pressure. In this model, the external radiation pressure has a limited impact and the internal radiation pressure clearly scales down the value of the surface gravity.

The von Zeipel (1924) theorem can be written

$$T^4 \propto \left\| \vec{g} \right\|, \tag{1.23}$$

The magnitude of the radiative acceleration is given by

$$a_{\text{rad}} = -\frac{\kappa\pi}{c}\mathcal{F}, \tag{1.24}$$

where κ is the flux mean opacity per unit mass and $\mathcal{F}$ is the astrophysical flux. If we introduce Γ, the ratio of the radiative to the gravitational acceleration: $a_{\text{rad}} = \Gamma g$ we obtain

$$\vec{g}_{\text{eff}} = (1 - \Gamma)\vec{g}, \tag{1.25}$$

From the previous equations, we have $\phi_{\rm eff} = (1-\Gamma)\phi$ and the scaling factor Γ can be written (following Castor et al. 1975)

$$\Gamma = \frac{\sigma_{Th}}{m_H c}\sigma_{SB}T_{\rm pole}^4\frac{1}{\left\|\vec{g}_{\rm pole}\right\|}, \tag{1.26}$$

with $\frac{\sigma_{Th}}{m_H} \approx 0.036\ \mathrm{m^2 kg^{-1}}$, σ_{Th} the Thomson scattering cross section and σ_{SB} the Stefan-Boltzmann constant.

The second part of the radiation pressure is the external one. Our method is based on the approach of Drechsel et al. (1995) and Phillips & Podsiadlowski (2002). The treatment consists in scaling the mass of the companion in the Roche potential with a scale parameter $\delta = \frac{F_{\rm rad}}{F_{\rm grav}}$. This parameter is computed iteratively for each surface point. The physical justification to this scaling is still in debate in the literature. However, the external radiation pressure can be seen as a force that decreases the attraction of the companion. Therefore, the companion seems less massive, which is equivalent to a decrease (scale down) of the mass of the companion. The new "Roche" potential can be written

$$\Omega = \frac{1}{r} + \frac{q(1-\delta(r,\theta,\varphi))}{\sqrt{r^2 - 2r\cos\varphi\sin\theta + 1}} + \frac{q+1}{2}\cdot r^2\sin^2\theta - qr\cos\varphi\sin\theta, \tag{1.27}$$

where $r = \sqrt{x^2+y^2+z^2}$, $q = \frac{m_2}{m_1}$, $x = r\cos\varphi\sin\theta$, $y = r\sin\varphi\sin\theta$, and $z = r\cos\theta$. Here, θ and φ are, respectively, the colatitude and longitude angle in the spherical coordinates centred on the star under consideration.

The problem consists in the determination of the δ factor. We first start from the classical Roche potential and determine the value of the δ factor. The determination is rather similar to the treatment of the reflection effect in the sense that we have to evaluate the flux received by a surface element from the companion. The radiation pressure is given by

$$P_{\rm rad} = \frac{1}{c}\int_0^\infty\int_\omega I_\nu\cos^2\gamma_1\,\mathrm{d}\omega\mathrm{d}\nu, \tag{1.28}$$

where γ_1 is the angle between the normal to the irradiated surface and the direction between the irradiated surface and the emitting surface. I_ν is the specific intensity of the external radiation field.

The radiation pressure gradient per unit mass is equal to (in the plane parallel approximation):

$$\begin{aligned} F_{\rm rad} &= -\frac{1}{\rho}\frac{{\rm d}P_{\rm rad}}{{\rm d}r} \\ &= \frac{1}{c}\int_\omega\int_0^\infty \kappa_\nu \frac{{\rm d}I_\nu}{{\rm d}\tau_\nu}\cos^2\gamma_1\,{\rm d}\nu{\rm d}\omega \\ &= \frac{1}{c}\int_\omega\int_0^\infty \kappa_\nu I_\nu\,\cos\gamma_1\,{\rm d}\nu{\rm d}\omega, \end{aligned} \tag{1.29}$$

At the stellar surface, the dominant source of opacity comes from electron scattering, thus, we have $\kappa_\nu = \frac{\sigma_{Th}}{m_H}$ which is independent of frequency. We also have $I_\nu = I_{\nu,0}\cdot(1-u+u\cos\gamma_2)$ where γ_2 is the angle between the normal to the emitting surface and direction between the irradiated surface and the emitting surface, u the linear limb-darkening coefficient. Moreover, we have ${\rm d}\omega = \frac{{\rm d}S_2 cos\gamma_2}{s^2}$ where s is the distance between the irradiated and the emitting surface and S_2 is the emitting surface. Finally, if the radiation comes only from the companion, we have

$$\int_0^\infty I_{\nu,0}\,{\rm d}\nu = \frac{\sigma_{SB}T^4}{\pi}. \tag{1.30}$$

The local δ factor is thus defined by $\delta = \frac{F_{\rm rad}*d^2}{GM}$ where d is the distance between the point and the centre of the emitting star. This factor can be written (for the radiation emitted by the secondary and received by the primary) as

$$\delta_2 = \frac{\sigma_{SB}\sigma_{Th}d^2}{\pi c m_H G M_2}\sum_{\substack{cos\gamma_1\geq 0\\ cos\gamma_2\geq 0}} T_2^4(1-u+u\cos\gamma_2)\cos\gamma_1\cos\gamma_2\frac{{\rm d}S_2}{s^2} \tag{1.31}$$

With the δ factor, we recompute the stellar surface with the modified Roche potential. Then, we re-evaluate the δ factor and surface until we reach convergence (see Fig. 1.21).

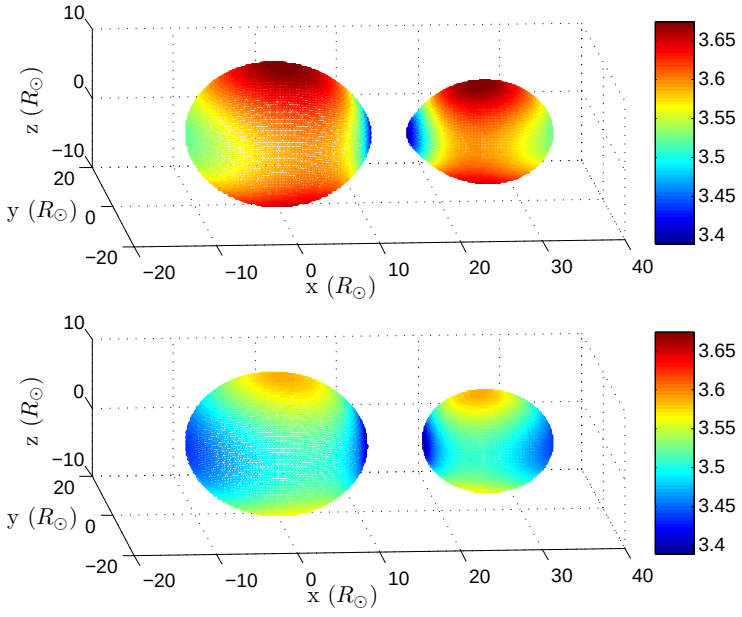

Figure 1.21: Example of gravity distribution for model D (see appendix B.4 for the parameters) without (*top*) and with (*bottom*) radiation pressure. The inclusion of the external radiation pressure clearly modifies the surface of the secondary star and the internal radiation pressure scales down the value of the surface gravity.

1.2 Spectroscopy

Spectroscopy is the study of the spectrum of the light due to a physical phenomenon. A spectrum is a convenient way to present the information conveyed by the light in the form of a plot of the distribution of the amount of light (flux, intensity, ...) as a function of energy (or wavelength). This information is related to the properties and to the composition of the environment where the light has been produced, and/or to those of the medium crossed by this light. In astrophysics, the spectra have various sources: planets, comets, interstellar clouds, nebulae, galaxies, AGN, ... and of course stars. Spectroscopy is an important field of astrophysics because the spectra are a fundamental source of information. We will present here which information is available and then, we will discuss some types of problems encountered when we deal with a binary spectrum. Before that, we have to define what we call the primary star and the secondary star because this definition varies depending on the authors. In spectroscopic binaries, the primary is sometimes defined as the most luminous star, i.e. the one that dominates the spectrum. However, in this thesis, the primary is always defined as the most massive star of the system. This definition has been chosen for computational reasons.

1.2.1 What can we learn from a spectrum ?

The main information we can deduce from a spectrum are: the effective temperature, $T_{\rm eff}$, the surface gravity, $\log g$, the chemical composition, and the projected equatorial rotational velocity, $v \sin i$. In the case of a binary system, we can also determine the radial velocity, the mass ratio, q, and the luminosity ratio, $\frac{L_P}{L_S}$. With the help of a synthetic spectral computation code we can also estimate the radii of the stars. Wind properties and signatures of a stellar magnetic field can also be found in the spectra. We will now describe the way to determine, for massive binaries, those properties that are modelled with CoMBiSpeC (see chap. 2).

Effective temperature $T_{\rm eff}$ can be determined through the spectral classification of the stars. The criterion of Conti & Alschuler (1971) - Mathys (1988; 1989) establishes a link between the ratio of the equivalent widths (EWs) of the He I λ 4471 and He II λ 4542 lines and the spectral class (see Tab. 1.1). Another way to establish the spectral classification is to use an atlas of reference stars (see e.g. the atlas of Walborn & Fitzpatrick 1990) and compare the studied spectrum to the reference (see Fig. 1.22). Then, we can use calibrations such as those of Martins et al. (2005) to estimate the temperature.

Subtype	log(EW')	Subtype	log(EW')
O3	< -0.90	O7.5	+0.00 to +0.09
O4	−0.90 to −0.61	O8	+0.10 to +0.19
O5	−0.60 to −0.46	O8.5	+0.20 to +0.29
O5.5	−0.45 to −0.31	O9	+0.30 to +0.44
O6	−0.30 to −0.21	O9.5	+0.45 to +0.64
O6.5	−0.20 to −0.11	O9.7	+0.65 to +1.00
O7	−0.10 to −0.01		

Table 1.1: Quantitative O-type star spectral classification based on the Conti & Alschuler (1971) – Mathys (1988; 1989) determination. log(EW') = log(EW(4471)) – log(EW(4542)).

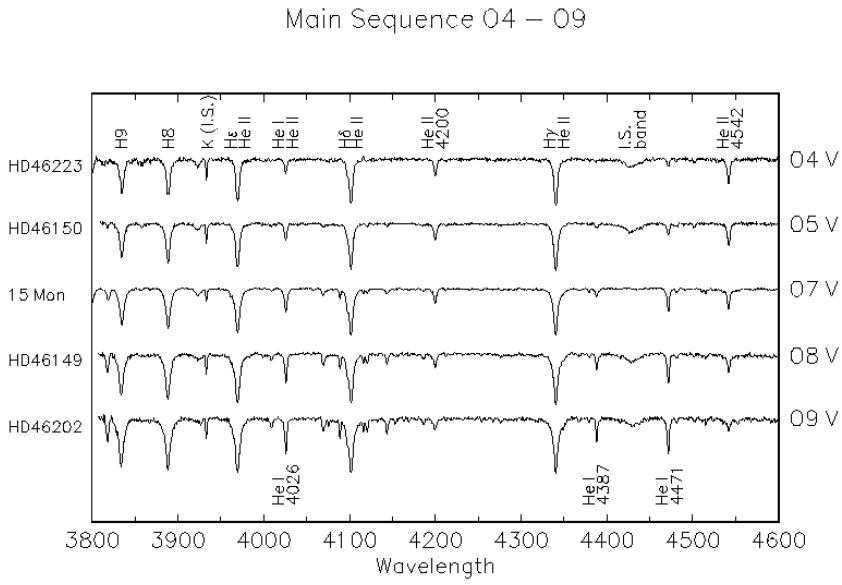

Figure 1.22: Examples of spectra of O-type stars of increasing temperatures from the website of R. O. Gray (A Digital Spectral Classification Atlas v1.02, http://ned.ipac.caltech.edu/level5/Gray/Gray_contents.html, accessed: 13/02/2014).

One can notice that the EWs of the lines vary with temperature. For example, the EW of the He II lines increases with the temperature over the range of O-type stars whilst the EW of the He I lines decreases. Finally, to refine the temperature, an atmosphere model computed with a code such as CMFGEN (Hillier & Miller 1998) or TLUSTY (Hubeny & Lanz 1992), ... can be used.

The main problem of these techniques is that the classification criteria and calibrations have been determined for single spherical stars and are not well suited for binary systems. For binaries, even the concept of the $T_{\rm eff}$ is less clear because the temperature is not uniform over the stellar surface. Moreover, the mean observed temperature can change during the orbital cycle. The non-sphericity of the stars is the main source of this problem that will be discussed in more details in the next section.

Surface gravity The line equivalent widths can change with the temperature but also with $\log g$. A first information can be found using the criteria of Conti & Alschuler (1971) or Mathys (1988; 1989) that indicates the luminosity class - supergiant (I), giant (III) or dwarf (V). These criteria are based on the ratio of the EW of the Si IV λ 4088 to the He I λ 4143 lines and the one of the He I λ 4388 to the He II λ 4686 lines (see Tab. 1.2). The Balmer series of hydrogen is also used since the width of the hydrogen Hδ, Hγ, Hβ lines is influenced by gravity through the Stark broadening. The larger $\log g$, the broader the line. Again, the use of a calibration and/or an atlas is required to completely estimate the $\log g$, and an atmosphere model will help to refine the value (see Fig. 1.23). For the binaries, the same problem as for the temperature appears because $\log g$ is not constant over the stellar surface.

Luminosity class	$\log(EW'')$	$\log(EW''')$
I	$\geq +0.31$	< 5.15
III	+0.11 to +0.30	+5.15 to +5.40
V	−0.20 to +0.10	> 5.40

Table 1.2: Quantitative O-type star luminosity classification based on the Conti & Alschuler (1971) determination: $\log(EW'')$ = log(EW(4088)) − log(EW(4143)) and the Mathys (1988; 1989) determination $\log(EW''')$ = log(EW(4388)) − log(EW(4686)).

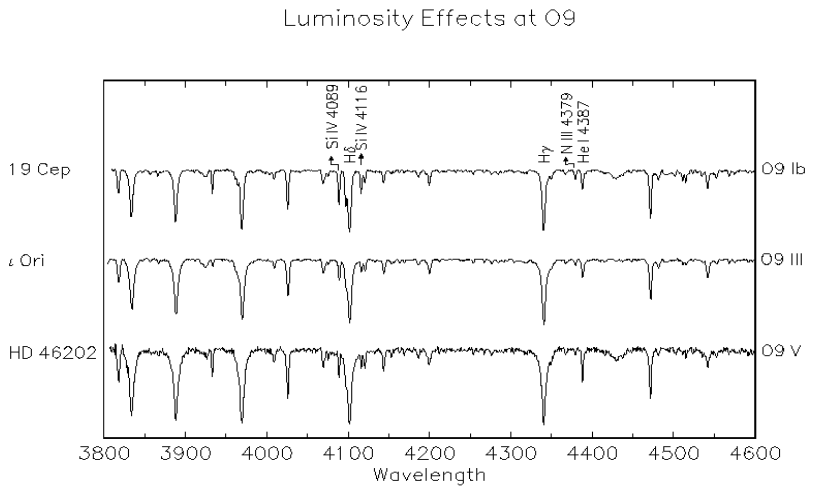

Figure 1.23: Examples of spectra of O-type stars of different luminosity class from the website of R. O. Gray (A Digital Spectral Classification Atlas v1.02, http://ned.ipac.caltech.edu/level5/Gray/Gray_contents.html, accessed: 13/02/2014).

Abundances The chemical composition of the star directly impacts the observed spectra. Over recent years, a major effort has been devoted to the determination of accurate atomic parameters. The rest wavelengths that have been compiled can be used to identify atoms, ions, and molecules present in the stellar atmosphere. We have mainly used the NIST Atomic Spectra Database available at: http://www.nist.gov/pml/data/asd.cfm. Usually, the EW of a line increases with the abundance of the element but the dependence of the EW with the abundance is complex and an abundance determination requires the use of curve of growth methods or model atmosphere codes.

Radial velocity The radial velocity, RV, determination is based on equation 1.7. The wavelength of a line is measured. The narrower the line, the more accurate is the measurement. The measured wavelength is then used in equation 1.7 to derive the RV. The procedure is repeated for a maximum of orbital phases, and often for several lines, in order to construct RV curves. In practice, the blend of the lines of the primary and secondary can render the measurement difficult. In any case, the RV curve is periodic with a period equal to that of the orbit of the binary.

Rotational velocity The projected rotational velocity at the stellar equator, v $\sin i$, is related to the width of a line. Determining v $\sin i$ is not easy. Simón-Díaz & Herrero (2007) listed four methods to measure this value: the measurement of the full-width-half-maximum of the observed line profile, cross-correlation with a template spectrum with a low rotational velocity (the cross-correlation function is related to the v $\sin i$), comparison with synthetic line profiles convolved with broadening functions, and the Fourier transform of the line profile. However, the broadening of a line is also influenced by other factors such as the micro- and macro-turbulences that render the v $\sin i$ determination more difficult.

Mass ratio As mentioned in the previous section, in SB2 systems, the mass ratio, q, can be determined from the semi-amplitude of the RV curve of the primary and secondary: $q = m_2/m_1 = K_1/K_2$. With our definition of the primary and secondary, we always have $q \leq 1$. We can also determine the minimal masses of the stars, $m_j \sin^3 i$ ($j = 1, 2$ for the primary and the secondary).

Luminosity ratio The luminosity ratio can be determined by measuring the EWs of prominent lines. For O-star binaries, one frequently uses the He I $\lambda\lambda$ 4026, 4143, 4388, 4471, 5876, He II $\lambda\lambda$ 4200, 4542, Si IV λ 4089, and O III λ 5592 lines. The ratio of the EWs of these lines compared to the average of the observed values reported by Conti & Alschuler (1971), Conti (1973), and Conti et al. (1977) allows to determine the luminosity ratio.

Before addressing the problems directly linked to the binary systems, we wish to mention the separation techniques of the spectra that are very useful and complementary to the spectral modelling. Mahy (2011) and Pavlovski & Hensberge (2010) gave a review of the different methods of reconstruction that can be divided in three groups: spectral separation, spectral disentangling, spectroastrometric splitting.

In this thesis, we have only used the spectral disentangling technique in which a time series of observed spectra gives the individual spectra of the components and the orbital elements in a self-consistent way. The disentangling can be divided in several groups depending on the technique used. The three main methods have been developed by Simon & Sturm (1994), Hadrava (1995), and González & Levato (2006). These techniques are powerful tools. However, for systems with a strong temperature gradient at their surface (e.g. HD 100213, Linder et al. 2007), the disentangling fails because different lines have different radial velocity amplitudes. In eclipsing binaries, disentangling cannot be used

for the phases near the eclipses. Finally, this technique provides mean spectra of both components, and even if we can measure variations with respect to this mean, we cannot compute the spectra at each orbital phase, at least not if the components feature a complex temperature distribution.

1.2.2 Problems linked to the binarity

In close binary systems, the stars are not spherical[5]. This might seem obvious but it is the main reason why the binary systems cannot be considered as single stars. As we have shown, the fact that the stars are deformed induces gravity and temperature gradients. In the case of non-equilibrium systems, the deformations of the stars change during the orbital cycle and can lead to line profile variations. These gradients, line profile variations and geometrical effects can perturb both the RV curve and the light curve, and have an impact on the spectra.

Some concepts are also more difficult to define for stars in binary systems. The effective temperature, the $\log g$, and the radius become non constant and have to be defined at a particular location at the stellar surface (for example: the pole or the equator).

The spectral synthesis code CoMBiSpeC that we have designed (see chap. 2) does not solve all problems but it does highlight new explanations on four problems frequently encountered in massive binaries: the luminosity classification, the Struve-Sahade effect, the line-to-line differences of the RV amplitude (or temperature distribution effect), and some line profile variations.

Luminosity classification

Several authors (e.g. Sana et al. 2005, Linder et al. 2007 and references therein) encountered difficulties to assign a proper luminosity class to the components of the binary that they studied. The indication of the classical Conti & Alschuler (1971) - Mathys (1988; 1989) criterion and the $\log g$ derived from other methods (photometry) where not compatible. The criterion overestimated the luminosity class (a dwarf as identified from the light curve was classified as a giant or a supergiant). Our CoMBiSpeC models (Palate & Rauw 2012) showed that the error does not come from blends of the primary and secondary lines because the criterion gives the same result if it is applied to individual spectra or on the spectra of the system (hereafter combined spectra). The slight changes between a single star spectrum and the CoMBiSpeC spectrum are sufficient to induce a change in the EWs that leads to the classification error. Therefore, this efficient

[5]Notice that deviation from spherical symmetry can also be the consequence of stellar rotation, and especially in fast rotating stars (see appendix A.1).

criterion for single stars has to be used with great caution in the case of massive binaries. A good approach to classify the star is to disentangle the spectra, and then to use an atlas (e.g. Walborn & Fitzpatrick 1990).

Struve-Sahade effect

The Struve-Sahade effect was first defined as the apparent strengthening of the secondary spectrum when this star is approaching the observer and its weakening as the star moves away (Howarth et al. 1997, Linder et al. 2007, see Fig. 1.24). Another, more general, definition is that the Struve-Sahade effect is the apparent variation of the line strengths of either of the binary components as a function of the orbital phase (Howarth et al. 1997, Linder et al. 2007).

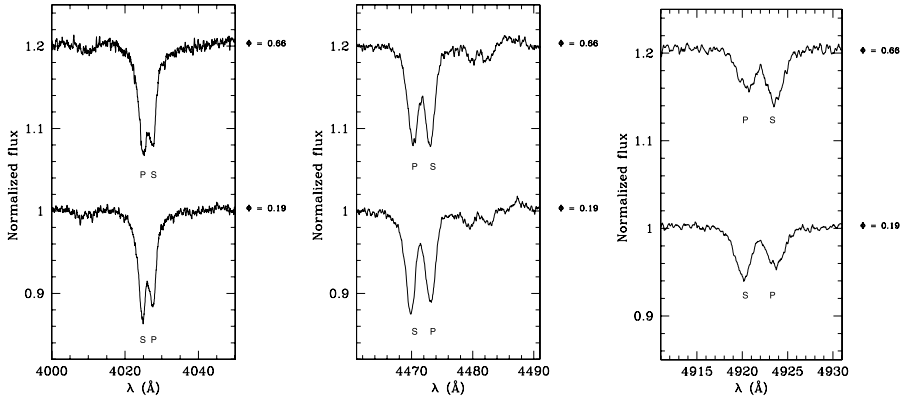

(a) He I λ 4026 (b) He I λ 4471 (c) He I λ 4921

Figure 1.24: Example of observed Struve-Sahade effect in the HD 165052 system (from Linder et al. 2007). The Struve-Sahade effect is clearly visible in the He I $\lambda\lambda$ 4026 and 4471 lines but less in He I λ 4921. The lines of the secondary seems stronger when the star approaches ($\phi = 0.19$, *bottom*) and weaker when it moves away ($\phi = 0.66$, *top*).

Pickering & Bailey (1896) were the first to report line strength variability. Then, Maury (1921) gave a more detailed description, but the first who really studied this phenomenon was Struve (1937). He proposed that the effect be caused by streams of gas moving towards the secondary and obscuring the latter. Later, Sahade (1959) performed further in-depth studies, and also suggested the presence of gas streams. Gies et al. (1997) instead suggested that the phenomenon might be due to heating by the back-scattering of photons by the stellar-wind interaction zone, while Stickland (1997) proposed that the Struve-

Sahade effect could be linked to a combination of several mechanisms. Finally, Gayley (2002) and Gayley et al. (2007) suggested that the Struve-Sahade effect be linked to flows at the stellar surface.

CoMBiSpeC has highlighted a new explanation. Our computations have shown that the use of de-blending routines that fit Gaussian or Lorentzian profiles to measure the EWs did not work properly in the cases where the intrinsic line profiles of the individual stars are asymmetric (see Fig. 1.25). In these cases, the de-blending routines introduce systematic effects that mimic the Struve-Sahade effect. The origin of this intrinsic asymmetry is due to the temperature and gravity distribution.

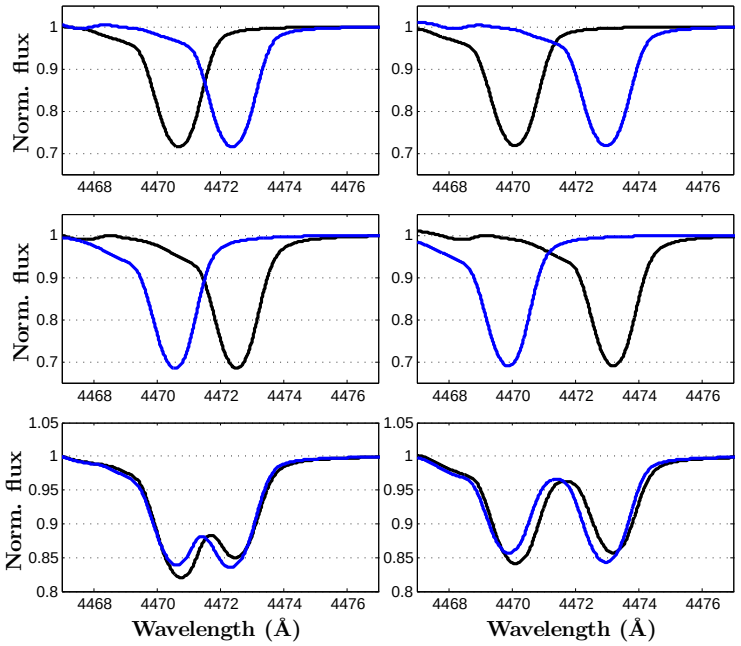

Figure 1.25: Synthetic spectra of the He I λ 4471 line of model C (see appendix B.4 for the parameters). *Left:* orbital phases 0.1 (*black*) and 0.9 (*blue*). *Right:* orbital phases 0.25 (*black*) and 0.75 (*blue*). *From top to bottom:* spectra of the primary, of the secondary, and of the system. The Struve-Sahade effect is more visible in the *left* situation where the extended blue wing of the line of either star reinforces the apparent strength of the line of its companion.

Temperature distribution effect

Linder et al. (2007) reported on a non-uniform surface temperature in the HD 100213 system. One can observe this non-uniformity through discrepancies between the RV semi-amplitude of the He I and He II lines. In the case of a uniform temperature distribution, the He lines are formed all over the surface without preference. However, in the case of a non-uniform temperature distribution, the He I lines are preferentially formed in "low-temperature" regions and He II lines are formed in "high-temperature" regions.

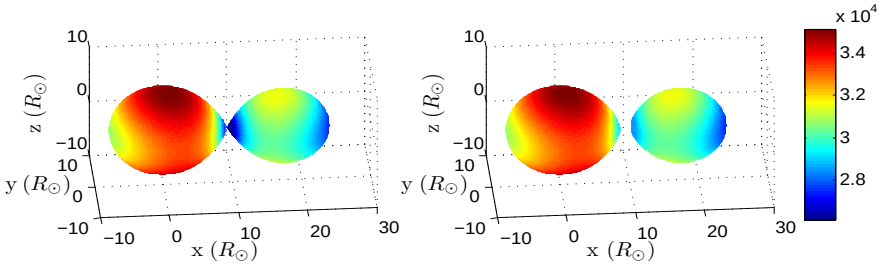

Figure 1.26: Temperature distribution for model B (see appendix B.4 for the parameters) without (*left*) and with (*right*) radiation pressure. The front temperatures are not the lowest when we account for radiation pressure.

The link between the RV semi-amplitude and the temperature is not obvious, but the highest semi-amplitude corresponds to the farthest surface point from the centre of the star, whilst the lowest semi-amplitude corresponds to the nearest surface point from the centre of the star. Therefore, if the RV semi-amplitude of He II lines is smaller than the one of the He I lines, it means that the hotter regions of the star are located closer to the companion than the cooler parts. This kind of temperature distribution can be reproduced with CoMBiSpeC but it requires to account for radiation pressure effects (see Tab. 1.3 and Fig. 1.26).

Line profile variations

Massive binaries that are not in equilibrium can present line profile variations. Usually, these variations were classified as β Cephei-type pulsations (e.g. Spica, Shobbrook et al. 1969; 1972). However, we have shown that the origin of the line profile variations could be the tidal flows induced by the interactions between the two stars. The variations are described as travelling "bumps" that move from the blue to the red wing of weak photospheric absorption lines. They are also strongly phase-dependent.

Line	$K_{1,obs}$	$K_{1,-p}$	$K_{1,+p}$	$K_{2,obs}$	$K_{2,-p}$	$K_{2,+p}$
He I λ 4026	246.5	223.4	245.4	363.8	372.3	362.2
He I λ 4471	244.5	234.7	245.7	372.3	368.7	361.0
He II λ 4686	251.3	255.9	240.6	355.2	383.9	343.6
He I λ 4921	245.9	(255.1)	(257.3)	373.0	(365.5)	(363.0)
He II λ 5412	239.8	249.3	238.8	351.2	360.1	338.8
He I λ 5876	(269.7)	229.6	244.9	(388.8)	357.2	357.7

Table 1.3: Amplitudes of the radial velocity curves (in $\mathrm{km\,s^{-1}}$) of the He lines in the HD 100213 (model B, see appendix B.4 for the parameters) spectra. Comparison observation - model B without (-p index) and with (+p index) radiation pressure. Values in brackets stand for larger error bars or problematic lines in the spectral modelling.

Because of non equilibrium, the surface of at least one of the stars of the system is perturbed by tidal interactions. Therefore, some oscillations appear at the stellar surface. These oscillations move surface elements to higher or lower RVs with respect to the non perturbed surface. These "excesses" of high/low RV surface elements introduce "excesses" of red/blue intensity in the lines. The excess of intensity in the lines changes during the orbital cycle which produces the migrating bumps and therefore the line profile variations (see Fig. 1.27). This effect mainly affects the absorption lines of intermediate intensity. The line profile variations can distort the RV curve and lead to an apparently higher eccentricity. One can notice that this line profile variation is not reproduced by single-star static atmosphere models.

1.3 Photometry and other techniques

CoMBiSpeC is not primarily designed to compute light curves. However, from spectral integration, we can compute synthetic light curves. We stress that it is not the main goal of CoMBiSpeC and that light curves are rather "by-products" of the spectral computation. Other codes such as *Nightfall*[6] or *PHOEBE*[7] are specifically designed to compute and fit light curves. We also briefly address other important techniques : astrometry, Doppler tomography, asteroseismology and polarimetry.

[6]For details see the *Nightfall User Manual* by Wichmann (1998) available at the URL: http://www.hs.uni-hamburg.de/DE/Ins/Per/Wichmann/Nightfall.html

[7]For details see the website of *PHOEBE* at the URL: http://phoebe-project.org

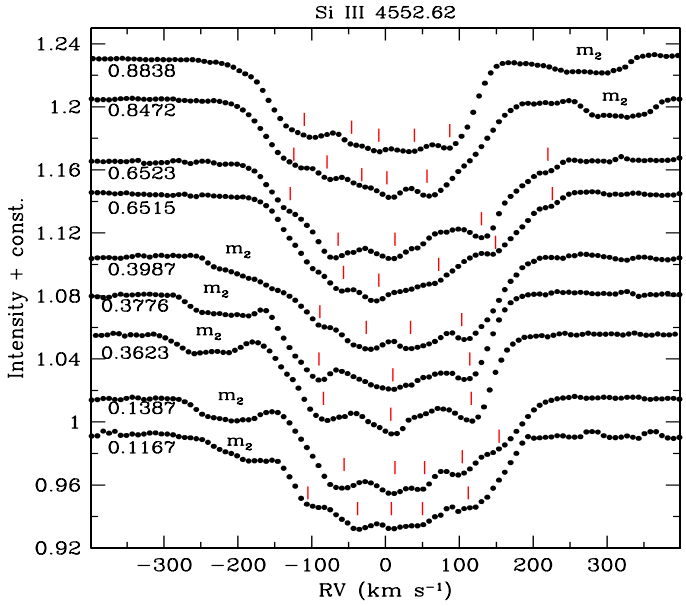

Figure 1.27: Montage of the observed Si III line profiles of Spica on a velocity scale centred on 4552.62 Å, and corrected for the orbital motion of the primary. The spectra are vertically arranged by orbital phase. The tick marks show the troughs of travelling bumps and the secondary's component is marked with m_2. Figure from Harrington et al. (2009).

1.3.1 Light curve

Photometry and spectroscopy are probably the two main techniques of investigation in astrophysics. Spectroscopy focuses on the distribution of the light as a function of wavelength whilst photometry is the study of the light flux integrated over some bandpass. In theory, the photometric data can be deduced by integration from the spectrum. However, in practice, it is very difficult to get a calibration in flux when we measure a spectrum, and part of the information is lost.

The photometry measures the flux of a star in a given bandpass at a given time. Multiple measurements of the flux allow to study the variability of a star. Standard photometric filter systems are used to compare the photometric data.

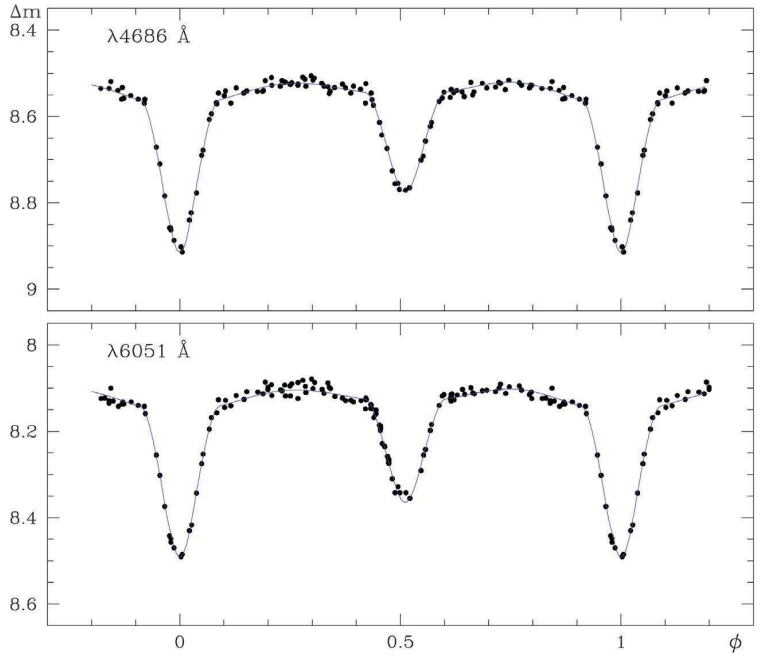

Figure 1.28: Observed (*dots*) and modelled (*solid lines*) light curves at λ4686 Å and λ6051 Å of the CPD -41°7742 system. The eclipses are clearly visible and correspond to a decrease of the flux. Figure from Sana et al. (2005).

In the binary context, the photometry is an important source of information and especially in the case of an eclipsing binary. It is possible from a light curve to determine several parameters by least square problem inversion (see Fig. 1.28). The work of Wilson & Devinney (1971) provides the fundamentals of this method. In the best cases, we can deduce 12 parameters ($j = 1, 2$ for primary and secondary): i, L_j (the luminosities), x_j (the limb-darkening coefficients), p_j (the gravity darkening parameters), T_j (the temperatures), q, Ω_j (the surface potentials). However, generally, some parameters have to be fixed (from spectroscopic data for instance). In the case of an eclipsing binary, part of the flux is blocked during the eclipses and there is a decrease of the total flux of the system received by the observer. It is therefore possible to evaluate the orbital inclination and the radii of the stars. CoMBiSpeC provides flux information in the wavelength range $[3500, 7100]$ Å (see chap. 2). Basic light curves can therefore be constructed (see Fig. 1.29).

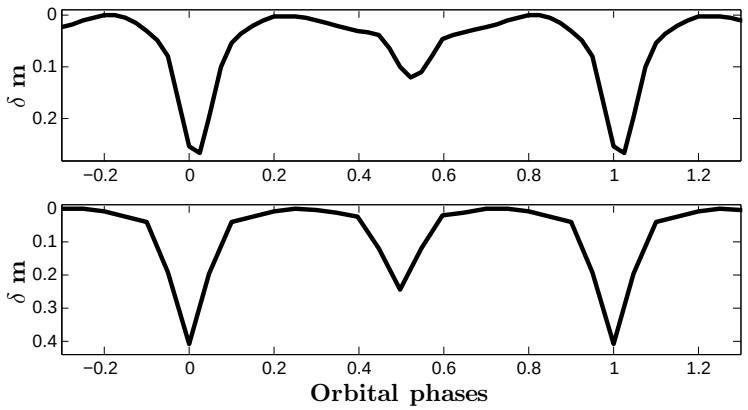

Figure 1.29: Synthetic light curves in the wavelength range [3500, 7100] Å. *Top:* Light curve of the model E (see appendix B.4 for the parameters) computed with a CoMBiSpeC + TIDES model. *Bottom:* Light curve of the model F (see appendix B.4) computed with a CoMBiSpeC model. The eclipses are visible in the two systems. The stiff aspect is due to the relatively small number of points (respectively 40 and 20 per orbital period) in the light curves.

1.3.2 Other techniques

Astrometry is the technique of astrophysics that studies the distance and position of celestial bodies in the sky. The distance can be deduced from parallax measurements. The recently launched satellite Gaia[8] will measure the parallax of about 1 billion stars with an accuracy of 10 μas at a magnitude $V = 15$. The distance information is very important to completely determine the absolute luminosities, or to study the evolutionary status of the stars, the structure of the galaxy and the interactions between the stars.

Doppler tomography is an image reconstruction method that allows to map the line-formation region of an emission line in velocity space of a binary system (see e.g. Marsh & Horne 1988) from a series of spectra. Doppler tomography requires high resolution spectra and good phase coverage. This method is particularly used to study line profile variations or wind structures (see Rauw et al. 2002; 2005 for examples of applications). Horne (1991) gives a detailed discussion of the Doppler tomography methods.

[8]For more details see the Gaia website: http://www.esa.int/Our_Activities/Space_Science/Gaia

Polarimetry is similar to photometry or spectroscopy except that a polarimetric analyser is used to measure the degree of polarisation. The polarisation of the light of a star can have multiple origins: magnetism, scattering by accretion disks or circumstellar matter, by the photosphere due to shape distortion, by a companion star (reflection). For example, the spectro-polarimetric analyses of Grunhut et al. (2013) suggest that there exists a magnetic field in Plaskett's star.

Asteroseismology is the discipline that studies the stellar seismology or, in other words, the surface oscillations of pulsating stars. It is the only technique that allows to study the internal structure of the stars as the oscillation modes penetrate to different depths inside the stars. The analyses of the frequencies of the oscillations help to determine the region where the waves originate and travel and also help to determine the internal chemical composition (see e.g. Brown & Gilliland 1994 or Aerts et al. 2010 for further information).

Chapter 2

CoMBiSpeC

Atmosphere models for single stars exist for several decades and have become powerful tools in spectral analyses. However, we have shown that stars in binary systems are not spherical, that is why these atmosphere models cannot account for all the spectral features of binary systems. In the latter cases, we have in principle to solve 3D radiative transfer equations, but solving such equations in 3D is a challenging problem that requires heavy computational power. To overcome this issue, we can rely on models such as the code of massive binary spectral computation, CoMBiSpeC that we have developed. This model provides a first order solution to the problem.

The history of models of non-spherical stars dates back to the work of Russell & Merrill (1952) that aimed at reproducing light-curves. Kopal (1959) introduced the Roche potential and then, Lucy (1968), Wilson & Devinney (1971), and numerous other authors used and extended this concept. However, all these works were done for light-curves analyses and not for spectral analyses. CoMBiSpeC allows to compute synthetic spectra of binary systems and consists in computing the stellar surface following the Roche potential approach and deriving the local gravity and temperature on each surface element. Non-LTE spectral model grids (TLUSTY, Lanz & Hubeny 2003; 2007) are used to compute the integrated spectrum of the star at each orbital phase (see also, e.g., Linnell & Hubeny 1994, Linnell et al. 2012). CoMBiSpeC also includes radiation pressure effects and, combined to the TIDES code, allows to compute the spectra of eccentric binaries and/or systems in non-synchronous rotation.

2.1 General information

CoMBiSpeC is written in C++. This language provides a good compromise between high-level and low-level language features and is very efficient for scientific computing. The code takes advantage of multiple CPUs because it uses parallel computing and thus needs the *Open MPI* library[1]. It has been developed for *Linux* OS and the compilation is done with the *mpic++* compilator. The code also uses several standard C++ libraries. A *makefile* helps to compile CoMBiSpeC.

The code is divided in 28 files (13 code files **.cpp*, and 15 header files **.h*). The main file of the code, *Binary.cpp*, initiates the computation and calls other subroutines that compute the geometrical elements (surfaces, $\log g$, temperatures, ...) and the spectra (see the flowchart of CoMBiSpeC in appendix B.4). The parameters of the systems to study are given in two *text* files: *Input.txt* and *Options.txt*. Several models can be read and computed one after another.

For circular synchronous binaries, the geometrical computation does not require any other files than the two *text* files. In the case of eccentric and/or asynchronous binaries, the surface computation is done with the TIDES code and the interfacing routine needs the *datos.paralelos* and *datos.propaz* files. Notice that we have to compute the *datos.propaz* file for each star with the same number of longitude and latitude angle steps in order to have the same *datos.paralelos* files.

For any binary system, the spectral computation requires a grid of synthetic spectra in a 2-columns format (wavelength - flux). This grid has been computed from the OSTAR2002 and BSTAR2006 databases built with TLUSTY[2]. The wavelength range is $\lambda \in [3400-7200]$ Å, the temperature range is $T_{\rm eff} \in$ [15000, 55000] K by steps of 1000 K between 15000 and 30000 K and by steps of 2500 K between 27500 and 55000 K, the maximal $\log g$ range is $\log g \in [1.75, 4.75]$ and depends on the temperature (see Fig. 2.1). High resolution ($\Delta\lambda = 0.02$ Å) and low resolution spectra ($\Delta\lambda = 2$ Å) are available (the latter are used for the continuum computation). A total number of 224 high resolution spectra are available in the grid. Note that since the TLUSTY code assumes a plan-parallel atmosphere, the models only account for photospheric lines.

The execution time mainly depends of the number of points of the surface grid. We give here the computation time for a grid of 100×30 points for the ϕ (longitude) and θ (colatitude) angles. The tests have been done on a *Linux 2.6.31.4* OS with an Intel® Core™ 2 Quad CPU Q9400 at 2.66GHz. The

[1] http://www.open-mpi.org

[2] http://nova.astro.umd.edu/Tlusty2002/tlusty-frames-guides.html

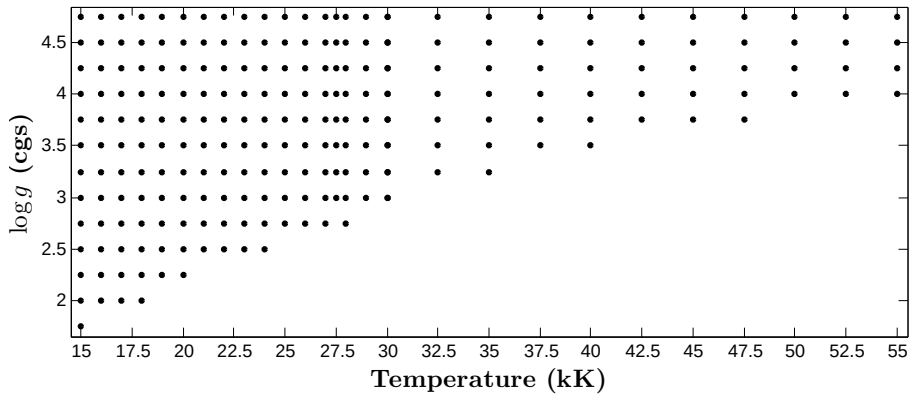

Figure 2.1: Synthetic spectra present in the grid.

computation time is measured with the *time* command of the OS and the results are given in Table 2.1. Therefore, the computation of a circular model with 20 orbital phases, takes about 13,5 hours with 4 CPUs. The memory (RAM) usage is relatively small but increases with the number of CPUs. The hard disk drive space usage is high because the spectral grid represents nearly 1 Go of data.

Table 2.1: Computation time for 1, 2, and 4 CPUs. The execution time has been evaluated for the surface computation only (with and without radiation pressure), for the black body curve computation and for the computation of one spectrum. The times are given in seconds. The gain in execution time when going from 1 to 4 CPUs is largest for spectral computation and amounts to a factor 1.94 for 2 CPUs and 3.76 for 4 CPUs.

Computation	1 CPU	2 CPUs	4 CPUs
Surface without p_{rad}	11.0	7.3	5.0
Surface with p_{rad}	51.7	26.9	16.0
Black body curves	0.9	0.5	1.3
Spectrum	939.5	483.6	249.7

2.2 Circular systems

We now describe the computation scheme for a circular system and we present some of the computational issues and solutions adopted to ensure the good processing. The schematic view of the main file for a circular system is

```
MPI initialisation operations
Reading of the input and option files

for(Loop on the phases){
  //Computation of the stellar surface & temperature
    Roche_T();

  //Computation of the black body curve and RV
    Black_body();

  //Computation of the spectrum of the stars and
  //Computation of the spectrum of visible part of the stars
    if(phase = 0){Spectrum_star();}
    Spectrum();
}
```

The first step of the code is to read the input files that contain the parameters of the binary system(s):

- Period (d)
- Eccentricity
- Longitude of periastron (°)
- Inclination (°)
- Mass of the primary star ($M_\odot$)
- Mass of the secondary star ($M_\odot$)
- Temperature at the pole of the primary star (K)
- Temperature at the pole of the secondary star (K)
- Polar radius of the primary star ($R_\odot$)

- Polar radius of the secondary star ($R_\odot$)
- von Zeipel parameter of the primary star
- von Zeipel parameter of the secondary star
- Albedo of the primary star
- Albedo of the secondary star
- β of the primary star (= 1 for a circular orbit)
- β of the secondary star (= 1 for a circular orbit)
- Calculation of the surface of the stars (if = 1)
- Inclusion of radiation pressure (if = 1)
- Call of black body function (if = 1)
- Call of spectrum function (if = 1)
- Storage of the result (if = 1)

The options files are also read and contain:

- Number of steps for ϕ angle ($\phi \in [0, 2\pi]$). A number of steps for the longitude angle between 120 and 240 is usually sufficient for a good computation.
- Number of steps for θ angle ($\theta \in [0, \pi]$). A number of steps for the latitude angle between 30 and 60 is usually sufficient for a good computation.
- Number of orbital phases. A computation of 20 orbital phases is a good compromise between computation time and time resolution.
- Number for optional calculation of a peculiar phase. A peculiar phase can be introduced here for the computation of one additional spectrum.
- Number of models that will be computed. As mentioned above, several models can be run simultaneously. This option indicates how many models will be computed.

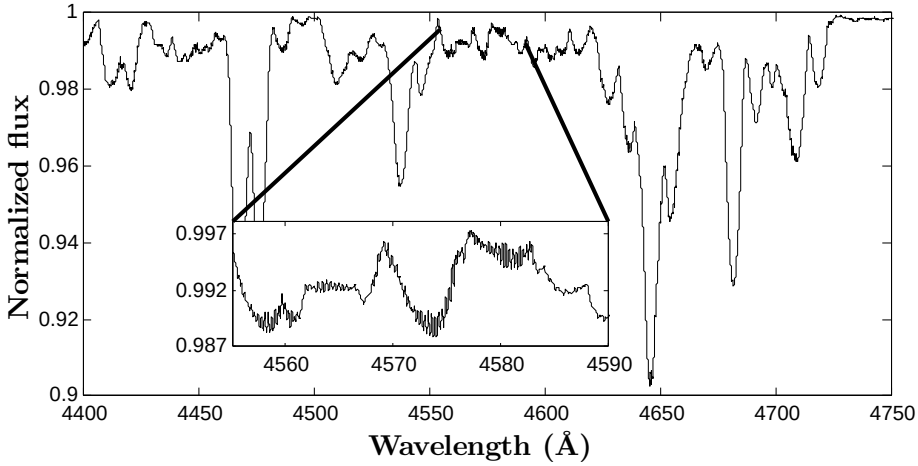

Figure 2.2: Synthetic spectra for model B (see appendix B.4 for the parameters) with under-sampling of the ϕ and θ angles (60×15). Numerical oscillations appear mainly in weak lines.

One can notice that a low number of steps for the ϕ and/or θ angles (below 100 and 20 steps) can lead to numerical oscillations in the spectra (see Fig. 2.2) due to the lack of points in the surface mesh grid. The origin of these oscillations is purely numerical and completely different from those observed in the spectra of Spica (see sect. 3.2). They are mainly localized in the core of the weakest lines and completely disappear if the number of steps increases.

Then, CoMBiSpeC computes the stellar surface, the $\log g$ distribution, and the $T_{\rm eff}$ distribution accounting for the radiation pressure if asked for by the user (`Roche_T` routine). The `Black_body` routine computes the emission from the visible part of the stars assuming each cell emits as a black body according to its temperature. It also provides the radial velocities of each surface point, indicates which are the visible surface points, and what is their area. The `Spectrum_star` routine computes the spectrum of the star accounting for all the points with the v_{rad} of the centre of mass of the star set equal to 0 and with the v_{rad} of all the points equal to 0. This computation can help identify the lines that are present in the spectra. Finally, the `Spectrum` routine computes the spectra of the visible part of the stars for several orbital phases accounting for the actual radial velocities.

2.2.1 Systems without radiation pressure

Geometrical computation

The computation of the surface is done in the following way ($i = 1, 2$ for the primary and the secondary).
Roche_T routine:

```
Choice of the equipotentials (depend on the specified radii)

for(Loop on surface points){
  //Computation of the surfaces
    ri = newton_raphson(ri, PHI, THETA, omega0i);
  //Computation of gradients of Roche potential
    grad_rochei = gradfct(ri, PHI, THETA);
  //Computation of temperatures (Von Zeipel + Reflection)
    Ti = Tpolei*|grad_rochei/grad_rochei[pole]|^(0.25*cvzi);
}
//Computation of temperatures (Reflection effect)
  Reflection();
```

To avoid dealing with large numbers (for example, at least a factor 10^8 for the radii) that render the convergence uncertain, we use dimensionless potentials (equations 1.13, 1.14) for the two stars. Therefore, the radii and surface gravity are computed without dimensions. With these dimensionless potentials, the radii are smaller than 1 which offers a good way to check the results of the computation. The dimensionless quantities are multiplied by the appropriate dimensions before being written to the output files. The radii are computed following an extended Newton-Raphson method in which the second derivative of the function is used to increase the convergence. The convergence criterion on the radii is small and equal to a tolerance between two iterations of $tol = 10^{-12}$. This method is described in Karniadakis & Kirby (2003). Let us consider the equation: $f(x) \equiv x - g(x)$ and $f(s) = 0$. We note h the distance between the exact solution s and an initial guess x_0, We have the Taylor expansion (to the second order) around x_0

$$\begin{aligned} f(s) = 0 &= f(x_0 + h) = f(x_0) + hf'(x_0) + \tfrac{h^2}{2} f''(x_0) \\ &= f(x_0) + h\,[f'(x_0) + \tfrac{h}{2} f''(x_0)] \end{aligned} \tag{2.1}$$

Therefore, we can write

$$h = -\frac{f(x_0)}{f'(x_0) + \frac{h}{2}f''(x_0)} \tag{2.2}$$

Now, we have to compute a provisional value for h in the denominator, say h^*. h^* is obtained from the linear Taylor expansion

$$h^* = -\frac{f(x_0)}{f'(x_0)} \tag{2.3}$$

At the iteration $n+1$, we have $x_{n+1} = x_n + h_n$ and from equations 2.2, and 2.3 we have

$$\frac{1}{h_n} = -\frac{f'(x_n)}{f(x_n)} + \frac{1}{2}\frac{f''(x_n)}{f'(x_n)} \tag{2.4}$$

This two-step approach is a *predictor-corrector* method that slightly improves the convergence rate of the classical Newton-Raphson method.

The $\log g$ value is obtained by taking the gradient of the Roche potential (`gradfct (ri, PHI, THETA)`). The temperature without reflection is computed with the theorem of Von Zeipel (`cvzi` is the parameter - also called coefficient - of Von Zeipel). The derivatives and gradient have been computed analytically to avoid numerical errors. The expressions of these quantities are given in the appendix B.3.

The reflection computation follows the theoretical formulae (see sect. 1.1.3). However, our computations have highlighted a convergence problem for binaries that are in contact or nearly so. A coupling between the surface points that lie close to the Lagrangian L_1 point occurred and led to a divergence of the temperature (the computations were stopped after reaching more that 100 kK for stars with a $T_{\rm pole} \approx 35$ kK).

Therefore, we have chosen to stop the iterations once at least 99 % of the surface points reached convergence. If this criterion is not reached after 15 iterations, the code returns an error message and stops. The convergence criterion generally prevents large increases of the temperature and ensures the success of the reflection computation. However, to avoid very high, non-physical temperatures, another check is made by comparing the difference between the temperature of two adjacent surface points (ΔT) to the initial highest temperature difference ($\Delta T_{\rm max,0}$). If $\Delta T > \Delta T_{\rm max,0}$, the temperature is interpolated between the nearest converged points (with a maximum of three steps). Finally, if there are no converged surface points for the interpolation, an error message is returned and the code stops. One can also notice that for symmetry reasons,

the computation is done only for one quarter of the stellar surface that receives flux. This allows to reduce the computation time that is relatively high because of the two loops needed to treat the reflection process; one loop concerning the illuminated star, and the other one relative to the illuminating star.

Black body curves computation

This part of the code computes the black body emission of the visible part of the star during the orbital cycle. It also stores the Cartesian coordinates of the visible points of the surface at a given orbital phase as well as their RV and projected area along the line of sight. The black body curves are not strictly speaking the spectral energy distributions but they can help us define the $T_{\rm eff}$ of the star at a given phase. The evolution of the black body emission with the orbital phases is also a good indicator of the level of deformation of the stars (see Fig. 2.3). Spherical stars will always present the same emission while contact binaries will display important variations of the maximum of the curves.

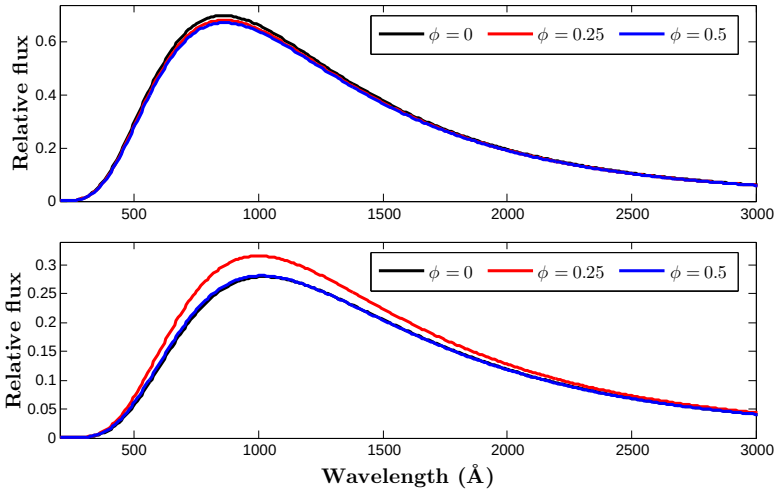

Figure 2.3: Black body emission for the primary (*top*) and secondary (*bottom*) star of model G (see appendix B.4 for the parameters) at orbital phases $\phi = 0, 0.25, 0.5$. In this system, the primary star is nearly spherical while the secondary nearly fills its Roche lobe.

The computation is done in the wavelength range $\lambda \in [100, 10000]$ Å and we use the Planck function:

$$BB(T) = \frac{2\pi hc^2}{\lambda^5}\left[\exp\left(\frac{hc}{\lambda kT}\right) - 1\right]^{-1} \times S_P \times I(\mu_P) \tag{2.5}$$

where h is the Planck constant ($h = 6.63\ 10^{-34}$ Js), c is the speed of light, S_P is the local area of the mesh around point P projected along the line of sight, $I(\mu_P)$ is the limb-darkening law.

Spectral computation

The computation of the spectra is done according to the following scheme ($i = 1, 2$ for the primary and the secondary).
Spectrum routine:

```
Initialisation operations
Reading of the data computed with Roche_T

for(loop on surface points){
   //Check if the point is visible
     if(check_vis(xi, yi, zi) {
     Search of the nearest log(g) & T in the grid
     Linear interpolation between
          the 4 nearest spectra of the grid
     Doppler shift
     Calculation of the local area
     Calculation of the output spectrum
   }
}
```

The first step of the spectral computation is to load the surface, gravity and temperature distributions previously computed. Then, we check if a surface point is visible or not at a given phase. If the point is visible, it contributes to the spectrum and therefore, we search for the 2 nearest spectra in $\log g$ and the 2 nearest spectra in $T_{\rm eff}$ in the grid. These 4 spectra are then linearly interpolated to get the local spectrum. If a spectrum is missing in the grid, the two nearest spectra in either temperature or $\log g$ are interpolated and an error file is created indicating which points are problematic and what are their temperature and $\log g$.

Remark 1 ***Interpolation***

The two interpolations are done in the following way:
Let us call g and T the $\log g$ *and* $T_{\rm eff}$ *of a point at the stellar surface and g_-, g_+, T_-, and T_+ the nearest value of the* $\log g$ *and* $T_{\rm eff}$ *of the spectra of the grid. If we denote by s_{--}, s_{-+}, s_{+-}, and s_{++} the value of the four spectra in the grid (the first index stands for* $T_{\rm eff}$ *and the second for* $\log g$*) and s the value of the local spectrum (see Fig. 2.4) we can write a first interpolation in* $\log g$ *as*

$$\begin{aligned} s_- &= \tfrac{g_+-g}{g_+-g_-}\times s_{--} + \tfrac{g-g_-}{g_+-g_-}\times s_{-+} = c_1 s_{--} + c_2 s_{-+} \\ s_+ &= \tfrac{g_+-g}{g_+-g_-}\times s_{+-} + \tfrac{g-g_-}{g_+-g_-}\times s_{++} = c_1 s_{+-} + c_2 s_{++} \end{aligned} \tag{2.6}$$

And the second interpolation in $T_{\rm eff}$ as

$$s = \frac{T_+ - T}{T_+ - T_-}\times s_- + \frac{T - T_-}{T_+ - T_-}\times s_+ = c_3 s_- + c_4 s_+ \tag{2.7}$$

These interpolations can be done in one step

$$s = c_1 c_3 s_{--} + c_2 c_3 s_{-+} + c_1 c_4 s_{+-} + c_2 c_4 s_{++} \tag{2.8}$$

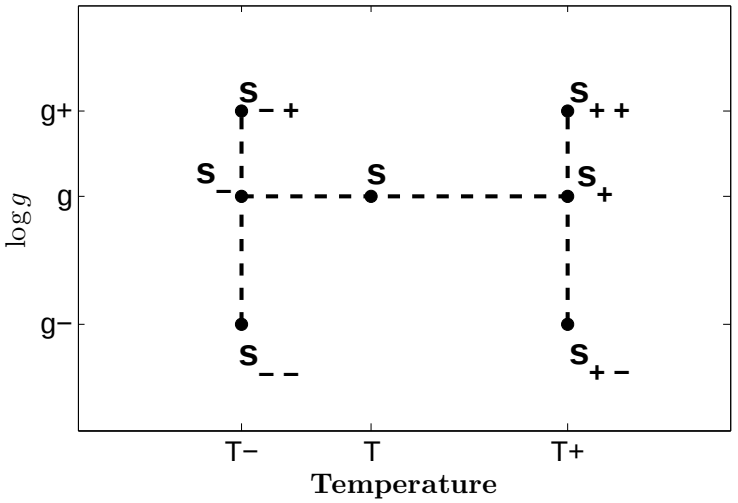

Figure 2.4: Interpolation between 4 spectra.

Afterwards, the local spectrum is Doppler shifted with the appropriate RV depending on the location of the point under consideration and the orbital phase.

Remark 2 ***RV of a point P of the stellar surface.***

Consider $\vec{v} = (v_x, v_y, 0)$ *the velocity vector of a point* $P(x, y, z)$*,* ω *the angular rotational velocity of the star equal to* $\vec{\omega} = \omega\vec{e_z}$ *and* $\vec{r} = x\vec{e_x} + y\vec{e_y} + z\vec{e_z}$*.* x *and* y *are measured from the centre of mass of the system. Notice that the change of coordinates from a frame of reference* (x_0, y_0, z_0) *centred on the centre of the primary to a system centred on the centre of mass* (x_{CM}, y_{CM}, z_{CM}) *is given by* $x_{CM} = x_0 - \frac{qa}{1+q}$*,* $y_{CM} = y_0$*, and* $z_{CM} = z_0$*. Therefore, we have*

$$\vec{v} = \vec{\omega} \otimes \vec{r} = -\omega y\vec{e_x} + \omega x\vec{e_y} \tag{2.9}$$

where $\omega = 2\pi/P$ *for systems in synchronous rotation.*

Moreover, we define the direction of observation as $\vec{n} = (n_x, n_y, n_z)$ *with* $n_x = \cos\psi \sin i$*,* $n_y = -\sin\psi \sin i$*,* $n_z = \cos i$ *and* ψ *the orbital phase. We have*

$$\begin{aligned} v_{rad} &= -\vec{v} \cdot \vec{n} = -[v_x \cos\psi \sin i - v_y \sin\psi \sin i] \\ &= \omega \sin i(y \cos\psi + x \sin\psi) \end{aligned} \tag{2.10}$$

At this stage, as a result of this Doppler shift, all the surface points have different wavelength vectors. In order to sum up their contributions and to get the whole spectrum, we need to re-interpolate the local spectra to a common wavelength vector. However, it sometimes happens that there is no point in the new wavelength base between two points of the old base, creating an empty gap (see Fig. 2.5). This empty gap leads to numerical errors that induce wrong spectral computation. To avoid this problem, the new wavelength vector is over-sampled by a factor 2. A message is displayed if an empty gap appears (this was never observed so far during the computation).

The local spectrum is finally multiplied by the area of the surface element perpendicular to the line of sight towards the observer and by the limb-darkening law before being summed to the total spectrum.

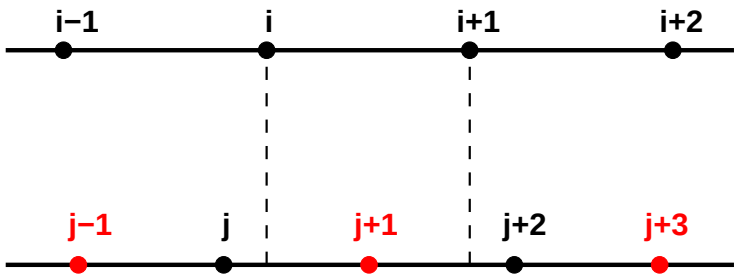

Figure 2.5: *Top:* wavelength base after Doppler shift. *Bottom:* wavelength base for summing up the spectra without (*black*) and with oversampling (*red*). One can see that without over-sampling, there is an empty gap between the point i and $i+1$. This gap induces numerical errors in the interpolation and leads to wrong spectral computation.

Remark 3 ***Local area associated with a point P.***

The equation of the local area associated with a point of the surface, $P(x, y, z)$, is given by

$$S_P = \frac{r^2 \sin\theta \mathrm{d}\theta \mathrm{d}\phi}{\cos\alpha} \tag{2.11}$$

where α is the angle between the normal to the surface $\vec{e_n}$ and the radial direction $\vec{e_r}$ (see Fig. 2.6, and sect. 1.1.3). Therefore, we have [3]

$$\cos\alpha = -\,\partial_r\Omega|_P \left\|\vec{\nabla}\Omega\right\|_P^{-1} \tag{2.12}$$

We define the direction of observation as $\vec{n} = (n_x, n_y, n_z)$ with $n_x = \cos\psi \sin i$, $n_y = -\sin\psi \sin i$, $n_z = \cos i$ and ψ the orbital phase.

[3] We denote $\partial_r\Omega$ the derivative of Ω with respect to r.

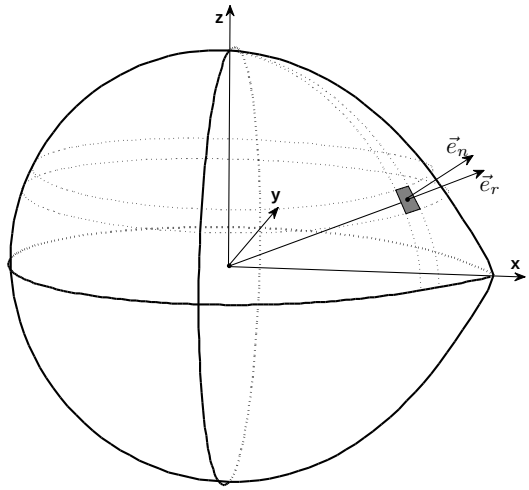

Figure 2.6: Normal vector to the surface, $\vec{e_n}$, and radial direction vector, $\vec{e_r}$.

The surface projected along the line of sight is equal to

$$\begin{aligned} S_{proj} &= S_P \left(\vec{n} \cdot - \frac{\vec{\nabla}\Omega}{\left\| \vec{\nabla}\Omega \right\|} \right) \\ &= -\frac{S_P}{\left\| \vec{\nabla}\Omega \right\|} (\vec{n} \cdot \vec{\nabla}\Omega) \\ &= \frac{r^2 \sin\theta \mathrm{d}\theta \mathrm{d}\phi}{\partial_r \Omega} (\vec{n} \cdot \vec{\nabla}\Omega) \\ &= \frac{r^2 \sin\theta \mathrm{d}\theta \mathrm{d}\phi}{\partial_r \Omega} (\partial_x \Omega \cos\psi \sin i - \partial_y \Omega \sin\psi \sin i + \partial_z \Omega \cos i) \end{aligned} \tag{2.13}$$

The equation of the derivative of Ω *with respect to* r *is given in the appendix B.3.*

This first approach has been tested to model 5 binary systems presented in Palate & Rauw (2012). An in-depth study of these systems has been performed on the combined binary spectra and on the individual spectra of the primary and secondary components. The problems of luminosity classification, Struve-Sahade effect, and temperature distribution effects were discussed. This first

simple approach has allowed to show that the classical criteria for the luminosity classification are not well suited for the binary systems and could lead to an overestimate of the luminosity class even if the individual spectra are used. A new explanation of the Struve-Sahade effect has also been proposed but we failed to reproduce the observationally inferred temperature distribution. The Struve-Sahade effect can result from the usage of deblending routines that rely on Gaussian/Lorentzian profiles to fit the asymmetrical lines of the spectra. These routines introduce systematic errors that mimic the Struve-Sahade effect when the actual lines have a non-Gaussian/non-Lorentzian and even asymmetric profile.

A&A 537, A119 (2012)
DOI: 10.1051/0004-6361/201117520

Astronomy & Astrophysics

Spectral modelling of circular massive binary systems

Towards an understanding of the Struve-Sahade effect?

M. Palate and G. Rauw

Institut d'Astrophysique et de Géophysique, Université de Liège, Bât. B5c, Allée du 6 Août 17, 4000 Liège, Belgium
e-mail: palate@astro.ulg.ac.be

Received 20 June 2011 / Accepted 2 September 2011

ABSTRACT

Context. Some secondary effects are known to introduce variations in spectra of massive binaries. These phenomena, such as the Struve-Sahade effect and the difficulties in determining properly the spectral type have been reported and documented in the literature.
Aims. We simulate the spectra of circular massive binaries at different phases of the orbital cycle and account for the gravitational influence of the companion star on the shape and physical properties of the stellar surface.
Methods. We use the Roche potential to compute the stellar surface, von Zeipel theorem, and reflection effects to compute the surface temperature. We then interpolate in a grid of non-local thermodynamic equilibrium (NLTE) plan-parallel atmosphere model spectra to obtain the local spectrum at each surface point. We finally sum all the contributions, accounting for the reflection, Doppler shift, and limb-darkening to obtain the total spectrum. The computation is done for different orbital phases and for different sets of physical and orbital parameters.
Results. Our models reproduce the Struve-Sahade effect for several lines. Another effect on the surface temperature distribution is visible but the distribution predicted by our current model is not yet consistent with observations.
Conclusions. In some cases, the Struve-Sahade effect as well as more complex line intensity variations could be linked to blends of intrinsically asymmetric line profiles that are not appropriately treated by the deblending routine. Systematic variations in the lines of (nearly) contact systems are also predicted by the model.

Key words. stars: massive – binaries: general – stars: fundamental parameters – stars: atmospheres – binaries: spectroscopic

1. Introduction

Massive stars are rare but very important objects. Their strong stellar winds interact with the ambient interstellar medium and can trigger the formation of new stars. They also play a key role in the production of various chemical elements. However, many open questions remain about these stars, regarding their formation, evolution, and physical properties. One of the most accurate ways to determine the physical properties (such as masses, temperatures, radii ...) of massive stars is to study eclipsing binary systems. However, to get yet more information, we need to improve our models and take into account effects related to the peculiarity of massive binary systems. Several authors (Sana et al. 2005; Linder et al. 2007; Linder 2008; and references therein) have presented evidence of the impact of these peculiar effects on both the spectral classification and the spectra themselves. These effects introduce complications in assigning the proper spectral types and luminosity classes. For example, main sequence stars are seen as giant stars (e.g. CPD-41°7742, Sana et al. 2005). As the spectral type of a star is one of the most important pieces of information that we can obtain from observation, it is crucial to have reliable criteria of classification for both isolated stars and binary systems. One of the most important phenomena that impact the spectral classification is the Struve-Sahade effect that consists in a variation in the relative intensity of some spectral lines of the secondary with respect to the primary star lines with orbital phase (Struve 1937). Another important effect is the surface temperature distribution that could affect the radial velocity determination. On a heavily deformed star, the temperature at the stellar surface is indeed non-uniform and the lines are not all formed at the same place. This leads to different radial velocity determinations as a function of the line that we use.

This work presents a novel way of simulating the spectra of binary systems at different phases of the orbital cycle. In a first approach, we model the case of binary systems with circular orbits containing main sequence stars. First, we use the Roche potential to compute the shape of the stars. We then apply the von Zeipel (1924) theorem and reflection effect to obtain the local temperature at the stellar surface. Finally, we use this geometrical information to compute synthetic spectra from a grid of model atmosphere spectra.

Section 2 describes the assumptions, the modelling of the geometry of the star, and the modelling of the spectra. We also present the important issues of the computation and the way in which we have treated them. Section 3 gives our first models and presents detailed analyses of the spectral classification, the Struve-Sahade effect, the light curves, and radial velocity curves. We provide a summary of our results and the future perspectives in Sect. 4.

2. Description of our method

Circular binary systems can be modelled in the following quite simple way that we can divide into two parts, one part involving the surface, gravity and temperature calculation and a second the spectra calculation. We now develop these two steps.

2.1. Geometric modelling

First of all, we need to calculate the surface of the stars of the binary system. Throughout this paper, we make the assumption of a circular orbit with both stars co-rotating with the binary motion, and acting like point-like masses. Under these assumptions, the stellar surface is an equipotential of the classical Roche potential (see e.g., Kopal 1959)

$$\phi = -\frac{Gm_1}{a\sqrt{x^2+y^2+z^2}} - \frac{Gm_2}{a\sqrt{(1-x)^2+y^2+z^2}} - \frac{G(m_2+m_1)}{2a}\left(x^2+y^2\right) + \frac{Gm_2 x}{a}, \quad (1)$$

where x is the axis running from the centre of the primary towards the secondary, z the axis from the centre of the primary and perpendicular to the orbital plane, and y is perpendicular to x and z. The x, y, and z coordinates are dimensionless, m_1 and m_2 are respectively the masses of the primary and the secondary, a is the separation between the stars, and G is the constant of gravity.

This can be written in adimensional form using spherical coordinates centred on the primary's centre of mass

$$\Omega = -\frac{a\phi}{Gm_1} = \frac{1}{r} + \frac{q}{\sqrt{r^2-2r\cos\varphi\sin\theta+1}} + \frac{q+1}{2}r^2\sin^2\theta - qr\cos\varphi\sin\theta, \quad (2)$$

where $r = \sqrt{x^2+y^2+z^2}$, $q = \frac{m_2}{m_1}$, $x = r\cos\varphi\sin\theta$, $y = r\sin\varphi\sin\theta$, and $z = r\cos\theta$. We represent the stellar surface with a discretised grid of 240×60 points (in θ and φ respectively). For a given value of Ω, $r(\Omega,\theta,\varphi)$ is obtained by an iterative solution of this equation using a simple Newton-Raphson technique. The knowledge of $r(\Omega,\theta,\varphi)$ over the discretised stellar surface allows us to calculate the gravity. The local acceleration of gravity is given by the gradient of the Roche potential

$$\underline{\nabla}\Omega = \begin{pmatrix} \frac{\partial\Omega}{\partial x} \\ \frac{\partial\Omega}{\partial y} \\ \frac{\partial\Omega}{\partial z} \end{pmatrix} = \begin{pmatrix} -\frac{x}{r^3} + \frac{q(1-x)}{r'^3} + (q+1)\,x - q \\ -\frac{y}{r^3} - \frac{qy}{r'^3} + (q+1)\,y \\ -\frac{z}{r^3} - \frac{qz}{r'^3} \end{pmatrix}, \quad (3)$$

where $r = \sqrt{x^2+y^2+z^2}$ as above, and $r' = \sqrt{(1-x)^2+y^2+z^2}$.

If we assume that we know the temperature at the pole, we can calculate the local temperature of each surface point following the von Zeipel (1924) theorem

$$T_{\rm local} = T_{\rm pole}\left(\frac{\left\|\underline{\nabla}\Omega_{\rm local}\right\|}{\left\|\underline{\nabla}\Omega_{\rm pole}\right\|}\right)^{0.25g}, \quad (4)$$

where $g = 1$ in the case of massive stars.

We have explicitly made the assumption of a co-rotating system, so that the stars always present the same face to each other. This leads to a local increase in temperature owing to the reflection effect between the two stars. We follow the approach of Wilson (1990) to treat this effect. This approach consists of an iterative process in which we assume a radiative equilibrium at each point of the surface and calculate a coefficient of reflection. Once we reach convergence, we update the temperature following

$$T_{\rm new} = T_{\rm old}\cdot\mathcal{R}^{0.25}, \quad (5)$$

where $\mathcal{R}$ is the coefficient of reflection.

2.2. Spectral modelling

The second part of the algorithm computes the spectrum of the binary by summing the incremental contributions of each surface point. We use a grid of OB star synthetic spectra computed with TLUSTY (Hubeny & Lanz 1992) assuming solar metallicity to create a database of spectra (Lanz & Hubeny 2003 2007). Each spectrum is defined by two parameters: gravity and temperature. As we know these parameters for each point at the stellar surfaces, we can compute the local spectrum. The computation consists of a linear interpolation between the four nearest spectra in the grid. The appropriate Doppler shift is then applied to the spectrum accounting for the orbital and rotational velocity (the latter under the assumption of co-rotation) of the surface element.

We multiply the spectrum by the area of the element projected along the line of sight towards the observer. The last corrective factor applied to the local contribution to the spectrum is the limb-darkening. The limb-darkening coefficient is based on the tabulation of Al-Naimiy (1978) for a linear limb-darkening law. Finally, we sum the contribution to the total spectrum. It has to be stressed that we assume that there is no (or little) cross-talk between the different surface elements as far as the formation of the spectrum is concerned.

We emphasize that we compute the spectra at different phases, only one "hemisphere" of each star being visible for an observer at any given time. However, as the stellar surface is not a sphere, the surface gravity and effective temperature of the surface elements visible at any given phase change with orbital phase. This leads to variations in the mean visible temperature of the stars and thus variations in the line properties. Furthermore, when the primary shows its hottest part, the secondary shows its coolest. The contrast between the spectra of the two stars therefore increases. In the following, phase zero corresponds to the eclipse of the primary by the secondary. Over the first half of the orbital cycle (phase = [0, 0.5[), the primary star has a negative radial velocity. It has to be emphasized that our simulations allow us to compute the individual spectra of each component at each phase. This information is not available for real binary systems, where disentangling can provide average individual spectra, but usually does not allow us to derive individual spectra for each phase. In this first version, we take into account neither the radiation pressure of the star that can possibly modify the shape of the atmosphere with respect to the Roche potential of very luminous stars, nor the possibility of eccentric systems. These improvements will be done in a subsequent paper.

2.3. Computational issues

For the contact binaries, some problems occur at the contact point (L1 point). If we follow the von Zeipel (1924) theorem, the temperature normally drops to zero because the gravity is null at the L1 point. However, this result is not very physical. In addition, numerical instabilities occur in the Newton-Raphson scheme for stars filling their Roche lobe at positions near L1, instabilities that affect the determination of the local radius and surface gravity. To avoid this problem, we do not follow the

Table 1. Parameters of the binary systems simulated in this paper.

Parameters	Model 1	Model 2	Model 3	Model 4	Model 5
Period (day)	3.36673	2.95515	1.3872	2.44070	3.52348
Mass ratio	0.96	0.87	0.68	0.55	0.62
Semi-major axis ($R_\odot$)	38.23	31.25	17.34	23.14	28.57
Inclination (°)	(48)	(23)	77.8	77	65.7
Mass of primary ($M_\odot$)	33.8	25.15	21.7	17.97	15.59
Mass of secondary ($M_\odot$)	32.41	21.79	14.7	9.96	9.65
Primary polar temperature (K)	38 000	35 500	35 100	34 000	33 700
Secondary polar temperature (K)	38 000	34 400	31 500	26 260	30 500
Ω_{L1}	3.68	3.53	3.20	2.98	3.10

Notes. Inclinations in brackets stand for non-eclipsing systems.

Table 2. Temperature and radius of stars.

Stars	$R_{\rm min}$ ($R_\odot$)	$R_{\rm max}$ ($R_\odot$)	$R_{\rm mean}$ ($R_\odot$)	T ($R_{\rm min}$) (K)	T ($R_{\rm max}$) (K)	$T_{\rm mean}$ (K)
Model 1[1]	9.37	9.79	9.49	38 008	37 328	37 617
Model 1[2]	8.94	9.31	9.05	38 008	37 516	37 664
Model 2[1]	9.10	9.82	9.29	35 520	34 178	34 896
Model 2[2]	8.47	9.14	8.65	34 424	33 570	33 896
Model 3[1]	6.73	9.22	7.06	35 146	44 772*	33 668
Model 3[2]	5.61	7.83	5.89	31 566	46 602**	30 370
Model 4[1]	7.45	8.02	7.61	34 016	31 954	33 338
Model 4[2]	5.39	5.77	5.49	26 287	27 603	26 114
Model 5[1]	4.60	4.64	4.61	33 712	34 230	33 675
Model 5[2]	8.99	12.06	9.43	30 544	21 631	29 239

Notes. [(1)] primary star, [(2)] secondary star. [(*)] and [(**)] these values are not physically acceptable due to the problems in treating the reflection effect near L_1, the most probable values based on the temperature of neighbouring grid points are: [(*)] 27 000 K; [(**)] 26 300 K.

equipotential strictly passing through the L1 point but an equipotential passing near this point. Another problem is the lack of some synthetic spectra in the model grid. This can occur, for instance, when a high temperature is coupled with a low gravity. The algorithm treats these problems by interpolating only between the two nearest spectra in the grid and notifies the user. However, this kind of situations occurs only for very few points located near the L1 point, which have a low temperature and a very small contribution to the total stellar spectrum. These points generally have little effect on the global result. Another surprising problem is caused by reflection. In the highly deformed binary, a coupling of some points near L1 leads to a high increase in temperature. At these positions, the convergence of the reflection computation is not guaranteed. In the approach of Wilson (1990), the convergence is evaluated for each point and the iterative procedure is stopped once all the points have converged. We modify this global convergence criterion to ensure that the end of the iteration process is reached. This criterion is that at least 99% of the points converged. In some cases, despite this revised criterion, very few points have an abnormal temperature unrelated to that of the surrounding points. These points are located near the L1 point and no spectra in the grid are available for these combinations of gravity and temperature.

3. First models

The number of well-known massive O-type binary systems with a circular orbit is rather small. Thus, we selected five well-studied massive binaries to both test our algorithm and try to model the effects of binarity on the spectrum. The five systems are: HD 159176, HD 165052, HD 100213, CPD-41°7742, and AO Cas. These systems were studied by Linder et al. (2007, Paper I) for the first three, Linder (2008, Paper III) for the fifth and Sana et al. (2005, Paper II) for the fourth, respectively. For the first three systems, Paper I reports a Struve-Sahade effect, which does not appear to affect the last two systems. These systems are main-sequence systems of massive OB-stars except for AO Cas in which the secondary is a giant star. Table 1 lists the adopted parameters for each star. The parameters come from the observational analysis carried out in Papers I, II, and III. However, some systems (HD 159176, HD 165052) are not eclipsing and some parameters are unavailable. To overcome this problem, we use the calibration of Martins et al. (2005) to assign "typical" values of radius and mass. Hence, our models do not strictly correspond to the five observed systems. To avoid any confusion, the models of HD 159176, HD 165052, HD 100213, CPD-41°7742, and AO Cas are named respectively models 1, 2, 3, 4, and 5. The first step of the computation is the surface, gravity, and temperature evaluation (see Tables 2 and 3). With these results, we can compare the simulated local gravity to the classical value for a single star given by $g = \frac{Gm_{\rm star}}{R^2_{\rm star}}$.

The most compact systems, model 1, model 2, model 4, and the primary star of model 5, are affected by small variations in their radius, $\log(g)$, and temperature. The agreement between the single star gravity and the gradient of the Roche potential is quite good. However, for model 3 and the secondary of model 5, the differences are more important. For model 3, the difference between the maximum and minimum radius is about 2.5 $R_\odot$ for the primary and 2.2 $R_\odot$ for the secondary, $\log(g)$ varies from 4.1 to 2.7 for both stars (Fig. 1 shows $\log(g)$ variations for model 3). These variations in the surface gravity lead to a change in temperature of about 8000 K for the primary star and 5000 K for the secondary star (Fig. 2 shows temperature variations for model 3). The difference between the single star $\log(g)$ and the binary model $\log(g)$ is 1.4. However, this difference appears only for the most deformed part of the star. At the poles, the difference between the single star model and binary model is negligible. For the secondary star of model 5, the difference between the maximum and minimum radius is 3 $R_\odot$, and $\log(g)$ varies from 3.5 to 2.6. These variations in the surface gravity lead to a change in temperature of about 8000 K. The difference between the single star $\log(g)$ and the binary system value is 1.24. This difference, again, concerns only the most deformed part of the star. Near the poles, the difference between the two models is negligible.

Table 3. Gravity (in cgs units).

Stars	$\log(g(R_{\rm min}))$	$\log(g(R_{\rm max}))$	$\overline{\log(g)}$	$\log\left(\frac{GM}{R^2_{\rm min}}\right)$	$\log\left(\frac{GM}{R^2_{\rm max}}\right)$	$\log\left(\frac{GM}{R^2_{\rm mean}}\right)$
Model 1[1]	4.03	3.95	4.01	4.02	3.99	4.01
Model 1[2]	4.05	3.98	4.03	4.05	4.01	4.04
Model 2[1]	3.93	3.78	3.89	3.92	3.85	3.90
Model 2[2]	3.93	3.78	3.89	3.92	3.85	3.90
Model 3[1]	4.13	2.67	4.05	4.12	3.84	4.08
Model 3[2]	4.13	2.67	4.04	4.11	3.82	4.06
Model 4[1]	3.96	3.81	3.92	3.95	3.88	3.93
Model 4[2]	3.98	3.85	3.95	3.97	3.91	3.96
Model 5[1]	4.31	4.29	4.30	4.31	4.30	4.30
Model 5[2]	3.53	2.62	3.45	3.51	3.26	3.47

Notes. Columns two to four indicate the extremal values and the average of the true value of $\log(g)$ on the deformed stellar surface accounting for the Roche potential, whilst the last three columns provide the corresponding $\log(g)$ computed with the single star formula.

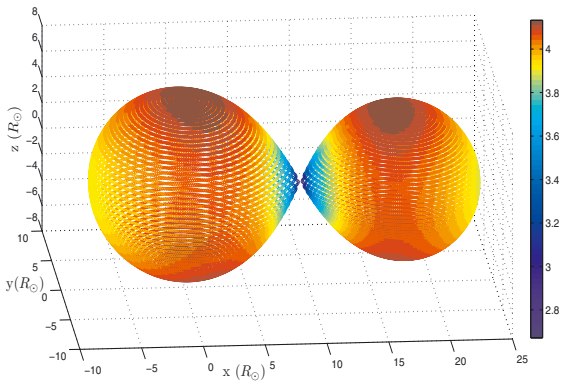

Fig. 1. Example of variations in $\log(g)$ for our model 3.

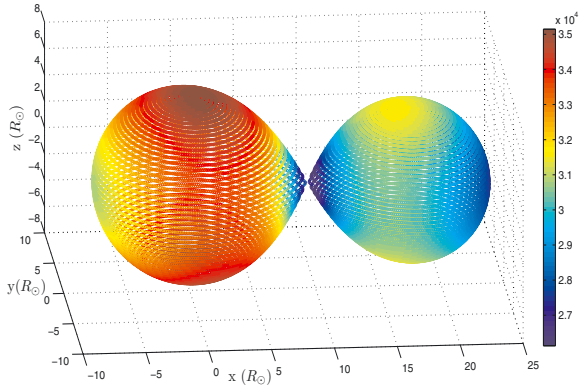

Fig. 2. Example of variations in temperature for our model 3.

We also apply a disentangling method to our combined spectra with the goal to compare its output with the true spectra of the binary components computed in our simulations. For this purpose, we use the disentangling algorithm implemented by Linder et al. (2007) and based on the González & Levato (2006) approach. We then compare the results to the individual spectra computed with our method. The disentangled spectra are in very good agreement with the computed ones.

We now consider two problems encountered in observational studies of massive binaries: the spectral classification and the Struve-Sahade effect.

3.1. Spectral classification

First, we apply the quantitative Conti (1971)–Mathys (1988 1989) criterion. This criterion is based on the ratio of the equivalent widths (EWs) of He I λ 4471 to He II λ 4542 for the spectral type determination and on the ratio of the EWs of Si IV λ 4089 to He I λ 4143 for the luminosity class determination. The spectral types that we obtain for our simulated spectra with this criterion are in good agreement with those obtained by the observational studies of the corresponding binary systems. However, the luminosity classes are very different. The criterion applied to simulated spectra identify supergiants, whilst observations find main-sequence stars (Table 4 gives the classification of the stars with the Conti-Mathys criterion). The problem seems to come from the He I λ 4143 line. This line is a singlet transition of He I. Najarro et al. (2006) reported pumping effects between He I and Fe IV lines that are not properly taken into account in model atmosphere codes and lead to incorrect He I line strengths for singlet transitions. To classify our synthetic stars, this line is therefore unsuitable and we use instead the Walborn & Fitzpatrick (1990) atlas. This atlas is more qualitative than the Conti-Mathys criterion but allows us to use a larger wavelength domain to classify the stars. The Conti-Mathys criterion was applied to the combined spectrum of the system, the individual spectra of each component, and the disentangled spectra. The disentangling is performed on 20 simulated spectra sampling the full orbital cycle. The classification based on the Walborn & Fitzpatrick (1990) atlas was performed for individual synthetic spectra. For observational data, we had to disentangle the spectra before being able to use the atlas. The atlas of Walborn & Fitzpatrick (1990) draws attention to many lines such as He I λ 4471, He I λ 4387, He II λ 4542, Si IV λ 4088, and He II λ 4200. By observing these lines (and their relative depth) and comparing our spectra to the references of the atlas, we reclassify the stars (see Table 5) achieving now a closer agreement with the classification of the real binary systems.

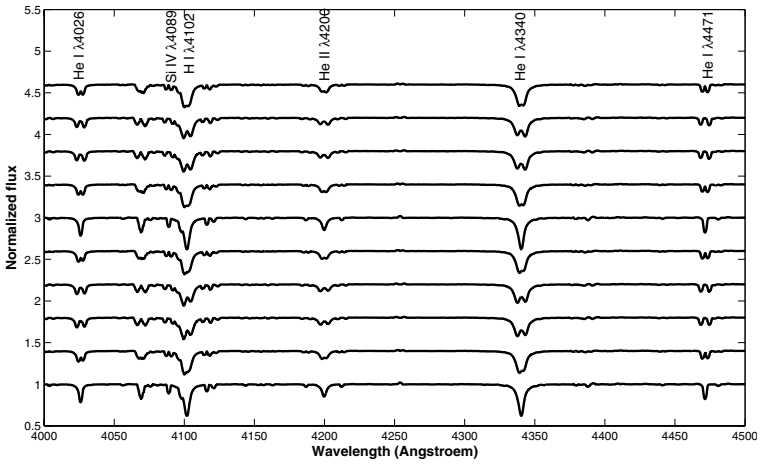

Fig. 3. Example of normalized simulated spectra computed for our model 1. From *bottom to top*: phases 0 to 0.9 by step of 0.1, the spectra are shifted vertically by 0.4 continuum units for clarity.

Table 4. Spectral classification using the Conti-Mathys criterion.

Stars	Combined spectra	Individual spectra	Disentangled spectra	Observational analysis
Model 1^1	O6.5I	O6.5I	O6.5I	O7V
Model 1^2	O6.5I	O6.5I	O6.5I	O7.5V
Model 2^1	O7.5I	O7.5I	O7.5I	O6V
Model 2^2	O7.5I	O8I	O8III	O6.5V
Model 3^1	O8.5V	O8.5V	O8.5V	O7.5V
Model 3^2	O9.5V	O9.7V	O9.7V	O9.5V
Model 4^1	O8.5I	O8.5III	O8.5III	O9III (or V)
Model 4^2	B-star	B-star	B-star	B1III (or V)
Model 5^1	O9III	O9V	O9V	O8III
Model 5^2	O9.5V	O9.5V	O9.5V	O9.5III

Table 5. Spectral classification using the Walborn & Fitzpatrick (1996) atlas.

Stars	Synthetic spectra	Observed spectra
Model 1^1	O6.5-O7V	O7V
Model 1^2	O7-O7.5V	O7V
Model 2^1	O7-O7.5V (or III)	O7V
Model 2^2	O8-O8.5V	O7.5-O8V
Model 3^1	O8-O8.5V (or III)	O7.5V
Model 3^2	O9.5-O9.7V (or III)	O9.5V
Model 4^1	O8.5-O8V (or III)	O9V
Model 4^2	B0.5-B0.2V	B1V
Model 5^1	O8.5-O9III (or V)	O9V
Model 5^2	O9.5-O9.7III (or V)	O9.5III

3.2. Struve-Sahade effect

The Struve-Sahade effect is usually defined as the apparent strengthening of the secondary spectrum when the star is approaching the observer and its weakening as it moves away (Linder et al. 2007). This effect was first reported by Struve (1937). He proposed that the effect is caused by streams of gas moving towards and obscuring the secondary. Gies et al. (1997) suggested instead that the phenomenon might be due to heating by the back-scattering of photons by the stellar-wind interaction zone. Stickland (1997) proposed that the Struve-Sahade effect could be linked to a combination of several mechanisms. Gayley (2002) and Gayley et al. (2007) argued that this effect could be linked to flows at the surface of the stars. For a more extensive discussion, we refer the reader to Linder et al. (2007). In our sample of binaries, three are known to present this effect: HD 159176, HD 165052, HD 100213 that respectively inspired our model 1, model 2, and model 3.

As a first step, we investigate the variation of some lines in the spectra at 20 different phases to look for variations in the profile. We inspect in particular the extremal phases 0.25 and 0.75, where differences in the relative strength of the lines can most easily be distinguished as the two components are the most separated at these phases. The result of this qualitative examination is given in Table 6. We must pay attention to possible blends that can modify the strength of a line leading to an apparent Struve-Sahade effect (see below).

First of all, we detect quite some of variations in the lines. However, many of these variations can be explained by blends with weak nearby lines rather than true variations in the line intensities. We stress that, a priori, we do not expect our simulations to display a genuine Struve-Sahade effect, because the simulations are axisymmetric about the binary axis and the largest difference, which is that caused by non-uniform surface gravity and temperature, is thus expected when comparing phases near 0.0 and 0.5, rather than 0.25 and 0.75, which are the phases most concerned with the Struve-Sahade effect (see for example Fig. 4). We also performed a quantitative study on several lines to evaluate the real variations. To check the influence of a possible blend, we measure the equivalent width in the simulated

Table 6. Visual variations in the line intensity.

Line	Model 1	Model 2	Model 3	Model 4	Model 5
He I λ 4026	1	1b	2	2	2
He II λ 4200	2	2	/	1B	2
He I λ 4471	1bs	1B	1b	2	1B
He II λ 4542	1s	1sB	1B	2	1B
He II λ 4686	2	2	2	2	1B
He I λ 4713	1B	1sB	1B	1B	1B
Hβ	1b	1B	1sb	2	2
He I λ 4921	1B	1B	2	2	2
He I λ 5016	1	2	1B	2	1b
He II λ 5412	1s	2	2	2	2
C III λ 5696	1B	1B	2	2	2
C IV $\lambda\lambda$ 5801, 5812	2	2	2	2	2
He I λ 5876	2	2	2	2	2

Notes. 1: variation, 2: no variation; b: suspicion of blend or small blend in the wings; B: blend with other lines; s: small variations.

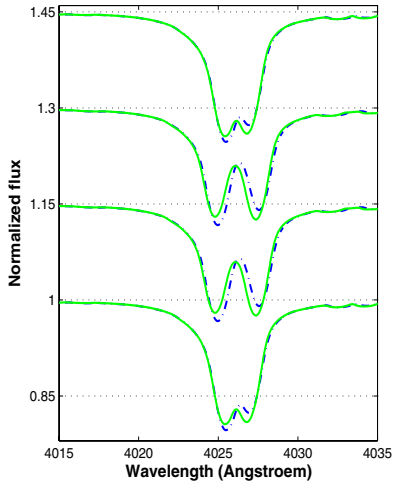

Fig. 4. Variations in the He I λ 4026 line in model 2. From *bottom to top*, in dotted blue: phases from 0.1 to 0.4 in steps of 0.1. From *top to bottom*, in green: phases from 0.6 to 0.9 in steps of 0.1.

combined spectra of the binary at different phases as well as in the spectra of the individual components of the binary at the same phases. The measurements of the line EWs are performed with the MIDAS software developed by ESO. The EWs of lines in the spectra of the individual stars are determined directly by simple integration with the integrate/line routine, whilst for the binary system, we use the deblend/line command as we would do for actual observations of binary system. The latter routine fits two Gaussian line profiles to the blend of the primary and secondary lines. We stress again that for real observations, we do not have access to the individual spectra of the primary and secondary at the various orbital phases. Our simulations allow us to compare the "observed" EWs (those measured by deblend/line) to the "real" ones (those measured in the individual spectra with integrate/line) and to distinguish real variations from apparent variations due to the biases of the deblending procedure. We now consider the simulations for the various systems listed in Table 1.

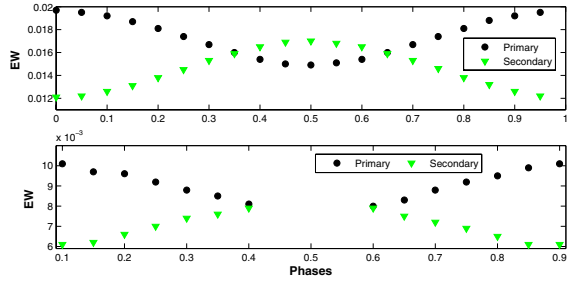

Fig. 5. EWs (in Å) of C III λ 5696 of model 1. *Upper panel*: EWs of primary and secondary measured in individual spectra. *Lower panel*: EWs of primary and secondary measured in combined spectra.

3.2.1. Model 1

We first study the individual spectra of each component. The lines listed in Table 6 display small variations of 1–3% over the orbital cycle. These variations are phase-locked. However, two lines vary by more than 20%: He I λ 4921 and C III λ 5696 (predicted in photospheric emission[1]). Unfortunately, the He I λ 4921 line is a singlet transition of He I and is thus subject to the effect described by Najarro et al. (2006), who showed that the singlet helium transitions are, in atmosphere codes such as TLUSTY, very sensitive to the treatment of the spectrum of Fe IV. The variation in the second line is more difficult to explain. There effectively exists a small blend in the blue component, but the blended line is very weak and it seems improbable that this small blend can explain the variations of 25–30%. The variations in the combined spectra are more difficult to see. Furthermore, the C III line is the only one that displays large variations in the combined spectra (see Fig. 5). We stress here that this line is rather easy to measure in our simulated data: the lines of the primary and secondary are very well-separated, and the continuum is well-defined. The results are then more reliable than for other lines. The variations are phase-locked and the lines are stronger when the stars display their hotter face. However, the predicted strength of the C III lines are rather weak and would make the measurement of real data (with noise) quite difficult.

[1] The apparent inverted P-Cygni profile is due to the proximity of an absorbtion Al III which is unrelated to the C III line.

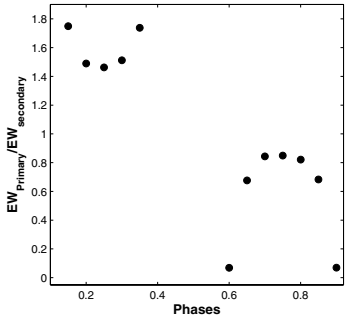

Fig. 6. EW ratio of primary to secondary for He I λ 4026 in model 2.

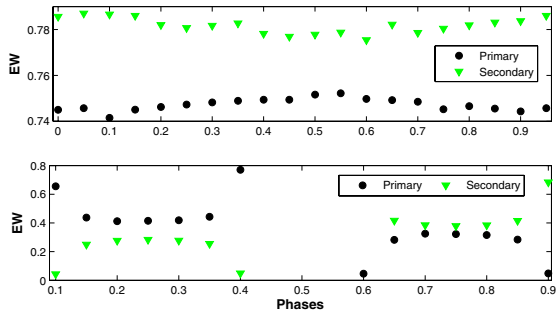

Fig. 7. Same as Fig. 5 for the He I λ 4026 line in model 2.

The primary/secondary EW ratios (all EW ratios in this paper have been measured on combined spectra with the deblend/line routine) also present variations such as these shown on Fig. 6 except for three lines. This pattern of variations appears in other models and we call it pattern 1. The He I λ 4713 line displays an inverse V variation pattern with a peak centred on phase 0.5. He I λ 4921 undergoes irregular variations with large differences between the first and the second half of the orbital cycle. Finally, C III λ 5696 shows a V-shape variation, which is expected in respect of previous results (see Fig. 5).

3.2.2. Model 2

First we study the individual spectra of each component. We can see variations in the intensities of all the lines. However, in most cases, these variations are very small of the order of 1–2% and will probably escape detection in real observations. The variations seem phase-locked, as we can see in Fig. 7, and reflect the temperature over the visible part of the stellar surface.

The analyses of the combined spectrum are affected by the same difficulties as for model 1, and are sometimes in opposition with what we observe in the individual simulated spectra: the EW of the primary line is always smaller than that of the secondary, while the combined spectrum shows the primary line to be deeper than the secondary at phases from 0.0 to 0.5 (e.g. He I λ 4026, He I λ 4471, see Fig. 7).

The He I λ 4921 line displays a more significant variation of the order of 15% (see however the remark about this line in the discussion of model 1). Moreover, in the combined spectrum, this line is blended with an O II line at λ 4924.5 so it is very difficult to determine whether the variation comes from the blend or from another effect.

Finally, we also study the ratios of the EWs of primary to secondary lines, which we find display pattern 1 variations (see Fig. 6).

Figure 8 illustrates the He I λ 4026 line at two opposite phases. Our individual spectra clearly reveal this line to be asymmetric with a steeper red wing for both stars. When fitting the combined binary spectra with two symmetric Gaussian profiles, the red component will be systematically assigned a lower flux, because the blue component will be apparently broader than the red one. Although the resulting fit can be of excellent quality, it will provide systematically larger EWs for the blue component and smaller EWs for the red. This situation therefore leads to an artificial Struve-Sahade behaviour.

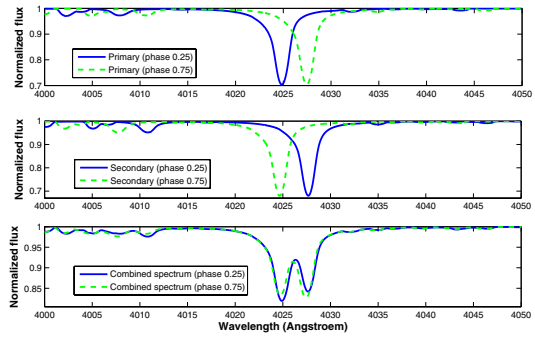

Fig. 8. He I λ 4026 line at phases 0.25 and 0.75 in model 2. *Upper panel*: Primary spectra. *Middle panel*: secondary spectra. *Lower panel*: combined spectra.

3.2.3. Model 3

The analysis of model 3 is more complex than for the two other systems. The results show different behaviours. The EW ratios of the primary to secondary measured in the combined spectra display different variation patterns (see Fig. 9). The He I λ 4471 line presents pattern 1-like variations. For the first part of the orbital cycle, He II λ 4542, He I λ 4713, and He I λ 5016 lines show variations that seem phase-locked. However, the second part of the orbital cycle is either constant or irregular. Finally, the He I λ 5876 line shows phase-locked variations, which are symmetric with respect to phase 0.5. The variations have a W-shape pattern (see Fig. 9).

The EWs of the He I λ 4471 line for the individual spectra of the primary show a maximum at phase 0.5 when the star displays its coolest face (the front part is never visible because of the eclipse). In contrast, the secondary shows a minimum at this phase when only the hottest parts of the star are visible (the coolest are occulted by the primary). The variations are of the order of 10%. The analysis of the combined spectra is more complex. For the first half of the orbital cycle, the EWs of the primary star have a similar behaviour to the measurements in individual spectra. For the second part of the orbital cycle and for the secondary star, the variations do not appear to be phase-locked. The EWs of the He II λ 4542 line for the individual spectra display a V-shape pattern for the primary and an inverse V-shape pattern for the secondary. The variations are of the order of 20% and phase-locked. The maximum (resp. minimum) of the curves

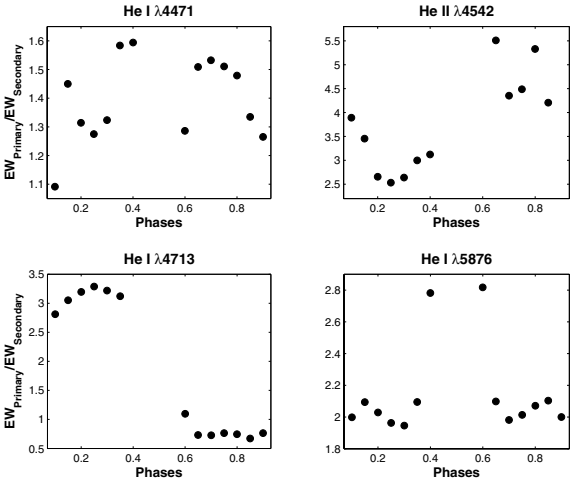

Fig. 9. The EW ratio of primary to secondary for several lines (from *left to right*, *top to bottom*: He I λ 4471, He II λ 4542, He I λ 4713, He I λ 5876) in model 3.

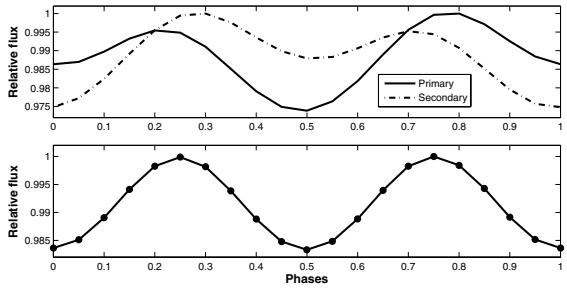

Fig. 10. Synthetic light curves of model 1 in the range $\lambda\lambda$ 3500, 7100. *Upper panel*: light curves of the primary and secondary stars (normalized to the maximum of emission). *Lower panel*: combined light curve of the binary system (normalized to the maximum of emission).

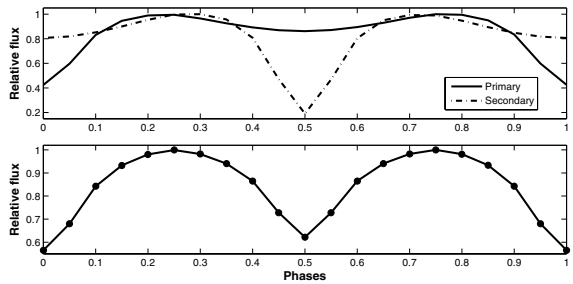

Fig. 11. Same as Fig.10, but for model 3.

occurs when the stars present their hottest (resp. coolest) face. The combined spectra again undergoes irregular variations of the same order of magnitude as found in the study of the individual spectra. For the He I λ 4713 and He I λ 5016 lines, the proximity of other lines renders the analysis more complex because of blends. The variations seem irregular, except for the He I λ 5016 line in the individual spectra of the primary star which exhibits an inverse V-shape pattern. Finally, the EWs of the He I λ 5876 line for the individual spectra of the primary are constant. The EWs for the individual spectra of the secondary are more interesting undergoing variations of about 10% and an inverse V-shape pattern with a peak at phases near 0.5. The EWs of the combined spectra of the primary present a maximum peaked at phase 0.5 and are quite constant over the rest of the orbital cycle. The secondary shows a minimum at phase 0.5 and small variations at other phases. As we see, this system is more complex than the other two. The variations are more significant but often symmetric with respect to phase 0.5. They also seem to be phase-locked and more significant than for the other stars (for the individual spectra at least).

3.3. Broad-band light curves

The analysis of the broad-band light curves is quite interesting because we can see variations in the intensity over the orbital cycle. In the case of an eclipsing binary, the light curve is, of course, dominated by the eclipses (Fig. 11). However, even for non-eclipsing systems such as model 1, variations occur as we can see in Fig. 10. These feature are the so-called ellipsoidal variations, which are well-known. Moreover, an interesting result is the asymmetry of the curve. In the first half of the orbital cycle, the primary star is fainter than during the second half. In contrast, the secondary star is brighter in the first half and fainter in the second. Adding both light curves together results in a roughly symmetrical light curve for this particular system.

Over the first half of the orbital cycle, the primary star has a negative radial velocity, and its spectral energy distribution is Doppler shifted to the blue, whilst that of the secondary is red-shifted. The behaviour of the light curves can indeed be explained by the displacement of the emission peak of the continuum. The difference between the flux emitted over the wavelength range $\lambda\lambda$ 4000, 6000 Å by an O9 star at rest and by an O9 star with a radial velocity of 100 km s^{-1} is about 1%. Therefore, the shift in the maximal peak of emission towards the blue (resp. red) in the first (resp. second) half of the orbital cycle for the primary (resp. secondary) and conversely for the second half of the orbital cycle induces the asymmetries in the broad-band light curve.

3.4. Radial velocity curve

Finally, we analyse the radial velocity (RV) curve. As we know the velocity of each visible point at a given phase, we can compute the mean value of these points and thus obtain a mean radial velocity. The curves are symmetric for all the five systems and the semi-amplitudes (K) are in good agreement with the observed ones. This shows that the lines that were used in the analyses of the observations represent the true RV of the star rather well. Table 7 compares the observed and simulated semi-amplitudes of the radial velocity curves.

A non-uniform surface temperature distribution in HD 100213 was reported by Linder et al. (2007), thus we investigated in more detail our model 3 to check whether such a distribution exists in our simulation. We studied the temperature distribution by computing the amplitude of the radial velocity curves of He I and He II lines. As we can see in Table 8, the agreement between the model and the observation is not very good. The observations suggest that the He I lines are formed over the rear part of the stars (because of the larger

Table 7. Comparison of the observed and computed radial velocity semi-amplitudes.

Stars	Computed K (km s^{-1})	Observed K (km s^{-1})
Model 1[1]	209.1	210.3
Model 1[2]	218.0	216.5
Model 2[1]	97.1	96.4
Model 2[2]	112.1	113.5
Model 3[1]	249.5	249.7
Model 3[2]	368.4	369.2
Model 4[1]	143.0	167.1
Model 4[2]	300.8	301.3
Model 5[1]	143.0	143.7
Model 5[2]	230.9	230.6

Table 8. Semi-amplitudes of the radial velocity curves (in km s^{-1}) of the He lines in the model 3 spectra.

Lines	K_1	K_2	$K_{1,m}$	$K_{2,m}$	$K_{1,obs}$	$K_{2,obs}$
He I λ 4026	245.0	354.4	223.4	372.3	246.5	363.8
He I λ 4471	236.0	353.7	234.7	368.8	244.5	372.3
He II λ 4686	265.5	364.4	255.9	383.9	251.3	355.2
He I λ 4921	284.5	364.9	255.1	365.5	245.9	373.0
He II λ 5412	233.5	332.4	249.3	360.1	239.8	351.2
He I λ 5876	247.9	354.6	229.6	357.2	269.7	388.8

Notes. The first two columns are computed from the measurement of the Doppler shift of the centre of the lines in the individual spectra of the primary and the secondary, the next two are the results obtained with the MIDAS (deblend/line) measurement of the centre of the lines and the last two are the semi-amplitudes observed by Linder et al. (2007) for HD 100213.

K values). This region then has to correspond to the lowest temperatures. However, in our model, the lowest temperatures are localized in both the front and rear parts of the stars. Hence, our model shows an intermediate amplitude resulting from the weighted average of the front and rear formation regions.

For the He II lines, the observations suggest that they are formed in the intermediate and lower radial-velocity amplitude region. Thus, the lines are formed over the front and middle parts of the star. However, our model shows that the lines are only formed in the middle part of the star and not its front. We can thus conclude that there is probably an additional mechanism that enhances the reflection process and heats the front part of the stars. This mechanism could be linked to the stellar wind interaction that might warm the stellar surface.

In Sect. 2.3, we have mentioned the problem of the increase in the temperature near the L1 point in the reflection treatment. We stress that, a priori, this increase cannot be responsible for the heating of the front parts of the stars. The problem instead concerns only the convergence and affects very few points. For model 3, after 50 iterations, the model has not yet converged and the temperature of the problematic points (3 points among 14 162 for this model) were at more than 100 kK. In comparison, the convergence for the non-problematic points is reached within fewer than five iterations.

4. Summary and future perspectives

We have presented a mathematical model, based on first principles, that allows us to compute the physical properties on the surface of stars in circular-orbit massive binary systems containing main-sequence O stars. We have assumed that the stars are corotating with their orbital motion, allowing us to use the Roche potential formalism to infer the shape of the stars and the local acceleration of gravity. We have included the effects of gravity darkening and reflection prior to inferring the surface temperature distribution of the stars. These results are then combined with the TLUSTY model atmosphere code to compute synthetic spectra of each binary component and the combined binary as a function of orbital phase. Many of the spectral lines are found to display a phase-locked profile and/or intensity variations in our simulated spectra. These variations are quite small for well-detached systems, but their amplitude strongly increases for heavily deformed stars. This variability mostly reflects the non-uniform temperature distribution over the stellar surface, which is seen under different orientations as a function of orbital phase. Given the assumptions that we have made in our model, we expect these variations a priori to be symmetric with respect to the conjunction phases. Our simulations demonstrate the impact of line blending on the measurement of lines in massive binary systems. Indeed, for a large number of lines, we have found that the true variations in the EWs (which are symmetric with respect to the conjunction phases) differ from those that are measured on the combined binary spectra using conventional deblending methods and are often found to be asymmetric with respect to the conjunction phases. The most dramatic effect is seen when the intrinsic line profiles of the individual stars are asymmetric (e.g. owing to blends with weaker lines in the wings of a strong line). In this case, deblending the binary spectra by assuming some type of symmetric line profile (Gaussian or Lorentzian) introduces a systematic effect that mimics the so-called Struve-Sahade effect. This result hence leads to an alternative explanation of the Struve-Sahade effect: in some binary systems and at least for some lines, this effect could simply be an artifact caused by the fitting of blended asymmetric lines with symmetric profiles. Therefore, at least in some cases, the Struve-Sahade effect does not stem from genuine physical processes, but rather reflects a bias in the measurement of the line profiles.

Whilst deblending appears problematic, our simulations demonstrate that spectral disentangling, assuming a reasonable sampling of the orbital cycle, yields good results, which provide a good representation of the average spectrum of a binary component and can hence be used for spectral classification and model atmosphere fitting. Comparing the RV amplitudes measured for different lines in the spectrum of the contact binary system HD 100213 with the predicted RV amplitudes for this system, we found that our model apparently fails to reproduce the surface temperature distribution of this system. Some additional heating of the parts of the stars that face each other would be needed to account for the observed distribution.

In subsequent future steps, we intend to generalize our code in different ways. We plan to extend our approach to more evolved stars that have extended atmospheres. This would requires both a revision of the Roche potential formalism to account for the effects of radiation pressure (see e.g. Howarth 1997) and the usage of a model atmosphere code that includes the effects of a stellar wind. Another important step would be to adapt our code to asynchronous and/or eccentric binary systems. In these systems, the Roche potential formalism is no longer valid and must be replaced with a proper handling of tidal effects (see e.g. Moreno et al. 2011). Finally, we plan to account for the presence of a wind interaction zone between the stars. The latter could contribute to the heating of the stellar surface in two different ways, either by the backscattering of the photospheric photons or the irradiation of X-ray photons emitted by

the shock-heated plasma in the wind interaction zone. These improvements will be the subject of forthcoming papers.

Acknowledgements. We acknowledge support through the XMM/INTEGRAL PRODEX contract (Belspo), from the Fonds de Recherche Scientifique (FRS/FNRS), as well as by the Communauté Française de Belgique – Action de recherche concertée – Académie Wallonie – Europe.

References

Al-Naimiy, H. M. 1978, Ap&SS, 53, 181
Conti, P. S., & Alschuler, W. R. 1971, ApJ, 170, 325
Gayley K. G. 2002, in Interacting Winds from Massive Stars, ed. A. F. J. Moffat, & N. St-Louis (San Francisco: ASP), 260, 583
Gayley, K. G., Townsend, R., Parsons, J., & Owocki, S. 2007, in Massive Stars in Interactive Binaries, ed. N. St.-Louis, & A. F. J. Moffat (San Francisco: ASP), 367, 393
Gies, D. R., Bagnuolo, W. G., & Penny, L. R. 1997, ApJ, 479, 408
González, J. F., & Levato, H. 2006, A&A, 448, 283
Howarth, I. D. 1997, Observatory, 117, 335
Hubeny, I., & Lanz, T. 1992, A&A, 262, 501
Kopal, Z. 1959, Close Binary Systems, in The International Astrophysics Series, ed. M. A. Ellison, & A. C. B. Lovell (London: Chapman & Hall Ltd.), 5
Lanz, T., & Hubeny, I. 2003, ApJS, 146, 417
Lanz, T., & Hubeny, I. 2007, ApJS, 169, 83
Linder, N. 2008, Ph.D. Thesis, University of Liège, ULg
Linder, N., Rauw, G., Sana, H., De Becker, M., & Gosset, E. 2007, A&A, 474, 193
Martins, F., Schaerer, D., & Hillier, D. J. 2005, A&A, 436, 1049
Mathys, G. 1988, A&AS, 76, 427
Mathys, G. 1989, A&AS, 81, 237
Moreno, E., Koenigsberger, G., & Harrington, D. M. 2011, A&A, 528, A48
Najarro, F., Hillier, D. J., Puls, J., Lanz, T., & Martins, F. 2006, A&A, 456, 659
Sana, H., Antokhina, E., Royer, P., et al. 2005, A&A, 441, 213
Stickland, D. J. 1997, Observatory, 117, 37
Struve, O. 1937, ApJ, 85, 41
von Zeipel, H. 1924, MNRAS, 84, 665
Walborn, N. R., & Fitzpatrick, E. L. 1990, PASP, 102, 379
Wilson R. E. 1990, ApJ 356, 613

2.2.2 Systems with radiation pressure

Radiation pressure is an important effect in massive binary systems. It can considerably modify the shapes of the stars. The computation of this shape with CoMBiSpeC requires some changes in the geometrical computation but not in the spectral computation. The treatment of the radiation pressure is, like the reflection effect, an iterative process. The convergence is reached when the radii of the stars do not change between two iterations.

The choice of the equipotential of the modified Roche potential can become difficult whenever the stars fill their "Roche lobe". The notion of Roche lobe changes if we account for radiation pressure. This comes from the fact that the concept of a Lagrangian L_1 point disappears or is at least altered. If at least one star fills its Roche lobe, the first Lagrangian point reached could be the L_2 or L_3 point. In this case, the star will lose material not towards its companion but at the benefit of a circumstellar envelop. The choice of the equipotential that will determine the surface of the star is thus a tricky issue. To solve this problem, we define a *pseudo-Lagrangian* point L_1' that depends on the highest $\delta(r, \phi, \theta)$ of the primary ($\delta_{1,m}$) and secondary ($\delta_{2,m}$). The coordinates of this L_1' point are (x_{L1}, 0, 0). The x_{L1} is the solution of

$$-\frac{1-\delta_{1,m}}{x_{L1}^2} + \frac{q(1-\delta_{2,m})}{(1-x_{L1})^2} + (q+1)x_{L1}^2 - q = 0 \tag{2.14}$$

Then, we compute the potential value of this point and we compare it to the value of the potential of the L_2 or L_3 points. Three situations are therefore possible:

- The input polar radii correspond to a higher value of the potential than the potential value of L_1' and L_2 or L_3. The system is detached, and we follow the equipotential corresponding to the input radii.
- The input polar radii correspond to a lower value of the potential than the potential value of L_1' and the potential value of the L_1' point is higher than the potential value of L_2 or L_3. In this case, we follow the potential corresponding to the potential value of L_1'. This corresponds to a classical contact binary.
- The input polar radii correspond to a lower value of the potential than the potential value of L_2 or L_3 and the potential value of the L_2 or L_3 point is higher than the potential value of L_1'. In this case, we follow the potential corresponding to the potential value of L_2 or L_3. The star is therefore in contact with L_2 or L_3 first, before being in contact with the L_1' point.

The general scheme of computation is ($i = 1, 2$ for the primary and the secondary) :

```
Choice of the equipotentials (depend on the specified radii)

Computation of the star surface without prad

for(iteration loop for radiation pressure){
 //Computation of the delta (extern prad)
 deltacalc(DELTAi, Ti, ri, grad_rochei, PHI, THETA);
 //Computation of the delta (intern prad)
 deltai = ctt*Tpolei^4/(loggi[pole]);

 //Computation of the equipotentials
 omega0i = omega0fct(...);

 for(loop on surface point){
  //Computation of the surfaces
  ri = newton_raphson(ri, PHI, THETA, omega0i, DELTAi);

  //Computation of gradients of Roche potential
  grad_rochei = (1-deltai)*gradfct(ri, PHI, THETA, DELTAi);

  //Computation of temperatures (Von Zeipel)
  Ti = Tpolei*|grad_rochei/grad_rochei[pole]|^(0.25*cvzi);
 }

 //Computation of temperatures (Reflection effect)
 Reflection();

 Check of convergence
}
```

In the case where the stars are in contact without radiation pressure, it can happen that the potential associated to the pseudo-L_1' point is too small to ensure a good convergence of the surface computation with radiation pressure. This is due to the fact that the computation is an iterative procedure and that the δ_{extern} is not constant over the whole surface. In these cases, we have to follow a higher equipotential. The convergence is usually reached after less than five iterations, but it can take more than 15 iterations. The code displays an error message

after 20 iterations. The other parts of the computation are the same as for the case without radiation pressure. However, we have to account for δ_{extern} in the quantities that involve the Roche potential (for example, the local area of the surface points).

It is not easy to say *a priori* when the radiation pressure will have a high impact on the stellar surface. It mainly depends on the distance between the two stars, their temperatures and radii. We have noticed that the impact seems to be higher when the stars are relatively close and have different sizes. For example, if the primary is bigger and hotter than the secondary, the shape of the secondary will be influenced by the radiation pressure. If the two stars are of the same order of size and temperature, the effect is quite low even if the stars are in contact. However, in this case, the small changes are important because they are needed to reproduce the temperature distribution effect. The treatment of the radiation pressure and the analysis of its impact on the stellar surface have been presented in Palate et al. (2013b).

2.3 Eccentric systems

The computation of eccentric systems is slightly different form the circular case. The general schematic view of the main file for one eccentric system is

```
MPI initialisation operations
Read of the input and option files

Read of the TIDES surface;
Read of the TIDES RVs corrections;
for(Loop on the phases){
Reflection_e;
}
for(Loop on the phases){
  //Computation of the black body curve and visible vrad
    Black_body_e();

  //Computation of the spectrum of visible part of the stars
    Spectrum_e();
}
```

In the eccentric cases, we have to account for the variation of the separation between the stars. The reflection effect is included even if the assumptions are

not fully respected. Finally, the surface gravity and the local area are computed with the classical Roche potential formula. This is of course an approximation but locally, the TIDES surface is equal to the Roche potential plus a perturbation that we assume to be small.

Remark 4 ***RV of a point P of the stellar surface.***

The radial velocity of the centre of mass of the primary is

$$v_{CM_1} = -K_1(\cos(\omega_2 + \phi) + e\cos(\omega_2)), \tag{2.15}$$

where ϕ is the true anomaly, ω_2 is the longitude of periastron of the secondary and K the semi amplitude

$$K_1 = \left(\frac{{m_2}^3}{(m_1+m_2)^2}\frac{2\pi G}{P(1-e^2)^{3/2}}\right)^{1/3}\sin i, \tag{2.16}$$

and for the secondary

$$v_{CM_2} = K_2(\cos(\omega_2 + \phi) + e\cos(\omega_2)), \tag{2.17}$$

$$K_2 = \left(\frac{{m_1}^3}{(m_1+m_2)^2}\frac{2\pi G}{P(1-e^2)^{3/2}}\right)^{1/3}\sin i. \tag{2.18}$$

Let us call $\vec{v} = (v_x, v_y, 0)$ the velocity vector of a point P(x,y,z), $\vec{\omega_{\text{star}}}$ the rotational angular velocity of the star equal to $\vec{\omega_{\text{star}}} = \beta\Omega_{\text{orbit}}\vec{e_z}$ and $\vec{r} = x\vec{e_x} + y\vec{e_y} + z\vec{e_z}$. Therefore,

$$\vec{v} = \vec{\omega}\otimes\vec{r} = -\Omega_{\text{orbit}}y\vec{e_x} + \Omega_{\text{orbit}}x\vec{e_y} \tag{2.19}$$

where $\Omega_{\text{orbit}} = \dfrac{2\pi}{P}\dfrac{(1+e)^{1/2}}{(1-e)^{3/2}}$ and β is the non-synchronicity parameter, $\beta = \frac{Pv_{rot}}{R}\times \frac{(1-e)^{3/2}}{(1+e)^{1/2}}$, where v_{rot} is the equatorial rotation velocity, R is the equilibrium radius, and e is the eccentricity.

Moreover, we define the direction of observation as $\vec{n} = (n_x, n_y, n_z)$ with $n_x = \cos(\omega_2 + \pi/2 + \phi)\sin i$, $n_y = -\sin(\omega_2 + \pi/2 + \phi)\sin i$, $n_z = \cos i$ and ϕ the true anomaly. The velocity distribution at the stellar surface is given by

$$\begin{aligned} v_{rad,d} &= -(\vec{\omega}\otimes\vec{r})\cdot\vec{n} \\ &= \beta\frac{2\pi}{P}\frac{(1+e)^{1/2}}{(1-e)^{3/2}}(x\cos(\phi+\omega_2)\sin i - y\sin(\phi+\omega_2)\sin i) \end{aligned}, \tag{2.20}$$

Finally, the velocity correction with respect to a rigid body rotation is given by $\delta v_r \vec{e_r}$ *and* $\delta v_\varphi \vec{e_\varphi}$ *respectively in the radial and azimuthal directions. In Cartesian coordinates we have:*

$$\begin{array}{rcl} \vec{e_r} & = & \cos\varphi \sin\theta \vec{e_x} + \sin\varphi \sin\theta \vec{e_y} + \cos\theta \vec{e_z} \\ \vec{e_\varphi} & = & \cos\varphi \vec{e_y} - \sin\varphi \vec{e_z} \end{array} , \tag{2.21}$$

The radial velocity correction is $v_{rad,c} = -\vec{v_c} \cdot \vec{n}$

$$v_{rad,c} = (\sin(\iota) \sin i \sin\theta - \cos i \cos\theta)\delta v_r + \cos(\iota) \sin i \delta v_\varphi \tag{2.22}$$

with $\iota = \varphi + \phi + \omega_2$.
And the total radial velocity is equal to

$$v_{rad} = v_{CM} + v_{rad,d} + v_{rad,c} \tag{2.23}$$

The spectral computation processing is the same as in circular binaries apart from two exceptions. First, we have to account for the change of the distance between the two stars: $a = a_0 \times (1 - e^2)/(1 + e \times \cos(\phi))$, where a_0 is the semi-major axis. Second, the longitude angle sampling ($d\varphi$) of the TIDES code is constant for a given latitude angle (θ) but is not constant between two values of the latitude angle. Therefore we have to compute the $d\theta d\varphi$ value for each value of the latitude. The results of the computations of eccentric systems are presented in Palate et al. (2013b).

A&A 552, A39 (2013)
DOI: 10.1051/0004-6361/201219754

Astronomy & Astrophysics

Spectral modelling of massive binary systems

M. Palate[1], G. Rauw[1], G. Koenigsberger[2], and E. Moreno[3]

[1] Institut d'Astrophysique et de Géophysique, Université de Liège, Bât. B5c, Allée du 6 Août 17, 4000 Liège, Belgium
e-mail: palate@astro.ulg.ac.be
[2] Instituto de Ciencias Físicas, Universidad Nacional Autónoma de México, Cuernavaca, 62210 Morelos, Mexico
e-mail: gloria@astro.unam.mx
[3] Instituto de Astronomía, Universidad Nacional Autónoma de México, 04510 México, D.F., Mexico
e-mail: edmundo@astro.unam.mx

Received 5 June 2012 / Accepted 13 February 2013

ABSTRACT

Context. The spectra of massive binaries may be affected by interactions between the stars in the system. These are believed to produce observational phenomena such as the Struve-Sahade effect.
Aims. We simulate the spectra of massive binaries at different phases of the orbital cycle, accounting for the gravitational influence of the companion star on the shape and physical properties of the stellar surface.
Methods. We used the Roche potential modified to account for radiation pressure to compute the stellar surface of close circular systems. We furthermore used the tidal interactions with dissipation of energy through shear code for surface computations of eccentric systems. In both cases, we accounted for gravity darkening and mutual heating generated by irradiation to compute the surface temperature. We then interpolated non-local thermodynamic equilibrium (NLTE) plane-parallel atmosphere model spectra in a grid to obtain the local spectrum at each surface point. We finally summed all contributions, accounting for the Doppler shift, limb-darkening, and visibility to obtain the total synthetic spectrum. We computed different orbital phases and different sets of physical and orbital parameters.
Results. Our models predict line strength variations through the orbital cycle, but fail to completely reproduce the Struve-Sahade effect. Including radiation pressure allows us to reproduce a surface temperature distribution that is consistent with observations of semi-detached binary systems.
Conclusions. Radiation pressure effects on the stellar surface are weak in (over)contact binaries and well-detached systems but can become very significant in semi-detached systems. The classical von Zeipel theorem is sufficient for the spectral computation. Broad-band light curves derived from the spectral computation are different from those computed with a model in which the stellar surfaces are equipotentials of the Roche potential scaled by the instantaneous orbital separation. In many cases, the fit of two Gaussian/Lorentzian profiles fails to properly measure the equivalent width of the lines and leads to apparent variations that could explain some of the effects reported in the literature.

Key words. stars: massive – binaries: general – stars: fundamental parameters – stars: atmospheres – binaries: spectroscopic

1. Introduction

Studing massive stars is important because they play a key role in galaxy evolution: their strong winds interact with the ambient interstellar medium and can trigger the formation of new stars, they produce heavy chemical elements, and they are an important source of UV radiation. Recent research indicates that a large part of massive stars (~50%) form a binary or a multiple system (Mahy et al. 2009; Sana & Evans 2011). The spectra of binary systems are an invaluable source of information for determining the physical properties (such as masses, temperatures, and radii) of stars. It has been shown, however, that the observational analysis of massive binaries is complicated by effects that are linked to interactions in these systems that affect the spectra and the spectral classification (Sana et al. 2005; Linder et al. 2007; Linder 2008, and references therein). Unfortunately, the majority of spectral modelling codes are designed for isolated spherical stars and cannot reproduce the particular effects of the binarity. Therefore, it is important to improve our models of spectral computation to accurately represent the spectra of these stars. In this context, we have developed a method that takes into account some of the effects that are produced by gravitational interactions in the system.

The first models of binary systems in which the stars are not spherical have been proposed by Russell & Merrill (1952) to reproduce the light curves of binaries. Then, Kopal (1959) introduced the Roche potential approach that was first used by Lucy (1968) and Wilson & Devinney (1971) followed by numerous other works. In a first step, we designed a similar code for circular massive binary systems (Palate & Rauw 2012, hereafter Paper I) in which the distorted shapes of the stellar surfaces are caused by gravitational interaction. The emerging spectra are then computed accounting for the shape of the stars and their local properties. In this paper we extend the method to incorporate radiation pressure effects on the stellar surface and the case of eccentric binaries. This new version of our CoMBiSpeC (code of massive binary spectral computation) model now allows spectral computation of (almost) any massive binary system.

2. Improvements of the method

Our method for modelling the spectra of circular binary systems, presented in Paper I, consists of computing the actual stellar surface following the Roche potential approach and accounting for the local gravity and temperature on each surface element.

Non-local thermodynamic equilibrium (NLTE) spectral model grids (TLUSTY, Lanz & Hubeny 2003, 2007) are used to compute the integrated spectrum of the star at each orbital phase (see also, e.g., Linnell & Hubeny 1994 and Linnell et al. 2012). Because our spectra are synthetic, they are free of observational noise. In this section we describe the two improvements that have been implemented to the method. The first is the inclusion of radiation pressure effects; i.e., the irradiation of each star by the companion and the effect of the radiation on each star's own surface. The second is the use of an explicit calculation of the stellar surface, from first principles, which here is applied to the case of eccentric binaries. In eccentric systems, the orbital separation changes as a function of phase, and accordingly, the deformations of the surface and the orientation of the tidal bulge are also variable.

2.1. Radiation pressure effects

There exists quite an extensive body of literature (see e.g. Dermine et al. 2009; Howarth 1997a; Schuerman 1972; Drechsel et al. 1995 and Phillips & Podsiadlowski 2002) on the impact of radiation pressure on the Roche potential in early-type binaries. According to Dermine et al. (2009), the effects of radiation pressure in a binary system can be separated into three parts: radiation pressure on each star's own surface, the effect on the companion, and radiation pressure on the matter outside the binary orbit. Here we focus on the two first effects, which are called internal and external radiation pressure (Drechsel et al. 1995). The impact of the radiation pressure on the matter outside the binary is, of course, very important for the surrounding medium but is irrelevant for calculating the shape of the stars. Howarth (1997a) pointed out that the effect of the internal radiation pressure can be treated as a simple scaling of the Roche potential of the stars. Another approach, proposed first by Schuerman (1972), consists of scaling the mass of the stars rather than the entire potential. The former approach is more appropriate because the emitted radiation bolometric flux and hence the radiation pressure scale with the local gradient of the potential (which also includes the attraction by the other star and the centrifugal forces). Therefore, according to Howarth (1997a), the stellar topology is not affected by internal radiation pressure and the latter simply scales the local surfaces gravity. The Newtonian gravity is defined by

$$\boldsymbol{g} = -\boldsymbol{\nabla}\phi, \tag{1}$$

where ϕ is a scalar gravity potential per unit mass.

The von Zeipel (1924) theorem can be written[1]

$$T^4 \propto \|\boldsymbol{g}\|. \tag{2}$$

The magnitude of the radiative acceleration is given by (Howarth 1997a)

$$a_{\rm rad} = -\frac{\kappa\pi}{c}\mathcal{F}, \tag{3}$$

where κ is the flux mean opacity per unit mass and $\mathcal{F}$ is the astrophysical bolometric flux ($\mathcal{F} \propto T^4$).

If we define Γ as the ratio of the radiative to the gravitational acceleration, $a_{\rm rad} = \Gamma g$. According to Howarth (1997a), this ratio is constant for a given star and independent of the position on the stellar surface since both accelerations vary with T^4. Therefore, we have that the effective potential is the potential without radiation pressure minus the radiative acceleration

$$\boldsymbol{g}_{\rm eff} = (1-\Gamma)\boldsymbol{g}. \tag{4}$$

From Eq. (1), $\phi_{\rm eff} = (1-\Gamma)\phi$ and the ratio Γ can be written as (following the Castor et al. 1975 theory for evaluating κ)

$$\begin{aligned}\Gamma &= \frac{\kappa\pi}{c}\mathcal{F}/g \\ &= \frac{\sigma_{\rm Th}}{m_{\rm H}c}\sigma T^4/g,\end{aligned} \tag{5}$$

with $\frac{\sigma_{\rm Th}}{m_{\rm H}} \approx 0.036\ {\rm m^2\,kg^{-1}}$, $\sigma_{\rm Th}$ the Thomson-scattering cross section and σ the Stefan-Boltzmann constant.

Because Γ is independent of the position on the stellar surface, we can compute it for $T = T_{\rm pole}$ and $g = g_{\rm pole}$

$$\Gamma = \frac{\sigma_{\rm Th}}{m_{\rm H}c}\sigma T_{\rm pole}^4 \frac{1}{\|\boldsymbol{g}_{\rm pole}\|}. \tag{6}$$

The advantage of this method is that the von Zeipel theorem remains valid. Another advantage is the simplicity of the method which does not require many computational resources.

The external radiation pressure is more difficult to treat. We have based our method on the approach of Drechsel et al. (1995) and Phillips & Podsiadlowski (2002). This method consists of scaling the mass of the companion in the Roche potential. The scale parameter $\delta = \frac{F_{\rm rad}}{F_{\rm grav}}$ is computed iteratively for each surface point. The external radiation pressure can be seen as a force that decreases the attraction of the companion. Therefore, the companion seems less massive, and consequently the mass has to be scaled. The new "Roche" potential can be written

$$\begin{aligned}\Omega = \frac{1}{r} + \frac{q(1-\delta(r,\theta,\varphi))}{\sqrt{r^2 - 2r\cos\varphi\sin\theta + 1}} + \frac{q+1}{2}r^2\sin^2\theta \\ -qr\cos\varphi\sin\theta\,,\end{aligned} \tag{7}$$

where $r = \sqrt{x^2+y^2+z^2}$, $q = \frac{m_2}{m_1}$, $x = r\cos\varphi\sin\theta$, $y = r\sin\varphi\sin\theta$, and $z = r\cos\theta$. Here, θ and φ are the colatitude and longitude angle in the spherical coordinates centred on the star. $\theta = 0$ and $\varphi = 0$ correspond respectively to the north pole of the star and the direction towards its companion.

The radiation pressure can be written

$$P_{\rm rad} = \frac{1}{c}\int_0^\infty \int_\omega I_\nu \cos^2\Psi_1\,{\rm d}\omega{\rm d}\nu, \tag{8}$$

where Ψ_1 is the angle between a local surface normal on the irradiated star and the direction to a surface element on the other star. I_ν is the specific intensity of the external radiation field, and ν is the frequency.

The radiation pressure gradient per unit mass is equal to (in plane-parallel approximation)

$$\begin{aligned}F_{\rm rad} &= -\frac{1}{\rho}\frac{{\rm d}P_{\rm rad}}{{\rm d}r} \\ &= \tfrac{1}{c}\textstyle\int_\omega\int_0^\infty \kappa_\nu \frac{{\rm d}I_\nu}{{\rm d}\tau_\nu}\cos^2\Psi_1\,{\rm d}\nu{\rm d}\omega \\ &= \tfrac{1}{c}\textstyle\int_\omega\int_0^\infty \kappa_\nu I_\nu \cos\Psi_1\,{\rm d}\nu{\rm d}\omega.\end{aligned} \tag{9}$$

Following Castor et al. (1975), we assume that the dominant source of opacity comes from electron scattering, thus, we have $\kappa_\nu = \frac{\sigma_{\rm Th}}{m_{\rm H}}$.

The value of δ is therefore computed with an iterative method. We start from the classical unmodified Roche potential

[1] Throughout this paper, the temperature is to be understood as effective temperature.

Table 1. Parameters of the circular binary systems simulated in this paper. Inclinations in brackets stand for non-eclipsing systems.

Parameters	Model 1	Model 2	Model 3	Model 4
Period (day)	3.36673	2.95515	1.3872	4.251
Mass ratio	0.96	0.87	0.68	0.42
Semi-major axis ($R_\odot$)	38.23	31.25	17.34	38.94
Inclination (°)	(48)	(23)	77.8	89.9
Mass of primary ($M_\odot$)	33.8	25.15	21.7	30.9
Mass of secondary ($M_\odot$)	32.41	21.79	14.7	13.0
Primary polar temperature (K)	38 000	35 500	35 100	35 000
Secondary polar temperature (K)	38 000	34 400	31 500	32 500
Polar radius of primary ($R_\odot$)	9.37	9.10	6.74	15.1
Polar radius of secondary ($R_\odot$)	8.94	8.47	5.62	11.14

References. Parameters from Linder et al. (2007): models 1 to 3, and Bonanos (2009): model 4.

and compute the radiation received by each surface element from its companion. The radiation is computed by summing the contribution of all points that are visible from the primary (resp. secondary) on the secondary (resp. primary). The method applied to compute the received bolometric flux by a point is derived from Eq. (9) and is similar to the reflection effect treatment of Wilson (1990). Indeed, we have $I_\nu = I_{\nu,0} \times (1 - u + u \cos \Psi_2)$, where Ψ_2 is the angle between a local surface normal on the emitting star and the direction towards an irradiated surface element on the other star, and u is the linear limb-darkening coefficient based on the tabulation of Claret & Bloemen (2011). Moreover, we can write $\mathrm{d}\omega = \frac{\mathrm{d}S_2 \cos \Psi_2}{s^2}$, where s is the distance between the irradiated and emitting surface. Finally, if the radiation comes only from the companion, we have $\int_0^\infty I_{\nu,0}\, \mathrm{d}\nu = \frac{\sigma T^4}{\pi}$. The local δ factor is thus defined by $\delta = \frac{F_{\mathrm{rad}} * d^2}{GM}$, where d is the distance between the point and the centre of the emitting star. This factor can be written (for the radiation emitted by the secondary and received by the primary) as

$$\delta_2 = \frac{\sigma \sigma_{\mathrm{th}} d^2}{\pi c m_{\mathrm{H}} G M_2} \sum_{\substack{\cos \Psi_1 > 0 \\ \cos \Psi_2 > 0}} T_2^4 (1 - u + u \cos \Psi_2) \cos \Psi_1 \cos \Psi_2 \frac{\mathrm{d}S_2}{s^2}. \tag{10}$$

Then, with the δ factor, we recompute the stellar surface with the modified Roche potential. Again, we evaluate the δ factor and surface until we reach convergence.

2.2. Eccentricity

The extension to eccentric systems uses the TIDES[2] code (Moreno et al. 1999, 2005, 2011). This code computes the time-dependant shape of the stellar surface for eccentric and/or asynchronous systems. It also provides velocity corrections for rigid body rotation. The method consists of modelling a deformable and perturbed surface layer that lies upon a rigid body that is in uniform rotation by solving the equations of motion of a grid of surface elements. These equations take into account centrifugal and Coriolis forces, gas pressure, and viscous effects in addition to those of the gravitational potential of both stars. It is important to note that in asynchronously rotating or eccentric systems, the linear approximation of the Roche potential is no longer valid and the presence of viscosity in the medium may lead to non-linear effects[3]. The surface shape and local velocities are obtained as a function of orbital phase from the solution of the equations of motion. Full details of the model are given in Moreno & Koenigsberger (1999), Toledano et al. (2007), and Moreno et al. (2005, 2011).

With the derived values of radius and velocity perturbations, we compute the surface gravity and temperature. Assuming the perturbations to be small, the gravity is computed by using a classical Roche gradient.

The temperature distribution is computed following the von Zeipel theorem

$$T_{\mathrm{local}} = T_{\mathrm{pole}} \left(\frac{\left\| \underline{\nabla} \Omega_{\mathrm{local}} \right\|}{\left\| \underline{\nabla} \Omega_{\mathrm{pole}} \right\|} \right)^{0.25p}, \tag{11}$$

where the gravity-darkening parameter $p = 1$ in the case of massive stars.

We also include reflection effects that heat the surface of the star through irradiation of each component by the other. The effect was treated by following the approach of Wilson (1990). We neglected any cross-talk between the surface elements (e.g. due to horizontal advection or radiative exchanges between neighbouring surface elements of different temperature). This is probably an important approximation because this effect might smooth out some of the temperature variations, especially near periastron (for eccentric systems) where the stars move faster and where the gravitational interactions are stronger. These interactions and velocity imply that energy dissipation due to viscosity effects is more significant near periastron and thus the cross-talk is expected to be higher.

The spectral computation was performed with the CoMBiSpeC code, which was described in Paper I. For this paper, some minor changes have been applied to take into account particularities linked to the eccentricity, such as the variation of the separation between the two stars.

3. Circular-orbit models

We present here models of four binary systems with circular orbits. Three of them were previously studied in Paper I, i.e., models 1, 2, and 3. These models are based on the HD 159176, HD 165052, and HD 100213 systems analysed by Linder et al. (2007). The fourth system, model 4 in this paper, is based on Sk-67°105 studied by Bonanos (2009). All four of these systems

[2] Tidal interactions with dissipation of energy through shear.

[3] The viscous stresses are included in the equations of motion and connect the surface elements to each other and to the inner rigid body.

Table 2. Comparison between the spectra with and without radiation pressure.

Models	$\|\|\Delta_{max}\|\|$	$\|\|\Delta_{mean}\|\|$	$\|\|\Delta_{median}\|\|$	$\|\|\sigma_\Delta\|\|$	$\Delta > 1\%$
Model 1	0.0113	6.8×10^{-4}	3.2×10^{-4}	0.0014	12
Model 2	0.0191	8.7×10^{-4}	3.8×10^{-4}	0.0018	213
Model 3	0.0063	5.1×10^{-4}	3.0×10^{-4}	8.7×10^{-4}	0
Model 4	0.1247	0.0069	0.0022	0.0171	95 820

are in synchronous rotation and, thus, are in equilibrium configuration so that the Roche potential approach is valid. For all models, we compared the shape, temperature, and gravity variations caused by radiation pressure. Table 1 gives a summary of the parameters (from Linder et al. 2007 and Bonanos 2009) used for the computation. We have chosen the polar temperature (rather than a surface mean temperature) as the reference effective temperature in Table 1. This is because T_{pole} is used to compute the local temperature via the von Zeipel theorem and remains essentially unaffected by radiation pressure effects. Finally, for model 4, we investigated the Struve-Sahade effect for some lines.

3.1. Models 1 and 2

We have analysed the spectra[4] of models 1 and 2 at 20 orbital phases and found that the impact of radiation pressure is rather low. The comparison was made by subtracting the normalized spectra with radiation pressure to the spectra without radiation pressure. On each of these "residual" spectra, we searched for the maximum, mean, and median values and the standard deviation. Then we searched for the maximum of the maxima (over the orbital phase) and computed a mean of the medians, the standard deviations, and means. We also looked for the spectral bins that present deviations higher than 1% (over a total of 360 000 bins). Table 2 gives a summary of these values for the combined spectra of the studied models. For example, the highest differences are 0.0113 and 0.0191 for models 1 and 2. These maxima occur in both cases at phase 0.5, i.e. at the conjunction with the primary in front of the secondary. These differences are significant but, the mean[5] difference is only $\sim 7-9 \times 10^{-4}$, which is very small. The general appearance of the spectra is preserved and the conclusions reached in Paper I remain valid. We can see in Fig. 1 that the spectra of model 1 with and without radiation pressure are nearly indistinguishable (top panels).

The largest and mean radii of the stars are smaller if radiation pressure effects are included. The radiation pressure also decreases the mean $\log(g)$ by ~ 0.05 despite the smaller radii. Finally, the mean temperatures increase by 100 K. This increase of the temperature and decrease of gravity cause a weak increase of a few per cent of the total flux emitted by the stars. Figure 1, lower panel, displays the log of the ratio of the fluxed spectra with and without radiation pressure and underlines the small differences in the continuum. Table 3 gives a summary of the radii and temperatures of circular models.

3.2. Model 3

This model leads to an (over)contact binary if radiation pressure is not included, but when it is included, the system becomes detached[6]. Surprisingly, however, the impact of radiation pressure on the spectrum is weak. This is because the parts of the star that contribute most to the spectrum come from the rear and side parts of the star which are less modified by the radiation pressure because δ is small (see Fig. 2). Moreover, the shape of the star is not strongly affected by the radiation of the companion. This is a priori unexpected but the reason for it is that the most deformed parts of the stars mainly see the coldest part of the companion, which leads to a rather low value of the maximum δ. We stress here that in systems where the two stars are in (over)contact (or nearly so) and are of similar size and temperature, the reflection effect is not sufficient to counterbalance the

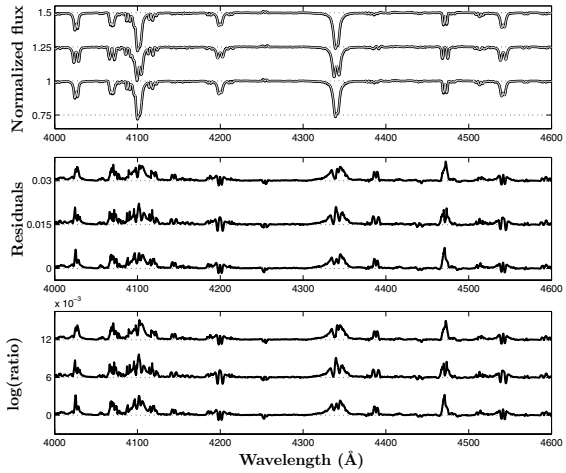

Fig. 1. *Top*: comparison between the normalized spectra computed without radiation pressure (in black) and with radiation pressure (in grey) for model 1. To better distinguish spectra, the black line is wider than the grey line. Orbital phases are, from bottom to top: phases 0.1, 0.25 and 0.4. The spectra are shifted vertically by 0.25 continuum units for clarity. *Middle*: corresponding residuals (spectrum with radiation pressure minus spectrum without radiation pressure). The residual plots are shifted by 0.015 for clarity. *Bottom*: logarithm of the ratio of the fluxed spectra with radiation pressure divided by the one without. These plot are shifted by 0.006 for clarity.

Table 3. Temperature and radius of stars at different locations at the stellar surface.

Stars	R_{side} ($R_\odot$)	R_{point} ($R_\odot$)	R_{back} ($R_\odot$)	T_{side} (K)	T_{point} (K)	T_{back} (K)
Model 1^1	9.51	9.46	9.70	37 442	38 061	36 705
Model 1^2	9.06	8.97	9.23	37 496	38 271	36 800
Model 2^1	9.32	9.44	9.62	34 654	34 937	33 577
Model 2^2	8.66	8.67	8.96	33 643	34 465	32 510
Model 3^1	7.12	8.44	7.63	33 198	29 306	29 211
Model 3^2	5.87	6.92	6.43	30 112	30 855	27 369
Model 4^1	15.80	15.95	16.42	33 411	33 882	32 121
Model 4^2	11.61	10.72	12.89	31 185	34 062	27 912

Notes. [(1)] primary star, [(2)] secondary star. *side*: $r(\phi, \theta) = r(\pi/2, \pi/2)$, *point*: $r(\phi, \theta) = r(0, \pi/2)$, *back*: $r(\phi, \theta) = r(\pi, \pi/2)$.

[4] Throughout this paper, the word "spectrum" refers to a synthetic spectrum.

[5] We only took into account the spectral bins that include spectral lines for this mean value.

[6] Strictly speaking, the CoMBiSpeC model cannot handle overcontact configuration, but the most extreme cases correspond to situations where both stars fill their Roche lobe.

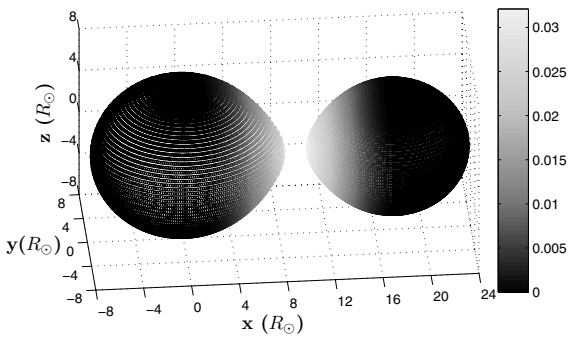

Fig. 2. Value of the radiation pressure parameter, δ, over the stellar surface for model 3. The highest values are located near the L1 point.

gravity darkening. Thus, the coldest parts of the stars are those near the L1 point.

In Paper I, we pointed out that we failed to reproduce the surface temperature distribution deduced by Linder et al. (2007) for HD 100213. These authors showed in their analysis through radial velocity measurements that the He II and He I lines were not formed in the same region of the stellar surfaces. The small changes of the stellar surface induced by the radiation pressure increase the importance of the reflection process and are sufficient to now explain the surface temperature distribution observed by Linder et al. The He II lines have a smaller radial velocity amplitude and thus are apparently stronger in the hemisphere facing the companion, whilst the He I lines have larger velocity amplitudes, indicating that they are stronger on the opposite hemisphere. This suggests that the hemisphere facing the companion is hotter than the opposite one. When radiation pressure is added, the stars are less deformed. This implies a weak temperature increase of the facing hemispheres caused by the decreasing gravity darkening and a higher effectiveness of the reflection process. This weak increase is therefore sufficient to explain the observations.

Espinosa Lara & Rieutord (2011) and Maeder (1999) have suggested that von Zeipel's (1924) classical theorem requires modifications. These theoretical studies present more complex models that could be, at first approximation, equivalent to the classical von Zeipel theorem with a gravity-darkening parameter (GDP) p smaller than 1.00. Therefore, we chose this very deformed system in which the von Zeipel theorem implies strong temperature variations to test the influence of p on the spectra. We computed the spectrum for values of the GDP of 0.25, 0.50, 0.75, 1.25 and 1.50, all other parameters having the same value as model 3 in Table 1. We found that for a moderate change of p (of $+/-0.25$) the spectra are not notably affected. We also found that the variations remain within the noise level of real data for variations of up to $+/-0.50$. Therefore, since we made some other important assumptions (no cross-talk, assumptions underlying the Roche potential), it is not useful to adopt another more complex formalism for gravity darkening because it does not notably affect our simulations.

3.3. Model 4

This system was chosen as an example of one in which the radiation pressure considerably modifies the shape of the stars (see

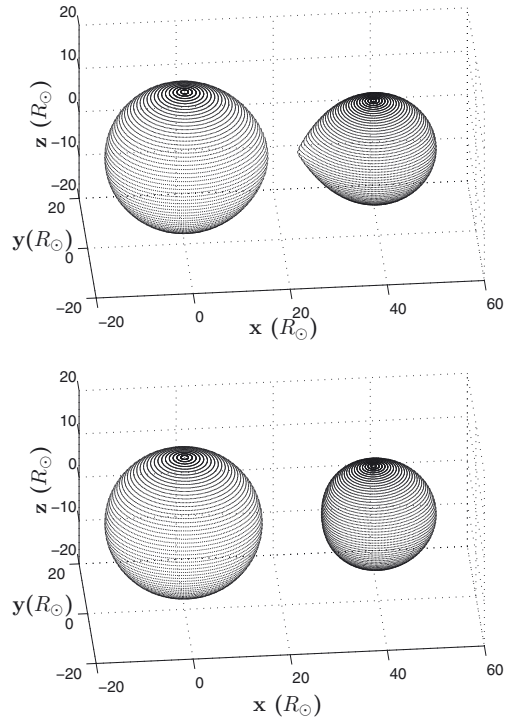

Fig. 3. Surface modification by the radiation pressure for model 4. *Top*: star surface without radiation pressure effect. *Bottom*: star surface with radiation pressure effect.

Fig. 3), underlining the potential significance of this effect. The system parameters (see Table 1) are based on the observational study of Sk-67°105 that was carried out by Bonanos (2009).

3.3.1. Spectral classification

Observational studies have shown that the primary and secondary are an O7-8V and an O8-8.5 III-V star. We first determined the spectral type of our synthetic spectra with the Conti (Conti & Alschuler 1971) – Mathys (1988, 1989) criterion (hereafter Conti-Mathys criterion). This criterion is based on the ratio of the equivalent widths (EWs) of He I λ 4471 to He II λ 4542 for the spectral-type determination and on the ratio of the EWs of Si IV λ 4089 to He I λ 4143 for the luminosity-class determination. We found that our model spectra that include radiation pressure correspond to an O6.5-7I type for the primary spectrum and an O7.5-O8I type for the secondary. The determination of the spectral type gives the same result whether the measurement is made on individual spectra or on combined spectra[7]. In our model, the stars seem hotter, and the problem encountered in Paper I concerning the luminosity class is again present because we overestimate the luminosity. In a second approach, we used the Walborn & Fitzpatrick (1990) atlas to compare individual spectra to the reference atlas and thus re-classify the stars. With the atlas we found for the primary and secondary an O(6.5)-7 V

[7] "Combined spectrum" refers to the spectrum of the primary plus the spectrum of the secondary, i.e. the spectrum of the entire system.

and an O8-8.5 (III)-V classification. The classification using the atlas is of course more qualitative, therefore we give a range and the best correspondence is in brackets. Within the uncertainties, the agreement with the observations is good.

3.3.2. Struve-Sahade effect

The Struve-Sahade effect (hereafter S-S effect) was originally defined as the apparent strengthening of the secondary spectrum when the star is approaching the observer and its weakening as it moves away (Howarth et al. 1997b; Linder et al. 2007). A more general definition is the apparent variation of the line strengths of either of the binary components as a function of the orbital phase (Howarth et al. 1997b). Bonanos (2009) reported a quite considerable S-S effect for several spectral lines of Sk-67°105. We studied eight of these lines in detail: He I $\lambda\lambda$ 4026, 4143, 4471, 4713, 5016, Si IV λ 4089, He II $\lambda\lambda$ 4542, and 5411.

First, we analysed the EWs on individual spectra of the primary and the secondary[8]. The measurements of the line EWs were performed with the MIDAS software developed by ESO. The EWs of lines in the spectra of the individual stars were determined directly by simple integration with the integrate/line MIDAS routine, whilst for the binary system, we used the deblend/line command as we would do for actual observations of a real binary spectrum. The latter routine fits two Gaussian line profiles to the blend of the primary and secondary lines.

The EWs of the different lines measured on the individual spectra display phase-locked variations. For the primary, the EWs of the He I lines reach a maximum at phase 0.5 (when the primary eclipses the secondary) because the coldest part of the star is the rear part. Two minima are visible at phases 0.05–0.1 and 0.9–0.95 because the observer starts to see the front part of the primary star. This part of the star is the hottest because of the very effective reflection in this system. The minimum is not observed at phase 0 because of the roughly annular eclipse that hides a substantial part of the stellar surface. The variation amplitude is line-dependent with ~5% for He I λ 4026, 60% for He I λ 4143, and 20% for the other He I lines. As expected for heating effects, the He II lines exhibit a reverse variation compared to the He I lines (see Fig. 4). The Si IV line displays a similar variation as the He I lines.

For the secondary, the EWs display the same variation as the primary, but shifted by 0.5 in phase. We can notice the zero value at phase 0.5 when the secondary is totally eclipsed. The variation amplitude of the He I $\lambda\lambda$ 4026, 4713, 5016, and Si IV lines is small and less than ~10%. The amplitude is greater than ~20% for the other lines (we did not account for the zero value).

The measurements of the combined spectra using a two-Gaussian fit to the blended lines agree relatively well with the variations measured on individual spectra for several lines: He I $\lambda\lambda$ 4026, 4143, 4713, 5016, He II $\lambda\lambda$ 4542, and 5411. The variation amplitude is sometimes overestimated, though. The EWs of He I λ 4471 are asymmetric before and after phase 0.5. The variation does not seem regular but is similar to the variations measured on individual spectra, i.e. a decrease of the EW of the secondary and an increase for the primary during the first half of the orbital cycle. Finally, the Si IV line displays irregular variations.

[8] The mean relative error of the normalized EWs can be estimated to $\sigma = 10^{-3}$–10^{-2}. The σ given by the deblend/line routine is of the same order of magnitude. This error estimation is valid for all studied lines throughout this paper.

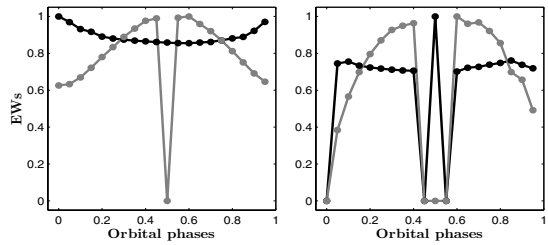

Fig. 4. Example of EW variations of the He II λ 4542 line. The EWs have been normalized to the highest value. Black: primary. Grey: secondary. *Left*: variations measured on individual spectra ($EW_{\rm p,\,max}$ = 0.53 Å, $EW_{\rm s,\,max}$ = 0.47 Å). *Right*: variations measured on combined spectra by fitting two Gaussians to the blended lines ($EW_{\rm p,\,max}$ = 0.52 Å, $EW_{\rm s,\,max}$ = 0.16 Å).

Bonanos (2009) reported a strong S-S effect in Sk-67°105 for several lines that we studied in the model. The variations observed are consistent with the definition of Linder et al. (2007), i.e. in the first half of the orbital cycle the secondary (resp. primary) line is deeper than the primary (resp. secondary) line and the situation is reversed in the second half of the orbital cycle. However, even though some lines in our synthetic spectra display strong EW variations, we did not observe this type of phase dependence.

3.3.3. Radial velocity and synthetic broad-band light curve

The last two characteristics that we studied are the light curve in the wavelength range 3800–7100 Å and the radial velocity curve. The two eclipses are clearly visible in the light curve. The depth of the eclipses agrees well with the observations. We stress that light curves are "by-products" of the spectral computation and that CoMBiSpeC is not primarily designed for light curve computation. The semi-amplitude of the radial velocity also agrees well with the observations. The radial velocity was computed by taking the mean value of the velocity of the visible points of the stellar surface at a given phase weighted by the surface projected along the line of sight. The values are given for the primary and the secondary (observational value in brackets): 138.3 (137) km s^{-1} and 332.9 (326) km s^{-1}. Finally, the synthetic light curve and radial velocity curve agree well with those derived by Bonanos (2009).

4. Eccentric models

We present here five models of eccentric binary systems. These models are inspired by the following massive binaries: HD 93205, HD 93403, HD 101131, HD 152218, and HD 152248, and are named models E1, E2, E3, E4, and E5. The stars were studied by: Antokhina et al. (2000), Rauw et al. (2000), Gies et al. (2002), Sana et al. (2008), Mayer et al. (2008), and Sana et al. (2001). The parameters used for the computation are given in Table 4. We studied the spectral classification, the radial velocity curves, the broad-band light curve, and finally the S-S effect. We computed the surface of these stars with the TIDES code (Table 4 bottom gives the specific parameters used in the TIDES code) and used a modified version of the CoMBiSpeC code to compute the gravity and temperature. These quantities are not uniformly distributed across the stellar surface and, in addition, change over the orbital cycle.

Table 4. Parameters of the eccentric binary systems. Inclinations in brackets stand for non-eclipsing systems.

Parameters	Model E1	Model E2	Model E3	Model E4	Model E5
Period (day)	6.08	15.093	9.6466	5.604	5.816
Eccentricity	0.46	0.234	0.156	0.259	0.133
Argument of periastron of secondary (°)	197.4	202.5	302	284	82
Mass ratio	0.44	0.54	0.63	0.74	0.98
Inclination (°)	(60)	(32)	(56)	(60)	67.2
Mass of primary ($M_\odot$)	45	68.5	36.2	24.5	27.8
Mass of secondary ($M_\odot$)	20	37.3	22.9	18.2	27.2
Primary polar temperature (K)	49 000	39 300	40 500	32 800	34 350
Secondary polar temperature (K)	36 500	40 100	35 000	31 200	34 000
Polar radius of primary ($R_\odot$)	9.2	24.0	9.5	10.3	16.0
Polar radius of secondary ($R_\odot$)	7.0	10.0	7.7	7.9	14.5
$v_1 \sin(i)$ (km s^{-1})	135	144	102	152	135
$v_2 \sin(i)$ (km s^{-1})	145	75	164	133	135
β^a of primary	0.64	2.06	1.80	1.09	0.81
β^a of secondary	0.91	2.59	3.57	1.24	0.89
TIDES code parameters					
Viscosity, ν, of primary ($R_\odot^2$ day^{-1})	0.05	0.045	0.028	0.05	0.05
Viscosity, ν, of secondary ($R_\odot^2$ day^{-1})	0.05	0.01	0.028	0.02	0.02
Layer depth	0.01	0.1	0.07	0.02	0.1
Polytropic index of primary	1.5	3	1.5	3	3
Polytropic index of secondary	1.5	1.5	1.5	1.5	3
Number of azimuthal × latitudinal partitions	500 × 20	500 × 20	500 × 20	500 × 20	500 × 20

Notes. [(a)] The β parameter measures the asynchronicity of the star at periastron and is defined by $\beta = 0.02 \frac{P v_{\rm rot}}{R} \times \frac{(1-e)^{3/2}}{(1+e)^{1/2}}$, where $v_{\rm rot}$ is the equatorial rotation velocity, R is the equilibrium radius, and e is the eccentricity.

References. From Antokhina et al. (2000), Rauw et al. (2000), Gies et al. (2002), Sana et al. (2008), Mayer et al. (2008), and Sana et al. (2001) for models E1 to E5.

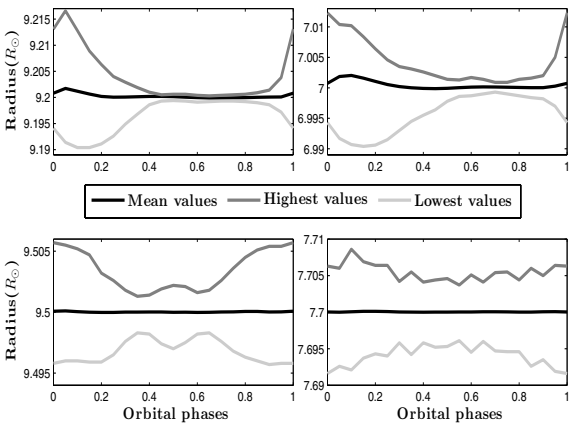

Fig. 5. Variations of the mean, highest and lowest visible radius (*left*: the primary radii, *right*: the secondary radii). *Top*: variations for model E1. *Bottom*: variations for model E3.

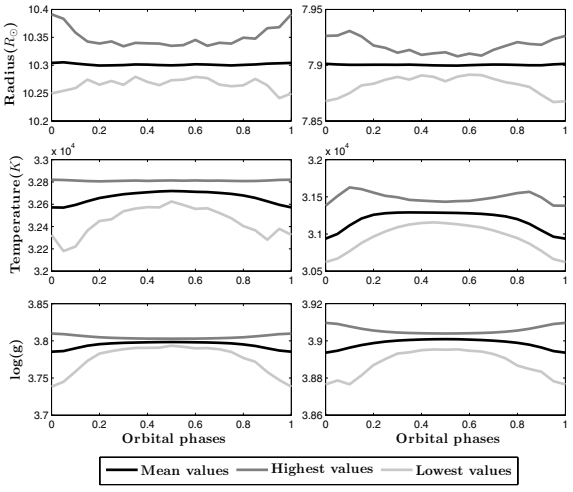

Fig. 6. Variations of the mean, highest and lowest visible radius, temperature, and log(g) for model E4. *Left*: values for the primary star. *Right*: values for the secondary star.

A sample of the phase-dependent behaviour of the mean radius, gravity, and temperature as well as their maximum and minimum values are shown in Figs. 5–7. The maximum radius is largest near periastron (just before and/or just after). A model based on an instantaneous Roche lobe, such as the *Nightfall*[9] program, presents the strongest variation strictly at the periastron passage. However, in the TIDES code, viscous effects that lead to a delay are taken into account. The most compact systems, model E1, the secondary of model E2, and model E3, remain nearly spherical during the entire orbital cycle (see Fig. 5) because the mean radii are nearly constant and the highest relative difference between the maximum and minimum radii is less than 0.5%. This is not surprising because models

[9] For details see the Nightfall User Manual by Wichmann (1998) available at the URL: http://www.hs.uni-hamburg.de/DE/Ins/Per/Wichmann/Nightfall.html

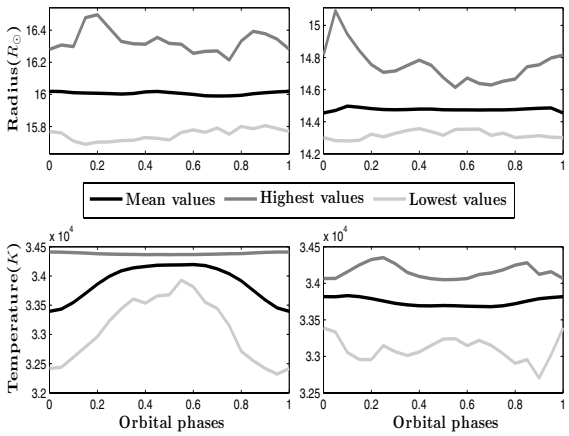

Fig. 7. Variations of the mean, highest and lowest visible radius and temperature for model E5. *Left*: values for the primary star. *Right*: values for the secondary star.

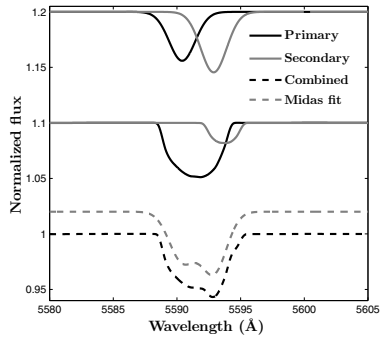

Fig. 8. Combination of the O III λ5592 line of the primary and the secondary for model E2 at phase 0.25. The deblend/line routine will not fit the line of the secondary properly. Top: the resulting lines of the two Gaussian fits. Middle: individual lines of the primary and secondary computed with our model and normalized to the continuum of the entire system. Bottom: spectrum of the system and corresponding fit of MIDAS.

E2, and E3 have the longest periods, hence the widest separation, and model E1 contains relatively compact main-sequence stars.

4.1. Spectral classification

First, we applied the quantitative Conti-Mathys criterion (Conti & Alschuler 1971, Mathys 1988, 1989). The spectral types that we found for our simulated spectra either agree well with the observations or are hotter than the observations. The hotter stars present a weak He I λ4143. This makes measuring the spectra of this system difficult and uncertain. The luminosity classes are, as in Paper I, overestimated for models E1, E3, and E5. Model E2 and the primary of model E1 are too hot for the Conti-Mathys luminosity criterion. The luminosity classes agree well for model E4. The problem of simulating singlet transition of He I reported by Najarro et al. (2006) and discussed in Paper I is probably responsible for the general luminosity classification problem. To refine our classification, we again used the Walborn & Fitzpatrick (1990) atlas. This atlas was used with the individual spectra, which for real observational data can only be assessed through spectral disentangling. The atlas is more qualitative than the Conti-Mathys criterion but relies on a large number of lines. We can now achieve a better agreement with the classification of the real binary systems (see Table 5).

4.2. Struve-Sahade effect

In our sample of binaries, two are known to present this effect: HD 93403 and HD 152248. They inspired our models E2 and E5. In our analysis, we detected variations of the line strength in models E1, E2, E4, and E5. However, we observe an S-S effect in the sense of Linder et al. (2007) only for some lines in model E2.

For all models, we investigated eight "well-chosen" lines in the spectra at 20 phases (the phase zero corresponds to the periastron passage). The lines were chosen following three criteria: first, we selected the lines for which an S-S effect is reported in the literature. The second criterion is based on a visual detection of variations in the line profile in the synthetic spectra, and finally, the third criterion is based on the fact that some lines present the S-S effect more often than others. As in Paper I, we draw attention to possible blends with nearby lines that can modify the strength and lead to misinterpretations.

We followed the same procedure as in Paper I and measured the EWs in the simulated combined spectra of the binary at different phases as well as in the simulated spectra of the individual components of the binary at the same phases. This approach allows us to compare the line strengths that are deblended from the combined spectrum with the actual individual spectra, which is not possible with the real observational data. We found variations in the EWs in many of the individual spectra as well as in the combined spectra. However, the agreement between the results of the deblend/line routine and the actual individual spectra is mostly poor. We present in Figs. 9 and 10 examples of typical variations observed in our analysis. The (inverse) U-pattern (Fig. 9 right, grey or Fig. 10 left, black) is often observed and is directly related to the orbital motion. Constant EWs or irregular variations are also often observed. A constant EW is mostly observed in long-period systems. We also encountered other types of variation patterns such as those presented in Fig. 10 (right, grey) during our analysis. The amplitude of the EW variations depends on the line and the system. The variations observed on individual spectra can be explained by the physical variations of the temperature and gravity at the stellar surface during the orbital cycle (we give an example of the interpretation of the variation in Sect. 4.2.1). The explanation of the S-S effect that we suggested in Paper I seems to be reinforced by these new analyses. The S-S effect seems to be due to the combination of the spectra in which the lines have a non-Gaussian/non-Lorentzian and even asymmetric profile. Under these conditions, the deblend/line routine introduces systematic errors that mimic the S-S effect. This is illustrated in Fig. 8, which shows that the deblending routine erroneously selects the bump that is created by the superposition of the two lines as the secondary star's absorption line. The secondary's line appears as a weak contribution on the red wing of the primary star's absorption. However, a fit with two Gaussian profiles will consider the bump as the core of the secondary line and thereby overestimate its strength.

Table 5. Spectral classification using the Conti-Mathys criterion and the Walborn & Fitzpatrick atlas.

Stars	Combined spectra	Individual spectra	W&F atlas	Observational analysis
Model E1[1]	O3	O3	O3-4 (IV)-V	O3V
Model E1[2]	O7.5I	O7I	O8-8.5 III-(V)	O8V
Model E2[1]	O5.5	O4	O5-6 (I)-III	O5.5I
Model E2[2]	O4	O4	O7-8 III-(V)	O7V
Model E3[1]	O6I	O5.5I	O6.5-7 III-(V)	O6.5V
Model E3[2]	O6.5I	O7I	O8.5 V	O8.5V
Model E4[1]	O8I	O8.5III	O9-9.5 (III)-V	O9III
Model E4[2]	O9III	O9.5V	O9.5-9.7 III-(V)	O9.7V
Model E5[1]	O6.5I	O7I	O7-8 III-(V)	O7III
Model E5[2]	O7I	O7I	O7.5-8.5 (III)-V	O7.5III

Notes. [(1)] Primary. [(2)] Secondary.

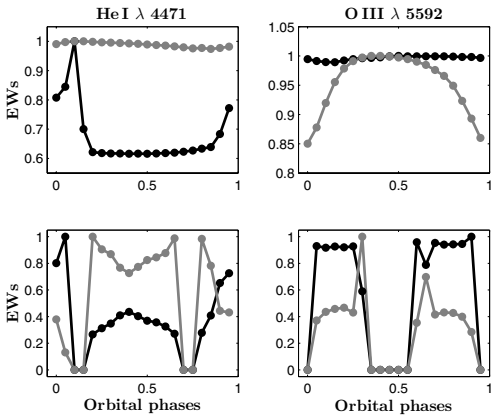

Fig. 9. Example of EW variations for the He I λ 4471 line for model E2 and for the O III λ 5592 line for model E4. The EWs have been normalized to the highest value. Black: primary. Grey: secondary. *Top*: variations measured on individual spectra ($EW_{\rm p,\,max,\,HeI}$ = 0.17 Å, $EW_{\rm p,\,max,\,OIII}$ = 0.18 Å, $EW_{\rm s,\,max,\,HeI}$ = 0.34 Å, $EW_{\rm s,\,max,\,OIII}$ = 0.11 Å). *Bottom*: variations measured on combined spectra ($EW_{\rm p,\,max,\,HeI}$ = 0.17 Å, $EW_{\rm p,\,max,\,OIII}$ = 0.14 Å, $EW_{\rm s,\,max,\,HeI}$ = 0.10 Å, $EW_{\rm s,\,max,\,OIII}$ = 0.08 Å).

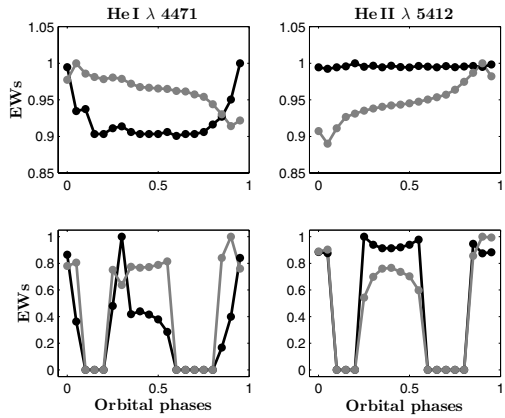

Fig. 10. Example of EW variations for the He I λ 4471 and He II λ 5412 lines for model E1. The EWs have been normalized to the highest value. Black: primary. Grey: secondary. *Top*: variations measured on individual spectra ($EW_{\rm p,\,max,\,HeI}$ = 0.04 Å, $EW_{\rm p,\,max,\,HeII}$ = 1.07 Å, $EW_{\rm s,\,max,\,HeI}$ = 0.59 Å, $EW_{\rm s,\,max,\,HeII}$ = 0.98 Å). *Bottom*: variations measured on combined spectra ($EW_{\rm p,\,max,\,HeI}$ = 0.05 Å, $EW_{\rm p,\,max,\,HeII}$ = 0.80 Å, $EW_{\rm s,\,max,\,HeI}$ = 0.21 Å, $EW_{\rm s,\,max,\,HeII}$ = 0.29 Å).

4.2.1. Model E1

In this model, we mainly observed variations illustrated in Fig. 10. These variations can be explained by the orbital motion of the stars and the variation of the visible part of the stars. At periastron passage, we see the rear side of the secondary. Because the stars are close, they are quite deformed and therefore the visible part of the secondary is cool, which leads to a reinforcement of the He I lines. For the primary the hemisphere facing the companion is visible at this phase. However, because the primary is deformed, and owing to the large temperature difference between the two stars, the reflection process does not heat the primary significantly. Thus it is also the coldest part of the primary that is visible at this phase. When the binary separation increases, the stars become nearly spherical. The temperature of the primary becomes nearly constant and the EW of its lines do not change. However, for the secondary, we begin to see the front part of the star. Whilst the reflection is not very effective for heating the primary, it is very effective for the secondary and accordingly, when we see the front part of the latter, the temperature increases. The increase is stronger because the separation between the stars decreases during the second half of the orbital cycle.

The EWs measured on combined spectra (see Fig. 10, bottom) are not consistent with those measured on the individual spectra (except for the He I λ 4143 line of the secondary). As mentioned above, this inconsistency is due to the deblending routine, which does not properly separate the lines of the primary and secondary stars. For example, the blue-shifted component may have a larger EW than when it is red-shifted. This inconsistency is reduced when the lines are measured at orbital phases at which they are clearly separated.

4.2.2. Model E5

For this last model, we investigated the He I $\lambda\lambda$ 4026, 4143, 4471, 4713, 5016, Si IV λ 4089, He II λ 4200, 4542, and O III λ 5592 lines. The EWs of the He I and Si IV lines in the primary display a U-pattern with a maximum at phase 0.0–0.05 and a minimum at phase 0.45–0.55. The EWs of the secondary

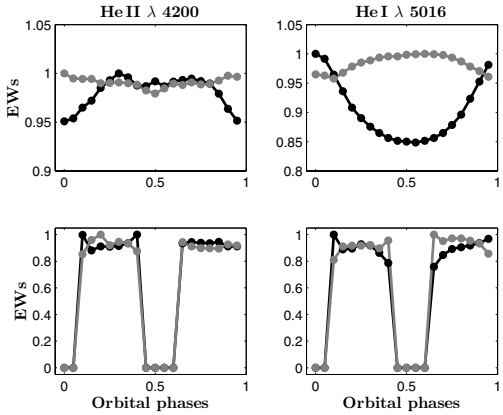

Fig. 11. Example of EW variations for He I λ 5016 and He II λ 4200 for model E5. The EWs have been normalized to the highest value. *Top*: variations measured on individual spectra ($EW_{\rm p,\,max,\,HeI}$ = 0.20 Å, $EW_{\rm p,\,max,\,HeII}$ = 0.48 Å, $EW_{\rm s,\,max,\,HeI}$ = 0.21 Å, $EW_{\rm s,\,max,\,HeII}$ = 0.48 Å. *Bottom*: variations measured on combined spectra ($EW_{\rm p,\,max,\,HeI}$ = 0.12 Å, $EW_{\rm p,\,max,\,HeII}$ = 0.27 Å, $EW_{\rm s,\,max,\,HeI}$ = 0.11 Å, $EW_{\rm s,\,max,\,HeII}$ = 0.24 Å).

display a symmetric variation with respect to the primary, however, the amplitude of the variation is smaller. The O III line displays the inverse behaviour compared to the previous lines. Finally, the He II lines in the primary display two maxima at phases 0.3 and 0.7 with an intermediate minimum at phase 0.5 that give us an M-pattern variation. The secondary presents a low-amplitude U-pattern variation.

The EWs measured on the combined spectra are nearly constant for the He I $\lambda\lambda$ 4026, 4471, 5016, He II λ 4200, 4542, and O III λ 5592 lines for the primary and secondary stars. The Si IV line displays irregular variations but a mean value of the primary higher than the secondary for phases before 0.5 and a mean value of the secondary higher for the second part of the orbital cycle. The He I λ 4713 line displays constant EWs for phases before and after 0.5 but the value is different before and after phase 0.5. Before phase 0.5 the primary has a lower EW than the secondary and after phase 0.5 the primary has a larger EW than the secondary. Finally, the variations observed for the He I λ 4143 line are consistent with the variations measured on individual spectra. All variations measured in our model underestimate the observed S-S effect.

In conclusion, our models display, in general, some variations of EWs during the orbital cycle. The variations on the spectra of individual components are caused by the orbital motion and the modulation of the visible part of the star. However, the variations that we measure on combined spectra and the visual variation of the relative strength of the line of the primary and secondary stars are not strong enough to completely explain the S-S effect as observed by Sana et al. (2001).

4.3. Synthetic broad-band light curves and radial velocity curve

The synthetic light curves were computed in the wavelength range 3800–7100 Å. We compared our light curves to those obtained with *Nightfall*. *Nightfall* provides synthetic light curves based on an instantaneous Roche potential and thus does not take any viscous stress into account. We point out here the

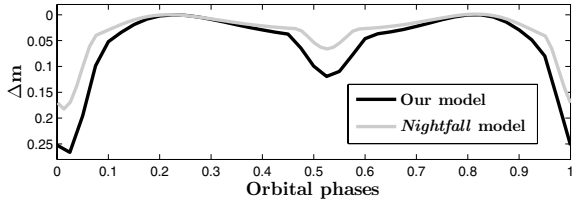

Fig. 12. Synthetic light curves of model E5 in the range $\lambda\lambda$ 3500, 7100. The light curves have been computed with the CoMBiSpeC + TIDES models (black) and with the Nightfall model (grey).

Table 6. Semi-amplitude of radial velocity curves for eccentric models and comparison with observations (in km s^{-1}).

Stars	K_1	K_2	$K_{1,\,\rm obs}$	$K_{2,\,\rm obs}$
Model E1	136.3	308.8	132.6	313.6
Model E2	77.3	142.8	79.3	139.0
Model E3	125.3	197.5	117.0	211.0
Model E4	157.6	213.9	162.4	213.9
Model E5	209.8	208.4	206.9	211.7

similarity and difference of the two models. For models E1 and E4, our light curves present qualitatively the same characteristics as *Nightfall*. The TIDES code leads to more compact objects than the instantaneous Roche potential. Therefore, because the stars are more compact, all other parameters being equal, the gravity darkening is less strong and the reflection effect is more effective and consequently the stars are hotter. Near periastron, the difference between the two models is stronger because our model predicts a weak variation of 0.02 mag and *Nightfall* predicts no variation. The very low inclination (60°) explains this small change of magnitude. Because the stars are less deformed (than in the Nightfall model), the reflection effect is more effective near periastron and accordingly, it also increases the temperature of the stars which enhances the difference between the two models. Some other differences arise because of the time delay induced by viscous stress. For model E1, the agreement between the two models and the light curve observed for HD 93205 by Antokhina et al. (2000) is poor, however. Models E2 and E3 give very different results with our code and *Nightfall*. These two systems have a longer period and are more compact in our model than in *Nightfall*. The discrepancies probably come from the different radii of the stars. Finally, the light curve of model E5 displays the two eclipses in both models but in our model, the eclipses are deeper than evaluated with *Nightfall* (see Fig. 12). Again the difference can be explained by the smaller radius of the star in our model. Some other small differences can be easily explained by the viscous effects. The agreement between our model and the observations of Mayer et al. (2008) is rather good, though we slightly overestimate the depth of the eclipse of the primary.

The mean brightness ratios in the wavelength range 3800−7100 Å are similar to the literature values. Finally, we determined the amplitude of the radial velocity curves and found a good agreement with the observations (see Table 6) for all simulated systems.

5. Summary and perspectives

We have presented improvements of our mathematical model that allow us to compute the physical properties on the surface

of massive stars in binary systems that contain main-sequence O(B) stars. The first improvement is the inclusion of the radiation pressure effect on the shape of the stars. The second improvement is the use of the TIDES code to compute the shape of the stars in eccentric and/or asynchronous systems. In both cases, we took into account various effects such as gravity darkening, reflection, and limb-darkening which allowed us to compute the temperature distribution at the stellar surface. Then we used the TLUSTY OSTAR2002 and BSTAR2006 grids (Lanz & Hubeny 2003, 2007) to compute the spectra of each star of the system as a function of orbital phase. We showed that in a number of cases, the radiation pressure does not have a strong impact on the shape of the stars and therefore on the spectra for the models studied in Paper I. This implies that the conclusions of Paper I for the S-S effect remain valid. Our results showed that the radiation pressure has a weak impact on the shape of highly deformed stars of (over)contact binary systems like model 3. However, in model 3, the small changes in the shape of the stars have resolved our previous problem of the surface temperature distribution that we failed to reproduce with our first version of the algorithm. We also studied the impact of the gravity-darkening parameter variation on the spectra of model 3. Our results indicate that, given the assumptions made for the computation, there is no need to use a more complex treatment of the gravity darkening than the classical von Zeipel theorem. The model 4 clearly showed that radiation pressure can have a strong impact on the shape of the stars. Many of the spectral lines in this model display phase-locked profile and/or strength variations. However, these variations are not sufficient to reproduce the S-S effect observed by Bonanos (2009).

The second part of this paper investigated the eccentric systems. We studied many lines and detected phase-locked profiles and/or strength variations in many cases in the individual spectra of both components. These variations are caused by the change of orientations of the stars as a function of orbital phase. They thus reflect the non-uniform temperature distribution across the stellar surface. The variations measured on the combined spectra of the systems, however, often disagree with the measurements made on individual spectra. Our results also showed that the deblending routines that fit two Gaussian or Lorentzian profiles often fail to measure the line EWs properly and lead to incorrect interpretations. The variations measured in models E2 and E5 underestimate the S-S effect observed in HD 93403 and HD 152248, which in turn might be caused by our not predict intrinsic asymmetric line profiles in these cases. In Paper I, this asymmetry was our explanation for the S-S effect: the sum of asymmetric intrinsic line profiles of individual stars are not properly deblended by Gaussian/Lorentzian profile fits. The absence of this asymmetry in eccentric systems is, however, not easy to explain and could be linked to weaker interactions between the stars in eccentric binaries than in close circular ones. Therefore, we cannot generalize the interpretation of the S-S effect of Paper I to the eccentric systems studied here. However, this highlights that analyses of binary system spectra are very difficult and some observational effects could be generated by analysing techniques and not by physical processes.

For clearly detached systems, spectral disentangling (Hadrava 1995; González & Levato 2006; Simon & Sturm 1994) helps to overcome the difficulties of the deblending routines. However, for systems with a strong temperature gradient at their surface (e.g. HD 100213, Linder et al. 2007), the technique fails because different lines have different radial velocity amplitudes. In eclipsing binaries, disentangling cannot be used for the phases near the eclipses. This technique provides mean spectra of both components, and even if we can measure variations with respect to this mean, we cannot compute the spectra at each orbital phase.

A future step could be to introduce cross-talk, which is surely substantial in eccentric and asynchronous systems. Finally, we plan to include a wind interaction zone between the stars, which could contribute to the heating of the stellar surface in two ways, either by backscattering of the photospheric photons, or by irradiation of X-ray photons emitted by the shock-heated plasma in the wind interaction zone. This requires, however, more sophisticated atmosphere models than what we have employed so far.

Acknowledgements. M.P. and G.R. acknowledge support through the XMM/INTEGRAL PRODEX contract (Belspo), from the Fonds de Recherche Scientifique (FRS/FNRS), as well as by the Communauté Française de Belgique – Action de recherche concertée – Académie Wallonie – Europe. G.K. and E.M. acknowledge support from UNAM/PAPIIT 107711.

References

Antokhina, E. A., Moffat, A. F. J., Antokhin, I. I., Bertrand, J.-F., & Lamontagne, R. 2000, ApJ, 529, 463
Bonanos, A. Z. 2009, ApJ, 691, 407
Castor, I. C., Abbott, D. C., & Klein, R. I. 1975, ApJ, 195, 157
Claret, A., & Bloemen, S. 2011, A&A, 529, A75
Conti, P. S., & Alschuler, W. R. 1971, ApJ, 170, 325
Dermine, T., Jorissen, A., Siess, L., & Frankowski, A. 2009, A&A, 507, 891
Drechsel, H., Haas, S., Lorenz, R., & Gayler, S. 1995, A&A, 294, 723
Espinosa Lara, F., & Rieutord, M. 2011, A&A, 533, A43
Gies, D. R., Penny, L. R., Mayer, P., Drechsel, H., & Lorenz, R. 2002, ApJ, 574, 957
González, J. F., & Levato, H. 2006, A&A, 448, 283
Hadrava, P. 1995, A&AS, 114, 393
Howarth, I. D. 1997, Observatory, 117, 335
Howarth, I. D., Siebert, K. W., Hussain, G. A. J., & Prinja, R. K. 1997, MNRAS, 284, 265
Kopal, Z. 1959, Close Binary Systems, in The International Astrophysics Series, ed. M. A. Ellison, & A. C. B. Lovell (London: Chapman & Hall Ltd.), 5
Lanz, T., & Hubeny, I. 2003, ApJS, 146, 417
Lanz, T., & Hubeny, I. 2007, ApJS, 169, 83
Linder, N. 2008, Ph.D. Thesis (University of Liège)
Linder, N., Rauw, G., Sana, H., De Becker, M., & Gosset, E. 2007, A&A, 474, 193
Linnell, A. P., & Hubeny, I. 1994, ApJ, 434, 738
Linnell, A. P., DeStefano, P., & Hubeny, I. 2012, PASP, 124, 885
Lucy, L. B. 1968, ApJ, 153, 877
Maeder, A. 1999, A&A, 347, 185
Mahy, L., Nazé, Y., Rauw, G., et al. 2009, A&A, 502, 937
Mathys, G. 1988, A&AS, 76, 427
Mathys, G. 1989, A&AS, 81, 237
Mayer, P., Harmanec, P., Nesslinger, S., et al. 2008, A&A, 481, 183
Moreno, E., & Koenigsberger, G. 1999, RMA&A, 35, 157
Moreno, E., Koenigsberger, G., & Toledano, O. 2005, A&A, 437, 641
Moreno, E., Koenigsberger, G., & Harrington, D. M. 2011, A&A, 528, A48
Najarro, F., Hillier, D. J., Puls, J., Lanz, T., & Martins, F. 2006, A&A, 456, 659
Palate, M., & Rauw, G. 2012, A&A, 537, A119
Phillips, S. N., & Podsiadlowski, Ph. 2002, MNRAS, 337, 431
Rauw, G., Sana, H., Gosset, E., et al. 2000, A&A, 360, 1003
Russell, H. N., & Merrill, J. E. 1952, Contrib. Princeton Obs., 23
Sana, H., & Evans, C. J. 2011, IAUS, 272, 474
Sana, H., Rauw, G., & Gosset, E. 2001, A&A, 370, 121
Sana, H., Antokhina, E., Royer, P., et al. 2005, A&A, 441, 213
Sana, H., Nazé, Y., O'Donnell, B., Rauw, G., & Gosset, E. 2008, New Astron., 13, 202
Schuerman, D. W. 1972, ApSS, 19, 351
Simon, K. P., & Sturm, E. 1994, A&A, 281, 286
Toledano, O., Moreno, E., Koenigsberger, G., Detmers, R., & Langer, N. 2007, A&A, 461, 1057
von Zeipel, H. 1924, MNRAS, 84, 665
Walborn, N. R., & Fitzpatrick, E. L. 1990, PASP, 102, 379
Wilson, R. E. 1990, ApJ, 356, 613
Wilson, R. E., & Devinney, E. J. 1971, ApJ, 166, 605

2.4 Limitations and developments

We discuss here the main limitations of CoMBiSpeC and the possible improvements of the code. The strength of CoMBiSpeC is its simplicity that allows to understand the impact of the temperature and $\log g$ distribution, the RV distribution, the radiation pressure, ... on the spectra. However, this strength is also a weakness because the assumptions made to compute the shape and the spectra of the stars are indeed strong. For example, when using the Roche potential, we assume that the stars act as point-like masses while this is not the case. For the eccentric orbits, we also assume that there exists an instantaneous reflection effect, or that the gravity is given by the gradient of the classical Roche potential. We also use the classical Von Zeipel theorem for the temperature computation while there exist more complicated models. Therefore, one could argue that CoMBiSpeC is too simple. Nevertheless, we have shown that this model is sufficient to reproduce and explain several issues encountered in massive binary systems. The conclusion is that, although some assumptions are not always fulfilled, the model is sufficiently accurate to reproduce quite well the observations. To first order, our code thus offers a significant improvement over stellar atmosphere models that assume static spherical stars.

Other important limits come from the grid of spectra, and these could be overcome. The first issue is the use of a grid in which the spectra are in flux units and not in intensity. An intensity grid would be better than our flux grid and would not require many changes in the code. The main adjustment would be an additional interpolation on the angle of the emergent light. This is not very difficult and will not lead to a large increase of the computational time. The interpolation could be combined to the temperature and $\log g$ interpolation in a one step multiple interpolation. The reason why this improvement has not been made is the difficulty to compute the grid itself. Some attempts have been made but computational issues with the SYNSPEC[4] routine prevent us to re-compute the grid. However, some tests with existing intensity spectra indicate that this improvement will not induce large changes in the normalized spectra. We have also to note that this improvement will substantially increase the size of the grid on the hard disk drive.

A second improvement related to the grid concerns the extended atmospheres. We know that massive stars have strong winds and that several spectral lines are formed in these winds. In a binary system, these winds interact leading to an enhanced X-ray emission in some systems. However, the grid from

[4]SYNSPEC is a routine designed by I. Hubeny that computes flux and intensity spectra from an atmosphere model. The latest version of SYNSPEC was obtained from http://nova.astro.umd.edu/Synspec49/synspec.html

TLUSTY only includes photospheric lines and does not account for extended atmospheres and thus some lines are not (well) represented.

To represent these lines, we first need to compute the winds and the interaction region geometry and physical characteristics (e.g. RV and temperature distributions). This would require new assumptions and introduce new free parameters such as the terminal velocity of the wind, the mass-loss rate, ... that render the model more complicated. Then, we need a new grid that accounts for the wind lines. Atmosphere models like FASTWIND (Santolaya-Rey et al. 1997), CMFGEN (Hillier & Miller 1998), PoWR (Gräfener et al. 2002, Hamann & Gräfener 2003), and PHOENIX (Hauschildt & Baron 1999) for extended atmospheres already exist for single stars and grids also exist. However, we cannot just use the grid of spectra for single stars with an extended atmosphere and interpolate in this grid because of the wind-wind interactions. The way to deal with the grid to model the spectra is thus a tricky problem.

Non-solar abundance grids could also be used or developed. Such grids already exist for particular metallicities and are available on the TLUSTY web site for example. We could treat this problem by adding an initial interpolation between the spectra of two values of metallicity to be as close as possible to the observed one. The result of this interpolation could be stored in a temporary grid. However, this solution does not allow to adjust the abundances of each element independently. We do not think that it is possible to change the abundance of one element without recomputing a full atmosphere model. Interpolating the value of the lines of one element from the spectra of two different metallicities is not recommended because a change of abundance has an impact on the opacity and can modify the line strengths of other elements.

As we can see, several limitations are directly linked to the grid. Solving the first point is the most crucial and "only" requires the processing of the atmosphere model with SYNSPEC. Solving the last two points is possible but more or less difficult and will introduce new free parameters. Therefore it will render even more complicated the search for a best-match agreement between the model and the observations. It will also complicate the determination of the origin of the observed phenomena.

The next improvement concerns the treatment of the reflection effects. A new model has been proposed by Budaj (2011) to account for temperature redistribution at the stellar surface (see Fig. 2.7). This work has been primarily designed for planet-star systems but could be adapted to binary systems. Budaj (2011) splits the irradiation process in three parts: the scattering of the light off the object which does not heat the irradiated surface, the heating of the irradiated surface by the companion, and the heat redistribution over the entire surface of

the object. The impact of this new treatment on light curves of exo-planets can be important. However, the parameters that influence the spectra are not the same as those that influence the light curve, and it is very difficult to predict the impact of a heat redistribution at the stellar surfaces on a spectrum. Moreover, the impact is more important if there exists a large temperature difference between the two objects which is seldom the case in massive binaries.

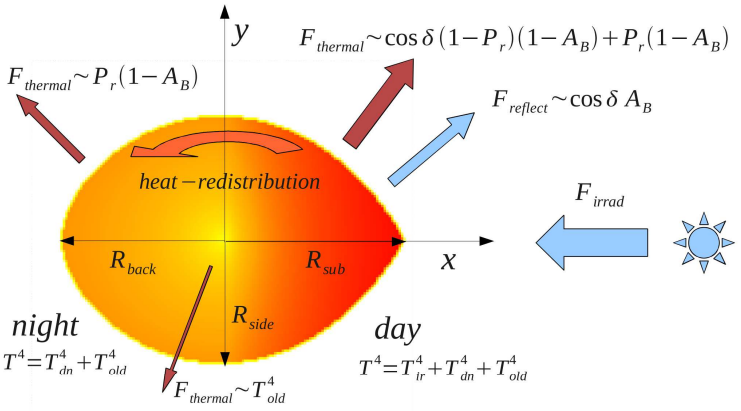

Figure 2.7: Reflection effect according to Budaj (2011).

In parallel to the heat redistribution we can cite the "cross-talk". The cross-talk consists in heat exchange between the adjacent surface elements due to, for example, horizontal advection or radiative exchanges between neighbouring surface elements of different temperatures. This effect is probably negligible in the case of circular systems in synchronous rotation but smoothes out some of the temperature variations for eccentric systems, especially near periastron where the stars move faster and where the gravitational interactions are stronger. Near periastron, the energy dissipation through shear is more important, and heat exchange could appear. The effect of the cross-talk is probably moderate because it corresponds to a decrease of the gravity-darkening.

In conclusion, we can see that new formalisms exist for the temperature computation (e.g. the Espinosa Lara & Rieutord (2011) model for the gravity-darkening, and the Budaj (2011) model for the reflection effects). These models go in the same direction: a decrease of the gravity-darkening effect and a smoothing of the temperature distribution. On the one hand, we have shown that a slight decrease of the gravity-darkening does not change much the spectra, on the other hand, there exist observational clues for gravity darkening. We thus think that the decrease of gravity darkening induced by these new treatments

have to be limited in order to account for the observed properties. The impact on the spectra should therefore, be limited.

Another interesting development would be the extension to over-contact binary systems. In these systems, the stars are not yet merged but are no longer clearly separated (see sect. 1.1.2). This situation raises the question of the validity of the classical gravity darkening law for the contact part of the system. The reflection effects might also be very important between the "facing" part of the stars of such system. However, the main issue comes from the shape computation that is more complex, and requires a more sophisticated treatment than the Newton-Raphson method.

Finally, the ultimate improvement would be the use of 3D radiative transfer. This is not strictly speaking an improvement but rather a new development in the spectral modelling. The 3D radiative transfer would answer many of the above questions but its implementation is a real challenge.

Chapter 3

Observational analyses

We have shown that classical tools developed for the analysis of single spherical stars are sometimes not well suited for the analysis of binary systems because the spectra of the components of binary systems are modified with respect to the spectra of single spherical stars. Therefore, new tools have to be used in addition to classical ones to improve our knowledge of massive stars. One of these new tools is a spectral modelling code for massive binary systems. The aim to develop such a code is not only to reproduce what we observe, but also to explain and understand what we observe. In that sense, CoMBiSpeC is well suited because it is simple. Therefore, we can easily understand the impact of the different parameters such as: gravity darkening, radiation pressure, polar radius and temperature, ...

Our code can also be used to improve and refine the physical parameters of the stars determined with classical tools. However, it does not fit a spectrum because the space parameters and the computation time would be prohibitive. The parameters have to be adjusted "by hand" to get the best-matching parameters. We present here some applications of CoMBiSpeC together with an example of the limits of the program.

3.1 LZ Cep

The first system that we have studied with CoMBiSpeC is LZ Cephei. It is an O 9III+O 9.7V circular binary system with an orbital period of 3.07 days. Mahy et al. (2011b) analysed the spectra and light curve of the system and proposed two possible solutions for the physical parameters of the stars. We have tried these two solutions with CoMBiSpeC and determined which one was the best. LZ Cep is an evolved system in which the stars have non-solar abundances, therefore

discrepancies between the model and the observations are always present, but the general matching between the model and the observation is good. The results are presented in the paper below.

ISSN 1845–8319

SPECTRAL MODELLING OF MASSIVE BINARY SYSTEMS: THE EXAMPLE OF LZ CEP

M. PALATE, G. RAUW and L. MAHY

Institut d'Astrophysique et de Géophysique,
Université de Liège, Bât. B5c, Allée du 6 Août 17, 4000 Liège, Belgium
email: palate@astro.ulg.ac.be

Abstract. Despite their importance for many astrophysical processes, massive stars are still not fully understood. Massive binaries offer an attractive way to improve our knowledge of the fundamental properties of these objects. However, some secondary effects are known to generate variations in the spectra of massive binaries, rendering their analyses more difficult. We present here a new approach to the computation of synthetic spectra of massive binaries at different phases of their orbital cycle. Our model starts with the Roche potential modified by radiation pressure and accounts for the influence of the companion star on the shape and physical properties of the stellar surface. We further account for gravity darkening and reflection effects to compute the surface temperature. Once the local gravity and temperature are determined, we interpolate in a grid of NLTE plan-parallel atmosphere model spectra to obtain the local contribution to the spectrum at each surface points. Then we sum all the contributions, accounting for the Doppler shift, and limb-darkening to obtain the total spectrum. The computation is repeated for different orbital phases and can be compared to the observations to determine the best parameters. We illustrate our method through the example of the LZ Cep system (O9III + ON9.7V).

Key words: massive stars - spectroscopic binaries

1. Introduction

Some effects linked to binarity complicate the spectral classification and/or the spectral analysis (see e.g., Sana *et al.* 2005, Linder *et al.* 2007, and references therein). For instance, the stars in binary systems are not spherical but atmosphere codes currently used to model observed spectra are designed for single spherical stars. In this context, we have developed a novel way of modelling the spectra of binary stars that account for deformations due to tidal effects and partially explain the peculiar effects observed in the spectra. CoMBiSpeC (Code of Massive Binary Spectral Computation) is designed for massive stars but could be modified and extended to low-mass

stars. The limitation to massive stars is an initial choice motivated by the fact that these stars are rare, not well-known but important for their surrounding and the galaxies. Moreover, a large fraction of massive stars (at least 50%) are part of binary or multiple system (Sana and Evans, 2011, and references therein; Sana *et al.*, 2012).

Non-spherical models were introduced in astrophysics by Russell (1952) to reproduce the light curves of binaries. Kopal (1959) introduced the Roche potential approach that was used by Lucy (1968) and Wilson and Devinney (1971). CoMBiSpeC is based, in a first step, on such models but we have incorporated radiation pressure effects and, of course, the computation of synthetic spectra.

Section 2 describes the assumptions, the modelling of the geometry of the stars, and the modelling of the spectra. In Section 3, we compare the predicted spectra to the observations and the new parameters found. We provide a summary of our results and future perspectives in Section 4.

2. Model

In this paper, we focus on the modelling of circular binary systems. For clarity, we divide the process into two parts, one part involving the surface, gravity and temperature calculation, and a second the spectra calculation. A full description of the model can be found in Palate and Rauw (2012) and Palate *et al.* (2013). The extension to eccentric orbits and/or asynchronous rotation is fully described in Palate *et al.* (2013) and consist in the use of the TIDES[1] code (Moreno *et al.*, 1999, 2005, 2011) for the surface and velocity field computation coupled to CoMBiSpeC for the spectral computation.

2.1. Geometrical modelling

In the case of circular systems in synchronous rotation, the stellar surface is an equipotential of the Roche potential. In massive stars, the radiation pressure is very important and acts on the shape of stars, we thus have modified the classical Roche potential by adding the inner radiation pressure (effect on each star's own surface) and the external radiation pressure (effect of the companion) effects. The treatment of the radiation pressure is a complex problem with an extensive literature. Our approach is based on

[1]Tidal interactions with dissipation of energy through shear.

the work of Drechsel *et al.* (1995) and Phillips and Podsiadlowski (2002) for the treatment of the external radiation pressure and the Howarth (1997) approach for the inner radiation pressure treatment. We refer the reader to these three papers as well as Palate *et al.* (2013) for the complete demonstrations and discussion.

The effect of the external radiation pressure can be seen as a force that decreases the attraction of the companion. Its treatment therefore consists of scaling the mass of the companion in the Roche potential. The scale parameter $\delta = \frac{F_{rad}}{F_{grav}}$ is computed iteratively for each surface point in a similar way to the reflection effect treatment of Wilson (1990). The modified "Roche" potential can be written

$$\Omega = \frac{1}{r} + \frac{q(1-\delta(r,\varphi,\theta))}{\sqrt{r^2 - 2r\cos\varphi\sin\theta + 1}} + \frac{q+1}{2}\cdot r^2\sin^2\theta - qr\cos\varphi\sin\theta, \quad (1)$$

where $r = \sqrt{x^2+y^2+z^2}$, $q = \frac{m_2}{m_1}$, $x = r\cos\varphi\sin\theta$, $y = r\sin\varphi\sin\theta$, and $z = r\cos\theta$. Here, θ and φ are, respectively, the colatitude and longitude angle in the spherical coordinates centred on the star under consideration.

According to Howarth (1997), the inner radiation pressure can be treated as a simple scaling of the Roche potential and thus, $\Omega_{eff} = (1-\Gamma)\Omega$, with $\Gamma = \frac{\sigma_{Th}}{m_h c}\sigma T_{pole}^4 \frac{1}{\|\vec{g}_{pole}\|}$ and where $\frac{\sigma_{Th}}{m_H} \approx 0.036$ m^{2}kg^{-1}, σ_{Th} is the Thomson scattering cross section and σ the Stefan-Boltzmann constant. The stellar surfaces are represented with a discretised grid of 240×60 points (in φ and θ respectively). The local acceleration of gravity is given by the gradient of the Roche potential. The temperature is computed accounting for gravity darkening and following the von Zeipel (1924) theorem

$$T_{\rm local} = T_{\rm pole}\left(\frac{\|\underline{\nabla}\Omega_{\rm local}\|}{\|\underline{\nabla}\Omega_{\rm pole}\|}\right)^{0.25}, \quad (2)$$

We have explicitly made the assumption of a co-rotating system, so that the stars always present the same face to each other. This leads to a local increase in temperature owing to the reflection effect between the two stars. We have followed the approach of Wilson (1990) to treat this effect. Figure 1 displays the gravity distribution at the stellar surfaces.

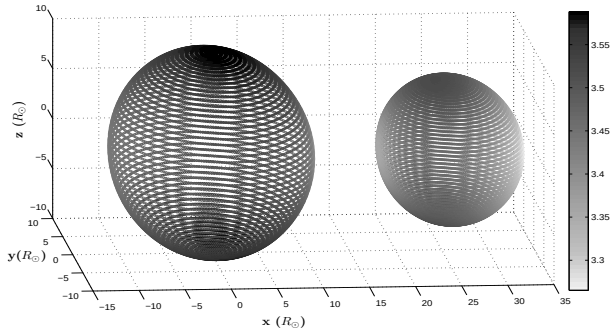

Figure 1: Distribution of $\log(g)$ at the stellar surface (cgs units) for the LZ Cep system computed with radiation pressure effects.

2.2. Spectral modelling

The second part of the algorithm computes the spectrum of the binary by summing the incremental contributions of each surface point. Non-LTE OB star spectral grids (TLUSTY OSTAR2002 and BSTAR2006 grid, Lanz and Hubeny, 2003, 2007) are used to compute the integrated spectrum of the star at each orbital phase. The spectral grid is computed for solar metallicity. Each spectrum is defined by two parameters: gravity and temperature. As we know these parameters for each point at the stellar surfaces, we can compute the local contribution to the spectrum. The computation consists of a linear interpolation between the flux of the four nearest spectra in the grid. The appropriate Doppler shift is then applied to the spectrum accounting for the orbital and rotational velocity of the surface element. We multiply the spectrum by the area of the element projected along the line of sight towards the observer and by a limb-darkening coefficient based on the tabulation of Claret and Bloemen (2011). Finally, we sum the contribution to the total spectrum. It has to be stressed that we have assumed that there is no cross-talk between the different surface elements as far as the formation of the spectrum is concerned. Phase zero corresponds to the "eclipse" of the primary by the secondary. Over the first half of the orbital cycle (phase $= [0, 0.5]$), the primary star has a negative radial velocity.

3. LZ Cep

LZ Cep is an O 9III+O 9.7V binary system with an orbital period of 3.070507 days. Its light curve displays ellipsoidal variations that are probably due to the deformation of at least one component. Mahy *et al.* (2011) recently determined dynamical masses of about 16 $M_{\odot}$ and of about 6.5 $M_{\odot}$ for the primary and the secondary components, respectively. Furthermore, they also found that the secondary is chemically more evolved than the primary. Indeed, the determinations of the CNO and He abundances show a depletion in C and in O whilst N and He are enriched. These results suggested that the secondary component is filling its Roche lobe and transfers its matter to the primary. The secondary thus appears to be a core He-burning object with a thin H-rich envelope.

Table I: Abundances derived by Mahy *et al.* (2011) compared to the solar abundances (Grevesse and Sauval 1998) used in the CoMBiSpeC model.

Abundances	Primary	Secondary	Solar
He/H	0.1	0.4	0.1
C/H $[\times 10^{-4}]$	1.0	0.3	2.45
N/H $[\times 10^{-4}]$	0.85	12.0	0.6
O/H $[\times 10^{-4}]$	3.0	0.5	4.57

LZ Cep was observed with NARVAL, the spectropolarimeter mounted on the Téléscope Bernard Lyot at the Pic du Midi Observatory in France. This instrument has a spectral resolution of $R = 65000$. The dataset contains ten spectra obtained on a timescale of 14 days between 2009 July 20 and 2009 August 03. These data were automatically reduced with the Libre ESpRIT package (Donati *et al.*, 1997).

Starting from these observations and from solutions derived by Mahy *et al.* (2011), we have refined the parameters of the stars. We have tried more or less 50 models in various ranges of temperatures and radii. The best agreement between observations and models is summarized in Table II. Figure 2 displays the observed spectrum and the CoMBiSpeC spectrum at phase 0.4. Some differences appear because of normalization errors of the observed spectra (e.g., the H δ and He I λ 4143 lines) and the fact that, the He and CNO abundances of the components of LZ Cep are non-solar while the grid of synthetic spectra used for computation is in solar abundances. Figure 2 (*zoom*) shows this difference for the carbon and nitrogen lines.

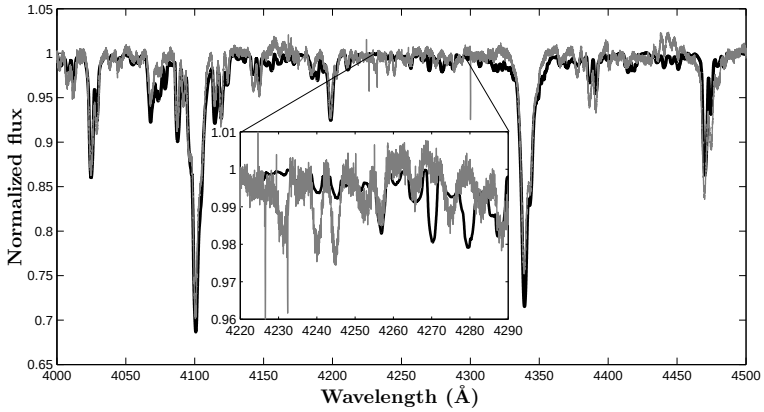

Figure 2: Comparison between observed spectrum (*in grey*) and the corresponding CoMBiSpeC model (*in black*) at phase 0.4. *Zoom:* Abundances difference for the N II $\lambda\lambda$ 4228, 4237, 4242 and O II $\lambda\lambda$ 4276, 4284 lines between observed spectrum (*in grey*) and the CoMBiSpeC model (*in black*).

Table II: Comparison between the solutions derived by Mahy *et al.* (2011) and the best solution found with the CoMBiSpeC model.

Parameters	Observations solution 1	Observations solution 2	CoMBiSpeC model solution
Mass$_p$ ($M_\odot$)	15.5 ± 1.0	16.9 ± 1.0	16.9
Mass$_s$ ($M_\odot$)	6.1 ± 1.0	6.7 ± 1.0	6.7
Polar temperature$_p$ (K)	32000(fixed)	32000(fixed)	33500 ± 500
Polar temperature$_s$ (K)	28000(fixed)	28000(fixed)	29500 ± 500
Polar radius$_p$ ($R_\odot$)	10.5 ± 1.2	10.5 ± 1.2	10.0
Equatorial radius$_p$ ($R_\odot$)	13.1 ± 1.2	12.4 ± 1.2	10.91
Maximal radius$_p$ ($R_\odot$)	13.1 ± 1.2	12.4 ± 1.2	10.91
Polar radius$_s$ ($R_\odot$)	6.1 ± 1.2	6.7 ± 1.2	6.7
Equatorial radius$_s$ ($R_\odot$)	6.9 ± 1.2	9.3 ± 1.2	7.33
Maximal radius$_s$ ($R_\odot$)	6.9 ± 1.2	9.3 ± 1.2	8.17

4. Discussion and Conclusion

We have presented the CoMBiSpeC model that is a first step in the spectral modelling of (massive) binaries. It allows us to compute the physical properties on the surface of massive stars in binary systems containing main-sequence O(B) stars. It includes various effects like reflection, radiation pressure, gravity darkening, limb-darkening that allow us to compute the temperature distribution at the stellar surface. Then, we use the TLUSTY OSTAR2002 and BSTAR2006 grids (Lanz and Hubeny, 2003, 2007) to compute the spectra of each star of the system as a function of orbital phase. For the first time, the CoMBiSpeC model has been used to refine the solution derived by classical analyses for the LZ Cep system. The example also underlines the improvements that could be done: extension to non-solar abundances, different turbulent velocity, lines affected by stellar winds, cross-talk between the surface elements. However, despite these limitations and assumptions, the results of the computation are quite encouraging, rendering CoMBiSpeC a promising tool for the analysis of massive binaries.

Acknowledgements

The authors would like to thank Dr. Fabrice Martins who provides the NARVAL spectra. We also acknowledge support through the XMM/INTEGRAL PRODEX contract (Belspo), from the Fonds de Recherche Scientifique (FRS/FNRS), as well as by the Communauté Française de Belgique - Action de recherche concertée - Académie Wallonie - Europe.

References

Castor, I. C., Abbott, D. C., and Klein, R. I.: 1975, *Astrophys. J.* **195**, 157.

Claret, A., and Bloemen, S.: 2011, *Astron. Astrophys.* **529**, 75.

Donati, J., Semel, M., Carter, B. D., Rees, D. E., and Collier Cameron, A.: 1997, *Mon. Not. R. Astron. Soc.* **291**, 658.

Drechsel, H., Haas, S., Lorenz, R., and Gayler, S.: 1995, *Astron. Astrophys.* **294**, 723.

Grevesse, N. and Sauval, A.: 1998, *Space Sci. Rev.* **85**, 161.

Howarth, I. D.: 1997, *The Observatory* **117**, 335.

Kopal, Z.: 1959, Close Binary Systems, in The International Astrophysics Series, eds. Ellison, M. A. and Lovell, A. C. B. (Chapman & Hall Ltd., London), 5.

Lanz, T. and Hubeny, I.: 2003, *Astrophys. J., Suppl. Ser.* **146**, 417.

Lanz, T. and Hubeny, I.: 2007, *Astrophys. J., Suppl. Ser.* **169**, 83.

Linder, N., Rauw, G., Sana, H., De Becker, M., and Gosset, E.: 2007, *Astron. Astrophys.* **474**, 193.

Lucy, L.B.: 1968, *Astrophys. J.* **153**, 877.

Mahy, L., Martins, F., Machado, C., Donati, J.-F., and Bouret, J.-C.: 2011, *Astron. Astrophys.* **533**, 9.

Moreno, E. and Koenigsberger, G.: 1999, *Revista Mexicana de Astronomia y Astrofisica* **35**, 157.

Moreno, E., Koenigsberger, G., and Toledano, O.: 2005, *Astron. Astrophys.*, **437**, 641.

Moreno, E., Koenigsberger, G., and Harrington, D. M.: 2011, *Astron. Astrophys.*, **528**, 48.

Palate, M. and Rauw, G.: 2012, *Astron. Astrophys.* **537**, 119.

Palate, M., Rauw, G., Koenigsberger, G., and Moreno, E.: 2013, *Astron. Astrophys.*, **552**, 39.

Phillips, S.N. and Podsiadlowski, Ph.: 2002, *Mon. Not. R. Astron. Soc.* **337**, 431.

Russell, H.N. and Merrill, J.E.: 1952, *Contrib. Princeton Obs.* **23**.

Sana, H., Antokhina, E., Royer, P., *et al.*: 2005, *Astron. Astrophys.* **441**, 213.

Sana, H. and Evans, C.J.: 2011, *Proceedings of the International Astronomical Union* **272**, 474.

Sana, H., de Mink, S.E., de Koter, A., *et al.*: 2012, *Science* **337**, 444.

von Zeipel, H.: 1924, *Mon. Not. R. Astron. Soc.* **84**, 665.

Wilson, R.E.: 1990, *Astrophys. J.* **356**, 613.

Wilson, R.E. and Devinney, E.J.: 1971, *Astrophys. J.* **166**, 605.

3.2 Spica

Our models have highlighted a new explanation of the Struve-Sahade effect, they allowed us to better understand the surface temperature distribution, and to get a better handle on the luminosity classification. The last effect for which we propose a new interpretation is the line profile variations. Such variations can be tidally induced by the interaction between the two components of a non-equilibrium binary system. The TIDES + CoMBiSpeC model has allowed to reproduce line profile variations in Spica. Spica is a double-lined, short-period ($\sim$ 4 days) spectroscopic binary in an eccentric orbit. The primary component is classified as B1.5 IV-V and it was believed to be a β Cephei-type star (Shobbrook et al. 1969; 1972). However, we have shown that the line profile variations could stem from the tidal flows at the stellar surface. These tidal flows are seen in the spectra in the form of travelling "bumps" that migrate from the blue to the red wing of the weak photospheric absorption lines. The spectral analysis of Spica also led us to refine the polar temperatures and radii for the two components. The tidal flows can also trigger a distortion of the RV curve leading to an apparently larger eccentricity. Our analyses have also underlined the importance of the micro-turbulence velocity that could be larger in binary systems than in single stars. In the case of Spica, a micro-turbulence velocity v_{turb} between 10 and 15 km s^{-1} was required to reproduce the line profile variations while Lanz & Hubeny (2007) suggested that $v_{turb} = 2$ km s^{-1} was sufficient for main sequence B-type stars.

A&A 556, A49 (2013)
DOI: 10.1051/0004-6361/201321909

Astronomy & Astrophysics

Spectral modelling of the α Virginis (Spica) binary system

M. Palate[1], G. Koenigsberger[2,⋆], G. Rauw[1], D. Harrington[3], and E. Moreno[4]

[1] Institut d'Astrophysique et de Géophysique, Université de Liège, Bât. B5c, Allée du 6 Août 17, 4000 Liège, Belgium
e-mail: palate@astro.ulg.ac.be
[2] Instituto de Ciencias Físicas, Universidad Nacional Autónoma de México, Cuernavaca, 62210 Morelos, México
[3] Institute for Astronomy, University of Hawaii, 2680 Woodlawn Drive, Honolulu, HI, 96822, USA
e-mail: dmh@ifa.hawaii.edu
[4] Instituto de Astronomía, Universidad Nacional Autónoma de México, México, D.F., México
e-mail: edmundo@astro.unam.mx

Received 17 May 2013 / Accepted 20 June 2013

ABSTRACT

Context. The technique of matching synthetic spectra computed with theoretical stellar atmosphere models to the observations is widely used in deriving fundamental parameters of massive stars. When applied to binaries, however, these models generally neglect the interaction effects present in these systems.
Aims. The aim of this paper is to explore the uncertainties in binary stellar parameters that are derived from single-star models.
Methods. Synthetic spectra that include the tidal perturbations and irradiation effects are computed for the binary system α Virginis (Spica) using our recently-developed CoMBiSpeC model. The synthetic spectra are compared to $S/N \sim 2000$ observations and optimum values of $T_{\rm eff}$ and $\log g$ are derived.
Results. The binary interactions have only a small effect on the strength of the photospheric absorption lines in Spica (<2% for the primary and <4% for the secondary). These differences are comparable to the uncertainties inherent to the process of matching synthetic spectra to the observations and thus the derived values of $T_{\rm eff}$ and $\log g$ are unaffected by the binary perturbations. On the other hand, the interactions do produce significant phase-dependent line profile variations in the primary star, leading to systematic distortions in the shape of its radial velocity curve. Migrating sub-features ("bumps") are predicted by our model to be present in the same photospheric lines as observed, and their appearance does not require any a priori assumptions regarding non-radial pulsation modes. Matching the strength of lines in which the most prominent "bumps" occur requires synthetic spectra computed with larger "microturbulence" than that required by other lines.

Key words. stars: massive – binaries: general – stars: fundamental parameters – stars: atmospheres – binaries: spectroscopic – stars: individual: α Virginis

1. Introduction

Massive stars play a key role in the evolution of galaxies through their high luminosity, powerful winds, heavy element enrichment of the ISM, and the explosions when they end their lives as supernovae. The importance of determining their fundamental parameters cannot be overstated, and considerable effort has been invested in obtaining high quality observations and applying theoretical stellar structure models to establish these parameters (see for example, Evans et al. 2011; Martins 2011; Massey et al. 2009, 2012). Although significant progress has been made, there are still some important gaps in our understanding of the physical processes that govern the structure and evolution of massive stars. One of these gaps involves the effects caused by a binary companion on the emergent spectrum, from which the fundamental parameters are generally derived.

Binary systems provide the only direct means of determining the masses of stars and thus they are used to test the models of stellar structure which are then applied to single stars. The usual method for obtaining the binary star parameters is through the use of the radial velocity (RV) curves and model atmosphere codes. This yields a lower limit to the masses of the two stars, $m \sin^3 i$, the stellar radii R, effective temperature $T_{\rm eff}$, surface gravitational acceleration $\log g$, and metallicity (see, for example, Massey et al. 2012).

The majority of stellar atmosphere models have been developed for single stars. Thus, one of the important questions that arises concerns the extent to which they can be used to properly model binary stars since the latter are subject to a variety of interaction effects. For example, gravity darkening and irradiation of the hemisphere facing the companion are expected to lead to different $T_{\rm eff}$ values over the surface, with analogous differences in $\log g$ values due to the tidal distortion. In addition, non-synchronous rotation and orbital eccentricity induce oscillations on the stellar surface that may lead to photospheric absorption line profiles that are significantly different from those that are predicted by single-star atmospheric models (Vogt & Penrod 1983). It is possible that the temporal variability of these line profiles can have a significant impact on the determination of the fundamental parameters through the distortion of the RV curves (Koenigsberger et al. 2012).

We have developed a method for computing the spectra of binary systems which takes into account interaction effects. In a first stage, the code was designed for circular massive binary systems (Palate & Rauw 2012) in which the distorted shape of the stellar surfaces due to the gravitational interaction is calculated

⋆ *Current address*: Instituto de Astronomía, UNAM, Apdo. Postal 70-264, México D.F., México, e-mail: gloria@astro.unam.mx

and then the emergent spectra at different orbital phases are computed. In a second paper the method was extended to include eccentric binaries and to incorporate radiation pressure effects (Palate et al. 2013). This new version of the CoMBiSpeC (Code of Massive Binary Spectral Computation) now allows spectral computation of massive binary systems in general. In this paper we use this code to address the question of the extent to which the binary interactions may affect the outcome of the standard procedure of matching stellar atmosphere models to observations in order to derive values of $T_{\rm eff}$ and $\log g$. This exploratory investigation will focus on the nearby and well-studied binary system α Virginis (=Spica = HD 116658).

In this paper we use local line-profiles obtained from a full radiative transfer computation using the standard model atmosphere code TLUSTY. This enables us to analyse the effects of the binary interaction on the determination of $T_{\rm eff}$ and $\log g$, in addition to the line-profile variability. In Sect. 2 we provide a brief review of Spica's properties; in Sect. 3 we describe the procedure that was followed to produce the synthetic spectra, in Sect. 4 we present the results, and in Sect. 5 the conclusion.

2. The Spica binary system

Spica is a double-lined, short-period (~4 days) spectroscopic binary in an eccentric orbit. The primary component is classified as B1.5 IV-V and based on early observations that disclosed a 4.17 h spectroscopic and photometric period, it was believed to be a β Cephei-type star (Shobbrook et al. 1969, 1972). However, the photometric variations seem to have vanished in 1970−1971 (Smith 1985a). On the other hand, the spectroscopic line-profile variations have persisted (Smak 1970; Smith 1985a,b; Riddle 2000; Harrington 2009). They are commonly described in terms of travelling "bumps" that migrate from the blue to the red wing of the weak photospheric absorption lines, but also include variations in the slope of the line wings. A periodicity of 6.5 and 3.2 h has been associated with these variations (Smith 1985a).

Spica was observed interferometrically by Herbison-Evans et al. (1971), allowing a direct determination of orbital separation, stellar radius of the primary ($R_1 = 8.1 \pm 0.5\ R_\odot$) and orbital inclination ($i = 65.9° \pm 1.8°$), which when combined with RV curves yield the masses, $M_1 = 10.9 \pm 0.9\ M_\odot$ and $M_2 = 6.8 \pm 0.8\ M_\odot$. More recently, it was observed with the CHARA and SUSI interferometric arrays by Aufdenberg (2007) and collaborators. The analysis followed that of Herbison-Evans et al. (1971) except that the stellar disks were no longer assumed to be of uniform brightness but were assumed to be rotationally and tidally distorted. The results of this analysis were kindly provided to us by Aufdenberg (2008, priv. comm.) and consist of slightly different values for the stellar and orbital parameters. They are listed in Table 1 together with those of Herbison-Evans et al. (1971).

The stellar rotation velocities, $v_{\rm rot}$, were derived by Smith (1985a), who modelled the line-profile variability under the assumption that it could be described in terms of high-order non-radial pulsation modes. To derive the order of the modes, Smith (1985a) used a trial and error profile-fitting method in which he included the presence of travelling "bumps" and tested combinations of rotational, macroturbulent and pulsational velocities and periods. The rotation velocities he derived are $v_1 \sin i = 161 \pm 2$ km s^{-1} and $v_2 \sin i = 70 \pm 5$ km s^{-1}.

Harrington et al. (2009) adopted the Aufdenberg et al. (2008) stellar and orbital parameters and Smith's (1985a) values for $v_{\rm rot}$, and performed an ab initio calculation of the line profiles at several orbital phases in order to study the variability that is caused by the response of the star to tidal perturbations. The calculation involves the solution of the equations of motion of the surface elements in the presence of gravitational, Coriolis, centrifugal, viscous and gas pressure forces, and the projection of the resulting velocity field along the line of sight to the observer in order to compute photospheric absorption lines in the observer's reference frame. Harrington et al. (2009) were able to reproduce the general trends in the line-profile variability and, in particular, the observed relative strength and number of "blue" to "red" migrating "bumps". These "bumps" were found to arise in what Harrington et al. describe as "tidal flows", a concept that differs from the non-radial pulsation representation in that the travelling waves on the stellar surface are a consequence entirely of the response of this surface to the forcing and restoring agents, the interior structure of the star playing no role. The line profile calculation performed by Harrington et al. (2009) was done for an arbitrary absorption line assuming that the local line profile at each location on the stellar surface has a Gaussian shape. Thus, their study was limited to the analysis of line-profile variability alone, and no comparison of the effects on different lines (particularly those used for temperature and gravity diagnostics) was possible.

Table 1. Spica parameters.

Parameter	H-E[a]	Aufdenberg et al.
Spectrum	B1.5 IV-V + B3V	B0.5 III-IV + B2.5-B3 V
m_1 ($M_\odot$)	10.9 ± 0.9	10.25 ± 0.68
m_2 ($M_\odot$)	6.8 ± 0.7	6.97 ± 0.46
R_1 ($R_\odot$)	8.1 ± 0.5	7.40 ± 0.57
R_2 ($R_\odot$)	–	3.64 ± 0.28
P (day)	4.014597	4.0145898
T_0 (JD)	2 440 678.09	2 440 678.09
e	0.146	0.067 ± 0.014[b]
i (°)	66 ± 2	54 ± 6
ω (°) at T_0	138 ±15	140 ± 10
Apsidal Period (yrs)	124 ± 11	130 ± 8
$v_1 \sin i$ (km s^{-1})	161 ± 2[c]	161 ± 2[c]
$v_{\rm rot1}$ (km s^{-1})	176 ± 5	199 ± 5
$v_2 \sin i$ (km s^{-1})	70 ± 5[c]	70 ± 5[c]
$v_{\rm rot2}$ (km s^{-1})	77 ± 6	87 ± 6
$\beta_0(m_1)$[d]	1.3	1.88 ± 0.19
$\beta_0(m_2)$	–	1.67 ± 0.5

Notes. [(a)] Herbison-Evans et al. (1971). [(b)] From Riddle (2000). [(c)] From Smith (1985a). [(d)] The β_0 parameter is the ratio of the rotation and orbital angular velocities at periastron and can be expressed as: $\beta_0 = 0.02 \frac{P\ v_{\rm rot}}{R} \frac{(1-e)^{3/2}}{(1+e)^{1/2}}$, where $v_{\rm rot}$ is the rigid body rotation velocity (in km s^{-1}), R is the equilibrium radius (in $R_\odot$), and e is the eccentricity.

3. Method of analysis

Synthetic spectra were produced for a binary system under the assumptions of a) no interaction effects; and b) tidal and irradiation effects. These spectra will henceforth be alluded to as "unperturbed" and "perturbed", respectively. The detailed procedure for generating the synthetic spectra is described below.

Rotating and binary stars are deformed from spherical symmetry and thus the gravity darkening effects[1] lead to a non-uniform value of effective temperature and gravity over the stellar surface. When synthetic spectra are produced from model atmosphere grids, they are characterized by the values of

[1] As in Palate et al. (2013) we used a gravity darkening parameter equal to 0.25.

effective temperature and surface gravity at the pole. Thus, we refer to our models with the values of $T_{\rm eff}^{\rm pole}$ and $\log g^{\rm pole}$.

The synthetic spectra were compared with observational data that were obtained on 2008 March 15–28 at the Canada France Hawaii (CFHT) 3.6 m telescope with the ESPaDOns spectropolarimeter, which are thoroughly discussed in Harrington et al. (2009). They consist of high resolution spectra (R = 68 000) in the wavelength range $\lambda\lambda$ 3700–9200 Å with typical signal-to-noise ratio $S/N \sim 2000$.

The synthetic spectra were produced as follows:

Step 1: the stellar surface deformation and velocity field of both stars in the binary system are computed using the TIDES code. This requires prior knowledge of the stellar masses, radii and rotation velocity, as well as the full set of orbital parameters. The masses and radii are those given by Aufdenberg et al. (2008) taking into account the uncertainties quoted by these authors, the eccentricity is from Riddle (2000), and the longitude of periastron $\omega_{\rm per}$ = 255° is from Harrington et al. (2009). The output consists of displacements and velocities (both radial and azimuthal) for each surface element as a function of time. A full description of the TIDES calculation is provided in Moreno et al. (2011) and a detailed description of the calculations that were performed for Spica can be found in Harrington et al. (2009).

Step 2: we use the grid of stellar atmosphere models computed with TLUSTY (Lanz & Hubeny 2007) to produce emergent flux spectra with microturbulent speeds in the range $v_{\rm turb}$ = 2–15 km s^{-1} using the routine SYNSPEC49[2]. The set of spectra for the primary star in Spica covers $T_{\rm eff}$ = 22 000 to 25 000 K and $\log g$ = 3.75 to 4.00, and for the secondary the corresponding ranges are 18 000–22 000 K and $\log g$ = 4.00 to 4.25. The metallicity of these models is Solar and the SYNSPEC49 calculation was performed using the NLTE option[3].

Step 3: CoMBiSpeC is used to compute the temperature and gravity distributions and then is used to linearly interpolate and Doppler-shift the spectra obtained from the SYNSPEC49 calculation to obtain the emergent spectrum for each surface element of the star (i.e., the "local" line profile) and then the final synthetic spectrum is produced by integration over the entire stellar surface. The Doppler shift is performed using the velocity field computed by TIDES projected along the line-of-sight to the observer.

Step 4: observational data obtained at one orbital phase when the lines of the primary and secondary are well-separated are compared to the synthetic spectra computed for the various sets of $T_{\rm eff}^{\rm pole}$ and $\log g^{\rm pole}$ at a similar orbital phase in order to determine the best match between the synthetic and observed photospheric lines. Preference is given to matching lines that are good $T_{\rm eff}$ and $\log g$ diagnostics[4] and, among these, those that lie in spectral regions where the uncertainties in the continuum normalization of the data are minimum. The atlas of Walborn & Fitzpatrick (1990) is used as a guide for the trends in He I, He II and Si III line strengths with increasing $T_{\rm eff}$ and $\log g$. For the present investigation, over 160 synthetic model spectra were tested against the observations. A "best match" of the synthetic spectrum to the observations is attained when synthetic spectra with adjacent values of $T_{\rm eff}^{\rm pole}$ and $\log g^{\rm pole}$ bracket the majority of observed spectral lines amongst the ones used for diagnostics purposes. As will be shown below, our best match synthetic spectra reproduce the observations to within ~5% of continuum unit.

We initiated the analysis using the orbital elements and stellar parameters derived by Aufdenberg et al. (2008) and the value of $v \sin i$ from Smith (1985a). The primary reason for this choice is that these parameters were found by Harrington et al. (2009) to produce line-profile variability that most resembled the one observed. The qualitative nature of the line profile variations predicted by the TIDES code depends not only on masses, stellar radii and orbital parameters but also on $v \sin i$, the depth of the layer that is modelled in TIDES, $\Delta R/R_1$, and on the kinematical viscosity, ν of the material. An adequate combination of all of these parameters is required to achieve a satisfactory match to the observations. For the present analysis we fixed M_1, M_2, e, $\Delta R/R_1$, ν and the computational parameters required by TIDES to the values that were found by Harrington et al. to best reproduce the line-profile variability. The parameters that were varied are: R_1, R_2, i (orbital inclination), and the values of $T_{\rm eff}$ and $\log g$ for the two stars.

After several iterations we found that the best fit to the observations was attained with $R_1^{\rm pole}$ = 6.84 $R_\odot$ and i = 60°. Both of these values lie within the uncertainties quoted by Aufdenberg et al. (2008) and hence, we shall refer to the input parameter set as that of Aufdenberg et al. (2008).

We used the ESPaDOns spectra obtained on 22 and 26 March 2008 (orbital phases 0.88 and 0.84, respectively[5]) as the guide for the first synthetic spectrum, since at these orbital phases the absorptions arising in each star are well separated. The velocity field computed in *Step 1* was applied to the grid of models described in *Step 2* and the synthetic spectra (*Step 3*) were compared with these ESPaDOns spectra.

In the initial iteration for finding the optimum values of $T_{\rm eff}^{\rm pole}$, $\log g^{\rm pole}$ an excellent match was attained for the H and He I lines with $v_{\rm turb}$ = 2 km s^{-1}, but the majority of the heavy element lines were too weak by factors of 2–3. Thus, the next iteration consisted of finding the value of $v_{\rm turb}$ for which the strength of the Si III $\lambda\lambda$ 4552-4574 triplet lines coincided with the observations[6]. We found that a good match to the Si III line strengths requires $10 \leq v_{\rm turb}/({\rm km\,s^{-1}}) \leq 15$, and the final model was computed with $v_{\rm turb}$ = 15 km s^{-1}. It must be noted, however, that this value of $v_{\rm turb}$ resulted in lines such as O II $\lambda\lambda$ 4072-79 being significantly stronger in the synthetic spectra than in the observations. Figure 1 illustrates the manner in which the Si III triplet changes for $v_{\rm turb}$ = 2, 10 and 15 km s^{-1}, and Fig. 2 shows the effect on other lines. Noteworthy is the very different behaviour of He I λ 4471 from that of Si III λ 4552 and other heavy-element lines. This difference may be traced to the atomic line-strength parameters which affect the shape of the line profiles.

[2] The grid of models is available at http://nova.astro.umd.edu/Tlusty2002/tlusty-frames-BS06.html and the latest version of SYNSPEC was obtained from http://nova.astro.umd.edu/Synspec49/synspec.html

[3] It is important to note that the NLTE calculation is actually only performed on a limited number of the lines (mainly H, He and C N O in later stages). Lanz & Hubeny (2007) argue that NLTE effects in the other lines are small.

[4] See, for example, Massey et al. (2009) for a more in-depth description of the spectrum-matching process.

[5] The phase ϕ = 0 corresponds to the periastron passage of the observations and we used the T_0 and the apsidal period derived by Aufdenberg et al. (2008).

[6] An in-depth description of the manner in which $v_{\rm turb}$ is generally determined may be found in Hunter et al. (2007). Included is a justification of the use of the Si III triplet for fixing the value of this parameter as well as a discussion of the manner in which the use of different lines results in different values.

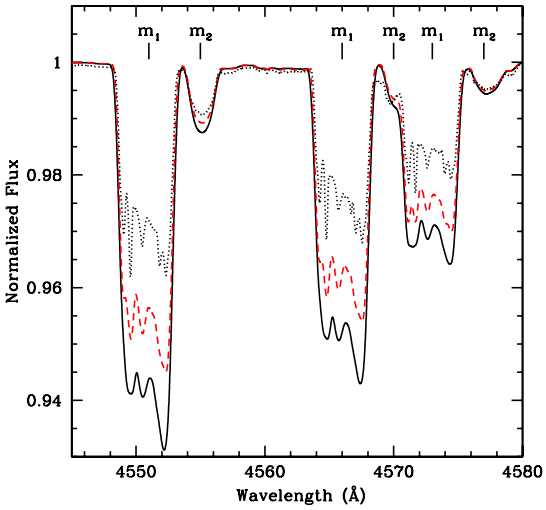

Fig. 1. Synthetic Si III line profiles computed for Spica with the TLUSTY stellar atmosphere models for $T_{\rm eff}$ and $\log g$ appropriate to each surface element and Doppler-shifted using the surface velocity field computed with TIDES. The three spectra correspond to microturbulent velocities $v_{\rm turb}$ = 2 (dots), 10 (dashes) and 15 (continuous) km s^{-1} and illustrate how the larger values of this parameter produce greater line-strength in the Si III λ 4552 line. The lines originating in the primary and secondary are indicated with m_1, and m_2 respectively. The depicted profiles correspond to orbital phase ϕ = 0.75.

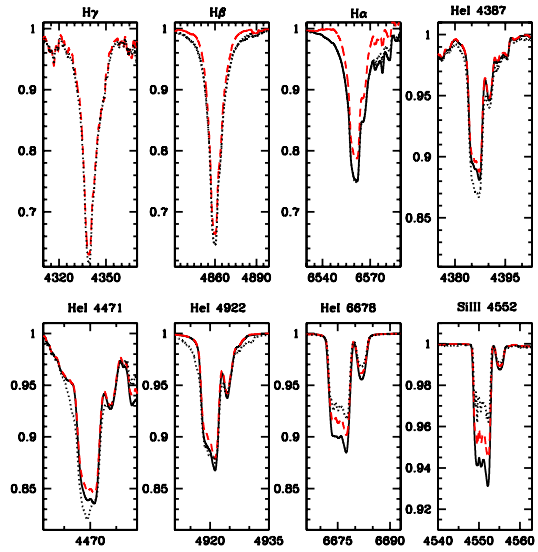

Fig. 2. Dependence of line strength on microturbulent speed $v_{\rm turb}$. As in Fig. 1, the same stellar atmosphere model computed with $v_{\rm turb}$ = 2 (dots), 10 (dashes) and 15 (continuous) km s^{-1} is shown. The behaviour of the stronger He I lines is different from that of weaker lines. In the H-lines, the dependence on $v_{\rm turb}$ is strongest in the line wings.

Once the set of parameters that best described the ESPaDOnS spectrum of 22 March were determined, these were held constant and we proceeded to compute the synthetic spectra at 20 equally spaced orbital phases. These are the spectra that are discussed in the next sections.

4. Results

4.1. The impact of interaction effects on $T_{\rm eff}$ and log g

The best match to the ESPaDOns spectra of 22 and 26 March was attained with ($T_{\rm eff}^{\rm pole}$, log $g^{\rm pole}$) of (24000 ± 500 K, 3.78) for the primary and (19500 ± 500 K, 4.16) for the secondary. These values are in good agreement with those found by Aufdenberg et al. (2008) for the primary star, (24750 ± 500, 3.71 ± 0.06). For the secondary, our result is in agreement with Aufdenberg et al.'s log $g^{\rm pole}$ = 4.16 ± 0.05, and Lyubimkov et al. (1995) $T_{\rm eff}^{\rm pole}$ = 20800 ± 1500 K.

The parameters of the final model are listed in Table 2, and selected spectral regions of these models and the corresponding observational data of 26 March (ϕ = 0.84) and 15 March (ϕ = 0.15) are shown in Figs. 3 and 4. Figures 5 and 6 illustrate the matching between observed and synthetic spectra for individual lines. The difference between the observed and the synthetic spectra is ≤5%, as shown by the plot at the bottom of these figures. For the 4060−4360 Å and 4360−4720 Å wavelength regions, the maximum difference is <4% except at λ 4078.4 (8.7%). For the 4730−5130 Å wavelength region, the maximum difference is 2.5% and appears in the wings of Hβ.

The maximum departure from sphericity in Spica's primary is ≤0.2 $R_\odot$, and thus the value of $\log g$ over the stellar surface is practically constant. The largest $T_{\rm eff}$ is found at the pole and decreases towards the equator, but the small gravity darkening leads to a $T_{\rm eff}$ decrease of only ~500 K. The irradiation effect is also small and thus the hemisphere facing the secondary is nearly at the same temperature as the opposite hemisphere. The small differences in $T_{\rm eff}$ and $\log g$ over the stellar surface in the primary lead to line strengths in the perturbed spectra that differ only slightly from those in the unperturbed spectrum. Figure 7 shows that the differences in the equivalent width (EW) of the lines in the perturbed and unperturbed spectra are ≤1.5%, which is

Table 2. Parameters used for computation with the TIDES + CoMBiSpeC model.

Parameters	Primary	Secondary
Common parameters		
Period (day)	4.01452	
Eccentricity	0.067	
ω^a (°)	255	
Inclination (°)	60	
CoMBiSpeC parameters		
Mass ($M_\odot$)	10.25	6.97
Polar temperature (K)	24 000	19 500
Polar radius ($R_\odot$)	6.84	3.64
Polar log (g) (cgs)	≃3.78	≃4.16
$v_{\rm rot}$ (km s^{-1})	199	87
$v \sin i$ (km s^{-1})	172	75
β_0	2.07	1.67
Microturbulent velocity (km s^{-1})	15	15
TIDES code parameters		
Viscosity, ν ($R_\odot^2$ day^{-1})^b	0.028	0.028
Layer depth ($\Delta R/R$)	0.07	0.07
Polytropic index	1.5	1.5
Number of azimuthal partitions	500	500
Number of latitudinal partitions	20	20

Notes. $^{(a)}$ Argument of periastron of the secondary. $^{(b)}$ 1 $R_\odot^2$ day^{-1} = 5.67 × 10^{16} cm^2 s^{-1}.

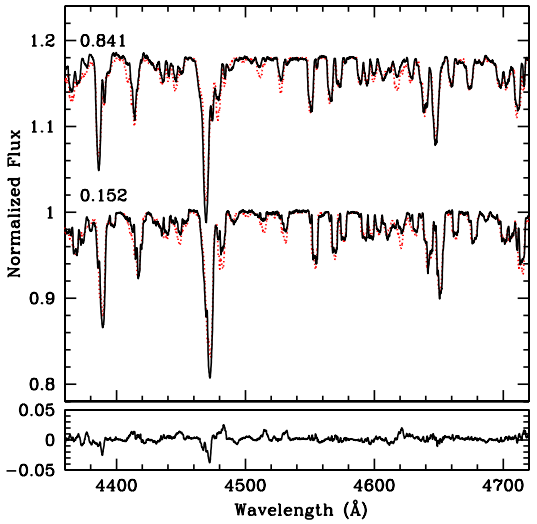

Fig. 3. Comparison of the best-fit CoMBiSpeC model (dots) with the ESPaDOns spectra of Spica at orbital phases 0.152 (15 March) and 0.841 (26 March; shifted by +0.2 continuum units). The tracing shown at the bottom is the difference between the 15 March spectrum and its corresponding synthetic spectrum and shows that the fit is good to ~3%.

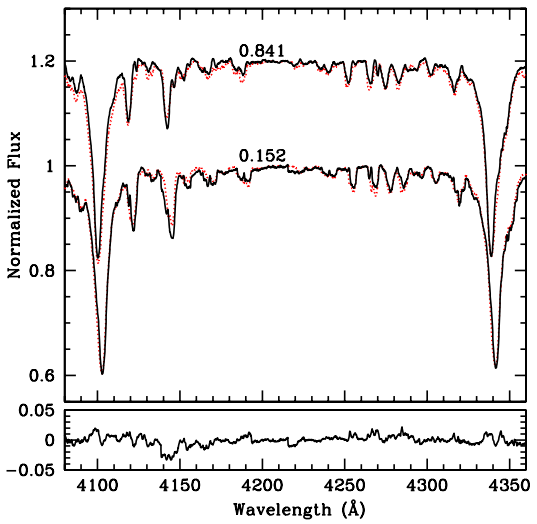

Fig. 4. Same as previous figure for the spectral region containing Hδ and Hγ.

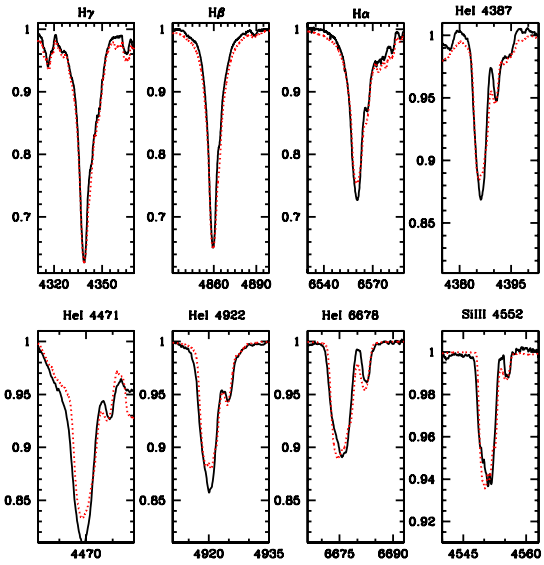

Fig. 5. Individual lines in the 26 March spectrum compared to the corresponding synthetic spectrum.

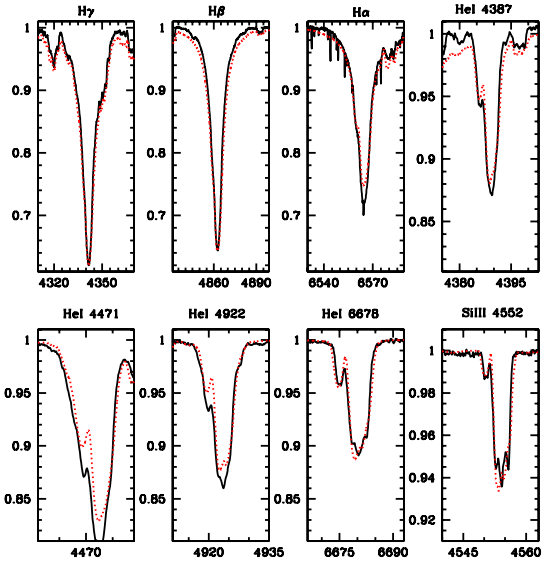

Fig. 6. Individual lines in the 28 March spectrum compared to the corresponding synthetic spectrum.

below the typical observational uncertainties and those inherent to the spectrum fitting technique. Thus we conclude that despite the strong line-profile variability in Spica's primary star, there is a negligible effect on the derivation of $T_{\rm eff}$ and $\log g$ values.

For the secondary, the effects caused by gravity darkening are also small, but due to the hotter primary the irradiation effects are more important. Hence, the largest $T_{\rm eff} \sim 20\,300$ K is on the equator of the hemisphere facing the primary while the lowest $T_{\rm eff} = 19\,400$ K occurs on the opposite hemisphere, also along the equator. The irradiated hemisphere of the secondary is viewed by the observer around periastron passage, at which time the EW of Si III λ4552 increases by ~5% while that of Hβ decreases by ~2%, as illustrated in Fig. 8.

It is interesting to note that despite the relatively small surface deformations, the observed light curve of Spica displays ellipsoidal variations (Shobbrook et al. 1969; Sterken et al. 1986) with peak-to-peak amplitudes ~0.03 mag. We computed the predicted light curve variations from out model results following the method described in Palate & Rauw (2012) and find a peak-to-peak amplitude ~0.02 mag. The difference between our predicted light curve and that which is observed may in part be due

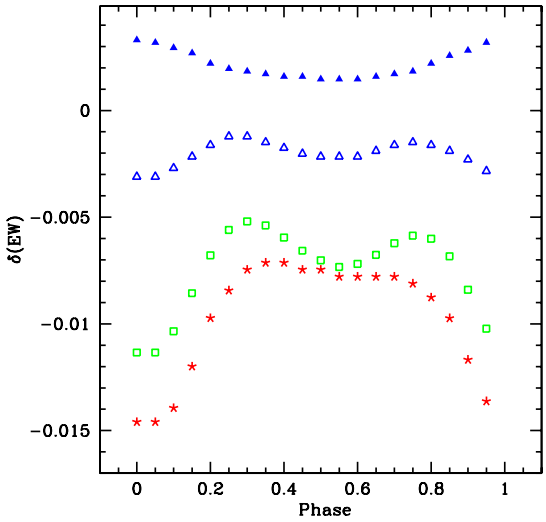

Fig. 7. Difference between equivalent widths measured on the perturbed and unperturbed spectra, $\Delta(EW) = [EW_p - EW_u]/EW_u$, of the primary star in Spica showing that the effects are ≤1.5%, and thus indicating that the interaction effects have a negligible impact on the spectral classification. Negative residuals indicate that the absorption in the perturbed profiles is weaker than in the unperturbed profiles. The different symbols correspond to: He I λ 4921(open triangles), He I λ 5875 (filled-in triangles), Si III λ 4552 (stars) and Hβ (squares).

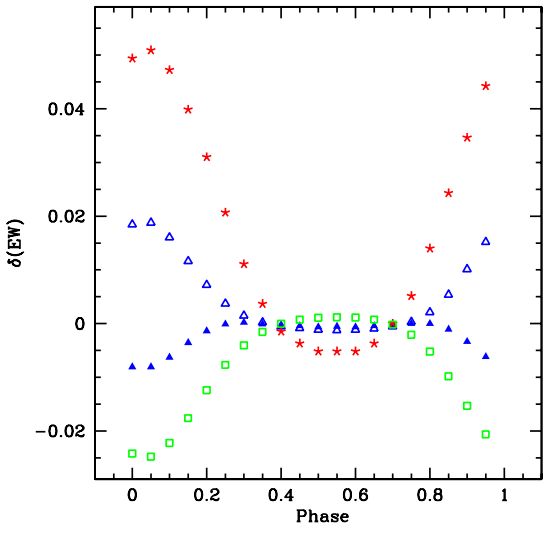

Fig. 8. Same as previous figure (Fig. 7) for the secondary showing that in this case, the effects are ≤5%. Note that around periastron, the Si III λ 4552 strength increases by ∼5% while that of Hβ decreases by ∼2.5%.

to the uncertainties introduced by the short-period photometric variability which is present in the observations.

4.2. Line profile variability

The binary interactions significantly affect the shape of the line profiles. Figure 9 shows the Si III triplet line profiles at 10 orbital

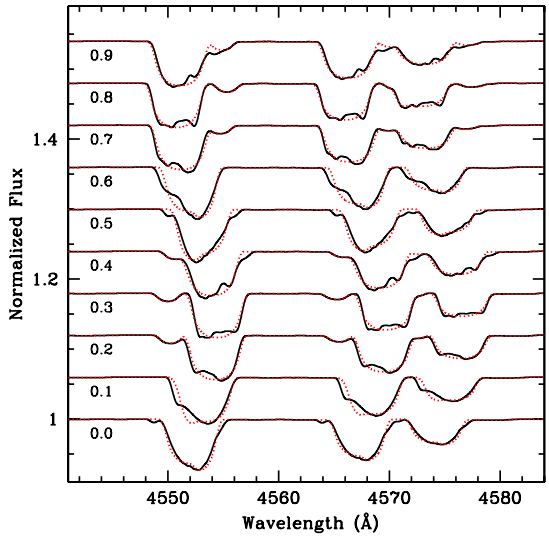

Fig. 9. Synthetic primary + secondary combined spectra of the Si III triplet are stacked in order of increasing orbital phase (ϕ = 0 corresponds to periastron). The perturbed spectra are displayed with the dark tracing and the unperturbed spectra with dots. The "bumps" in the primary star's perturbed profiles are evident as is the difficulty they introduce in properly locating the contribution of the secondary except at $\phi \sim 0.3 \pm 0.05$ and 0.8 ± 0.05 when the contribution from the secondary is clearly resolved.

phases in the perturbed and the unperturbed spectra. The strong phase-dependent variations in the perturbed profiles are clearly seen and can be described primarily in terms of "bumps" and asymmetries, similar to those present in the observational data[7]. The same behaviour is present in numerous other photospheric absorptions, such as He I λ 5875 (Fig. 10), but is at the ∼1.5% level.

The most prominent perturbations occur in absorption lines of intermediate intensity, as is shown in Fig. 11, where we plot the difference between the perturbed and unperturbed synthetic spectra at 10 phases in the orbital cycle for the $\lambda\lambda$ 4310−4580 Å region. Strong lines, such as Hγ, undergo weaker perturbations than lines such as He I λ 4471 and the Si III triplet.

4.3. Distortion of the RV curve

The line-profile variations introduce an intrinsic uncertainty in the RV measurements which, as will be shown below, leads to systematic distortions in the RV curve. To illustrate this point, the centroid of the lines He I λ 4921 and λ 5875, Si III λ 4552 and Hβ were measured in the perturbed and unperturbed spectra by numerical integration between two fixed positions at the continuum level on both sides of the absorption minimum[8].

Figure 12 shows the difference $\delta(\mathrm{RV}) = (\mathrm{RV})_p - (\mathrm{RV})_u$ for the primary, where the subscripts "p" and "u" represent the perturbed and unperturbed spectra, respectively, and the

[7] See Harrington et al. (2009) where a set of spectra computed at very short time steps and showing the moving "bumps" is illustrated.

[8] The functional form is $\frac{\Sigma x_i(1-y_i)}{\Sigma(1-y_i)}$, where x_i, y_i are the values of wavelength and flux at each wavelength step. The wavelength step of our synthetic spectra is 0.01 Å and integration intervals typically contained ∼2000 points.

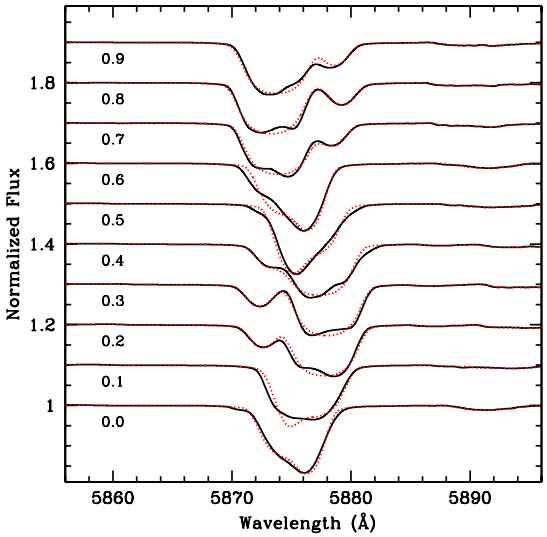

Fig. 10. Same as previous figure for He I λ 5875.

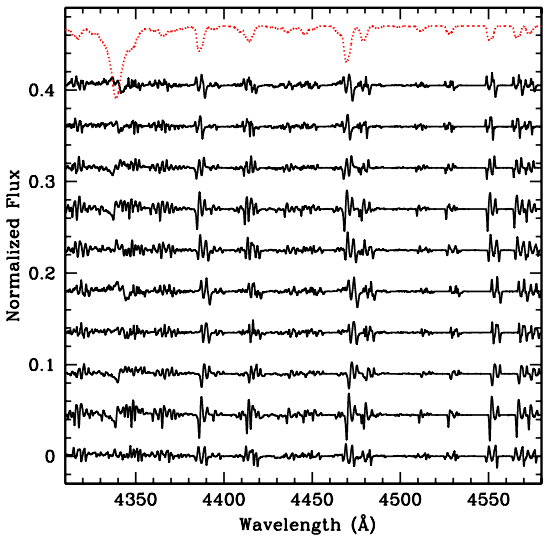

Fig. 11. Difference between the synthetic perturbed spectra of the primary and the corresponding unperturbed spectra showing that the lines of intermediate intensity display the most prominent variations in the "bump" structure. The orbital phases increase from bottom to top with increments of $\Delta\phi = 0.1$ and starting with $\phi = 0$. Differences are shifted along the vertical axis for clarity. The dotted tracing at the top is the perturbed spectrum at $\phi = 0.90$, scaled and shifted to fit in this figure.

RV_u correspond to the actual orbital motion. The maximum semi-amplitudes of δ(RV) range between 6 and 10 km s^{-1}, depending on the particular line being measured. A similar analysis performed using a cross-correlation method[9] yields a semi-amplitude δ(RV) $\sim$ 7 km s^{-1} for the two wavelength intervals that were cross-correlated ($\lambda\lambda$ 4150–4300 Å and

[9] The FXCOR routine in the Image Reduction Analysis Facility (IRAF) package.

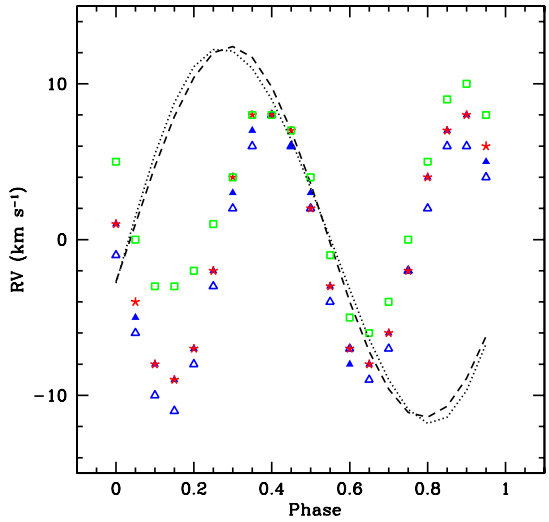

Fig. 12. Difference between RV measurements made on the perturbed and unperturbed spectra $\delta(RV) = (RV)_p - (RV)_u$ for He I λ 4921 (open triangles), He I λ 5875 (filled-in triangles), Si III λ 4552 (stars) and Hβ (squares). Also shown is the shape of the perturbed (dash) and unperturbed (dots) RV curves for He I λ 5875 after down-scaling by a factor of 10 for illustration purposes. The perturbation leads to a RV curve corresponding to a more eccentric orbit than the actual orbit.

$\lambda\lambda$ 5200–5800 Å), consistent with the result obtained for individual lines. The shape of the perturbed and unperturbed RV curves for He I λ 5875 is also shown in Fig. 12 (after scaling by a factor of 10 for illustration purposes) showing that the strongest distortion occurs on the ascending and descending branches of the RV curve, on both sides of the extrema; i.e., at orbital phases ~0.15, 0.40, 0.65 and 0.90. The combined effect of these distortions is to skew the RV curve, giving it the appearance of one with a larger eccentricity than that of the actual orbit.

For the secondary star, its weaker line-profile variability leads to much smaller deformations in the RV curves (see Fig. 13), δ(RV) = 2 km s^{-1}, with extrema at $\phi \sim 0.2$ and 0.85. The most strongly perturbed RV curve is that of Si III λ 4552 due to the greater sensitivity of this line to the heating by irradiation of the companion.

4.4. Comparison of CoMBiSpeC and TIDES model line profiles

The CoMBiSpeC calculation uses the velocity field computed by TIDES to compute the line profiles. A line-profile calculation is also implemented in TIDES (Moreno et al. 2011) which in the original version employed in Harrington et al. (2009) assumed a Gaussian local line profile instead of a line profile generated from a stellar atmosphere calculation. In Fig. 14 we compare the line profiles produced by both calculations, but in this case TIDES uses a Voigt shape for the local line profiles with a Lorentzian coefficient $a_L = 0.3$. Both calculations use the same surface velocity field (calculated by TIDES) and microturbulent speeds of 15 km s^{-1}, and all the binary parameters are the same. The differences between the TIDES and the CoMBiSpeC calculations are minimal.

Because TIDES computes the line profile variability very rapidly, its use is desirable for the analysis of a large parameter

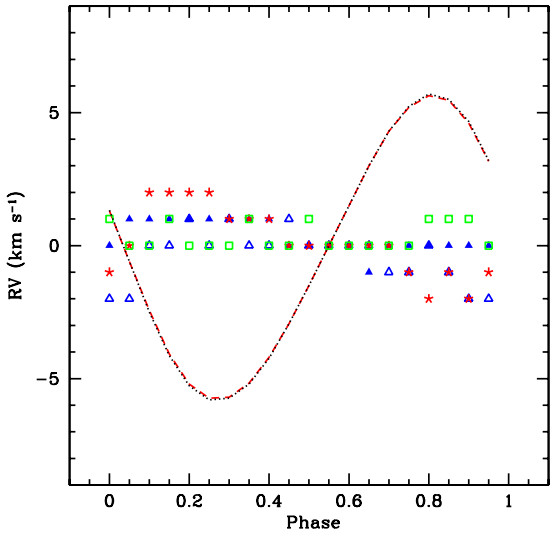

Fig. 13. As in the previous figure, the difference between RV measurements made on the perturbed and unperturbed spectra are plotted but here for the secondary star, and the scaled RV curves are those of Si III λ 4552, which shows the strongest perturbation effects.

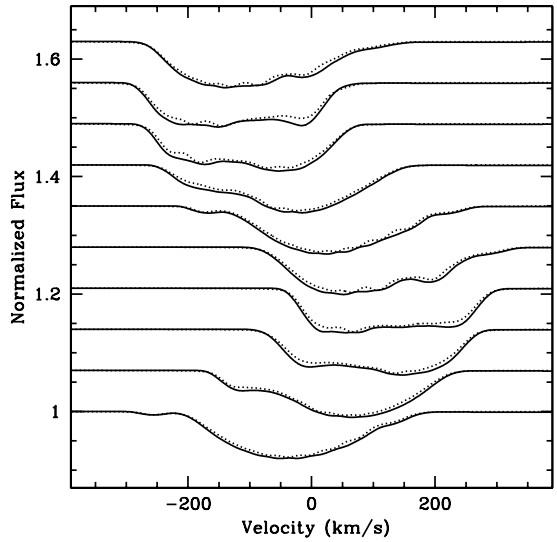

Fig. 14. The Si III λ 4552 line profiles computed with ComBiSpeC compared with the line profiles computed with the TIDES code (dots). In this TIDES calculation, the computation is performed using Voigt local line profiles. The ComBiSpeC code uses the same velocity field that is computed with TIDES, but the local line profile is obtained from the non-LTE TLUSTY radiative transfer calculation. Only the profiles computed for the primary star are shown here.

space such as that involving stellar radius, rotation velocity, eccentricity, orbital inclination, layer depth and viscosity, and the above justifies its use for these purposes.

5. Summary and conclusions

In this paper we explore the uncertainties that binary interaction effects may introduce in the derivation of fundamental stellar parameters when using stellar atmosphere models constructed for single stars. Our test case is Spica, a relatively close B-type binary system with unevolved, detached components. We use the TIDES code to compute the surface deformation and velocity field, the TLUSTY model atmosphere synthetic spectral grids, and the CoMBiSpeC model to synthesize output spectra that include the effects of irradiation by the companion and the tidal perturbations. These synthetic spectra are compared to high S/N and high resolution observations from which the following results are derived:

1. The phase-dependent variations in line strength (EW) due to the interactions is ≤2% for the primary and ≤4% for the secondary, leading to values of $T_{\rm eff}$ and $\log g$ that are indistinguishable, within the uncertainties, from those derived from models that neglect the interactions. The reason for this is that the irradiation effects and the departure from sphericity of both stellar surfaces are very small. The radius of the secondary is ∼7 times smaller than the orbital separation, so even though the primary is hotter, this large separation guarantees that only a small irradiation effect is present. Similar considerations apply to the tidal deformations. The radius of the primary is only ∼3.6 times smaller than the orbital separation, but the irradiation from the secondary is insignificant due to its cooler temperature and, due to it's smaller mass, the tidal deformations are also negligible.
2. The primary star rotates super-synchronously, which significantly perturbs its surface, leading to strong phase-dependent line profile variations. As a result, the RV curve is distorted with respect to the curve that describes the orbital motion, with maximum deviations of ≤10 km s^{-1}. Although the peak-to-peak amplitude of the RV curve is not affected, the shape is skewed so that a larger eccentricity than the actual value is inferred. We note that this effect may be the source of the discrepancy between the values of e that are given by Riddle (e = 0.067) and Herbison-Evans et al. (e = 0.146).
3. The velocity structure that is computed by TIDES leads naturally to the presence of bumps on the profiles of lines such as the Si III $\lambda\lambda$ 4552-72 triplet and other lines of intermediate strength without the need of any ad hoc assumption regarding non-radial pulsations. The nature of the bumps in the synthetic spectra is qualitatively similar to that in the observations for all lines contained in our spectra.
4. The weaker lines in the spectrum require $v_{\rm turb}$ = 10−15 km s^{-1}, whereas He I lines such as λ 4471 and O II favour a smaller value. Interestingly, the lines that show the clearest bumps are the ones that require the larger values of $v_{\rm turb}$ to attain an adequate match to the line-strengths.

We conclude that for a binary system such as Spica, the uncertainties in the model-fitting process (NLTE effects, microturbulence, rectification of the continuum level in the observations) are larger than those introduced by the tidal velocity field and heating effects. Future work will extend the exploration introduced in this paper to systems with parameters that are different from Spica's, where irradiation and tidal deformations are more important, in order to evaluate the uncertainties that are introduced in these cases with the use of single-star atmosphere models.

The above being said, it must be noted that nearly all of the synthetic model atmospheres are computed under the assumptions of hydrostatic and radiative equilibrium. However, the shear produced by different surface layers as they slide with

respect to each other in response to the tidal perturbation leads to energy dissipation (Toledano et al. 2007; Moreno et al. 2011). Depending on the particular regions where this energy is deposited, the temperature structure of the outer layers may be altered with respect to that derived when radiative equilibrium is strictly enforced. Furthermore, the dynamical nature of the stellar photosphere could influence the assumptions that are used for fixing $v_{\rm turb}$, for example, assuming that it is constant over the stellar surface. A hint pointing towards a non-constant value of $v_{\rm turb}$ is suggested by our results. Thus, the applicability of single-star models to close binary stars may need to be critically assessed.

Acknowledgements. We wish to express our gratitude to Ivan Hubeny for guidance in the use and implementation of SYNSPEC49 and Andres Sixtos for performing the IRAF cross-correlation computation of the RVs. The authors also would like to acknowledge Jason Aufdenberg for a careful reading of this paper and helpful comments. We acknowledge support through the XMM/INTEGRAL PRODEX contract (Belspo), from the Fonds de Recherche Scientifique (FRS/FNRS); UNAM/DGAPA/PAPIIT grant IN-105313, and CONACYT grant 129343.

References

Aufdenberg, J. 2007, AAS, 211, 6301
Evans C. J., Taylor W. D., Hénault-Brunet V., et al. 2011, A&A, 530, A108
Harrington, D. M., Koenigsberger, G., Moreno, E., & Kuhn, J. 2009, ApJ, 704, 813
Herbison-Evans, D., Hanbury B. R., Davis, J., & Allen, L. R. 1971, MNRAS, 151, 161
Hunter, I., Dufton, P. L., Smartt, S. J., et al. 2007, A&A, 466, 277
Koenigsberger, G., Moreno, E., & Harrington, D. M. 2012, A&A, 539, A84
Lanz, T., & Hubeny, I. 2007, ApJS, 169, 83
Lyubimkov, L. S., Rachkovskaya, T. M., Rostopchin, S. I., & Tarasov, A. E. 1995, ARep, 39, 186
Martins F. 2011, BSRSL, 80, 29
Massey, P., Zangari, A. M., Morrell, N. I., et al. 2009, ApJ, 692, 618
Massey, P., Morrell, N. I., Neugent, K. F., et al. 2012, ApJ, 748, 96
Mokiem, M. R., de Koter, A., Puls, J., et al. 2005, A&A, 441, 711
Moreno, E., Koenigsberger, G., & Harrington, D. M. 2011, A&A, 528, A48
Palate, M., & Rauw, G. 2012, A A, 537, 119
Palate, M., Rauw, G., Koenigsberger, G., & Moreno, E. 2013, A&A, 552, A39
Riddle, R. L. 2000, Ph.D. Thesis, Georgia State Univ.
Shobbrook, R. R., Herbison-Evans, D., Johnson, I. D., & Lomb, N. R. 1969, MNRAS, 145, 131
Shobbrook, R. R., Lomb, N. R., & Herbison-Evans, D. 1972, MNRAS, 156, 165
Smak, J. 1970, Acta Astron., 20, 75
Smith, M. A. 1985a, ApJ, 297, 206
Smith, M. A. 1985b, ApJ, 297, 224
Sterken, C., Jerzykiewicz, M., & Manfroid, J. 1986, A&A, 169, 166
Tassoul, J.-L. 1987, ApJ, 322, 856
Toledano, O., Moreno, E., Koenigsberger, G., Detmers, R., & Langer, N. 2007, A&A, 461, 1057
Vogt, S. S., & Penrod, G. D. 1983, ApJ, 275, 661
Walborn, N. R., & Fitzpatrick, E. L. 1990, PASP, 102, 379

3.3 Plaskett's star

Plaskett's star (HD 47129) is a very massive O-star binary in a post Roche-lobe overflow stage in which line profile variations and photometric variations have been observed (see e.g. Linder et al. 2006; 2008, Mahy et al. 2011a, Grunhut et al. 2013). The origin of these line profile variations is subject to debate: non-radial pulsations (NRPs), magnetic fields, wind interactions, or even unknown processes. In order to identify the origin of these variations, we have performed a Fourier analysis of a series of optical spectra of Plaskett's star. The first step of our analysis was to disentangle the primary and secondary spectral feature (following the González & Levato 2006 technique) to restore their mean spectra. Then, we Doppler shifted the mean spectrum of the primary (secondary) to the appropriate RV and subtracted it from the observation to get the individual spectra of the secondary (primary). Finally, we performed a Fourier analysis on several lines of these reconstructed individual spectra to characterize and to determine the origin of the line profile variations. Several frequencies have been identified and are listed in Tables 3.1, and 3.2. In this first identification, some frequencies seem to be aliases or harmonics of other ones. Therefore, we used a prewhitening technique to clean the Fourier spectra and finally kept six frequencies: 0.4, 0.8, 1.1, 1.6, 2.2, and 3.2 d^{-1}. The first one (0.4 d^{-1}) seems to be the fundamental frequency of the series: 0.4, 0.8, 1.6, and 3.2 d^{-1}. The 1.1 d^{-1} frequency is probably linked to the observational sampling while the origin of the 2.2 d^{-1} frequency is more uncertain. The main conclusion of our analysis is that NRPs are probably not responsible for the line profile variations of HD 47129. As suggested by Mahy et al. (2011a), the 0.4 d^{-1} frequency can probably be associated to the rotational period of the secondary star. This is also in good agreement with the fact that tidal interactions can lead to line profile variations. A TIDES + CoMBiSpeC model has shown that we could reproduce variations of the same order of magnitude than those observed. Unfortunately, the non-solar metallicity and the large parameters space prevent us from establishing the best parameters that reproduce the spectra of HD 47129.

Table 3.1: Frequencies (in d^{-1}) of the strongest peaks in the power spectra of the primary star of Plaskett's star (by order of peak strength).

He I λ 4471			N III λ 4510-4518			He II λ 4542		
2009	2010	2009 & 2010	2009	2010	2009 & 2010	2009	2010	2009 & 2010
1.64	0.74	0.76	1.71	0.71	1.73	1.63	0.62	1.62
0.80	0.25	0.82	0.73	1.72	1.68	0.77	1.63	0.62
0.66	1.74	0.18	2.70	0.30	0.73	2.65	0.41	1.68
2.10	1.23	0.24	0.36	2.71	0.68	0.62	0.91	1.73
0.55	2.73	1.76	0.26	1.37	2.73	0.22	2.64	0.56
2.64	2.21	1.70	1.34	1.17	2.68	1.22	1.88	2.68
1.10		0.09	1.24	2.39	0.32	2.20	1.40	1.56
0.44		1.65	1.08	3.71	1.32	3.64	2.88	2.62
2.20		1.13	2.21	3.41	3.73	0.38	3.68	2.73
		1.19	3.69		1.06	3.20	1.13	0.88
		1.08	3.13		3.68	4.63		0.13
		2.70	2.35		2.06	4.17		0.38
		2.19	4.12		2.38			0.44

Table 3.2: Frequencies (in d^{-1}) of the strongest peaks in the power spectra of the secondary star of Plaskett's star (by order of peak strength).

He I λ 4471			N III λ 4510-4518			He II λ 4542		
2009	2010	2009 & 2010	2009	2010	2009 & 2010	2009	2010	2009 & 2010
1.66	0.72	0.69	0.24	0.43	0.59	1.22	0.87	0.88
0.67	0.28	1.70 (+1)	1.22	0.58	0.16	0.20	1.85	0.15
2.64	1.72	1.64 (+1)	0.76	1.38	0.42	2.21	0.55	0.26
0.52	1.28	0.75	2.20	1.63	1.16	0.83	1.18	1.16
0.29	2.71	0.11 (+1)	1.73	2.36	0.64	1.54	2.85	1.26
1.23	2.28	0.90 (+1)	0.62	1.13	0.36	2.54	1.57	1.88
1.07	3.60	1.06	3.16	2.64	1.26	1.82	0.44	1.59
2.24	3.32	0.64	2.68	3.52	1.64	3.20	2.57	0.55
2.08		0.94 (+1)	3.61		2.16	3.55	2.18	2.22
		0.25 (+1)	4.13			2.81	3.85	2.59
		0.31					3.54	2.88
		2.60						
		1.55						

Astronomy & Astrophysics manuscript no. Plaskett_these
June 17, 2014

Short-term spectroscopic variability of Plaskett's star⋆

M. Palate and G. Rauw

Institut d'Astrophysique et de Géophysique, Université de Liège, Bât. B5c, Allée du 6 Août 17, 4000 Liège, Belgium

Received 10 February 2014 / Accepted <date>

ABSTRACT

Context. Plaskett's star (HD 47129) is a very massive O-star binary in a post Roche-lobe overflow stage. CoRoT observations revealed photometric variability with a number of frequencies. The origin of these variations could be related to pulsations, a recently detected magnetic field or tidal interactions.
Aims. The aim of this paper is to characterize the variations in spectroscopy and determine their origin.
Methods. To sample its short-term variability, HD 47129 was intensively monitored during two spectroscopic campaigns of six nights each. The spectra were disentangled and Fourier analyses of the primary and secondary line spectra were performed to determine possible periodicities and to investigate the phase constant of the periodicities as a function of wavelength.
Results. Several periods are detected consistently in the He I λ 4471, He II λ 4542, and N III λ 4510-4518 absorption lines. The significant periods are consistent with periodicities detected in photometry and are associated with a fundamental frequency near 0.4 d^{-1}. Simulations of synthetic spectra, accounting for tidal interaction due to non-synchronous rotation of the secondary star, indicate variations similar to those that are observed.
Conclusions. The most likely origin of the 0.4 d^{-1} frequency and its harmonics is the rotational frequency of the secondary star. The variations of the absorption lines of HD 47129 with this frequency could stem from tidal interactions.

Key words. stars: early-type – stars: oscillations – stars: individual: HD 47129 – binaries: general

1. Introduction

The massive binary nature of HD 47129 was first reported by Plaskett (1922) who inferred a total mass of 138.9 $M_\odot$, the highest ever observed at that time. Plaskett (1922) described the binary as consisting of two early-type stars: an Oe5 primary and a fainter secondary with weak and broad lines. For almost a century, HD 47129, also known as Plaskett's star, has been the target of many studies, with tremendous progress in the last twenty years (e.g. Bagnuolo et al. 1992, Wiggs & Gies 1992, Linder et al. 2006, 2008, Mahy et al. 2011, Grunhut et al. 2013a). The masses of the components have been revised downwards to $m_1 \sin^3 i = 45.4$ and $m_2 \sin^3 i = 47.3\ M_\odot$ for the primary and the secondary respectively, leading to a mass ratio of about 1.05 ± 0.05 (Linder et al. 2008). Unfortunately, Plaskett's star is a non-eclipsing binary, preventing a precise determination of its orbital inclination. The latter was estimated from polarimetry to $71 \pm 9°$ (Rudy & Herman 1978). Plaskett's star is usually considered a member of the Mon OB2 association. However, Linder et al. (2008) found a discrepancy between the luminosity and the dynamical masses of the two components of the system, which could be solved by assuming a larger distance of the star.

HD 47129 offers in many respects a textbook example of evolutionary effects and effects of interactions in massive binaries. Linder et al. (2008) used a disentangling technique, based on the method of González & Levato (2006), on high-resolution optical spectra to derive the spectral types O8 III/I and O7.5 V/III for the primary and secondary star, respectively. The broad and shallow absorption lines of the secondary star suggest that this star rotates rapidly ($v \sin i \sim 300 \mathrm{km\,s^{-1}}$), whereas the much sharper absorption lines of the primary indicate a projected rotational velocity of $v \sin i \sim 75 \mathrm{km\,s^{-1}}$ (Linder et al. 2008). Using the CMFGEN model atmosphere code (Hillier & Miller 1998) to analyse the disentangled spectra, Linder et al. (2008) showed that the atmosphere of the primary has an enhanced N and He abundance and a depletion of C. The secondary atmosphere is possibly depleted in N. These results indicate that the binary system is in a post-Roche lobe overflow evolutionary stage where matter and angular momentum have been transferred from the primary to the secondary.

Because of its high rotation speed, the wind of the secondary star could be rotationally flattened. Such a situation would impact the properties of the wind interaction zone in this binary. This was confirmed by the studies of the Hα emission region by Wiggs & Gies (1992) and Linder et al. (2008), as well as the study of the X-ray emission of the system by Linder et al. (2006). An alternative explanation for the origin of the equatorial wind of the secondary could be magnetic confinement. Indeed, Grunhut et al. (2013a) recently reported the presence of a magnetic field in Plaskett's star. In the framework of the Magnetism in Massive Stars (MiMeS) survey, they detected Zeeman signatures from the rapidly rotating secondary in high-resolution Stokes V spectra. The strength of the highly organized field has to be at least 2850 ± 500 G and variations compatible with rotational modulation of an oblique field were also found (Grunhut et al. 2013a).

Mahy et al. (2011) studied the CoRoT (Convection, Rotation and planetary Transits, Baglin et al. 2006; Auvergne et al. 2009) light curve of Plaskett's Star and extracted 43 significant frequencies. Among these frequencies there are three major groups: 0.823 d^{-1} and six harmonics, the orbital frequency 0.069 d^{-1} and

Send offprint requests to: M. Palate
⋆ Based on observations collected at the Observatoire de Haute Provence (OHP, France).

two harmonics, as well as two frequencies at 0.368 d^{-1} and 0.399 d^{-1}. The latter two could be related to the rotation period of the secondary.

The discovery of the 0.823 d^{-1} frequency by Mahy et al. (2011) prompted us to perform a spectroscopic monitoring of the system, to constrain the origin of this variation. In this paper, we report the results of this study. The paper is organized as follows. Sect. 2 describes the observations, data reduction and disentangling treatment. In Sect. 3, the results of the Fourier analyses are given. We also discuss the phase and amplitude variations and their interpretations. Finally, in Sect. 4, we present a spectral modelling of Plaskett's star, and in Sect. 5 we summarize our results and present our conclusions.

2. Observations and data reduction

2.1. OHP spectroscopy

Spectroscopic time series of HD 47129 were obtained during two six-nights observing campaigns in December 2009 and December 2010 at the Observatoire de Haute Provence (OHP, France). We used the Aurélie spectrograph fed by the 1.52 m telescope. The spectrograph was equipped with a 1200 lines mm^{-1} grating blazed at 5000 Å and a CCD EEV42-20 detector with 2048×1024 pixels of 13.5 μm^2. Our set-up covered the wavelength domain from 4460 to 4670 Å with a resolving power of 20000. Typical exposure times were 20 – 30 minutes, depending on the weather conditions, and a total of 118 spectra were collected. To achieve the most accurate wavelength calibration, Th-Ar lamp exposures were taken regularly over each observing night (typically once every 90 minutes).

The data were reduced using the MIDAS software provided by ESO. The normalization was done self-consistently using a series of continuum windows. Table 1 provides a summary of our observing campaigns and the characteristics of the sampling.

2.2. Disentangling

The first step in our analysis was to disentangle the spectra of the primary and secondary components. For this purpose, we used our code based on the González & Levato (2006) technique. This method allows to derive the radial velocities as well as the individual spectra of the components. However, because of the very broad and shallow lines of the secondary, its radial velocities (RVs) obtained with the disentangling were sometimes not well constrained. To avoid artefacts, we thus fixed the RVs of the secondary to the theoretical values derived from the orbital solution of Linder et al. (2008). The situation for the primary was better, but we decided to also fix the RVs noting that the results of the disentangling were very similar, as far as the reconstructed spectra of the individual components are concerned, whether or not we fixed the RVs. At first, we performed the disentangling on the two observing campaigns separately, and in a second step, simultaneously on both campaigns. Having compared the output of the various approaches with each other and with the results of Linder et al. (2008), we finally decided to adopt the simultaneous disentangling of the data from both observing campaigns with fixed RVs (see Fig.1).

3. Fourier analysis

The second step of our analysis was to subtract the mean disentangled spectrum of the primary (respectively secondary) shifted

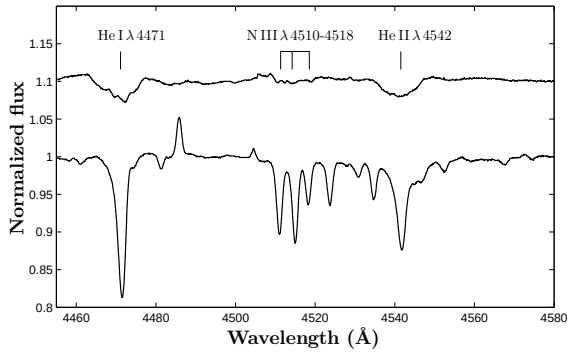

Fig. 1. Mean disentangled spectra of the primary and secondary (shifted upwards by 0.1 continuum units). The spectral lines analysed in the following are identified by the labels.

to the appropriate RVs from the observed spectra. Therefore, we obtained the "individual spectra" of the secondary (respectively primary) in the frame of reference of this star for each observation. The He I λ 4471, He II λ 4542, and N III λ 4510-4518 lines present clear profile variations. Fig. 2 displays the dynamic spectrum and the line profile variations of the secondary (obtained by subtracting the mean spectrum of the primary from the observations) for the He I λ 4471 line. We also computed residual spectra

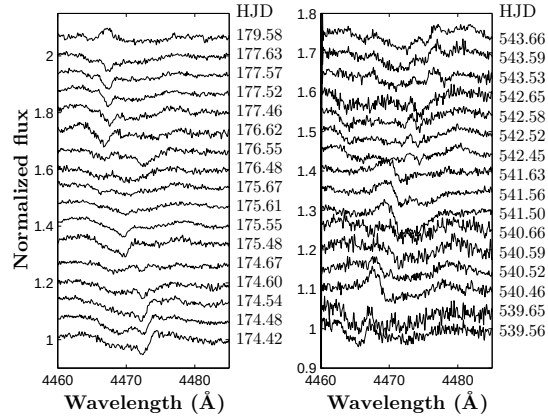

Fig. 2. Examples of line-profile variations for the He I λ 4471 line of the secondary (*left:* 2009 campaign, *right:* 2010 campaign). The spectra are vertically shifted by 0.067 continuum units for clarity (time is given as HJD–2455000).

(i.e. the observation minus the mean spectra of the primary and secondary). Because the variations extend over a wider wavelength range than the widths of the primary lines, we conclude that the secondary displays variations. However, we cannot *a priori* exclude that the primary is also variable.

Then, we computed a temporal variation spectrum (TVS, see Fullerton et al. 1996) to identify the lines of our spectral range that are significantly variable. This analysis confirms our visual impression that the He I λ 4471, He II λ 4542, and N III λ 4510-4518 lines are variable. Fig.3 confirms that the wavelength domain over which the He I λ 4471 line varies is broader than the line of the primary. However, we still cannot totally exclude that

Table 1. Summary of the time sampling of the observing campaigns.

Campaign	Starting and ending dates (HJD-2450000)	Starting and ending phases	n	<S/N>	ΔT (days)	$< \Delta t >$ (hours)	$\Delta\nu_{nat}$ $(\text{days})^{-1}$	ν_{max} $(\text{days})^{-1}$
2009	5174.415 - 5179.665	0.47 - 0.84	68	180	5.25	0.40	$1.90\ 10^{-1}$	119
2010	5539.454 - 5543.657	0.83 - 0.12	50	146	4.20	0.55	$2.38\ 10^{-1}$	87.7

Notes. Note that for both campaigns, there are no observations for one night due to bad weather. n is the total number of spectra, <S/N> indicates the mean signal-to-noise ratio, ΔT indicates the total time between the first and last observations, Δt provides the average time interval between two consecutive exposures of a same night. The last two columns indicate the natural width of the peaks in the periodogram $\Delta\nu_{nat} = \Delta T^{-1}$ and $\nu_{max} = (2 < \Delta t >)^{-1}$ provides an indication of the highest frequency that can possibly be sampled with our time series.

the primary is also variable. In fact, the spectral features of the secondary are so broad that the primary lines are always seen on top of the secondary lines, even at quadrature phases. Therefore, cross contamination between the secondary and primary spectra makes it very difficult to make a firm statement about the primary.

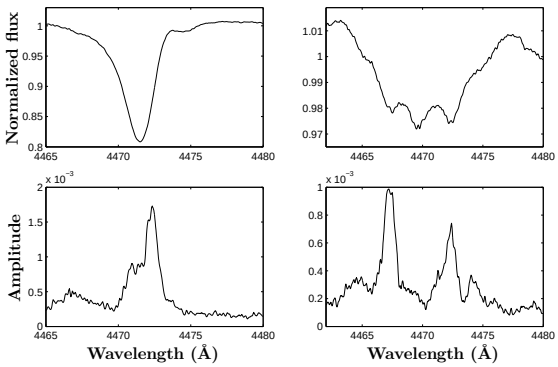

Fig. 3. Mean primary (*left*) and secondary (*right*) spectra (2009 campaign) of the He I λ 4471 line and corresponding square root of the TVS (*lower panels*).

A 2D Fourier analysis (Rauw et al. 2008) was performed based on the periodogram method of Heck et al. (1985), refined by Gosset et al. (2001). This method is designed to account for the uneven sampling of the time series. The three lines and line complexes that show significant variations were analysed this way. These analyses were performed on the data of both observing campaigns separately and simultaneously. For the primary, the most important frequencies are around 0.75 ± 0.10, 1.15 ± 0.10, and 1.65 ± 0.10 d^{-1} with their aliases and/or harmonics. We note for instance that 0.8 d^{-1} would be the fundamental frequency of 1.6 d^{-1}. The error on the centre of the peak can be estimated as $\Delta\nu = 0.1/\Delta T$[1] where ΔT is the time interval between the first and the last observations of the complete time-series (assuming the uncertainty on the peak frequency amounts to 10% of the peak width). The uncertainties are of 0.02 d^{-1} for the campaigns separately and of 3×10^{-4} d^{-1} when both campaigns are considered simultaneously[2]. However, in the present case, these estimates are very optimistic because they neither account for the signal to noise ratio of the observations nor for the impact of the treatment of the data prior to the Fourier analysis. Therefore, we estimate a global error of ± 0.05 d^{-1} on the peak values.

To go one step further, we used a prewhitening technique that allows us to remove three frequencies from the initial Fourier spectra (Rauw et al. 2008). This first attempt did not allow to remove all significant frequencies in the Fourier spectra. Therefore, we used a modified version of the prewhitening technique allowing to remove three frequencies and their first harmonic (i.e. six frequencies). This harmonic prewhitening allows to remove all significant frequencies from the Fourier spectra. Fig. 4, 5, and 6 display the Fourier spectra before and after the harmonic prewhitening for the primary and secondary. Table 2 gives the values of the removed frequencies and their first harmonic for the different campaigns. We notice that three frequencies seem to be dominating: 0.4, 1.1, and 1.6 d^{-1}. Unfortunately, these Fourier studies do not allow either to determine which of the binary components is variable.

In an attempt to solve this problem we computed a 1D Fourier periodogram of the primary RVs deviation between the value computed from the orbital solution of Linder et al. (2008) and the value obtained via disentangling of the present data (see Table 3). We prewithened the spectrum with the same iterative procedure as described in Mahy et al. (2011). The latter consists in removing the most prominent frequencies and its harmonics and recompute the Fourier spectra until reaching the noise level of the data. The strongest frequency, 0.75 ± 0.05 or 1.75 ± 0.05 d^{-1}, is close to the 0.8 d^{-1} frequency found in the previous analyses. Two other important frequencies are 0.4 d^{-1} and 0.6 d^{-1} (and/or some aliases). The former frequency was already present in the previous analyses while the latter is an alias of both the 0.4 or the 1.6 d^{-1} frequencies. Higher frequencies (6.8 or 12.7 d^{-1}) and an additional frequency at 0.25 ± 0.05 that were not present in the previous Fourier spectra are now observed. Finally, some frequencies (1.02, 0.99, 2.04 d^{-1}) are problematic because they are close to 1 and 2 d^{-1} and could be artefacts due to the observational sampling. Because the most significant frequencies found here are the same as those found in the line profile variations, we cannot rule out that the primary is also variable.

As a consistency check, we have also computed the Fourier transform of the observations simply shifted into the frame of reference of the secondary, without subtracting the mean profile of the primary. As can be expected, the resulting Fourier periodograms are dominated by low frequencies associated with the relative orbital motion of the primary line across the secondary line profile. However, apart from these low frequencies, the rest of the periodogram is indeed very similar to the ones obtained from the Fourier analyses of the disentangled spectra, thereby lending further support to the robustness of the results described above.

[1] This corresponds to an uncertainty on the period of $\Delta P = 0.1 \times \frac{P^2}{\Delta T}$.

[2] We caution though that the sampling of the combined dataset is very odd, leading to a large number of closely spaced aliases, and the effective uncertainties on the peak position are thus significantly larger than estimated here.

Table 3. Frequencies (in d^{-1}) in the prewhitened power spectra of the primary's RVs deviation between the value computed from the orbital solution of Linder et al. (2008) and the value obtained via disentangling of the present data.

Year	Frequencies						
2009	1.74	1.54	1.02	5.61	8.72	12.97	2.23
2010	0.72	2.51	0.99	3.22	12.70	7.81	4.42

Both stars could thus be variable, although cross-contamination in the reconstruction of the individual profiles could cause this result. The frequencies found in the Fourier analyses are the same whether we consider the reconstructed primary or secondary spectra. They are equal to 0.4 ± 0.05, 1.1 ± 0.05, 1.6 ± 0.05 and their first harmonic 0.8 ± 0.1, 2.2 ± 0.1, and 3.2 ± 0.1. Within the error bar, these frequencies are consistent with values found by Mahy et al. (2011) in the CoRoT ligth curve (except for 2.2 d^{-1}). Table 4 lists the frequencies from the CoRoT data that are potentially consistent with the frequencies found in the current analysis.

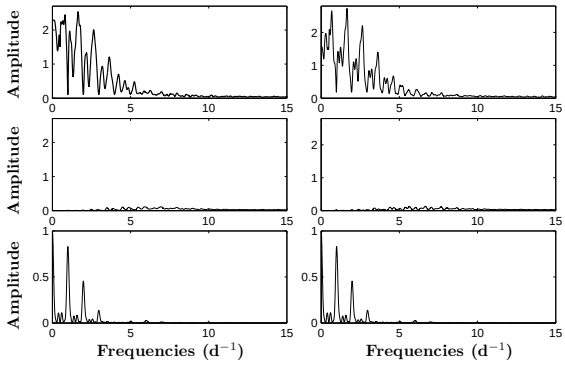

Fig. 4. Fourier spectra of the He I λ 4471 line (2009 campaign) before (*top panels*) and after (*middle panels*) the harmonic prewhitening for the reconstructed primary (*left panels*) and secondary (*right panels*) spectra. The spectral windows are in the *lower panels*.

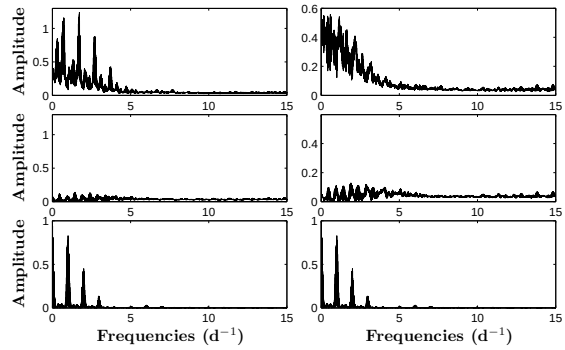

Fig. 5. Same as Fig.4 but for the N III λ 4510-4518 lines (2009 and 2010 campaigns combined).

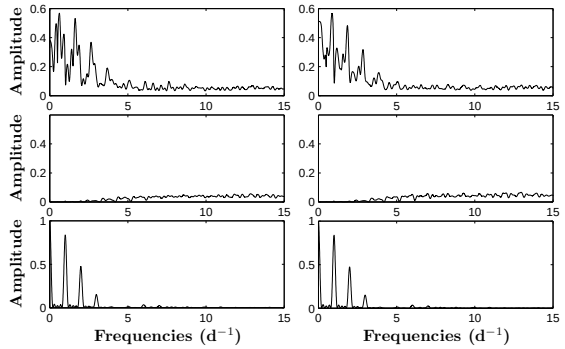

Fig. 6. Same as Fig.4 but for the He II λ 4542 line (2010 campaign).

Table 4. Correspondence between the best frequencies (in d^{-1}) found in this paper and those found by Mahy et al. (2011) in the CoRoT light curve.

Our Frequencies	CoRoT Frequencies		
0.4 ± 0.05	0.368	0.399	0.441
0.8 ± 0.10	0.799	0.823	0.888
1.1 ± 0.05	1.056	1.000	
1.6 ± 0.05	1.646	(1.686)	
2.2 ± 0.10	/		
3.2 ± 0.10	3.292		

3.1. Phases and amplitudes

The Fourier analyses provide us with the amplitude (A) and the phase constant (φ_0) of the variation as a function of the wavelength. These quantities can help us determine whether the star presents non-radial pulsations (NRPs). NRP modes are usually characterized by a progressive change of the phase constant as a function of wavelength across the line profile (e.g. Schrijvers & Telting 1999, Zima et al. 2004). For instance, the models of Schrijvers & Telting (1999) show that, in the case of NRPs with moderate degrees l, the value of the phase constant usually changes monotonically across the line profile, and that the difference between the phase constant in the red wing and in the blue wing is directly related to the values of l and m of the pulsation. For low l numbers, Zima et al. (2004) showed that a sudden phase-shift of π associated to an amplitude that drops to zero only in the centre of the line, indicates a pulsation of degree $l = 0$ or 1 and $m = 0$. In our case, the phase constant either remains constant across the line profile or varies in a rather erratic way (see Fig. 7). Only the behaviour of the phase constant of the variations associated with the 0.8 d^{-1} frequency of the He I λ 4471 line of the primary could possibly hint at NRPs of degree $l = 0$ or 1 and $m = 0$. For the other lines and frequencies, we only note that when the amplitude of the variations increases or decreases, the phase constant often changes rapidly, but in a less systematic way than predicted by the models of Zima et al. (2004).

The amplitude distribution as a function of wavelength of the different frequencies depends on the line under consideration and changes also between the two epochs of observations. The peak amplitudes range from ∼ 2% to ∼ 7% of the continuum. In general, the variations associated with the 0.4 - 0.8 - 1.6 d^{-1} frequencies have the largest amplitudes. Fig. 7 displays three examples of amplitude and phase variations.

Table 2. Frequencies (in d^{-1}) removed with the harmonics routine in the power spectra.

Lines - Year	ν_1 ($2\nu_1$)	ν_2 ($2\nu_2$)	ν_3 ($2\nu_3$)
Primary			
He I λ 4471 - 2009	0.40 (0.80)	1.10 (2.20)	1.65 (3.30)
He I λ 4471 - 2010	0.40 (0.80)	0.95 (1.90)	1.60 (3.20)
N III λ 4510-4518 - 2009 or 2010	0.40 (0.80)	1.10 (2.20)	1.60 (3.20)
He II λ 4542 - 2009 or 2010	0.40 (0.80)	1.10 (2.20)	1.60 (3.20)
Secondary			
He I λ 4471 - 2009	0.40 (0.80)	1.10 (2.20)	1.60 (3.20)
He I λ 4471 - 2010	0.40 (0.80)	1.10 (2.20)	1.60 (3.20)
N III λ 4510-4518 - 2009 or 2010	0.40 (0.80)	1.10 (2.20)	1.60 (3.20)
He II λ 4542 - 2009 or 2010	0.40 (0.80)	1.10 (2.20)	1.60 (3.20)

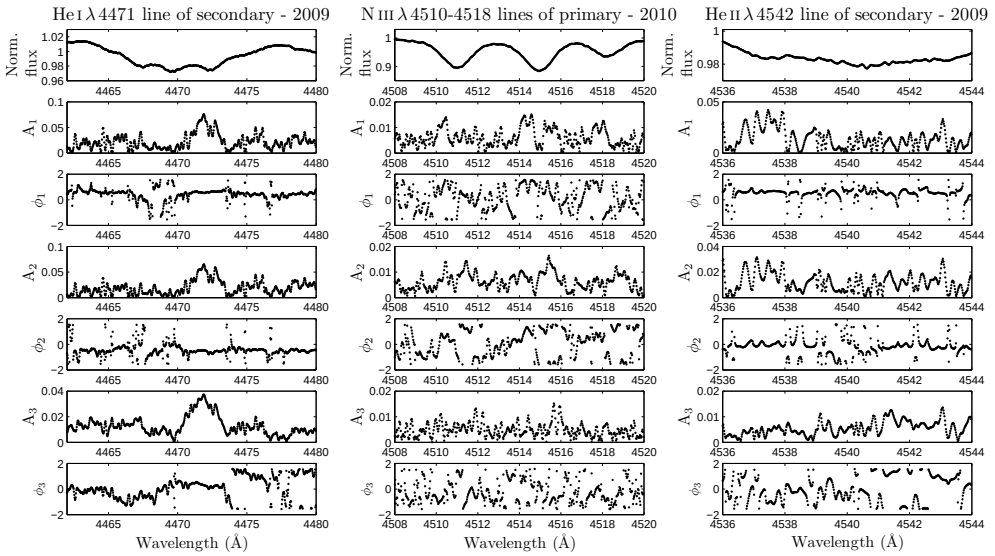

Fig. 7. Examples of amplitude and phase variations for the He I λ 4471 and He II λ 4542 lines of the secondary during the 2009 campaign (*left* and *right*), and for the N III λ 4510-4518 lines of the primary during the 2010 campaign (*middle*). The *top* panel displays the mean spectrum of the lines. The next panels display alternatively the amplitude and the corresponding phase of the fundamental frequencies quoted in Table 2 (i.e. $\nu_1 = 0.4$, $\nu_2 = 0.8$, and $\nu_3 = 1.6$).

From the amplitudes and phases we can reconstruct a diagram of the variations assuming that they are represented by sine functions:

$$I(\lambda, t) = I_0(\lambda) + \sum_{i=1}^{N} A_i(\lambda) sin[2\pi\nu_i t + \phi_i(\lambda)] \quad (1)$$

where, $I(\lambda, t)$ is the line intensity at wavelength λ, and at time, t. ν_i are the frequencies corresponding to the highest peaks in the periodogram and $A_i(\lambda)$ and $\phi_i(\lambda)$ are respectively the amplitudes and the phases for these frequencies as a function of wavelength. Fig. 8 presents examples of this reconstruction for a number of frequencies equal to 1 or 3 corresponding to the fundamental frequency 0.4 d^{-1} and its two harmonics (0.8 and 1.6 d^{-1}).

The reconstruction of the variations gives similar results for all the lines (see Fig. 8, middle and bottom) except the He I λ 4471 line of the primary. The reconstructed profiles of the lines (except He I λ 4471) display three minima and two maxima that are either very close or correspond to a single broad maximum. The location of these maxima and minima is variable (see Table 5). The 0.4 and 0.8 d^{-1} frequencies are responsible of the main part of the variations. The pattern of the reconstruction for the He I λ 4471 line of the primary is different and displays a discontinuity located at 4472.5 Å or 4471.5 Å (for the 2009 campaign and for the 2010 campaign, see Fig. 8, top). This discontinuity stems from a rapid change of π of the phase constant for the 0.8 d^{-1} frequency at these wavelengths. We also observed a slight decrease of the amplitudes at these two wavelengths.

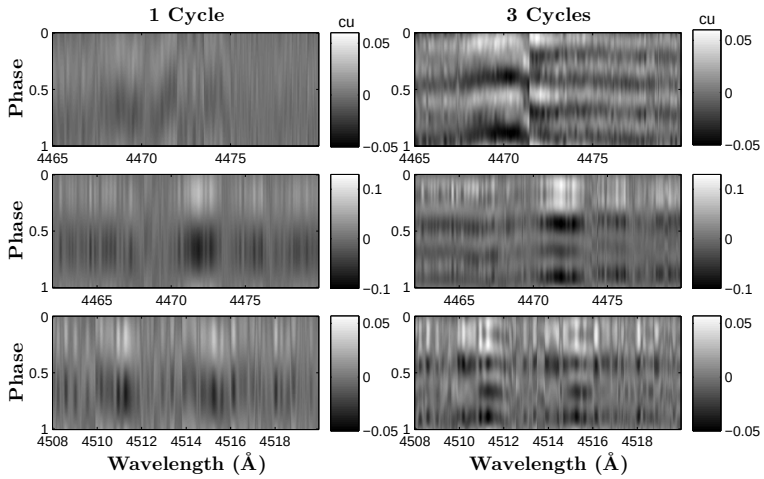

Fig. 8. Reconstruction of the variations for the He I λ 4471 line of the primary for the 2010 campaign (*top*), for the He I λ 4471 line of the secondary (*middle*) and the N III λ 4510-4518 lines of the primary (*bottom*) for the 2009 campaign. 1 cycle corresponds to the reconstruction of the 0.4 d^{-1} variations, and 3 cycles to the simultaneous reconstruction of the 0.4, 0.8 and 1.6 d^{-1} frequencies. The greyscale is given in continuum units (cu).

Table 5. Location of the maximum of the variations in the line profile (bw: blue wing, rw: red wing, c: centre, a: all over the wavelength range, v: variable depending on the number of frequencies).

Year - Star	He I λ 4471	N III λ 4510-4518	He II λ 4542
2009 - P	a	c	c
2009 - S	c	c	bw
2010 - P	bw-c	v: c-a	c
2010 - S	v: bw-c-a	v: c-a	c

3.2. Interpretation

As we can see in Table 4, the three main frequencies are 0.4, 1.1 and 1.6 d^{-1}, which correspond to periods equal to 2.5, 0.91, and 0.63 d. The three harmonics are 0.8, 2.2 and 3.2 d^{-1}, which correspond to periods equal to 1.25, 0.45, and 0.31 d. The 1.1 frequency is the most uncertain one because it is close to 1 d^{-1} and could be affected by sampling effects. If we assume that the 0.4 d^{-1} frequency is the fundamental frequency, ν_1 we have that $0.8 = 2\nu_1$ and $1.6 = 4\nu_1$.

If we exclude NRPs as the main cause of the variations (see previous section), this fundamental frequency of 0.4 d^{-1} could be linked to the rotation period of the secondary. The projected equatorial rotational velocity of the secondary has been evaluated to $\sim$ 310 km s^{-1} by Linder et al. 2008. **These authors** also derived a $\log g$ equal to 3.5. Adopting an inclination of 67° as proposed by Mahy et al. (2011), and considering that the rotation frequency is 0.4 d^{-1}, the projected rotational velocity of 310 km s^{-1} yields a radius of 15.3 $R_\odot$ for the secondary. The $\log g$ and minimum mass of the secondary ($m_S \sin^3 i = 47.3\, M_\odot$, Linder et al. 2008) along with the adopted inclination of 67° (Mahy et al. 2011) rather suggest a radius of 20.5 $R_\odot$. In this latter case, the projected rotational velocity would be equal to $\sim$ 415 km s^{-1}. The discrepancy between these rotational velocities can be explained by several factors: the uncertainties on the inclination (Mahy et al. 2011 indicated a range from 30 to 80°), the error on the rotational velocity determination, on the $\log g$, and on the frequency. For instance, reducing the inclination by 15° is sufficient to explain the 100 km s^{-1} discrepancy.

Our interpretation of the 0.4 d^{-1} frequency as the secondary's rotational frequency differs from the one of Grunhut et al. (2013b), who rather favour a rotational period of 1.215 d, corresponding to a frequency of 0.82 d^{-1}. Their result is based on a periodicity search in the variations of the Hα equivalent width and the longitudinal magnetic field. Grunhut et al. (2013b) accordingly interpret their results in terms of an oblique dipolar magnetic rotator model. Whilst we cannot rule out from our analysis that the true rotational frequency could be close to 0.8 d^{-1}, we stress that such a value would lead to a radius estimate from the projected rotational velocity twice smaller than what we have obtained hereabove, thus enhancing the discrepancy between the radius estimated from $v \sin i$ and the one estimated from $\log g$.

4. Spectral modelling

The analysis of the line profile variations of the slightly eccentric binary system Spica (Palate et al. 2013) has shown that tidal interactions can explain the presence of those variations. Plaskett's star is not an eccentric system, however, the non-synchronicity of the secondary rotation could lead to tidally induced variations such as those reported by Moreno et al. (2005). Therefore, we have tried to model Plaskett's star with the TIDES code (see Moreno et al. 1999, 2005, 2011) combined to CoMBiSpeC[3] (see Palate & Rauw 2012 and Palate et al. 2013). The TIDES code computes the time-dependent shape of the stellar surface for eccentric and/or asynchronous systems accounting for centrifugal and Coriolis forces, gas pressure, viscous effects and gravitational interactions. From that, CoMBiSpeC computes the synthetic spectra of the stars at several orbital phases. We stress that our goal here is not to fine tune the parameters that reproduce perfectly the spectra of the components of Plaskett's star and their observed variations. Here, we rather wish to test whether or not tidal interactions can indeed produce detectable variations in the spectra of this system. Indeed, fitting the spectra rigorously is a challenging task because of a large number of free/unknown parameters and the non-solar composition of the stars (see Linder et al. 2008); CoMBiSpeC currently only works with atmosphere models that have a solar composition. In the present paper, we have only adjusted the temperatures to reproduce the observed strength of the He I λ 4471 and He II λ 4542 lines. The parameters used are listed in Table 6. A full fit of the spectra is deferred to a future study.

[3] TIDES: tidal interaction with dissipation of energy through shear. CoMBiSpeC: code of massive binary spectral computation.

Table 6. Parameters used for computation with the TIDES + CoMBiSpeC model.

Parameters	Primary	Secondary
Period (day)	14.396	
Eccentricity	0	
Inclination (°)	67	
Mass ($M_\odot$)	58.2	60.6
Polar temperature (K)	33000	32000
Polar radius ($R_\odot$)	22.1	20.5
Polar log(g) (cgs)	$\simeq 3.5$	$\simeq 3.6$
v_{rot} (km s^{-1})	77.7	296
$v \sin i$ (km s^{-1})	71.5	273
β [(a)]	1.0	4.16
Viscosity, ν ($R_\odot{}^2$d^{-1})	0.028	0.035
Layer depth ($\Delta R/R$)	0.07	0.07
Polytropic index	1.5	1.5
Number of azimuthal partitions	500	500
Number of latitudinal partitions	20	20

Notes. [(a)]The β parameter measures the asynchronicity of the star at periastron and is defined by $\beta = 0.02\frac{Pv_{rot}}{R} \times \frac{(1-e)^{3/2}}{(1+e)^{1/2}}$, where v_{rot} is the equatorial rotation velocity, R is the equilibrium radius, and e is the eccentricity.

Our simulations show that tidal interactions can produce visible variations in the lines of the secondary. Because the primary is thought to be in synchronous rotation in a circular orbit, it is expected that there is no variability of the primary due to tidal interactions. The strength of the simulated variations is comparable to the observed ones. The radii needed to get a $\log g \simeq 3.5$ are close to 20 $R_\odot$. In light of the discussion in the previous section, we note that a larger radius leads to larger tidally induced variations. Fig 9 displays the simulated line profile variations of the secondary during the orbital cycle.

We have performed a Fourier analysis of the individual simulated spectra of the primary and secondary stars. The Fourier spectrum of the primary only displays the window signal, as expected for a star with non-variable line profiles. The Fourier spectrum of the secondary displays a peak at the secondary's rotation frequency imposed in the model. Therefore, our test calculations show that tidal interactions can induce line profile variations compatible with the observed ones, provided the stellar radii are sufficiently large. Our calculations further indicate that the signature of these variations in the Fourier spectrum occurs at the rotation frequency of the asynchronously rotating star.

5. Summary and conclusion

Our analysis of the He I λ 4471, N III λ 4510-4518, and He II λ 4542 lines of Plaskett's star revealed variations at six frequencies: 0.4, 0.8, 1.1, 1.6, 2.2, and 3.2 d^{-1}. The lowest frequency, 0.4 d^{-1}, seems to be the fundamental frequency of the series: 0.4, 0.8, 1.6, and 3.2 d^{-1} while 1.1 d^{-1} could be linked to the data sampling. The origin of the 2.2 d^{-1} frequency is more uncertain. As already suggested by Mahy et al. (2011), the 0.4d^{-1} frequency could be associated with the rotation period of the secondary star. Combined with the observed projected equatorial rotational velocity and $\log g$, this rotational frequency implies a radius of the secondary star between 15 and 20 $R_\odot$. One can notice that this value of the radius is well below the radius of the Roche lobe which can be estimated with the formalism of Eggleton (1983) to $\sim$ 45.9 $R_\odot$. The 0.4 d^{-1} frequency could also be compatible with the 2.78 d period (0.36 d^{-1}) found by Wiggs & Gies (1992) in the equivalent width of the Hα emission wings[4]. A corollary of our interpretation of 0.4 d^{-1} as the secondary's rotational frequency would be that the variations of the longitudinal magnetic field presented by Grunhut et al. (2013b) would probably have to be interpreted as due to a more complex magnetic field than a simple dipole.

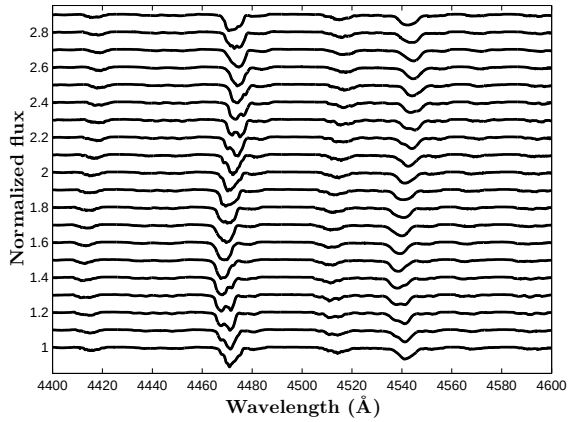

Fig. 9. Line profile variations of the synthetic spectra of the secondary during the orbital cycle. The spectra (separated by 0.05 in phase) have been shifted vertically by 0.1 continuum unit for clarity.

Our simulations of synthetic spectra with the TIDES and CoMBiSpeC codes indicate that the asynchronous rotation of the secondary star induces oscillations at the surface of the secondary that could be responsible for at least some part of the line profile variations seen in the spectra of Plaskett's star. We have also shown that the Fourier spectrum, computed from the model, displays a peak associated with the rotation frequency of the asynchronously rotating star (the secondary star in the present case). This result brings up the interesting possibility that breaking tidal waves near the secondary's equator could produce an enhanced mass-loss in this region (see Osaki 1999). Combined with wind confinement due to the magnetic field (Grunhut et al. 2013a, 2013b), this effect could produce the equatorial torrus of circumstellar material that was advocated by Wiggs & Gies (1992) and Linder et al. (2006, 2008). The much smaller radius (10.7 $R_\odot$) proposed by Grunhut et al. (2013a) not only fails to reproduce the $\log g$ value inferred from the model atmosphere code fits, but would also considerably reduce the amplitude of surface oscillations due to tidal interactions.

Whilst our Fourier periodograms of the spectroscopic data suggest that the 0.8 and 1.6 d^{-1} frequencies are harmonics of the rotational frequency, we stress that the analysis of the CoRoT photometry by Mahy et al. (2011) revealed a periodogram with a complex frequency content, and some of the frequencies found in our spectroscopy analysis are most probably blends of several frequencies that were resolved in the photometric time series. Whilst we did not find clear evidence for non-radial pulsations in the spectroscopic time series, we stress that our result does not rule out the existence of NRPs in HD 47129. Indeed, some of the photometric frequencies could be related to pulsations. However, if such pulsations do exist, they are not the main drivers behind the spectroscopic variability. Finally, we note that, whilst we

[4] Wiggs & Gies 1992 suggested an origin in the winds of the stars.

cannot attribute the origin of the spectroscopic variations to the secondary star only, our interpretation of the 0.4 d^{-1} frequency and the detection of this frequency in the N III λ 4510-4518 multiplet indicate that the secondary spectrum also contains these nitrogen lines. Linder et al. (2008) came to the conclusion that nitrogen could be underabundant in the atmosphere of the secondary. Our new results rather suggest that the apparent underabundance of nitrogen was an artefact due to the heavy rotational broadening of the secondary's nitrogen lines and the difficulties to detect such shallow features in the disentangled spectra.

Acknowledgements. We would like to thank Pr. G. Koenigsberger who provided us with the TIDES code and helped us to use it. We acknowledge support through the XMM/INTEGRAL PRODEX contract (Belspo), from the Fonds de Recherche Scientifique (FRS/FNRS), as well as by the Communauté Française de Belgique - Action de recherche concertée - Académie Wallonie - Europe.

References

Auvergne, M., Bodin, P., Boisnard, L., et al. 2009, A&A, 506, 411
Baglin, A., Auvergne, M., Barge, P., et al. 2006, in ESA SP, ed. M. Fridlund, A. Baglin, J. Lochard, & L. Conroy, 1306, 33
Bagnuolo, W.G.Jr., Gies, D.R., & Wiggs, M.S. 1992, ApJ, 385, 708
Eggleton, P.P. 1983, ApJ, 268, 368
Fullerton, A.W., Gies, D.R., & Bolton, C.T. 1996, ApJS, 103, 475
González, J. F., & Levato, H. 2006, A&A, 448, 283
Gosset, E., Royer, P., Rauw, G., Manfroid, J., & Vreux, J.-M. 2001, MNRAS, 327, 435
Grunhut, J.H., Wade, G.A., Leutenegger, M., et al. 2013a, MNRAS, 428, 1686
Grunhut, J.H., Wade, G.A., and the MiMeS Collaboration 2013b, in Setting a New Standard in the Analysis of Binary Stars, eds. K. Pavlovski, A. Tkachenko, & G. Torres, EAS Publication Series, 64, 67
Heck, A., Manfroid, J., & Mersch, G. 1985, A&AS, 59, 63
Hillier, D.J., & Miller, D.L. 1998, ApJ, 496, 407
Linder, N., Rauw, G., Pollock, A.M.T., & Stevens, I.R. 2006, MNRAS, 370, 1623
Linder, N., Rauw, G., Martins, F., et al. 2008, A&A, 489, 713
Mahy, L., Gosset, E., Baudin, F., et al. 2011, A&A, 525, 101
Moreno, E. & Koenigsberger, G. 1999, RMA&A, 35, 157
Moreno, E., Koenigsberger, G. , & Toledano, O. 2005, A&A, 437, 641
Moreno, E., Koenigsberger, G., & Harrington, D. M. 2011, A&A, 528, 48
Osaki, Y. 1999, in Variable and Non-spherical Stellar Winds in Luminous Hot Stars, IAU coll. 169, eds B. Wolf, O. Stoll, & A.W. Fullerton, Lecture Notes in Physics 523, 329
Palate, M., & Rauw, G. 2012, A A, 537, 119
Palate, M., Koenigsberger, G., Rauw, G., Harrington, D., & Moreno, E. 2013, A&A, 556, 49
Palate, M., Rauw, G., Koenigsberger, G., & Moreno, E. 2013, A&A , 552, 39
Plaskett, J.S. 1922, JRASC, 16, 284
Rauw, G., De Becker, M., van Winkel, H., et al. 2008, A&A, 487, 659
Rudy, R.J., & Herman, L.C. 1978, PASP, 90, 163
Schrijvers, C., & Telting, J.H. 1999, A&A, 342, 453
Wiggs, M.S., & Gies, D.R. 1992, ApJ, 396, 238
Zima, W., Kolenberg, K., Briquet, M., & Breger, M. 2004, CoAst, 144, 5

3.4 WR 138

The last system that we have studied is WR 138. The multiplicity of WR 138 has been subjected to many debates. Massey (1980) first classified the system as a single Wolf-Rayet (WR) star or a binary system. Then, Lamontagne et al. (1982) proposed that WR 138 would be a triple system consisting of a WN6 star orbited by an unseen low-mass compact companion in a short orbit and an O-type star in a wider orbit. Finally, Annuk (1990) identified WR 138 as a binary system with a WN star orbited by an O-type star in a 1538 d orbit. In order to clarify the situation, we have studied both optical and X-ray spectra and found no spectroscopic evidence of a compact companion around WR 138. We conclude that WR 138 is a normal long-period ($P \equiv 1521$ d) eccentric WN5-6+OB system. During our analysis, we have noticed that optical spectra display emission-line profile variations. However, contrary to Plaskett's star or Spica, these line profile variations are most probably caused by clumps inside the dense stellar wind of the WN5-6 component. Unfortunately, CoMBiSpeC does not model the wind of massive stars which plays a key role in the formation of the spectra of WR stars, because this wind is optically thick over most parts of the spectrum and out to large distances. Therefore, in this last case, CoMBiSpeC is not sufficient. This shows that important improvements are still needed to completely model the spectra of binary systems.

A&A 560, A27 (2013)
DOI: 10.1051/0004-6361/201322162

Astronomy & Astrophysics

WR 138: new results from X-ray and optical spectroscopy⋆,⋆⋆

M. Palate[1], G. Rauw[1], M. De Becker[1], Y. Nazé[1]⋆⋆⋆, and P. Eenens[2]

[1] Institut d'Astrophysique et de Géophysique, Université de Liège, Bât. B5c, Allée du 6 Août 17, 4000 Liège, Belgium
e-mail: palate@astro.ulg.ac.be
[2] Departamento de Astronomia, Universidad de Guanajuato, Apartado 144, 36000 Guanajuato, GTO, Mexico

Received 28 June 2013 / Accepted 8 October 2013

ABSTRACT

Context. Massive-binary evolution models predict that some systems will go through an evolutionary phase where the original primary has become a supernova and left a compact object behind that then orbits a Wolf-Rayet (WR) star. WR 138 is an X-ray bright WR star that has been described as a triple system, including a compact companion in a short-period orbit.
Aims. Our goal is to search for spectroscopic evidence of a compact companion around WR 138.
Methods. We used optical and X-ray spectra to search for signatures of a compact companion, which can be revealed by systematic variations in WR optical spectral lines induced by orbital motion of the compact companion or by hard, luminous X-rays from accretion onto this companion.
Results. The optical spectra display emission-line profile variations that are most probably caused by clumps inside the stellar winds. The radial velocities do not vary on a short time-scale compatible with the suggested orbital period of a putative compact companion. The X-ray spectra are found to be normal for a WN5-6+OB system with no indication of accretion by a compact companion.
Conclusions. There is no evidence for the presence of a compact companion, and we therefore conclude that WR 138 is a normal long-period ($P \sim 1521$ d) eccentric WR+OB system.

Key words. stars: early-type – stars: Wolf-Rayet – stars: massive – stars: individual: WR 138 (HD 193077) – X-rays: stars

1. Introduction

Whilst absorption lines in the spectrum of WR 138 were recognized several decades ago, the multiplicity of this star has been an open question for a long time. Massey (1980) found no evidence for significant ($K \geq 30\,\mathrm{km\,s^{-1}}$) radial velocity (RV) variations that would have been attributable to an orbital motion of the emission lines and suggested that the broad ($v \sin i \simeq 500\,\mathrm{km\,s^{-1}}$) absorption lines were intrinsic to the WN star. From a series of photographic spectra, Lamontagne et al. (1982) noted low-amplitude RV variations of the N IV λ 4058 line on a period of 2.3238 d, although other periods, such as 0.39 d, could not be fully excluded. These variations were not seen in the He II λ 4686 line. The absorption lines did not display variations on this period either. In addition, Lamontagne et al. (1982) noted that the RVs of both the emission and absorption lines vary on a long period of about 1763 or 1533 d. As a result, they classified WR 138 as a triple system consisting of a WN6 star orbited by an unseen low-mass companion, probably a neutron star, in a 2.3238 d orbit and an O-type star in a 1763 d orbit. The interpretation of the short-period variations as the orbital period of a compact companion was questioned by Vreux (1985), who drew attention to the ambiguity of the period determination due to the aliasing problem. He suggested that alternative mechanisms, such as non-radial pulsations, could produce modulations of the spectra of Wolf-Rayet (WR) stars on periods that could be aliases of those reported in the literature. Annuk (1990) analysed a series of medium-dispersion spectra of WR 138 and reported RV variations with a period of 1538 ± 14 d (although a period of 1420 d could not be fully excluded), an amplitude of about $60\,\mathrm{km\,s^{-1}}$, and a moderate eccentricity of 0.3. He was unable, however, to confirm the short-period variations of the RVs reported by Lamontagne et al. (1982). X-ray observations are expected to provide an independent indication about the presence or absence of a compact companion in WR 138. Indeed, the presence of a neutron star in a close orbit around a WN star should lead to substantial accretion by the former and would thus produce a strong and hard X-ray emission, as seen in high-mass X-ray binaries (see e.g. Negueruela 2010). The X-ray emission from WR 138 was detected with the *Einstein* observatory (Pollock 1987) and within the All Sky Survey of ROSAT (Pollock et al. 1995). However, these observations did not provide the level of detail required to clarify the nature of the X-ray emission. In this paper, we present new X-ray observations of WR 138 augmented by several new series of optical spectra to re-investigate whether there is a compact companion in a short-period orbit around the WN star.

2. Observations

2.1. X-ray observations

WR 138 was observed serendipitously with *XMM-Newton* (Jansen et al. 2001) in May 2011, during three exposures of 20 ks each centred on the massive binary HDE 228766 (Rauw et al., in prep.; ID 067048). EPIC instruments (Turner et al. 2001; Strüder et al. 2001) were operated in full-frame mode and the medium filter was used to reject optical and UV photons.

⋆ Based on observations collected at the Observatoire de Haute-Provence (France), the San Pedro Mártir observatory (Mexico), and with *XMM-Newton*, an ESA science mission with instruments and contributions directly funded by ESA member states and the USA (NASA).
⋆⋆ Tables 2–5 are available in electronic form at http://www.aanda.org
⋆⋆⋆ Research Associate FRS-FNRS.

Table 1. Journal of the *XMM-Newton* observations.

Date	Date	Useful exposure time	
	HJD−2 450 000	MOS 2	*pn*
(dd-mm-yyyy)		(ks)	(ks)
05-05-2011	5686.713	21.6	14.1
13-05-2011	5694.768	19.9	13.0
18-05-2011	5700.152	23.8	18.0 (gap)

Notes. The date of the observation is given at mid-exposure.

The raw data were processed with SAS software version 12.0. The first two observations were affected by background flares, and we therefore rejected these high-background episodes from further processing. Because WR 138 was located 9′ off-axis in these pointings, the source sometimes fell on a gap between the detector chips or on the dead CCD of the MOS 1 detector. As a consequence, not all EPIC instruments provided useful data for WR 138 for each exposure. In particular, we decided to restrict our analysis to MOS 2 and pn data. The extraction zones consist of a circle of 40″ centred on the source and a nearby circular zone of 35″ radius in a source-free region for the background. The spectra were binned with a minimum of 25 counts per bin of energy channel and a maximum oversampling of the resolution element by a factor 5.

Several other X-ray observations were also available in the HEASARC archives. WR 138 was observed with ROSAT in October 1993, in June 1994 with the PSPC instrument, and in November 1994 with the HRI instruments (SEQ ID RP500248N00, RP500248A01, and RH500341N00). The exposure durations were 3.6, 4.2, and 42.8 ks, respectively. WR 138 was also observed with *Swift* in March 2011 (OBS ID 00040153001) with an exposure time of 1 ks. Finally, a *Chandra* observation of 69.3 ks made in January 2010 (OBS ID 11092) was also available. In all the ROSAT and *Chandra* observations, WR 138 is located far off-axis, leading to a severe degradation of the PSF. We downloaded the processed data and extracted the spectra of WR 138 for these five archival observations. The extraction zone for the *Swift* data consists of a circular zone with a radius of 50″ around the star and the surrounding annulus with an outer radius of 213″ for the background. The extraction zone for the *Chandra* data is an ellipse of 33″ × 47″ semi-axes for the source and a nearby circle of 43″ radius for the background. The ROSAT HRI and PSPC extraction zones consist of circles of 1′ and 3.5′, respectively, centred on the source and surrounding annuli with outer radii of 2′ and 5′ for the background. The minimum numbers of counts per bin for the *Chandra* and ROSAT mission are 10 cts/bin and 15 cts/bin.

2.2. Optical spectroscopy

WR 138 was monitored with the Aurélie spectrograph (Gillet et al. 1994) at the 1.52 m telescope of the Observatoire de Haute-Provence (OHP) during two observing campaigns in September 2011 and June 2012. The 2011 data were taken with a 1200 lines mm^{-1} grating blazed at 5000 Å and cover a wavelength domain from 4453 to 4675 Å with a resolving power of ≃20 000. The 2012 spectra were obtained with a 600 lines mm^{-1} grating also blazed at 5000 Å. The wavelength domain covered by these data extends from 4448 to 4886 Å with a resolving power of ≃10 000. The detector was an EEV 42-20 CCD with 2048 × 1024 pixels. The data were reduced in the standard way (see Rauw et al. 2003) using the MIDAS software provided by ESO. The optical spectrum of WR 138 consists of many strong and broad emission lines with only very few line-free regions. We normalized the spectra of each campaign using a number of (pseudo) continuum windows. Given the different spectral ranges of the two datasets and especially in view of the narrow spectral range of the 2011 data, it was not possible to normalize both datasets consistently. Nevertheless, within a given dataset, the normalizations are consistent, allowing us to search for line-profile variability. In the time of August to September 2012, we furthermore collected a series of échelle spectra of WR 138 with the ESPRESSO spectrograph mounted on the 2.12 m telescope at the Observatorio Astronómico of San Pedro Mártir (SPM) in Mexico. These data cover the spectral region from 3900 to 7200 Å with a resolving power of ≃18 000. The integration times of individual spectra was 15 min. The data were reduced using the IRAF échelle packages. Due to the strongly peaked blaze of the ESPRESSO spectrograph and the broad spectral lines of the WR star, the normalization of the spectra was very difficult. Therefore, we used the SPM data mainly for measuring RVs and for classification purposes.

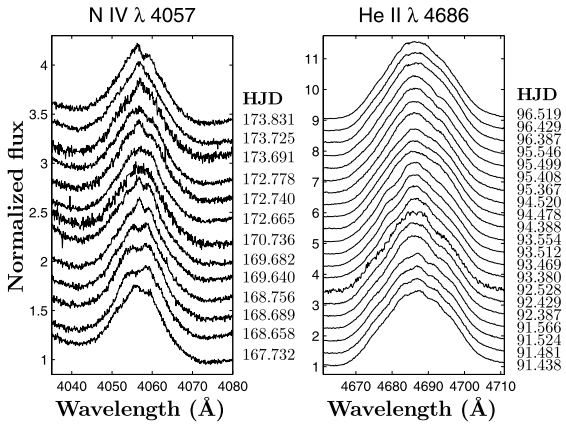

Fig. 1. Line-profile variations for the SPM (*left*) and OHP 2012 (*right*) observations. The observations are vertically shifted by 0.2 (*left*) and 0.4 (*right*) continuum units for clarity (time is given as HJD–2 456 000).

3. Optical spectra

The OHP spectra display several emission lines: N III $\lambda\lambda$ 4510-4534 and 4634-4640; N V $\lambda\lambda$ 4604 and 4620; He II $\lambda\lambda$ 4542, 4686, 4859, and Hβ. They also display one absorption line: He I λ 4471. We first performed a temporal variation spectrum (TVS, see Fullerton et al. 1996) analysis on these spectra and found that three regions were variable: the N III $\lambda\lambda$ 4510-4534 complex, the He II λ 4686 line, and the He II λ 4859 + Hβ blend. The He II λ 4686 line presents the strongest variations, especially in the core of the line. These variations are clearly visible and take the form of changing subpeaks in the line core with a timescale of a few hours to days, as can be seen in Fig. 1. The Hβ region displays the weakest variation, which is at the limit of the significance level (at 1%). The variations of these emission lines are reminiscent of those of other WR stars. They are commonly attributed to wind inhomogeneities (clumps) and more specifically to the statistical fluctuation of the number of clumps emitting at a specific line-of-sight velocity (see e.g. Lépine et al. 1996, 1999).

The SPM spectra were mainly used for RV measurements and spectral-type determination. We studied the same emission lines as in the OHP data plus the N IV λ 4058 and He II $\lambda\lambda$ 4100 and 4200 lines, as well as two more absorption lines (He I $\lambda\lambda$ 4143 and 4921). The lines in the SPM spectra also present line profile variations that are clearly visible in Fig. 1. We determined the spectral type of WR 138 using the criteria of Smith et al. (1996). We found that the peak-over-continuum ratios of N V λ 4604 over N III λ 4640, He II λ 5411 over He I λ 5875, C IV λ 5808 over He II λ 5411, and C IV λ 5808 over He I λ 5875 are equal to ∼1.05, ∼1.57, ∼0.80, and ∼1.25, respectively, which corresponds to a spectral type between WN5 and WN6. Annuk (1990) and Lamontagne et al. (1982) found a WN6 spectral type using the old criterion of Smith (1968). Adopting this old criterion, we also derive a WN6-type. We therefore classify WR 138 as a WN5-6 star. Annuk (1990) suggested an O9-9.5I-II type for the companion, with a high rotational velocity $v \sin i \sim 500$ km s^{-1}. This high rotational velocity would be unusual for a bright giant or supergiant in a well-detached binary system. Unfortunately, we cannot refine this classification because our data do not allow us to clearly identify a sufficient number of lines belonging to the OB companion.

3.1. Radial velocities

As mentioned above, several scenarios have been proposed concerning the multiplicity of WR 138. Massey (1980) favoured a single-star scenario, whilst Lamontagne et al. (1982) suggested that it might be a triple system with a WR + O system in a wide orbit and a compact object closely orbiting the WR star. Finally, Annuk (1990) concluded that the system consists of only of a WR + O pair in a wide orbit. To determine whether a compact companion is present close to the WR star, we performed an RV analysis on the basis of several lines. We used the above-mentioned spectral lines except for the N III lines and N V λ 4620, which were too blended to provide accurate measurements. We stress that the lines are very broad and shallow and therefore lead to quite large uncertainties on the RVs. Moreover, as pointed out above, several lines present profile variations that make the RV measurement more difficult. Using the MIDAS software, we fitted Gaussians to the lines, starting from various heights above the continuum, to determine their centroid, and for this we computed the corresponding RVs. The RVs quoted in the present paper are expressed in the heliocentric standard of rest (by applying appropriate RV corrections). The RVs reported in Tables 2–5 correspond to the mean value obtained for each series of measurements performed for each spectral line[1].

We note that the He I $\lambda\lambda$ 4143 and 4921 absorption lines have positive mean RVs, whilst the He I λ 4471 absorption line has a negative mean RV. The He I λ 4471 line also presents a strong variation compatible with the motion of a probable secondary component. For example, the mean RVs of He I λ 4471 change from 36 (OHP 2011) to −44 (OHP 2012) and −26 (SPM 2012) km s^{-1}, while the mean RVs of He II λ 4542 change from 36 to 85 and 85 km s^{-1}, respectively (the error is of the order of ±10 km s^{-1}).

It is also interesting to note that the N IV λ 4058 emission line has a negative mean RV, whilst all the other emission lines have positive mean RVs. Several WN-type stars display such differences between velocities of N IV λ 4058 and other lines such as He II λ 4686 (see e.g. Shylaja 1987). This can most probably be interpreted in terms of different formation sites, from close to the stellar surface to farther out in the wind.

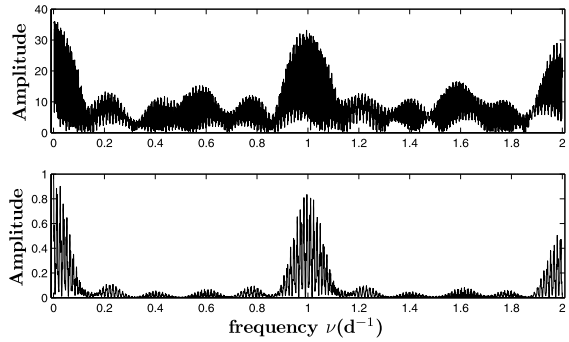

Fig. 2. *Uppper panel*: power spectrum computed on the basis of the RVs of the N V λ 4604 line. *Lower panel*: associated spectral window.

We used our spectral time-series to search for the presence of a compact object in a close orbit. We first tried without success to fit a sine function to the series of RVs with the period of 2.3238 d proposed by Lamontagne et al. (1982). We then applied the generalized Fourier technique developed by Heck et al. (1985), which was refined by Gosset et al. (2001), to the RV time-series obtained from OHP and SPM data. The power spectrum did not present a significant peak in the frequency domain that would have been compatible with such a short period (see Fig. 2). In conclusion, we did not find evidence for a short period in the WR 138 system. We suggest that the line profile variations previously mentioned may be responsible for stochastic RV variations, which could have been mistaken for periodic changes.

Our data were obtained over a time basis that is too short to investigate time-scales as long as 1500 d. We therefore complemented our time-series with the measurements published by Massey (1980), Lamontagne et al. (1982), and Annuk (1990). We selected the spectral lines common to all studies. Even though this time-series is sparse and not homogeneous in terms of spectral resolution and signal-to-noise ratio, it offers the advantage of covering several decades. We caution, however, that the errors on the older measurements cannot be quantified, and neither do we have any information on the rest-wavelengths[2] used by previous authors to compute their RVs. Systematic biases are therefore possible. The results of the Fourier analysis of this extended time-series are interesting, however, because the power spectrum is clearly dominated by a peak at 6.5×10^{-4} d^{-1} for the N IV λ 4058 (see Fig. 3) and He II λ 4542 lines. For the He II λ 4686 and N V λ 4604 lines, the highest peaks are found at frequencies of 6.6×10^{-4} and 6.7×10^{-4}d^{-1}. These peaks correspond to periods of 1538.5, 1515.2, and 1492.5 d. We estimate the uncertainty on the period as $\Delta P = 0.2 \times \frac{P^2}{\Delta T}$, where ΔT is the time interval between the first and the last observations of the complete time-series (assuming the uncertainty on the peak frequency amounts to 20% of the peak width), giving a value of ∼35 d. In conclusion, we thus argue that WR 138 is a binary

[1] The bluest and reddest measurements yielded the error interval quoted in Tables 2–5. The tables also give a mean RV for each observing run and the mean of the error intervals.

[2] The rest-wavelengths used in this paper come from the NIST Atomic Spectra Database available at: http://www.nist.gov/pml/data/asd.cfm.

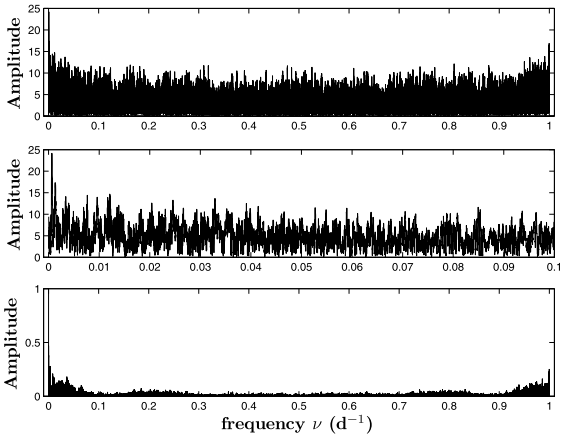

Fig. 3. *Uppper and middle panels*: power spectrum computed on the basis of the RVs of the N IV λ 4058 line. The peak lies at 6.5×10^{-4} d^{-1}, which corresponds to a period of 1538.5 d. *Lower panel*: associated spectral window (the highest value, 1, lies at $\nu = 0$).

system with a period of 1521.2 ± 35 d, which agrees quite well with the value derived by Annuk (1990, P = 1538 d).

4. X-ray emission

4.1. Spectral fits

To determine the nature of the system, we fitted several models to the EPIC spectra. Very few individual lines are visible, which is due to the low resolution. The fits were calculated with the XSPEC software, v 12.6.0 (Arnaud 1996). Our spectra present the highest emission peak around 0.8−1 keV, but extend to more or less 8 keV, which is quite high assuming a (single) O-type star, but is more typical of a colliding-wind binary. The X-ray emission of an individual massive star can be, in first approximation, described by an optically thin thermal plasma heated to a few 10^6 K by shocks intrinsic to its stellar wind (Feldmeier et al. 1997; Lucy & White 1980; Lucy 1982; Owocki et al. 1988). Whether or not the same mechanism also operates in the winds of individual WR stars is currently still an open question. In fact, unlike O-type stars, single WRs do not exhibit a clear relation between their X-ray luminosity and their stellar wind parameters (Wessolowski 1996). While some (apparently) single WR stars are detected as X-ray sources, others remain undetected, even with *XMM-Newton* and *Chandra* (e.g. Oskinova 2003; Gosset et al. 2005; Skinner et al. 2010, 2012). In the case of a WR+OB binary system, an additional site for thermal X-ray production is the colliding-wind region, where strong shocks can heat the plasma to temperatures of several 10^7 K (Pittard & Parkin 2010). In addition, a power-law component may be required to account for a possible inverse-Compton-scattering emission that can occur in the wind-collision region (De Becker 2007). Finally, a combination of an optically thin thermal plasma and a blackbody emission can be considered in the case of a WR + neutron star system. We investigated all these models, restricting our analyses to the energy range 0.3−10 keV to avoid data with very low S/N ratio. In the third *XMM-Newton* observation, WR 138 partially fell in a gap of the pn detector. We tried to fit the data, but the results obtained with this set give a very poor quality fit. To avoid a misinterpretation, we therefore decided to reject these pn data. We adopted an equivalent interstellar column of neutral hydrogen of $N_{\rm H,ism} = 0.58 \times 10^{22}$ $E(B-V) = 0.37 \times 10^{22}$ cm^{-2} (Bohlin et al. 1978) using the star's colour excess obtained from $E(B-V) = 1.21/4.1\ A_v = 0.63$ mag (van der Hucht 2001). WR stars are evolved objects and are characterized by non-solar abundances. We therefore used models with adjustable abundances. However, in view of the low spectral resolution, we had to reduce the number of free parameters to avoid local minima or non-physical solutions. We therefore fixed the abundances to common values for WN stars found in the literature (Crowther et al. 1993; Hamann & Koesterke 1998; Hamann & Gräfener 2004). These cases correspond to a H/He ratio equal to 0.05, 0.15, and 0.25. The C/He, N/He, and O/He are equal to 0.00048, 0.048, and 0, while all other elements were kept fixed to their solar value. Table 6 recalls the relative abundances adopted for the different chemical elements.

Table 6. Relative and solar abundances used for the X-ray spectral modelling.

	H/He = 0.25	H/He = 0.15	H/He = 0.05
$(He/H)/(He/H)_\odot$	46.998	78.330	234.990
$(N/H)/(N/H)_\odot$	23.077	38.462	115.385
$(C/H)/(C/H)_\odot$	5.818	9.697	29.091
$(O/H)/(O/H)_\odot$	0.000	0.000	0.000
$(X/H)/(X/H)_\odot$	4.000	6.666	20.000
Solar abundances (Grevesse & Sauval 1998)			
$(He/H)_\odot$	0.08511		
$(N/H)_\odot$	0.00832		
$(C/H)_\odot$	0.00033		
$(O/H)_\odot$	0.00068		

Notes. X stand for the other metal elements (Fe, Ni, Ar, etc.).

We first tried a single-temperature plasma model (APEC) and an intrinsic absorption column. As expected, this simple model gives poor quality fits, and therefore we switched to a more complex two-temperature model with an intrinsic absorption column ($wabs_{ISM}$*wabs*(APEC+APEC)). We point out that the absorption is dominated by the interstellar absorption, therefore we used a wabs model with solar abundances (Anders & Ebihara 1982) instead of a vphabs model with non-solar abundances. The two models led to solutions with similar reduced χ^2, temperatures, normalization factors, and a low $N_{\rm H}$. The three sets of non-solar abundances yielded solutions with similar reduced χ^2, temperatures, and intrinsic absorption column. The normalization factors were different, however, which is expected because in modifying the relative abundances, we changed the number of available free electrons and hence the emission measure of the plasma. We therefore adopted the intermediate value of the abundance for the rest of the study (i.e. H/He = 0.15). Table 7 gives a summary of the best-fit parameters. If we simultaneously fit the data from the two detectors (except for the third observation where the pn data were rejected), the results of the fits suggest a weaker variability than in the case of the fits of the MOS 2 data alone.

We also used a one-temperature plasma plus a power-law model with an intrinsic absorption column ($wabs_{ISM}$*wabs*(APEC+power-law)). The quality of the fit is similar to those obtained with the previous model except for the third observation, for which this model gives a better fit. Notice that the poorer response at energy <0.5 and >5 keV mainly explains the high χ^2 of the 2-T plasma and the 1-T plasma plus power-law model fit. Table 8 gives a summary of the best-fit parameters. Because of the low S/N ratio above 2 keV, it is difficult to determine which of these models is

Table 7. Best-fit parameter results for the two-temperature plasma model.

HJD −2 440 000	n_H (10^{20} cm^{-2})	kT_1 (keV)	Norm$_1$ (10^{-5} cm^{-5})	kT_2 (keV)	Norm$_2$ (10^{-5} cm^{-5})	χ^2_ν (d.o.f.)
XMM-Newton						
15 686.713	$5.74^{+3.53}_{-3.75}$	0.64 ± 0.04	$5.98^{+5.69}_{-1.24}$	$1.27^{+0.36}_{-0.15}$	$0.72^{+0.57}_{-0.09}$	1.40 (88)
15 694.768	<3.98	0.63 ± 0.04	$4.15^{+1.17}_{-0.42}$	$1.27^{+0.21}_{-0.13}$	$1.81^{+0.47}_{-0.47}$	1.13 (78)
15 700.152	<2.35	$0.65^{+0.08}_{-0.05}$	$4.41^{+1.84}_{-0.84}$	$1.42^{+0.38}_{-0.29}$	$1.99^{+0.94}_{-0.98}$	1.89 (32)
Chandra						
15 213.113	<1.1	$0.58^{+0.03}_{-0.07}$	$5.4^{+0.44}_{-0.82}$	$1.12^{+0.11}_{-0.13}$	$1.94^{+8.75}_{-0.38}$	1.20 (170)
15 213.113	<0.8	0.64 (fixed)	$5.8^{+0.30}_{-0.32}$	1.32 (fixed)	$1.28^{+0.23}_{-0.21}$	1.27 (172)
ROSAT						
6928.585	<13.0	0.64 (fixed)	$6.91^{+3.43}_{-1.48}$	1.32 (fixed)	1.5 (fixed)	1.42 (17)
9508.604	<15.7	0.64 (fixed)	$5.21^{+3.06}_{-1.42}$	1.32 (fixed)	1.5 (fixed)	1.12 (17)

Notes. The best-fit parameters of the *XMM-Newton* observation correspond to a simultaneous fit of the MOS2 and pn spectra (except for the last observation where the pn data were rejected). The errors correspond to the 90% confidence interval. All fits were performed including an ISM absorption column of 37×10^{20} cm^{-2}.

Table 8. Same as Table 7, but for the one-temperature plasma plus power-law model.

HJD −2 440 000	n_H (10^{20} cm^{-2})	kT_1 (keV)	Norm$_1$ (10^{-5} cm^{-5})	PhoIndex	Norm$_2$ (10^{-5} ph keV^{-1} cm^{-2} s^{-1})	χ^2_ν (d.o.f.)
XMM-Newton						
15 686.713	$16.6^{+4.25}_{-4.36}$	0.64 ± 0.03	$10.1^{+1.59}_{-1.74}$	$1.16^{+0.51}_{-0.96}$	$1.32^{+3.56}_{-1.04}$	1.39 (88)
15 694.768	$8.21^{+5.28}_{-4.27}$	0.64 ± 0.03	$6.24^{+2.97}_{-1.23}$	$2.67^{+0.71}_{-0.57}$	$8.03^{+6.30}_{-7.45}$	1.29 (78)
15 700.152	$13.3^{+9.94}_{-7.92}$	$0.63^{+0.08}_{-0.06}$	$6.49^{+3.03}_{-1.86}$	$3.47^{+1.26}_{-1.39}$	$17.7^{+14.6}_{-14.7}$	0.99 (32)
Chandra						
15 213.113	$2.26^{+4.99}_{-2.26}$	0.64 (fixed)	$5.45^{+0.93}_{-0.65}$	$3.93^{+0.72}_{-0.44}$	$2.26^{+4.99}_{-2.26}$	1.28 (171)
ROSAT						
6928.585	<28.8	0.64 (fixed)	7.31 ± 6.41	2.43 (fixed)	9.2 (fixed)	1.42 (17)
9508.604	<32.9	0.64 (fixed)	5.64 ± 5.64	2.43 (fixed)	9.2 (fixed)	1.25 (17)

Notes. Same note as Table 7.

best-suited to the WR 138 system. It has to be stressed that the photon index and normalization of the power-law component are found to be highly variable in this model. In particular, we had to deal with multiple local minima that severely affected our capability to derive consistent parameters from one data set to the other. It is clear, for instance, that the fit in some cases predicted excessive normalization parameter values, which were therefore accompanied by large absorption columns to compensate the flux excess at lower energies. This probably points to a significant inadequacy of the 1T+power-law model. Finally, the APEC plus black-body model gives low-quality fits ($\chi^2_\nu \geq 2$).

In conclusion, the two-temperature plasma model seems to be the most adequate one. This model is dominated by the lowest temperature at 0.6 keV. Hamann et al. (1995) reported a luminosity of $\log L_{bol} = 38.9$ (assuming a photometric distance of d = 1.82 kpc, Lundström & Stenholm 1984) for WR 138, which is well inside the range of values of the other WN5-6 stars, that is, $\log L_{bol} = [38.5, 39.2]$. The X-ray luminosity that we derive with the distance used by Hamann et al. (1995) is about $\log L_x = 32.65$. With this value, we can derive a $\log(L_x/L_{bol})$ ratio of −6.25. Oskinova (2005) suggested a distance of d = 1.26 kpc and a $\log L_{bol} = 38.88$. With this distance and bolometric luminosity, the X-ray luminosity lies in the range $\log L_x = [32.33, 32.48]$, which leads to a $\log(L_x/L_{bol}) = [-6.55, -6.41]$.

The X-ray analysis shows that WR 138 is no exceptional star in this wavelength domain. Oskinova (2005) reported on other WN+OB star binaries whose spectra could be represented by a two-temperature plasma model dominated by a soft component $kT_1 \approx 0.6$ keV and a hard component $kT_2 \approx 2$ keV. Our modelling agrees well for the temperature of the soft component, but gives a sightly lower value for the temperature of the hard component.

Our results (moderate X-ray luminosity, X-ray spectral morphology) argue against the presence of an accreting compact companion. They instead suggest a more conventional long-period WR + OB binary.

4.2. Long-term behaviour

Several pointed observations from *Swift*, ROSAT, and *Chandra* (see Sect. 2.1) were also used to determine whether WR 138 presents long-term variations in its X-ray emission. Such long-term variations exist in long-period highly eccentric WN + OB colliding wind binaries (e.g. WR 22, Gosset et al. 2009; WR 25, Pollock & Corcoran 2006). We also fitted the two-temperature plasma model and the one-temperature plus power-law model to the ROSAT and *Chandra* data. For the ROSAT data, the spectra have a very low resolution and do not cover the energies beyond 2.2 keV. A fit of the data without fixing the temperature gives

Table 9. X-ray flux.

HJD	2-T plasma model (10^{-13} erg s^{-1} cm^{-2})				1-T plasma +power-law model (10^{-13} erg s^{-1} cm^{-2})			
–2 440 000	$F^{corr}_{x,s}$	$F^{corr}_{x,m}$	$F^{corr}_{x,h}$	$F^{obs}_{x,tot}$	$F^{corr}_{x,s}$	$F^{corr}_{x,m}$	$F^{corr}_{x,h}$	$F^{obs}_{x,tot}$
XMM-Newton								
15 686.710	7.16	4.42	1.15	5.49 ± 0.18	6.87	4.33	1.97	5.60 ± 0.18
15 694.768	6.63	3.70	0.98	4.67 ± 0.17	6.58	3.54	1.22	4.91 ± 0.18
15 700.152	7.06	4.04	1.28	5.27 ± 0.16	6.58	3.78	1.04	4.83 ± 0.16
Chandra								
15 213.113[1]	8.51	4.24	0.87	5.30 ± 0.1				
15 213.113[2]	8.40	4.10	0.95	5.26 ± 0.1	10.77	3.99	0.81	5.34 ± 0.1
ROSAT								
6928.585[2]	9.97	4.91		5.28 ± 0.58	10.73	4.70		5.32 ± 0.59
9508.604[2]	7.75	4.02		4.23 ± 0.64	8.54	3.83		4.29 ± 0.64

Notes. $F^{corr}_{x,s}$: X-ray flux corrected for ISM_{abs} in the band 0.5–1.0 keV, $F^{corr}_{x,m}$ in the band 1.0–2.0 keV, and $F^{corr}_{x,h}$ in the band 2.0–10.0 keV. $F^{obs}_{x,tot}$: observed X-ray flux in the band 0.5–10.0 keV (or 0.5–2.0 keV for the ROSAT mission). [(1)] Corresponds to the spectral fit where the temperatures are free parameters. [(2)] Corresponds to the spectral fit with fixed temperatures.

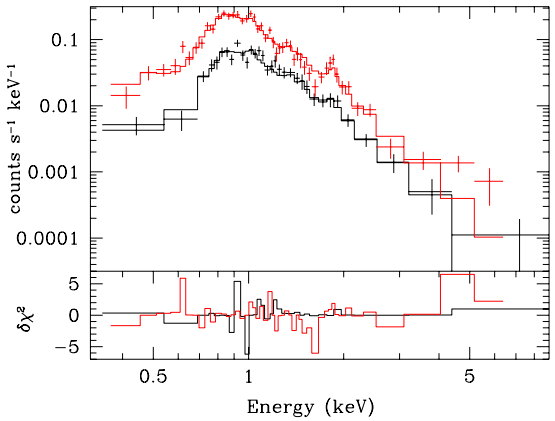

Fig. 4. *Top panel*: spectra (MOS2, *in black*, and pn, *in red*, instrument) of the *XMM-Newton* observation of HJD = 2 455 694.768 and best-parameter fit obtained with *XSPEC*. *Lower panel*: χ^2 increments multiplied by the sign of the data – model difference.

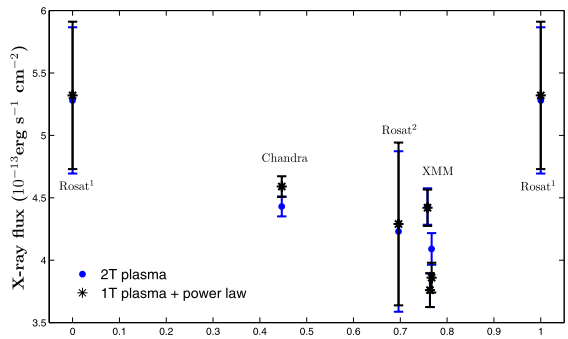

Fig. 5. Variation of the observed X-ray fluxes derived with *XSPEC* for the ROSAT, *Chandra*, and *XMM-Newton* observations in the energy band 0.5–2 keV. [1]ROSAT observation 2 446 928.585, [2]ROSAT observation 2 449 508.604. The phase 0 has been arbitrary chosen to the oldest ROSAT observation. We did not use the T_0 derived by Annuk (1990) because they strongly depend on the line considered. The period has been fixed to P = 1521.1 d. Error bars are related to the relative error of the count rate (see text).

unrealistically high temperatures (kT > 10 keV). Therefore, we fixed the temperature to the mean value of the *XMM-Newton* best-fit temperatures. For the *Chandra* data, we tried to fit the data with or without fixed temperatures. In the first case (fixed temperatures), the normalization factors (and intrinsic absorption) are similar to the *XMM-Newton* fits. In the second case (no fixed temperature), the fit indicates slightly lower temperatures. These slight differences could be due to remaining cross-calibration uncertainties. The best-fit parameters are given in Tables 7 and 8.

From these fits, we computed the X-ray fluxes in three spectral bands: soft (0.5–1.0 keV), medium (1.0–2.0 keV), and hard (2.0–10.0 kev). These fluxes are quoted in Table 9. We assumed that the relative error on the observed X-ray fluxes is the same as for the count rates, and chose the oldest ROSAT observation as the starting point for arbitrary ephemeris (using the P = 1521.1 d period found in Sect. 3). The error estimate is probably underestimated because some parameters such $N_{H,ism}$ are poorly known. The flux also strongly depends on the model used, which is affected by uncertainties. These additional errors are unfortunately difficult to estimate. We tried to use the *flux err* command of XSPEC to calculate another evaluation of the error. The results are of the same order of magnitude (few percent) for the upper limit. The lower limit derived from XSPEC is much lower, but a model computed from this lower limit cannot account for the observed flux. Figure 5 shows that WR 138 displays only modest, if any, flux variations, although because of the uncertainties on the long-term orbital solution, it is not clear whether or not our data sample critical phases (such as the periastron passage) of the orbital motion in the WN5-6 + OB binary. A dedicated monitoring of WR 138 around periastron might reveal a significant increase in flux. However, this requires an accurate ephemeris and needs a dedicated and long-term optical monitoring of WR 138.

Table 10 gives the value of the count rates given by XSPEC for the different missions (observed count rates) and those simulated with XSPEC using the model parameters of a simultaneous fit of all *XMM-Newton* spectra with a two-temperature plasma model (simulated count rates) folded through the appropriate instrumental response matrices. We stress that the count rates are those within the extraction regions and are therefore depending on where the source lies on the detector and the size of chosen regions; consequently, they are linked to the ancillary response files (arf). Because the exposure time and arf are different

Table 10. X-ray count rates.

Mission – Instrument	HJD	Observed count rate	Relative error	Simulated count rate	Relative deviation[1]	Energy range
	–2 440 000	(10^{-2} cts s^{-1})	(%)	(10^{-2} cts s^{-1})	(%)	keV
XMM–Newton MOS2	15 686.713	5.42 ± 0.18	3.3	4.97 ± 0.15	8.4	0.2–10
	15 694.768	5.03 ± 0.18	3.6	5.00 ± 0.16	0.5	0.2–10
	15 700.152	5.54 ± 0.17	3.1	5.14 ± 0.15	7.1	0.2–10
XMM–Newton pn	15686.713	17.95 ± 0.41	2.3	15.87 ± 0.34	11.6	0.2–10
	15 694.768	15.28 ± 0.40	2.6	15.84 ± 0.35	–3.7	0.2–10
Einstein–IPC[2]	3972.050	1.00 ± 0.40	40.0	2.09 ± 0.20	–109.4	0.2–4.5
ROSAT All Sky Survey	8210.000	3.26 ± 0.87[3]	26.7	3.20 ± 0.57	1.8	0.1–2
ROSAT PSPC	6928.585	4.50 ± 0.50	11.1	2.66 ± 0.25	40.8	0.1–2
	9508.604	3.30 ± 0.50	15.2	2.54 ± 0.26	23.1	0.1–2
ROSAT HRI	9669.924	1.17 ± 0.11	9.8	1.68 ± 0.06	–43.6	0.1–2
Swift	15 635.350	1.75 ± 0.42	24.1	1.20 ± 0.24	31.5	0.3–10
Chandra	15 213.113	6.58 ± 0.12	1.8	6.30 ± 0.10	4.3	0.2–10

Notes. [(1)] The relative error corresponds to 100 × (obs − simulation)/obs. The count rates have been obtained with XSPEC. [(2)] Values from Pollock (1987). [(3)] This value is in good agreement with the one derived by Pollock et al. (1995) who reported a ROSAT All Sky Survey PSPC count rate of $(3.26 \pm 0.87) \times 10^{-2}$ cts s^{-1}. Note that ROSAT HRI had little or no energy resolution.

for each observation, we see small differences in the simulated count rates of the same instruments. The comparison between observed and simulated count rate is aimed at providing an estimate of the potential long-term variations between the epoch of the *XMM-Newton* observations and that of all previous observations. The count rates of the three *XMM-Newton* observations present variations of less than 10%, that is, less than 3-σ except for the first pn observation (see Table 10). The first MOS2 observation also presents a quite high variation that is just below 3-σ. Therefore there is no contradiction between the pn and MOS2 results. The oldest ROSAT PSPC and HRI observations also display count-rate variations stronger than 3-σ, which are therefore considered to be significant.

5. Summary and conclusion

Throughout this paper we have investigated the validity of a scenario where the WR 138 system harbours a close compact companion. We found that neither the optical spectra nor the X-ray spectra analysis provided clear clues for such a companion.

The optical campaigns have shown that, as for many WR stars, the broad emission lines of WR 138 display variable subpeaks (Lépine et al. 1996, see Fig. 1) that might affect the determination of the RV of the WN star. The Fourier analyses of RVs do not show any clear short period compatible with that derived by Lamontagne et al. (1982). Photometric studies have also been conducted by Martin & Plummer (1919), Gaposchkin (1946), and Ross (1961), who first reported on the low-level irregular variability of WR 138, and a photometric period of 11.6 d was reported by Moffat & Shara (1986). However, these results are based on limited and sparse time-series that are not adequate for distinguishing between periodic and sporadic variations such as are frequently found in photometric observations of WR stars (e.g. Gosset et al. 1994). Indeed, from the longer-term *Hipparcos* photometry of WR 138, Marchenko et al. (1998) reported on stochastic variability. The X-ray analysis seem to point in the same direction, that is, the absence of a compact companion. Indeed, the luminosity of WR 138 lies in the range $\log L_x = [32.33, 32.48]$, while the luminosity of the Cyg X-3 system ($\log L_x \sim 10^{38}$ ergs^{-1}, Skinner et al. 2010), which is the best-known system including a compact companion that accretes the wind material from a WR star, is several orders of magnitude higher.

The question of a long-period OB companion has also been raised. The presence of this OB companion is now ascertained and supported by both optical and X-ray analyses. The Fourier analysis of the new RVs added to the previously reported ones of Massey (1980), Lamontagne (1982), and Annuk (1990) clearly reveals a peak associated to a long period. Moreover, the variations of the measured RVs cannot be completely explained by intrinsic wind inhomogeneities. The most probable scenario is that WR 138 is composed of a WN 5-6 star with an OB-type companion in a wide eccentric orbit of about 1521 d.

The X-ray spectra present an extension to high energies that would be unusual for single-star emission, but which is more common for a long-period system. The typical X-ray luminosity of WN-type stars displays large scatter. For example, WR 25 displays an X-ray luminosity of $\log L_x = 33.9$, while some other stars remain below detection level ($\log L_x < 30.0$, Oskinova 2005), such as WR 40 ($\log L_x < 31.6$, Gosset et al. 2005). Oskinova (2005) reported that the typical value of $\log(L_x/L_{bol})$ is ~ -7. Our results ($\log L_x = [32.33, 32.48]$ and $\log(L_x/L_{bol}) = [-6.55, -6.41]$) allow us to conclude that WR 138 is not particularly luminous in X-rays, but it is not particularly faint either. In fact, WR 138 seems to lie in the mean range of what we can observe for WN-type stars. This moderate X-ray luminosity also agrees well with a companion in a wide orbit. Skinner et al. (2010, 2012) and Oskinova (2005) also suggested that a two-temperature plasma model reproduces the spectra of a WN+OB binary system well. Our best-fit parameter again agrees well with this suggestion.

We also noticed variation in the X-ray emission, but, because of the small number of observations, we cannot deduce a phase-locked variability, but we cannot exclude that the variation is due to a weak wind-wind interaction between the WN 5-6 and an OB companion. Finally, the radio emission of WR 138 was reported to be thermal by Montes et al. (2009) with a corresponding mass-loss rate of $1.18 \times 10^{-5}\ M_\odot\ \mathrm{yr}^{-1}$ (assuming a distance of 1.4 kpc). Montes et al. (2009) inferred a radio spectral index close to unity, higher than expected for the free-free emission of the wind of a single star. These authors suggested that this might reflect either a clumpy wind or be due to a radiative-wind interaction zone in a binary system, which agrees well with the scenario of a WN+OB companion.

In conclusion, we can confidently reject the scenario of a compact companion in a close orbit around the WN star because

no clues (level of X-ray emission, lack of short-term RV variations) support this assumption. The OB companion proposed by Annuk (1990) can be confirmed by both optical analysis (RV variations, peak in Fourier analysis) and X-ray analysis (moderate luminosity, extension of the spectra to high energies, variations). Finally, the orbital period can be refined to $P = 1521.2 \pm 35$ d.

Acknowledgements. We acknowledge support through the XMM/INTEGRAL PRODEX contract (Belspo), from the Fonds de Recherche Scientifique (FRS/FNRS), and CONACYT grant.

References

Anders, E., & Ebihara, M. 1982, Geochim. Cosmochim. Acta, 46, 2363
Annuk, K. 1990, Acta Astron., 40, 267
Arnaud, K. A. 1996, in Astronomical Data Analysis Software and Systems V, XSPEC: The First Ten Years, eds. G. H. Jacoby, & J. Barnes, ASP Conf. Ser., 101, 17
Bohlin, R. C., Savage, B. D., & Drake, J. F. 1978, ApJ, 224, 132
Crowther, P. A., Smith, L. J., & Hillier, D. J. 1993, Space Sci. Rev., 66, 271
De Becker, M. 2007, A&AR, 14, 171
Feldmeier, A., Puls, J., & Pauldrach, A. W. A. 1997, A&A, 322, 878
Fullerton, A. W., Gies, D. R., & Bolton, C. T. 1996, ApJS, 103, 475
Gaposchkin, S. 1946, Publ. AAS, 10, 250
Gillet, D., Burnage, R., Kohler, D., et al. 1994, A&AS, 108, 181
Grevesse, N., & Sauval, A. 1998, Space Sci. Rev., 85, 161
Gosset, E., Rauw, G., Manfroid, J., Vreux, J.-M., & Sterken, C. 1994, in The Impact of Long-Term Monitoring on Variable Star Research, eds. C. Sterken, & M. de Groot (Dordrecht: Kluwer), 436, 101
Gosset, E., Royer, P., Rauw, G., Manfroid, J., & Vreux, J.-M. 2001, MNRAS, 327, 435
Gosset, E., Nazé, Y., Claeskens, J.-F., et al. 2005, A&A, 429, 685
Gosset, E., Nazé, Y., Sana, H., Rauw, G., & Vreux, J.-M. 2009, A&A, 508, 805
Hamann, W.-R., & Gräfener, G. 2004, A&A, 427, 697
Hamann, W.-R., & Koesterke, L. 1998, A&A, 335, 1003
Hamann, W.-R., Koesterke, L., & Wessolowski, U. 1995, A&A, 299, 151
Heck, A., Manfroid, J., & Mersch, G. 1985, A&AS, 59, 63
Jansen, F., Lumb, D., Altieri, B., et al. 2001, A&A, 365, L1
Lamontagne, R., Moffat, A. F. J., Koenigsberger, G., & Seggewiss, W. 1982, ApJ, 253, 230
Lépine, S., & Moffat, A. F. J. 1999, ApJ, 514, 909
Lépine, S., Moffat, A. F. J., & Henriksen, R. N. 1996, ApJ, 466, 392
Lucy, L. B. 1982, ApJ, 255, 286
Lucy, L. B., & White, R. L. 1980, ApJ, 241, 300
Lundström, I., & Stenholm, B. 1984, A&AS, 58, 163
Marchenko, S. V., Moffat, A. F. J., van der Hucht, K. A., et al. 1998, A&A, 331, 1022
Martin, C., & Plummer, H. C. 1919, MNRAS, 79, 196
Massey, P. 1980, ApJ, 236, 526
Moffat, A. F. J., & Shara, M. M. 1986, AJ, 92, 952
Moffat, A. F. J., Lamontagne, R., Shara, M. M., & McAlister, H. A. 1986, AJ, 91, 1392
Montes, G., Pérez-Torres, M. A., Alberdi, A., & González, R. F. 2009, ApJ, 705, 899
Negueruela, I. 2010, in High Energy Phenomena in Massive Stars, ASP Conf. Ser., 422, 57
Oskinova, L. M. 2005, MNRAS, 361, 679
Oskinova, L. M., Ignace, R., Hamann, W.-R., Pollock, A. M. T., & Brown, J. C. 2003, A&A, 402, 755
Owocki, S. P., Castor, J. I., & Rybicki, G. B. 1988, ApJ, 335, 914
Pittard, J. M., & Parkin, E. R. 2010, MNRAS, 403, 1657
Pollock, A. M. T. 1987, ApJ, 320, 283
Pollock, A. M. T., & Corcoran, M. F. 2006, A&A, 445, 1093
Pollock, A. M. T., Haberl, F., & Corcoran, M. F. 1995, in Wolf-Rayet Stars: Binaries, Colliding Winds, Evolution, eds. K. A. van der Hucht, & P. M. Williams (Dordrecht, Kluwer), 512
Rauw, G., De Becker, M., & Vreux, J.-M. 2003, A&A, 399, 287
Ross, L. W. 1961, PASP, 73, 354
Shylaja, B. S., 1987, JApA, 8, 183
Skinner, S. L., Zhekov, S. A., Güdel, M., Schmutz, W., & Sokal, K. R. 2010, AJ, 139, 825
Skinner, S. L., Zhekov, S. A., Güdel, M., Schmutz, W., & Sokal, K. R. 2012, AJ, 143, 116
Smith, L. F. 1968, MNRAS, 138, 109
Smith, L. F., Shara, M. M., & Moffat, A. F. J. 1996, MNRAS, 281, 163
Strüder, L., Briel, U., Dennerl, K., et al. 2001, A&A, 365, L18
Turner, M. J. L., Abbey, A., Arnaud, M., et al. 2001, A&A, 365, L27
van der Hucht, K. A. 2001, New Astron. Rev., 45, 135
Vreux, J.-M. 1985, PASP, 97, 274
Wessolowski, U. 1996, in Röntgenstrahlung from the Universe (MPE Report 263), eds. H. U. Zimmerman, J. E. Trümper, & H. York (Garching: MaxPlanck-Inst. für Extraterrestrische Physik), 75

Pages 9 to 12 are available in the electronic edition of the journal at http://www.aanda.org

Table 2. Radial velocities (in km s^{-1}) measured for the OHP 2011 campaign.

HJD	He I	He II	N V	S/N
–2 450 000	λ 4471	λ 4542	λ 4604	
5825.292	49^{+6}_{-4}	42^{+8}_{-6}	36^{+4}_{-3}	93
5825.314	34^{+3}_{-6}	38^{+2}_{-2}	40^{+4}_{-3}	92
5826.453	29^{+2}_{-2}	27^{+4}_{-3}	42^{+4}_{-4}	83
5826.474	3^{+4}_{-5}	22.7^{+4}_{-2}	32^{+7}_{-7}	90
5827.282	11^{+2}_{-1}	34.6^{+6}_{-9}	51^{+8}_{-8}	58
5827.303	72^{+16}_{-10}	46.8^{+10}_{-13}	54^{+9}_{-10}	65
5828.278	30^{+6}_{-5}	49^{+1}_{-1}	35^{+6}_{-7}	103
5828.298	47^{+5}_{-5}	44.7^{+1}_{-2}	35^{+9}_{-9}	100
5830.287	45^{+4}_{-5}	31.6^{+2}_{-3}	39^{+8}_{-8}	99
5830.309	44^{+5}_{-6}	27^{+5}_{-5}	46^{+3}_{-3}	86
Mean	36^{+5}_{-5}	36^{+4}_{-5}	41^{+6}_{-6}	87

Table 3. Same as Table 2, but for the OHP 2012 campaign.

HJD–2 450 000	He I λ 4471	He II λ 4542	N V λ 4604	He II λ 4686	Hβ	S/N
6091.417	-37^{+2}_{-1}	95^{+7}_{-6}	94^{+3}_{-2}	100^{+12}_{-28}	90^{+17}_{-14}	104
6091.438	-57^{+12}_{-9}	81^{+3}_{-6}	98^{+4}_{-4}	97^{+17}_{-21}	73^{+19}_{-22}	89
6091.459	-30^{+2}_{-1}	77^{+3}_{-5}	91^{+7}_{-4}	95^{+17}_{-25}	69^{+8}_{-9}	93
6091.481	-51^{+4}_{-7}	87^{+7}_{-6}	88^{+6}_{-4}	93^{+16}_{-30}	71^{+12}_{-15}	94
6091.502	-35^{+7}_{-6}	91^{+3}_{-5}	91^{+4}_{-4}	92^{+17}_{-27}	70^{+13}_{-11}	97
6091.524	-49^{+1}_{-1}	87^{+4}_{-4}	87^{+3}_{-4}	87^{+19}_{-22}	62^{+10}_{-10}	110
6091.545	-41^{+3}_{-3}	78^{+9}_{-10}	83^{+7}_{-8}	87^{+18}_{-22}	61^{+14}_{-17}	102
6091.566	$-46^{+2}_{-4.5}$	83^{+7}_{-7}	87^{+8}_{-12}	88^{+17}_{-23}	58^{+15}_{-22}	94
6092.364	-41^{+12}_{-15}	82^{+16}_{-10}	93^{+4}_{-2}	79^{+19}_{-33}	43^{+12}_{-13}	81
6092.386	-26^{+6}_{-3}	76^{+10}_{-8}	99^{+5}_{-5}	71^{+25}_{-23}	37^{+8}_{-10}	106
6092.408	-33^{+1}_{-1}	78^{+3}_{-1}	100^{+4}_{-7}	82^{+17}_{-25}	52^{+4}_{-7}	76
6092.429	-26^{+1}_{-1}	73^{+6}_{-5}	88^{+8}_{-8}	71^{+23}_{-23}	47^{+9}_{-9}	89
6092.500	/	102^{+12}_{-2}	86^{+1}_{-1}	74^{+22}_{-25}	61^{+11}_{-8}	33
6092.528	/	81^{+5}_{-5}	92^{+5}_{-5}	68^{+16}_{-19}	36^{+12}_{-10}	37
6093.359	-62^{+7}_{-7}	72^{+2}_{-4}	95^{+8}_{-10}	89^{+15}_{-19}	57^{+4}_{-7}	95
6093.380	-40^{+1}_{-1}	79^{+3}_{-8}	93^{+8}_{-4}	88^{+15}_{-17}	55^{+8}_{-18}	103
6093.401	-42^{+7}_{-4}	69^{+6}_{-9}	91^{+5}_{-4}	83^{+20}_{-25}	61^{+7}_{-25}	99
6093.469	-51^{+1}_{-2}	81^{+4}_{-4}	98^{+6}_{-4}	75^{+23}_{-28}	56^{+19}_{-19}	107
6093.490	-41^{+3}_{-5}	86^{+5}_{-11}	101^{+9}_{-6}	78^{+21}_{-30}	69^{+13}_{-13}	92
6093.512	-44^{+2}_{-5}	89^{+8}_{-13}	100^{+8}_{-5}	78^{+22}_{-34}	61^{+25}_{-26}	113
6093.533	-45^{+5}_{-4}	96^{+4}_{-7}	100^{+9}_{-5}	73^{+26}_{-32}	64^{+19}_{-28}	114
6093.554	-40^{+3}_{-3}	99^{+8}_{-7}	96^{+13}_{-6}	78^{+22}_{-33}	61^{+24}_{-24}	104.1
6094.367	-32^{+4}_{-4}	85^{+4}_{-10}	97^{+6}_{-4}	90^{+22}_{-41}	78^{+18}_{-16}	81
6094.388	-38^{+6}_{-3}	77^{+6}_{-8}	101^{+6}_{-7}	87^{+23}_{-42}	77^{+17}_{-14}	99
6094.410	-58^{+1}_{-1}	89^{+4}_{-9}	101^{+7}_{-8}	85^{+25}_{-40}	75^{+17}_{-21}	101
6094.478	-46^{+3}_{-2}	86^{+7}_{-12}	100^{+5}_{-3}	87^{+21}_{-36}	75^{+18}_{-14}	107
6094.499	-43^{+3}_{-3}	90^{+8}_{-11}	99^{+4}_{-4}	91^{+19}_{-35}	79^{+10}_{-13}	112
6094.520	-53^{+4}_{-5}	85^{+6}_{-9}	96^{+8}_{-4}	87^{+23}_{-35}	77^{+4}_{-8}	104
6094.544	-43^{+10}_{-9}	81^{+8}_{-6}	4^{+6}_{-3}	87^{+24}_{-35}	64^{+7}_{-6}	94
6095.367	-56^{+2}_{-2}	89^{+7}_{-3}	108^{+2}_{-3}	77^{+25}_{-32}	78^{+6}_{-11}	106
6095.387	-42^{+4}_{-2}	91^{+2}_{-3}	100^{+5}_{-4}	77^{+26}_{-31}	74^{+8}_{-9}	91
6095.408	-45^{+4}_{-4}	89^{+12}_{-8}	97^{+6}_{-3}	80^{+23}_{-34}	67^{+8}_{-9}	104
6095.478	-42^{+7}_{-8}	82^{+5}_{-2}	98^{+5}_{-3}	81^{+24}_{-33}	47^{+16}_{-15}	101
6095.499	-28^{+3}_{-3}	90^{+7}_{-5}	97^{+8}_{-5}	78^{+26}_{-30}	47^{+13}_{-10}	111
6095.524	-54^{+5}_{-3}	88^{+8}_{-6}	92^{+10}_{-5}	78^{+25}_{-25}	54^{+10}_{-12}	106
6095.546	-51^{+3}_{-5}	85^{+2}_{-3}	91^{+9}_{-4}	76^{+28}_{-26}	60^{+14}_{-12}	101
6096.366	-47^{+5}_{-10}	81^{+8}_{-5}	96^{+9}_{-7}	95^{+17}_{-28}	79^{+10}_{-14}	111
6096.387	-47^{+4}_{-10}	81^{+2}_{-3}	96^{+7}_{-5}	92^{+20}_{-30}	78^{+12}_{-17}	146
6096.408	-31^{+11}_{-8}	85^{+7}_{-4}	88^{+10}_{-5}	88^{+20}_{-28}	76^{+14}_{-16}	114
6096.429	-53^{+4}_{-6}	91^{+10}_{-9}	106^{+4}_{-2}	93^{+15}_{-30}	78^{+15}_{-19}	112
6096.499	-40^{+1}_{-1}	89^{+5}_{-4}	89^{+11}_{-11}	83^{+22}_{-28}	78^{+23}_{-18}	115
6096.519	-55^{+7}_{-34}	91^{+3}_{-3}	95^{+6}_{-3}	82^{+23}_{-28}	88^{+25}_{-23}	116
6096.541	-59^{+6}_{-8}	97^{+5}_{-4}	100^{+3}_{-3}	87^{+17}_{-23}	91^{+28}_{-25}	97
Mean	-44^{+4}_{-5}	85^{+6}_{-6}	95^{+6}_{-5}	84^{+21}_{-29}	66^{+13}_{-15}	99

Table 4. Same as Table 2, but for the SPM 2012 campaign (emission lines).

HJD–2 450 000	N IV λ 4058	He II λ 4100	He II λ 4200	He II λ 4542	He II λ 4686	Hβ
6167.717	-85^{+12}_{-17}	119^{+4}_{-3}	144^{+0}_{-0}	$102^{+8.6}_{-6}$	107^{+0}_{-1}	109^{+11}_{-6}
6167.732	-104^{+16}_{-10}	205^{+7}_{-8}	145^{+1}_{-1}	92^{+8}_{-7}	98^{+0}_{-0}	133^{+6}_{-6}
6167.747	-79^{+18}_{-14}	84^{+27}_{-17}	141^{+2}_{-2}	98^{+6}_{-5}	108^{+1}_{-0}	94^{+6}_{-5}
6168.658	-70^{+4}_{-5}	86^{+26}_{-17}	147^{+2}_{-1}	108^{+11}_{-11}	113^{+0}_{-0}	91^{+6}_{-6}
6168.673	-98^{+6}_{-17}	193^{+4}_{-6}	155^{+1}_{-1}	118^{+7}_{-5}	113^{+1}_{-1}	125^{+5}_{-3}
6168.689	-85^{+11}_{-12}	19^{+20}_{-12}	142^{+1}_{-1}	106^{+10}_{-16}	111^{+1}_{-1}	113^{+3}_{-3}
6168.745	-93^{+16}_{-14}	152^{+4}_{-3}	152^{+0}_{-0}	102^{+12}_{-10}	112^{+1}_{-1}	125^{+4}_{-4}
6168.756	-86^{+15}_{-13}	149^{+11}_{-15}	154^{+1}_{-1}	103^{+9}_{-8}	113^{+2}_{-1}	118^{+6}_{-4}
6168.771	-90^{+11}_{-11}	150^{+17}_{-18}	149^{+2}_{-1}	99^{+9}_{-10}	114^{+0}_{-0}	118^{+4}_{-5}
6169.640	-79^{+17}_{-13}	121^{+13}_{-11}	138^{+3}_{-3}	86^{+8}_{-8}	109^{+2}_{-2}	83^{+6}_{-6}
6169.665	-90^{+19}_{-21}	178^{+15}_{-14}	135^{+0}_{-0}	68^{+8}_{-9}	112^{+5}_{-4}	87^{+6}_{-5}
6169.682	-92^{+23}_{-23}	262^{+12}_{-7}	119^{+2}_{-2}	58^{+9}_{-7}	101^{+3}_{-2}	116^{+4}_{-4}
6170.722	-82^{+6}_{-14}	184^{+3}_{-3}	137^{+3}_{4}	72^{+7}_{-10}	142^{+2}_{-2}	117^{+7}_{-7}
6170.736	-84^{+12}_{-22}	222^{+7}_{-24}	127^{+4}_{-6}	/	/	/
6172.647	-61^{+17}_{-14}	32^{+2}_{-1}	128^{+1}_{-1}	100^{+6}_{-11}	106^{+1}_{-1}	111^{+8}_{-6}
6172.665	-70^{+17}_{-19}	92^{+3}_{-3}	134^{+2}_{-3}	98^{+6}_{-8}	107^{+1}_{-1}	107^{+8}_{-6}
6172.682	-70^{+15}_{-9}	50^{+2}_{-2}	119^{+11}_{-24}	90^{+4}_{-6}	108^{+0}_{-0}	104^{+4}_{-4}
6172.740	-84^{+6}_{-8}	83^{+3}_{-3}	129^{+4}_{-4}	93^{+7}_{-6}	102^{+0}_{-0}	97^{+5}_{-3}
6172.765	-108^{+5}_{-8}	57^{+2}_{-2}	110^{+2}_{-2}	70^{+5}_{-6}	117^{+2}_{-1}	122^{+6}_{-6}
6172.778	-96^{+7}_{-13}	87^{+5}_{-5}	101^{+7}_{-15}	96^{+4}_{-6}	100^{+1}_{-1}	105^{+8}_{-5}
6173.680	-76^{+17}_{-12}	27^{+2}_{-2}	135^{+1}_{-1}	101^{+7}_{-6}	112^{+1}_{-1}	106^{+4}_{-4}
6173.691	-66^{+11}_{-9}	-44^{+3}_{-3}	112^{+2}_{-2}	80^{+3}_{-2}	119^{+2}_{-2}	76^{+3}_{-2}
6173.706	-66^{+10}_{-11}	17^{+1}_{-1}	101^{+4}_{-5}	91^{+5}_{-7}	110^{+0}_{-0}	102^{+2}_{-2}
6173.725	-91^{+12}_{-16}	109^{+6}_{-4}	124^{+1}_{-1}	83^{+6}_{-6}	108^{+1}_{-1}	106^{+6}_{-5}
6173.820	-88^{+6}_{-9}	46^{+3}_{-3}	116^{+1}_{-1}	79^{+5}_{-5}	102^{+2}_{-1}	79^{+5}_{-5}
6173.831	-99^{+19}_{-25}	115^{+3}_{-3}	124^{+1}_{-1}	71^{+8}_{-10}	99^{+1}_{-1}	97^{+9}_{-6}
6173.845	-101^{+4}_{-7}	103^{+2}_{-2}	119^{+2}_{-4}	40^{+4}_{-6}	100^{+1}_{-1}	86^{+8}_{-7}
Mean	-85^{+12}_{-14}	112^{+8}_{-7}	131^{+2}_{-3}	85^{+7}_{-7}	105^{+1}_{-1}	101^{+5}_{-5}

Table 5. Same as Table 2, but for the SPM 2012 campaign (absorption lines).

HJD	He I	He I	He I	S/N
−2 450 000	λ 4143	λ 4471	λ 4921	
6167.717	72^{+3}_{-4}	-30^{+1}_{-1}	75^{+7}_{-7}	37
6167.732	116^{+39}_{-29}	-44^{+4}_{-3}	87^{+4}_{-4}	38
6167.747	82^{+7}_{-6}	-7^{+3}_{-3}	36^{+1}_{-1}	33
6168.658	115^{+15}_{-14}	-6^{+8}_{-4}	54^{+5}_{-4}	35
6168.673	90^{+26}_{-24}	-30^{+4}_{-4}	132^{+4}_{-3}	49
6168.689	82^{+3}_{-3}	-33^{+4}_{-4}	109^{+3}_{-3}	38
6168.745	35^{+13}_{-12}	-43^{+5}_{-3}	71^{+7}_{-6}	44
6168.756	92^{+6}_{-5}	-1^{+12}_{-9}	85^{+5}_{-5}	42
6168.771	111^{+2}_{-2}	-21^{+4}_{-6}	94^{+6}_{-7}	49
6169.640	42^{+1}_{-1}	-24^{+5}_{-5}	80^{+8}_{-6}	54
6169.665	71^{+9}_{-12}	-22^{+5}_{-4}	126^{+5}_{-7}	47
6169.682	134^{+20}_{-17}	-48^{+1}_{-0}	117^{+8}_{-8}	52
6170.722	41^{+3}_{-3}	-3^{+11}_{-9}	88^{+16}_{-13}	52
6170.736	-149^{+27}_{-38}	/	/	45
6172.647	-13^{+5}_{-3}	-12^{+3}_{-4}	47^{+4}_{-3}	41
6172.665	70^{+15}_{-12}	-22^{+7}_{-4}	69^{+4}_{-3}	42
6172.682	-4^{+24}_{-18}	-33^{+7}_{-5}	48^{+4}_{-3}	31
6172.740	-40^{+1}_{-1}	-42^{+4}_{-4}	39^{+6}_{-7}	37
6172.765	-120^{+1}_{-1}	-20^{+1}_{-1}	91^{+1}_{-1}	30
6172.778	-46^{+31}_{-22}	-4^{+3}_{-3}	55^{+4}_{-2}	42
6173.680	54^{+6}_{-5}	-31^{+2}_{-1}	36^{+4}_{-8}	28
6173.691	18^{+2}_{-1}	-36^{+3}_{-2}	-55^{+3}_{-3}	21
6173.706	162^{+0}_{-0}	-69^{+1}_{-1}	20^{+2}_{-2}	31
6173.725	39^{+9}_{-9}	-40^{+4}_{-3}	72^{+4}_{-3}	40
6173.820	46^{+1}_{-1}	-14^{+7}_{-5}	34^{+3}_{-3}	41
6173.831	37^{+7}_{-7}	-29^{+3}_{-3}	61^{+8}_{-9}	46
6173.845	84^{+10}_{-7}	-34^{+4}_{-3}	76^{+2}_{-3}	54
Mean	45^{+11}_{-9}	-26^{+4}_{-4}	65^{+5}_{-5}	41

Chapter 4

Conclusions

Massive stars have extraordinary characteristics: their mass, higher than 10 $M_{\odot}$, their luminosity, of the order of 10^6 $L_{\odot}$, their stellar wind that can reach a terminal velocity of 3000 km s^{-1}, and their mass-loss rate of $\sim$ 10^{-6} $M_{\odot}$yr^{-1}. Although they are rare, massive stars have a huge impact on their surroundings: their UV emission can ionize the interstellar medium, they can trigger the formation of new stars, and they enhance the metallicity of the galaxies through their wind and also when they explode as a supernova. Another characteristic seems to be their proclivity to lie in a binary (or multiple) system. Even though some assumptions exist the deeper reason is still a mystery. Understanding the exceptional objects that are massive stars is thus very important and, in fact, quite challenging.

We have started this thesis by a description of massive binary systems: their orbits, their gravitation potential (the Roche potential), and the darkening and radiative effects that affect these systems. The Roche potential is used to compute the shape of the stars in circular binary systems. In eccentric binaries, this potential is unfortunately not sufficient and we need to use more complex models such the one developed in the TIDES code (Moreno & Koenigsberger 1999 and Moreno et al. 2011). The important radiation pressure of massive stars can also modify this potential. We have shown how to combine the Drechsel et al. (1995) and Howarth (1997) approaches to better treat the potential modification. We have also underlined the importance of the (limb and gravity) darkening effects and of the reflection effects in the computation of the temperature distribution. We have then discussed the contribution of spectroscopy to stellar astrophysics and what we can learn from a spectrum. For examples: the effective temperature, the surface gravity, the chemical composition, and the equatorial rotational velocity. We have also described four problems linked to binarity that affect the study of massive binaries: the luminosity class determination, the Struve-Sahade

effect, the temperature distribution, and the line profile variations. Finally, we have explained in a few words, other techniques used in stellar astrophysics: photometry, astrometry, Doppler tomography, and polarimetry.

The second chapter was dedicated to the code we have developed: CoMBiSpeC. The study of spectra of massive binary systems is crucial to better understand these objects. One way to improve our knowledge is spectral modelling: for this purpose, we have developed CoMBiSpeC, the code of massive binary spectral computation. The principle of this code is rather simple: for binaries with circular orbits, we start by computing the shape of the stars with the Roche potential, modified, if necessary, by radiation pressure. The surface of the stars is described as a peculiar equipotential of the Roche potential. Then, we compute the gravity distribution which is given by the gradient of the Roche potential. Finally, the temperature distribution is computed according to the gravity darkening law and accounting for reflection effects. For binaries with eccentric orbits, the shape computation is performed with the TIDES code that accounts for centrifugal and Coriolis forces, gas pressure, viscous effects, and the gravitational potential of both stars. Again, the temperature distribution is computed according to the gravity darkening law and accounting for reflection effects. Once the shapes of the stars are established, the spectral computation consists in computing a local spectrum from a spectral grid for each surface point. The local grid has been computed from the OSTAR2002 and BSTAR2006 databases built with TLUSTY (Lanz & Hubeny 2003; 2007) and the local spectrum is obtained by interpolation of the four nearest spectra in the grid. The local spectrum depends on the local properties ($T_{\rm eff}$, $\log g$). Then, the spectra are Doppler shifted according to the radial velocity of the surface point and multiplied by the area of the element projected along the line of sight towards the observer, and by a limb-darkening coefficient. Finally, the local contributions are summed up to obtain the total spectrum. These operations are repeated for several orbital phases.

Our spectral modelling of massive binary systems with CoMBiSpeC has allowed to highlight new explanations for the four previously mentioned problems linked to binarity.

Luminosity classification. We have shown that classical luminosity classification criteria based on a limited number of gravity-sensitive spectral lines, are not well suited for the stars in binary systems even when the individual spectra of each component are studied separately. This is due to the gravity and temperature distributions over the stellar surface that are not uniform. Therefore, the comparison of the individual spectra (obtained by

disentangling for example) to a reference atlas seems to be the best way to assign proper luminosity classes.

Temperature distribution effect. The non-uniform temperature distribution over the stellar surfaces was shown to produce different RV semi-amplitudes for the He I and He II lines as observed in some systems. Indeed, "high-temperature" regions, where He II lines are formed, are located in low RV semi-amplitude regions closer to the centre of mass of the binary. "Low-temperature" regions, where He I lines are formed, are located in high RV regions. Therefore, an RV semi-amplitude difference is observed since the RV semi-amplitude of He II lines is smaller than the one of the He I lines. This observed effect can be reproduced by CoMBiSpeC provided that radiation pressure is accounted for.

Struve-Sahade effect. This effect is the apparent variation of the line strengths of either of the binary components as a function of the orbital phase. The results of our code show that this effect comes from the equivalent width measurement method rather than reflecting a genuine physical process. The use of de-blending routines that fit two Gaussian or Lorentzian profiles to intrinsic asymmetric line profiles leads to an incorrect measurement of the equivalent widths of the lines that mimics the Struve-Sahade effect. The asymmetry of the lines is due to several factors including the non-uniform temperature and gravity distribution.

Line profile variations. CoMBiSpeC coupled to the TIDES code have highlighted a new origin for line profile variations that appear in massive binary systems: the tidal interactions. These interactions induce oscillations at the stellar surface known as tidal flows. The oscillations move surface elements to higher or lower RVs with respect to the non-perturbed surface. This is translated in the spectrum by red or blue intensity excesses in the lines. These red and blue excesses move across the lines during the orbital cycle producing migrating bumps and therefore line profile variations.

In the last point of chapter 2, we considered possible future developments of CoMBiSpeC. The improvements of the grid of spectra, notably extending it to non-solar metallicity, and to the case of expanding atmosphere, as well as expressing the spectra in terms of specific intensities are probably the most important ones. A more sophisticated treatment of the reflection effects and the extension to over-contact binary systems could also be implemented.

In the third chapter, we have presented four observational analyses. In the first study, we analysed the LZ Cep system with CoMBiSpeC. It is the first time

that our code was used to better determine the physical parameters of stars and refine the solution obtained by classical tools.
The second observational study presented in this thesis concerned Spica. The spectra of Spica present line profile variations that were previously attributed to β Cephei-type pulsation. The TIDES + CoMBiSpeC model has allowed to reproduce the line profile variations and showed that the origin of these variations is the tidal interaction. Thanks to our model, we have also refined the polar temperatures and radii for the two components.
Plaskett's star (HD 47129) was the object of our third study. This very massive O-star binary in a post Roche-lobe overflow stage displays line profile variations and photometric variations. An in-depth Fourier analysis of several lines of the spectra of the Plaskett's star helped us to characterize and to determine the origin of the line profile variations. We have shown that the main frequencies are probably linked to the rotational period of the secondary star. Again, we have computed a TIDES + CoMBiSpeC model that has shown that line profile variations of the same order of magnitude as those observed could be reproduced. This provided a new explanation on the origin of the variations which could be again the tidal interactions.
The last system studied was WR 138. Our analyses of the optical and X-ray spectra have shown that this system is a long-period ($P \equiv 1521$ d) eccentric WN5-6+OB system rather than a triple system with a compact object as previously claimed by Lamontagne et al. (1982). This system also displays emission-line profile variations, however they are probably due to clumps inside the wind of the WR star of the system. Unfortunately, CoMBiSpeC does not allow modelling WR stars because the wind has a very important impact on the spectra of such stars and cannot be neglected.

In this thesis, we have presented a first step in the spectral modelling of massive binary systems. We have worked on models inspired by real systems to demonstrate that this simple code can reproduce several observed phenomena. Then, we have used our code to study three systems and confront the model to the observations. The aim of CoMBiSpeC is not to replace classical tools but to be a complementary tool that helps to better understand massive binary systems. The code has now to be used to model other systems to continue to fulfil its objectives. Of course, the code can still be improved and further developed. The eventual goal would be the resolution of the 3D radiative transfer equations.

Massive stars, and massive binary systems in particular, are really important objects for the galaxies. We often read that they are the engines of the galaxies. This is certainly true, but they are also the birthplace of elements such as carbon, nitrogen and oxygen that are the building blocks of life. The next starry night you watch the sky, remember that this show is partly due to the massive stars.

Appendix A

Publications as co-author and proceedings

A.1 HD 93521

HD 93521 is known to be a rapid rotator. Its surface is therefore flattened and gravity darkening is present. In this context, we have developed a simplified version of CoMBiSpeC that computes the spectrum of a single star in rapid rotation. In this case, the surface of the star in hydrostatic equilibrium is an equipotential of

$$\Psi = \frac{GM}{r} + \frac{1}{2}\Omega^2 r^2 \sin^2\theta, \tag{A.1}$$

with $r = \sqrt{x^2 + y^2 + z^2}$, $\Omega = \frac{v_e}{R_e}$, v_e is the equatorial rotational velocity and R_e the equatorial radius and $\theta \in [0, \pi]$ is the colatitude angle. Because of axial symmetry there is no dependence in longitude, φ. The surface gravity is the gradient of this potential

$$\underline{\nabla}\Psi = \begin{pmatrix} \partial_r\Psi \\ \partial_\theta\Psi \\ \partial_\varphi\Psi \end{pmatrix} = \begin{pmatrix} -\frac{GM}{r^2} + \Omega^2 r \sin^2\theta \\ \Omega^2 r^2 \sin\theta\cos\theta \\ 0 \end{pmatrix}, \tag{A.2}$$

Two quantities are also interesting in rapid rotators: the equatorial radius, R_e and the critical angular velocity, Ω_c above which the star is tidally disrupted.

$$\Psi(R_e) = \frac{GM}{R_e} + \frac{1}{2}{v_e}^2 = \Psi_0 \tag{A.3}$$

with $\Psi_0 = \dfrac{GM}{R_p}$ and therefore, $R_e = \dfrac{-GM}{\frac{{v_e}^2}{2} - \Psi_0}$.

Ω_c implies that $\partial_r \Psi = 0$. Therefore, we have

$$\begin{aligned} -\frac{GM}{r^2} + \Omega^2 r \sin^2\theta &= 0 \\ \Omega^2 r^3 \sin^2\theta &= GM \end{aligned} , \tag{A.4}$$

The disruption occurs at the equator ($\theta = \pi/2$, $r = R_e$), hence $\Omega_c = \sqrt{\dfrac{GM}{{R_e}^3}}$ and the corresponding linear velocity is: $v_{e,c} = \sqrt{\dfrac{GM}{R_e}}$.

The temperature computation only includes gravity darkening treated with the classical von Zeipel theorem. The spectral computation is done in the same way as in the case of binary systems. This code has been used to study the abundances of HD 93521 and the results are presented in Rauw et al. (2012) (see below).

A.2 λ Cep

The last paper (Uuh-Sonda et al. 2014, see below) concerns the O6 Ief star λ Cep which displays line profile variations in its spectrum and for which we have performed an observational campaign in 2011.

A.3 Proceedings

We give a summary of our research in the proceedings (Palate 2013) of the conference: "Setting a new standard in the analysis of binary stars" held in Leuven (Belgium) in September 2013.

A&A 546, A77 (2012)
DOI: 10.1051/0004-6361/201219865

Astronomy & Astrophysics

The nature of the high Galactic latitude O-star HD 93521: new results from X-ray and optical spectroscopy⋆,⋆⋆

G. Rauw⋆⋆⋆, T. Morel, and M. Palate

Groupe d'Astrophysique des Hautes Énergies, Institut d'Astrophysique et de Géophysique, Université de Liège, Allée du 6 Août, Bât. B5c, 4000 Liège, Belgium
e-mail: rauw@astro.ulg.ac.be

Received 22 June 2012 / Accepted 4 September 2012

ABSTRACT

Context. Owing to its unusual location and its isolation, the nature of the high Galactic latitude O9.5 Vp object HD 93521 is still uncertain.
Aims. We have collected X-ray and optical observations to characterize the star and its surroundings.
Methods. X-ray images and spectra are analysed to search for traces of a recent star formation event around HD 93521 and to search for the signature of a possible compact companion. Optical echelle spectra are analysed with plane-parallel model atmosphere codes, assuming either a spherical star or a gravity darkened rotationally flattened star, to infer the effective temperature and surface gravity, and to derive the He, C, N and O abundances of HD 93521.
Results. The X-ray images reveal no traces of a population of young low-mass stars coeval with HD 93521. The X-ray spectrum of HD 93521 is consistent with a normal late O-type star although with subsolar metallicity. No trace of a compact companion is found in the X-ray data. In the optical spectrum, He and N are found to be overabundant, in line with the effect of rotational mixing in this very fast rotator, whilst C and O are subsolar. A critical comparison with the properties of subdwarf OB stars, indicates that, despite some apparent similarities, HD 93521 does not belong to this category.
Conclusions. Despite some ambiguities on the runaway status of the star, the most likely explanation is that HD 93521 is a Population I massive O-type star that was ejected from the Galactic plane either through dynamical interactions or a result of a supernova event in a binary system.

Key words. stars: early-type – stars: fundamental parameters – stars: abundances – stars: massive – stars: individual: HD 93521 – X-rays: stars

1. Introduction

O-type stars, the hottest and most massive main-sequence stars of Population I, are seldom found in isolation. They are preferentially found in open clusters and OB associations, which are therefore most likely to be their birth places (e.g. de Wit et al. 2005). The few O-type stars that are not directly located inside a cluster or association are usually runaways and are hence believed to have been ejected from their parent cluster either by the kick of a supernova explosion in a binary system or as a result of dynamical interactions in a dense cluster core.

The high Galactic latitude O-type star HD 93521 (l_{II} = 183.14°, b_{II} = 62.15°), located very far away from any known site of recent star formation, challenges this general picture. While the optical spectrum of HD 93521 leads to an O9.5 Vp classification, the nature of this star has been subject to debate over many years (see e.g. Ebbets & Savage 1982; Irvine 1989; Howarth & Smith 2001) and the case is still not settled.

HD 93521 has one of the largest rotational velocities known among Galactic O-stars (390 km s^{-1}, Rauw et al. 2008). The stellar wind has an apparently low terminal velocity and is likely heavily distorted into a Be-like decretion disk wind (Howarth & Reid 1993; Bjorkman et al. 1994; Massa 1995). In the optical domain, the wind produces emission features in the wings of the Hα line, although they are far less prominent than in genuine Oe stars. In addition, HD 93521 displays bi-periodic (1.75 and 2.89 h) absorption line profile variability that is commonly interpreted as the signature of two non-radial pulsation (NRP) modes with $l \approx 8 \pm 1$ and $l \approx 4 \pm 1$ (see Rauw et al. 2008, and references therein). An alternative explanation for the optical line profile variations, that cannot totally be ruled out a priori, would be the effect of a compact companion (formed in the supernova explosion that ejected the system from the Galactic plane) orbiting the O-star and accreting material from its rotationally flattened wind. Indeed, in the case of Be/X-ray binaries, the decretion disk can be truncated by resonance with the orbit of the neutron star companion (Okazaki & Negueruela 2001) and higher order resonance could possibly trigger periodic density waves in the disk that would contaminate the photospheric absoption lines via variable residual emission.

To help clarify the nature of HD 93521, we have collected new optical and, for the first time, X-ray observations. Our observations are presented in Sect. 2. Section 3 is devoted to the study of the surroundings of HD 93521 as seen in our X-ray images.

⋆ Based on observations collected at the Observatoire de Haute Provence (France) and with *XMM-Newton*, an ESA science mission with instruments and contributions directly funded by ESA member states and the USA (NASA).
⋆⋆ Hα images are only available at the CDS via anonymous ftp to cdsarc.u-strasbg.fr (130.79.128.5) or via http://cdsarc.u-strasbg.fr/viz-bin/qcat?J/A+A/546/A77
⋆⋆⋆ Honorary Research Associate FRS-FNRS (Belgium).

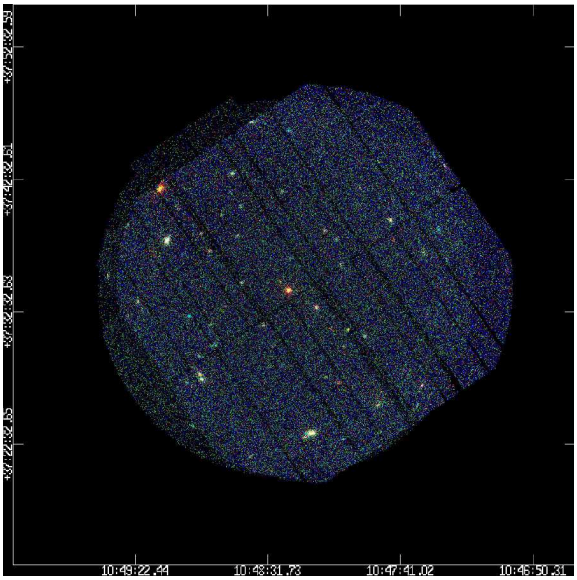

Fig. 1. Energy-coded three-colour image built from our *XMM-Newton* observation of HD 93521 (the reddish source near the centre of the image). The red, green and blue colours correspond to the soft, medium and hard energy bands used throughout this paper (see text). The individual EPIC images were exposure corrected before they were combined. A colour version of the figure can be found in the electronic version of the journal.

The X-ray spectrum of HD 93521 is analysed in Sect. 4, whilst the optical spectra are studied in Sect. 5 using plane-parallel atmosphere models assuming either spherical or rotationally flattened geometries for the star. The results are discussed in Sect. 6 and Sect. 7 presents our conclusions.

2. Observations

2.1. X-ray data

A 40 ks X-ray observation was obtained on 2–3 November 2009 with the *XMM-Newton* satellite (Jansen et al. 2001). To reject optical and UV photons, the EPIC cameras (Turner et al. 2001; Strüder et al. 2001) were used with the thick filter.

The raw data were processed with the SAS software version 10.0. The end of the observation was affected by the raise of a background flare. We discarded this part of the observation, ending up with an effective exposure time of 38 ks for EPIC-MOS1, 37 ks for EPIC-MOS2 and 30 ks for EPIC-pn. Images were built over soft (0.5–1.0 keV), medium (1.0–2.0 keV) and hard (2.0–8.0 keV) energy bands with a pixel size of $2.5'' \times 2.5''$. These images were exposure corrected and combined into an energy-coded three-colour image of the field of view (Fig. 1).

2.2. Optical spectroscopy

A series of twenty four optical spectra were obtained over four nights in April–May 2004 with the ELODIE échelle spectrograph (Baranne et al. 1996) at the 1.93 m telescope at Observatoire de Haute Provence (OHP). ELODIE was an échelle spectrograph with a resolving power of $R \approx 42\,000$ over the 3850–6800 Å wavelength domain. Our initial intention was to use these data for our study of the line profile variability (Rauw et al. 2008). However, due to the very poor weather conditions during this run, individual spectra lacked a sufficient signal-to-noise ratio (S/N) and we thus decided to combine all the spectra into a single high-quality spectrum. This average spectrum, with a S/N of 390 at 5500 Å, was obtained from data collected at many different phases of the line profile variation cycles and should hence be relatively free of any signatures of the latter.

Another échelle spectrum was obtained in November 2010 with the SOPHIE spectrograph (Perruchot et al. 2008) also at the 1.93 m telescope at OHP. SOPHIE covers the wavelength domain from 3870 to 6940 Å. The spectrum was reduced with IRAF. This spectrum is of higher resolution than the ELODIE ones with a resolving power, $R \approx 74\,000$, as measured from calibration lamps. The S/N of this spectrum is ≈310 at 5500 Å.

2.3. Hα imaging

Since there are apparently no Hα images available for the region around HD 93521, we collected some images with the help of two amateur astronomers, Gaston Dessy and Joël Bavais. For this purpose, Dessy used a TMB-92 9.2 cm refractor with a focal length of 40.8 cm equipped with an Atik 16IC CCD (659 × 494 pixels), and for a second run with an Atik 4000M CCD (2048 × 2048 pixels). Both CCDs have pixel sizes of 7.4 × 7.4 μm^2, corresponding to $3.7'' \times 3.7''$ on the sky. Bavais used a SkyWatcher 80/600 ED refractor equipped with an Atik 314L CCD (1392 × 1040 pixels of 6.45 × 6.45 μm^2 corresponding to $2.2'' \times 2.2''$ on the sky). In all cases, commercial Hα (70 Å bandwidth) and V-band filters manufactured by Baader Planetarium were used. For each set-up, integration times were 1 h in Hα (split into 12 exposures of 5 min each) and 15 min in V (split into 5 exposures of 3 min each, except for the last run where no V-band images were taken). All data were processed with the MIDAS software developed at ESO. The surface brightness of the sky measured on our images amounts to about 17.8 mag arcsec^{-2} in V. After subtracting a flat sky background, the residual 1-σ fluctuations in the V band images correspond to a surface brightness around 22.0 mag arcsec^{-2}. The Hα images are about 1.5 mag shallower than the V-band data. No trace of a nebular emission was found on the images before or after sky subtraction.

3. The surroundings of HD 93521

The position of HD 93521 far away from the Galactic plane and from any open cluster naturally raises the question of the origin of this star. There are currently only a few known examples of massive stars that have likely formed in isolation. For instance, de Wit et al. (2005) conclude that $4 \pm 2\%$ of the Galactic O-stars could have formed outside clusters[1].

Models for massive star formation based on the competitive accretion scenario imply that a high-mass star must be associated

[1] In the same context, Bressert et al. (2012) recently identified a sample of massive stars, earlier than spectral type O7, within a projected distance of 125 pc around the 30 Dor complex, that are not associated with any cluster and are thus candidates for massive stars formed in isolation. It has to be stressed though that the case of HD 93521 requires a far more extreme form of isolation than considered by Bressert et al. (2012).

Table 1. Spectral properties of the brightest X-ray sources other than HD 93521.

Source	Model	$N_{\rm H}$ (10^{22} cm^{-2})	kT (keV)	Γ	$f_{\rm X}$ (0.5–10 keV) (erg cm^{-2} s^{-1})	$f_{\rm X}^{\rm unabs}$ (0.5–10 keV) (erg cm^{-2} s^{-1})	χ^2_ν	d.o.f.
BD+38° 2183	wabs*apec	<0.020	$0.56^{+.05}_{-.07}$	–	1.11×10^{-13}	1.11×10^{-13}	0.90	11
BZQ J1049+3737	wabs*power	$0.024^{+.020}_{-.016}$	–	$1.67^{+.10}_{-.11}$	2.12×10^{-13}	2.18×10^{-13}	1.05	65
source 4	wabs*power	$0.045^{+.018}_{-.015}$	–	$2.02^{+.13}_{-.12}$	2.27×10^{-13}	2.43×10^{-13}	1.54	73

with a population of low-mass stars (Bonnell et al. 2004)[2]. Core accretion models of massive stars on the contrary allow rather isolated O-stars to form (Krumholz et al. 2009). Isolated O-type stars that are still in their formation region are surrounded by residual gas that can be seen through Hα observations (Lamb et al. 2010; Selier et al. 2011) and some of them are found in sparse clusters with less than ten lower-mass companions (Lamb et al. 2010). Monte Carlo simulations by Lamb et al. (2010) indicate that the existence of such sparse clusters is more in favour of the core accretion models and suggest that "clusters are built stochastically by randomly sampling stars from a universal initial mass function (IMF)".

X-ray observations can help us uncover low-mass, optically dim members of very young open clusters. Indeed, X-ray images of massive stars in dense open clusters usually reveal a rather rich population of X-ray bright, low-mass pre-main sequence stars (e.g. Damiani et al. 2006; Sana et al. 2007). This statement also holds to some extent for rather scarce open clusters such as NGC 6383 (Rauw et al. 2003) and to less densely populated OB associations (e.g. Rauw 2011). The brightness of very young low-mass stars in the X-ray domain makes this the ideal energy range to distinguish between foreground or background field stars and genuine cluster members coeval with the massive stars. This technique was successfully applied to reveal the population of low-mass pre-main sequence (PMS) stars associated with two rather isolated B0 stars in the diffuse H II regions S 255 and S 257 (Mucciarelli et al. 2011).

By analogy with the two B0 stars investigated by Mucciarelli et al. (2011), one expects about 300 low-mass pre-main sequence stars associated with HD 93521 if this stellar population follows a standard IMF[3]. We can now estimate what fraction of these low-mass objects would be detected with our X-ray observation and compare this to the actual number of sources in the field of view.

The three-colour image of the field of view around HD 93521 (Fig. 1) does not reveal any obvious concentration of X-ray sources around HD 93521. Applying the SAS source detection routines with a significance threshold[4] of 10 yields a total of 55 sources. After visual inspection, 10 sources were removed from the list because their detection was affected by gaps between CCDs or because they were at the edge of the field of view. Two more faint sources that were apparently missed by the detection algorithm were added to our final list of 47 X-ray sources. Assuming an optically thin thermal plasma model with a typical temperature of 1 keV, our detection limit corresponds to an observed flux of about 3×10^{-15} erg cm^{-2} s^{-1}. At an adopted distance of HD 93521 of 1.2 kpc (see below), this flux would correspond to an X-ray luminosity of 5×10^{29} erg s^{-1}. If we compare this number with the cumulative X-ray luminosity functions of the Orion Nebular Cluster (Preibisch & Feigelson 2005), we estimate that we should detect about 90, 85 and 50% of the PMS stars in the mass ranges 0.9–1.2, 0.5–0.9 and 0.1–0.5 $M_\odot$ respectively. Therefore, we would expect to observe of order 100–200 X-ray sources in the vicinity of HD 93521. This is clearly not the case here.

To assess the impact of background X-ray sources, we have repeated the detection chain on two different energy bands 0.5–2.0 keV and 2.0–8.0 keV. In the 0.5–2.0 keV band, 42 sources are detected with a limiting flux of order $3–4 \times 10^{-15}$ erg cm^{-2} s^{-1}. From the $\log N - \log S$ relation of Giacconi et al. (2001) derived from the *Chandra* Deep Field South, we would expect about 50 detections of extragalactic point sources in this energy band and with this flux limit. This result implies that the bulk of the detected sources must be extragalactic background objects, unrelated to HD 93521. Very similar conclusions are reached with the results for the 2.0–8.0 keV band. This conclusion is further supported by the fact that only five X-ray sources in our field of view have a 2MASS near-IR counterpart within a correlation radius of 4 arcsec. Out of these five sources, four are among the brightest X-ray sources: HD 93521 itself, the blazar [MGL2009]BZQ J1049+3737 (Massaro et al. 2009), the star BD+38° 2183 (with a SIMBAD spectral type F8), and an unknown source at 10:48:14.9 +37:23:24 (hereafter source 4).

We have analysed the EPIC spectra of the three brightest sources in addition to HD 93521. The results are listed in Table 1. The blazar and the unknown source are best fitted with a power-law model (see Fig. 2), suggesting that the latter is most probably also related to an AGN. The spectrum of the late-type star is well represented by a single temperature optically thin thermal plasma model.

We thus conclude that our *XMM-Newton* data do not reveal any evidence for a lower mass stellar population that could be associated with the formation of the O-type star HD 93521. This is in line with the lack of nebular emission from residual gas in our Hα images (see Sect. 2.3).

4. The EPIC spectrum of HD 93521

HD 93521 is detected as a moderate X-ray source with net count rates of 7.3×10^{-3}, 8.2×10^{-3} and 3.6×10^{-2} cts s^{-1} for EPIC-MOS1, MOS2 and pn, respectively. The EPIC spectra of HD 93521 were analysed using the `xspec` software (version 12.6.0, Arnaud 1996). Unless stated otherwise, the interstellar neutral hydrogen (H I + H_2) column density was set to 1.3×10^{20} cm^{-2} (Bohlin et al. 1978). To account for the possible presence of an additional circumstellar absorption column due to the partially ionized stellar wind, we further included an ionized

[2] Although dynamical interaction could lead the sparsest clusters to disperse rather quickly, on time scales of a few Myr.

[3] This estimate is in line with the relation between the total cluster mass and the mass of its most massive member as proposed by Weidner et al. (2010). Indeed, applying this relation to HD 93521, one would expect a cluster with a total mass in the range 100–150 $M_\odot$.

[4] This implies a probability of $\leq e^{-10}$ that a random Poissonian fluctuation could have caused the observed source counts inside the 5×5 pixel^2 detection cell. Over the entire EPIC field of view, the expected number of spurious detections amounts to about 2% of the total number of detected sources.

Table 2. Spectral fits of HD 93521.

Model	$\log N_{\rm wind}$ ($\rm cm^{-2}$)	kT_1 (keV)	$\rm Norm_1$	kT_2 (keV)	Γ_2	$\rm Norm_2$	Z $Z_\odot$	$f_{\rm X}$ (10^{-14} erg $\rm cm^{-2}$ $\rm s^{-1}$)	$f_{\rm X}^{\rm unabs}$	χ^2_ν (d.o.f.)
[1]	$21.63^{+.08}_{-.09}$	$0.27^{+.01}_{-.01}$	$(0.89^{+0.14}_{-0.14})\,10^{-4}$	$3.01^{+3.51}_{-0.96}$	–	$(0.18^{+.05}_{-0.05})\,10^{-4}$	1 (fixed)	6.20	6.52	1.49 (65)
[2]	$21.54^{+.12}_{-.21}$	$0.28^{+.02}_{-.01}$	$(2.65^{+1.44}_{-0.93})\,10^{-4}$	$2.94^{+7.32}_{-1.14}$	–	$(0.22^{+0.09}_{-0.09})\,10^{-4}$	$0.22^{+.12}_{-.09}$	5.89	6.19	1.34 (64)
[3]	$21.37^{+.18}_{-.23}$	$0.29^{+.03}_{-.02}$	$(1.15^{+0.27}_{-0.29})\,10^{-4}$	$2.96^{+10.05}_{-1.35}$	–	$(0.14^{+.05}_{-0.06})\,10^{-4}$	model	5.57	6.02	1.32 (63)
[4]	$21.26^{+.17}_{-.33}$	$0.30^{+.01}_{-.01}$	$(1.08^{+0.35}_{-0.26})\,10^{-4}$	$4.03^{+63.7}_{-2.30}$	–	$(0.12^{+0.05}_{-0.04})\,10^{-4}$	model	5.72	6.00	1.31 (65)
[5]	$21.54^{+.09}_{-.11}$	$0.28^{+.01}_{-.01}$	$(0.62^{+0.23}_{-0.17})\,10^{-4}$	–	$2.54^{+.29}_{-.36}$	$(0.10^{+.03}_{-.03})\,10^{-4}$	1 (fixed)	5.97	6.27	1.35 (65)
[6]	–	$0.152^{+.008}_{-.006}$	$(8.5^{+0.8}_{-0.7})\,10^{-7}$	–	$1.44^{+.36}_{-.29}$	$(3.0^{+1.8}_{-1.5})\,10^{-6}$	–	6.15	6.41	1.46 (66)

Notes. All fits were performed with the interstellar neutral hydrogen column density set to 1.3×10^{20} $\rm cm^{-2}$. Models [1] and [2] correspond to `wabs*wind*apec(2T)` with solar and free metallicity respectively. Models [3] and [4] correspond to `wabs*wind*vapec(2T)` with the abundances of He, C, N and O set to 2.14, 0.19, 1.51 and 0.30 times solar. In model [3], the abundances of Ne and Fe are free (see text), whilst they are fixed at 0.30 solar in model [4]. Models [5] and [6] correspond to `wabs*wind*(apec+power)` and `wabs*(bbody+power)` respectively. The fluxes are evaluated over the energy range 0.5–10 keV. The normalization of apec models are defined as $\frac{10^{-14}}{4\pi d^2}\int n_{\rm e}\, n_{\rm H}\, {\rm d}V$ where d is the distance in cm, $n_{\rm e}$ and $n_{\rm H}$ are the electron and proton densities and V is the volume of the emitting plasma. The normalization parameters of the power law and black-body component are respectively the number of photons $\rm keV^{-1}$ $\rm cm^{-2}$ $\rm s^{-1}$ at 1 keV and the source luminosity in units 10^{39} erg $\rm s^{-1}$ divided by the square of the distance in units of 10 kpc.

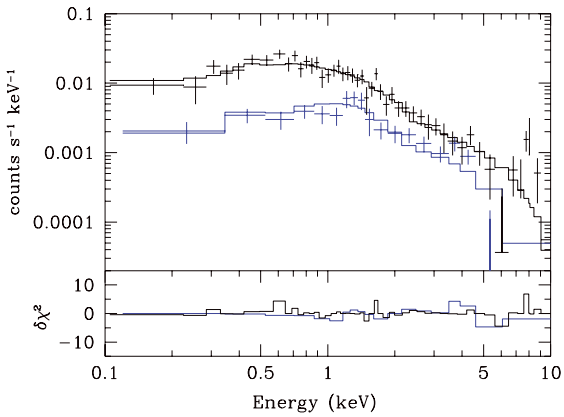

Fig. 2. Best-fit absorbed power-law model (see Table 1) of the X-ray spectrum of the blazar BZQ J1049+3737. The black and blue data points refer to the pn and MOS2 data, respectively. The lower panel shows the contribution of the various energy bins to the χ^2 of the fit times the sign of the difference between the data and the model.

wind absorption model (Nazé et al. 2004) with the wind column density treated as a free parameter.

We have tested a variety of models that are potentially adequate depending on the actual nature of HD 93521.

Medium resolution X-ray spectra of normal O-type stars are usually well fitted with absorbed optically thin thermal plasma models (see e.g. Nazé 2009). A model with a single plasma component does not fit the EPIC spectra of HD 93521 simultaneously at low and high energies. We have therefore tested two-temperature apec models (Smith et al. 2001), either with solar metallicity or with the global metallicity of the plasma taken as a free parameter (see models [1] and [2] in Table 2). In the latter case, the best fit is achieved with a metallicity near 0.22. This fit provides a significant improvement over the solar metallicity solution.

Using the He and CNO abundances derived from our best fit of the optical spectrum (see Sect. 5), we have then tested a two temperature apec model with variable abundances (vapec). The He, C, N and O abundances were fixed at respectively 2.14, 0.19, 1.51 and 0.30 times solar. As a first step, all other elements were taken to have solar abundances. This led to a relatively poor fit with $\chi^2_\nu = 1.52$. Apart from C, N and O, Fe and Ne have strong lines in the X-ray domain covered by our EPIC data. Therefore, we allowed the abundances of these two elements to vary in the fit. This results in an improved fit with Ne and Fe abundances of respectively $0.28^{+.20}_{-.15}$ and $0.43^{+.14}_{.15}$ relative to solar (see Fig. 3 and model [3] in Table 2). Assuming that Ne and Fe have the same abundances as O (i.e. 0.30 solar), which is our best indicator of the metallicity as the O abundance is only little affected by the CNO process, yields an equivalent fit (see model [4] in Table 2).

Whatever the metallicity, we find that the spectrum can be represented by two plasma components of temperatures near 0.3 and 3.0 keV, though the hotter component is poorly constrained (especially towards higher temperatures). We further find that a significant wind absorption is needed to provide a reasonable fit and that the interstellar absorption corrected flux corresponding to thermal plasma models is of order 6.0–6.5 $\times$ 10^{-14} erg $\rm cm^{-2}$ $\rm s^{-1}$. Assuming a distance of 1.2 kpc, this flux corresponds to an X-ray luminosity of 1.0–1.1 $\times$ 10^{31} erg $\rm s^{-1}$, which translates into an $L_{\rm X}/L_{\rm bol}$ ratio of 8.7–9.4 $\times$ 10^{-8}. This number is towards the lower end of, but compatible with, the range of $L_{\rm X}/L_{\rm bol}$ values measured for normal O-type stars with *XMM-Newton* (Nazé 2009).

A plasma component as hot as 3 keV is somewhat surprising for intrinsic X-ray emission by a single ordinary O-type star. This is especially true if the star has indeed a low equatorial wind velocity, of order $v_\infty = 400$ km $\rm s^{-1}$, as derived by Howarth et al. (1997, although the polar wind component is likely much faster, $v_\infty = 2000$ km $\rm s^{-1}$, see Howarth & Reid 1993). Nazé (2009) found that many O-type stars feature a faint hot plasma contribution around 2 keV, but only a few objects have a plasma that is actually as hot as in the case of HD 93521. Over recent years, a new category of intrinsic hard X-ray sources associated with early-type stars was identified, the so-called γ Cas analogs (e.g. Smith et al. 2004; Rakowski et al. 2006). These are late O or early B-type emission-line stars which have X-ray spectra dominated by plasma components with kT up to 12 keV, located rather close to the Be star and its disk. However, unlike HD 93521, these objects are highly overluminous (by a factor $\approx$40, Rakowski et al. 2006) with respect to the typical $L_{\rm X}/L_{\rm bol}$ ratio of OB stars. Therefore, HD 93521 has rather normal X-ray

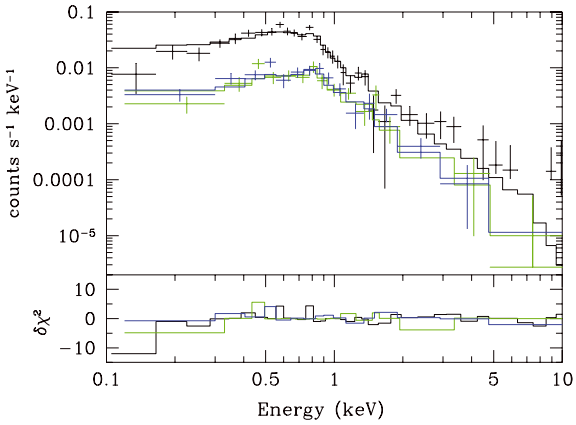

Fig. 3. Same as Fig. 2, but for the best-fit model [3] (see Table 2) of the X-ray spectrum of HD 93521. The black, green and blue data points refer to the pn, MOS1 and MOS2 data respectively.

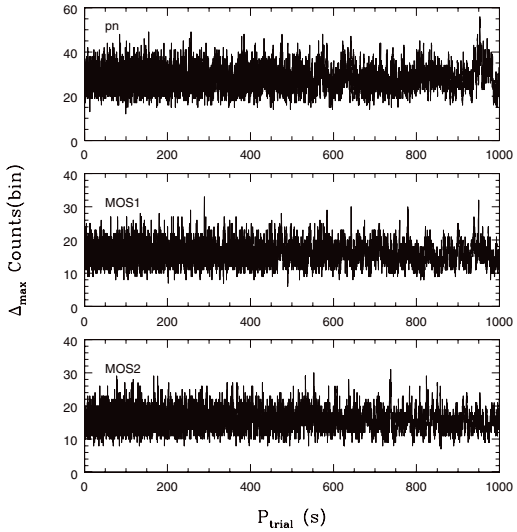

Fig. 4. Maximum difference between the number of X-ray counts recorded per 0.05 phase bin as a function of the trial period. The various panels yield the results for the three EPIC detectors. The total number of counts (source + background) recorded in the source region were 363, 362 and 1143 respectively for the MOS1, MOS2 and pn detectors.

properties for an O-type star, except for the somewhat higher secondary plasma temperature.

As an alternative, we have tested the possibility that the hard emission might be non-thermal. Such a non-thermal emission could arise either from an accretion process in a binary system featuring a compact companion or from inverse Compton scattering of photospheric UV photons, if the wind of HD 93521 contains a population of relativistic electrons. The fit is of similar quality to the best fit purely thermal model (see model [5] in Table 2). The softer emission still requires a thermal plasma component at about 0.3 keV. For this kind of model, we have also attempted to let the metallicity of the apec component vary during the fit. There is no improvement of the fit quality and, apart from the metallicity which goes to $0.29^{+.77}_{-.14}$ $Z_\odot$ and the normalization parameter, there are no changes in the best fit parameters. Finally, we also tested a model with the individual abundances of He, C, N and O set to the values derived from our best fit of the optical spectrum and letting the Ne and Fe abundances vary. Again, there is no improvement of the fit and the abundances of Ne and Fe converge to values very similar to those obtained with model [3].

Finally, we have tested a model consisting of a black-body and a power law. This kind of model was found to adequatly describe the EPIC spectra of the sdO + compact companion system HD 49798 (Tiengo et al. 2004). The results are listed as model [6] in Table 2. If we keep the interstellar column fixed, the best fit is of lower quality than what can be achieved with thermal plasma models. We stress that the best-fit black-body component of HD 93521 would be much hotter (kT = 0.15 vs. 0.034 keV) and the power law significantly steeper (Γ = 1.4 vs. 2.0) than in the case of HD 49798 (Tiengo et al. 2004). A significantly better fit (χ^2_ν = 1.08) could be obtained with the black-body + power law model if the interstellar column density would be treated as a free parameter. However, in this case, the fitted ISM column density would reach 0.14×10^{22} cm^{-2}, i.e. it would exceed the observationally determined column density by a factor 10. Such a large discrepancy seems rather unlikely.

To further test the possibility that HD 93521 could be a binary system hosting a compact companion (either a white dwarf or a neutron star), we have searched the X-ray data for periodicities that could be related to X-ray pulses from the compact companion accreting material from the O9.5 component. For this purpose, we have extracted event lists from the source region of HD 93521 (containing photons from the source and the background[5]) for each of the three EPIC instruments. The arrival times of these photons were corrected into the barycentric frame of reference. We then folded the arrival times of all the photons with a trial period and built a histogram of the resulting arrival phases (adopting phase bins of 0.05). We finally compute the maximum difference between the number of counts in the phase bins of the histogram. The whole process was repeated for 10 000 trial periods between 1.0 and 1000 s[6] and the maximum difference in the number of counts was plotted as a function of the trial period. If there was a periodic signal in the X-ray data of HD 93521, we would expect a peak in this diagram. No such peak is found in our data (see Fig. 4) and we thus conclude that the X-ray emission of HD 93521 does not contain any signature of short-period pulsations that could hint at the presence of an accreting compact companion.

5. Analysis of the optical spectrum

5.1. Previous work

The optical spectrum of HD 93521 has been investigated previously with model atmosphere codes. The most sophisticated approach so far, was the work of Howarth & Smith (2001). These authors used non-LTE, hydrostatic, plane-parallel H/He model atmospheres to analyse the spectrum of HD 93521, accounting for the variation of the local gravity (and hence temperature) as a function of stellar latitude at the surface of a rotationally distorted star. Howarth & Smith (2001) assumed an inclination of 90° and their best-fit model yielded $T^{\rm p}_{\rm eff}$ = 38 000 ± 1500 K,

[5] The source accounts for roughly 70% of the photons, the remainder are due to the background.

[6] In the full frame modes used in our observation, the pn and MOS detectors have a time resolution of 0.0734 and 2.6 s respectively.

Table 3. Atmospheric parameters and metal abundances (on the scale in which log ϵ[H] = 12) for the reference stars and for HD 93521.

	$T_{\rm eff}$ [K]	log g	y	log ϵ(C) [4060–4082 Å]	log ϵ(N) [4995–5011 Å]	log ϵ(O) [4060–4082 Å]	log ϵ(O) [4691–4709 Å]	[N/C]	[N/O]
10 Lac	**34 000**	**4.15**	**0.097**	**8.31**	**7.55**	**8.39**	**8.39**	**–0.76**	**–0.84**
	34 254	4.20	0.079	8.22	7.44	8.34	8.28	–0.78	–0.87
$v \sin i$ = 390 km s^{-1}	33 975	4.27	0.075	8.30	7.52	8.42	8.34	–0.78	–0.86
τ Sco	**31 500**	**4.05**	**0.085**	**8.19**	**8.15**	**8.62**	**8.62**	**–0.04**	**–0.47**
	31 088	4.15	0.101	8.18	7.92	8.48	8.48	–0.26	–0.56
$v \sin i$ = 390 km s^{-1}	30 983	4.18	0.096	8.42	8.08	8.74	8.64	–0.34	–0.61
HD 57682	**33 000**	**4.00**	**0.096**	**8.20**	**7.52**	**8.31**	**8.31**	**–0.68**	**–0.79**
	33 958	4.17	0.096	8.14	7.58	8.34	8.36	–0.56	–0.77
$v \sin i$ = 390 km s^{-1}	31 814	3.97	0.079	8.04	7.52	8.54	8.38	–0.52	–0.94
HD 93521, sph. symm.									
SOPHIE	30 944	3.72	0.182	7.70	8.00	8.20	8.16	+0.30	–0.18
ELODIE	30 892	3.62	0.174	7.42	7.94	8.28	8.32	+0.52	–0.36
Mean	30 918	3.67	0.178	7.56	7.97	8.24	8.24	+0.41	–0.27
HD 93521, non sph.									
SOPHIE				7.74	8.03	8.22	8.22	+0.29	–0.19
ELODIE				7.49	7.97	8.32	8.34	+0.48	–0.36
Mean				7.62	8.00	8.27	8.28	+0.38	–0.27

Notes. The reference values based on classical methods are shown in boldface. For the standard stars, the second line yields the results of our analysis of the actual spectra of these stars using the same approach as for HD 93521, whilst the third line gives the corresponding results for the spectra degraded to the $v \sin i$ of HD 93521. The solar [N/C] and [N/O] abundance ratios are –0.60 and –0.86, respectively (Asplund et al. 2009).

$T_{\rm eff}^{\rm e}$ = 33 500 K, log $g^{\rm p}$ = 3.9±0.1 and log $g^{\rm e}$ = 3.5 (in cgs units), a helium abundance by number of y = 0.18 ± 0.03 and a star rotating at 90% of its critical velocity. Here the "p" and "e" superscripts refer to the parameters respectively at the poles and at the equator of the star.

5.2. 1D model atmospheres

In this section we first analyse the spectrum assuming a spherically symmetric star to derive stellar parameters as well as abundances of He, C, N and O. These results are used in Sect. 5.3 as starting points for a model where we account for the effects of gravity darkening on a rotationally flattened star.

5.2.1. Atmospheric parameters and helium abundance

The atmospheric parameters ($T_{\rm eff}$ and log g) and helium abundance by number, $y = \mathcal{N}$(He)/[$\mathcal{N}$(H)+$\mathcal{N}$(He)], have been estimated by finding the best match between a set of observed H and He line profiles and a grid of rotationally-broadened, synthetic profiles computed using the non-LTE line-formation code DETAIL/SURFACE coupled with LTE Kurucz models (Butler & Giddings 1985; Giddings 1981)[7]. Such a hybrid approach (LTE atmospheric models, but a full non-LTE treatment for the line formation) has been shown to be adequate for late O and early B-type stars on the main sequence (Nieva & Przybilla 2007; Przybilla et al. 2011).

The analysis has been independently carried out on the SOPHIE and mean ELODIE spectrum. The results are listed separately in the following but, as only relatively small differences are found, the values eventually adopted will be the averaged ones. A SOPHIE spectrum of the narrow-lined O9 V star 10 Lac was continuum normalised and broadened to $v \sin i$ = 390 km s^{-1}, as found for HD 93521 based on Fourier techniques (Rauw et al. 2008). The continuum regions were subsequently defined and used to normalise the two spectra of HD 93521.

A set of unblended helium features (6 He I and 3 He II lines)[8] was chosen after an inspection of a spectral atlas and the 10 Lac spectrum which was taken as reference. Three narrow-lined stars were analysed to validate the procedures used to derive the atmospheric parameters and abundances: 10 Lac (O9 V; $v \sin i$ = 25 km s^{-1}), τ Sco (B0.2 V; $v \sin i$ = 8 km s^{-1}) and HD 57682 (O9 IV; $v \sin i$ = 25 km s^{-1}). Such a differential approach is expected to minimise the systematic errors (see, e.g., Vrancken et al. 1997). These stars have their parameters and abundances derived using the same codes from classical techniques whereby $T_{\rm eff}$ is based on the ionisation balance of various elements (namely He, C, N and Si), log g on the fit of the wings of the Balmer lines and the abundances on curve-of-growth techniques (10 Lac: this study; τ Sco: Hubrig et al. 2008; HD 57682: Morel 2011). The H and He features used may be contaminated by some weak metallic lines. The synthetic spectra were computed taking these lines into account and using the abundances derived from the curve-of-growth analysis. Some portions of the line profiles encompassing metal lines not modelled by DETAIL/SURFACE were masked out. For HD 93521, the same metal abundances and microturbulence (ξ = 10 km s^{-1}) as for 10 Lac were adopted. Model atmospheres with a helium abundance twice solar were used for HD 93521 in accordance with the high abundance found (see below).

An iterative scheme was used to estimate $T_{\rm eff}$, log g and y. The temperature is taken as the value providing the best fit to the He I and He II features with the same weight given to these two ions. The gravity is determined by fitting the wings of the Balmer lines and y by fitting the He I features. This procedure was repeated until the gravity used to fit the helium lines was identical to the value yielded by the Balmer lines, and proved for the narrow-lined stars to provide the best match to the reference values obtained using classical methods. As already noted for HD 93521 (Howarth & Smith 2001), the fit was

[7] The spectra were convolved using the ROTIN3 programme in the SYNSPEC suite of routines (see http://nova.astro.umd.edu/Synspec43/synspec.html).

[8] The relevant lines are He I $\lambda\lambda$ 4026, 4388, 4471, 4713, 4922, 5016 and He II 4542, 4686, 5412.

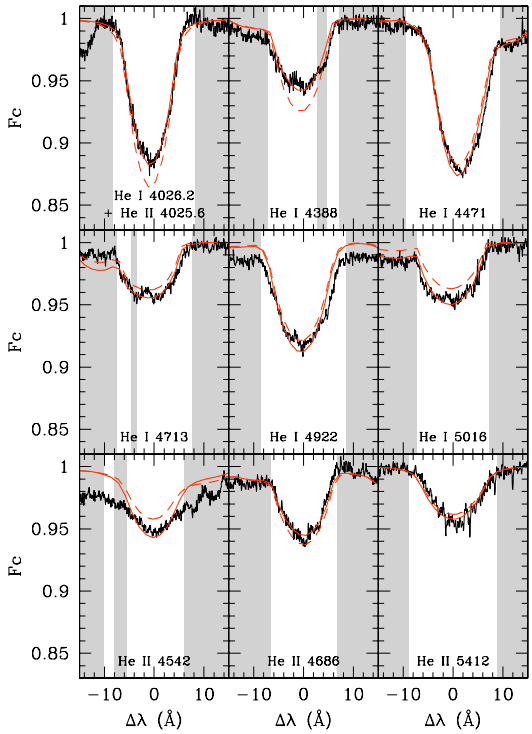

Fig. 5. Comparison for HD 93521 between the SOPHIE (black) and best-fitting He synthetic line profiles (solid red). The dashed, red lines show the line profiles computed for the final parameters derived from the analysis of the SOPHIE spectrum (Table 3). The light grey-shaded areas delineate the regions where the quality of the fit has been evaluated.

much better for Hϵ than for the other Balmer lines. However, the gravity estimated from Hϵ was indistinguishable from the mean value computed taking all lines into account. This analysis has also been repeated after convolving the observed spectra of the reference stars with a rotational broadening function with $v \sin i = 390$ km s^{-1}. The results are shown in Table 3. For the three standard stars, the mean differences between the reference values and the results obtained through the synthesis are: $\Delta T_{\rm eff} = +155 \pm 733$ K, $\Delta \log g = -0.09 \pm 0.07$ dex and $\Delta y = +0.005 \pm 0.016$. We finally obtain the following parameters for HD 93521 assuming a spherical star: $T_{\rm eff} = 30\,900 \pm 700$ K, $\log g = 3.67 \pm 0.12$ dex and $y = 0.18 \pm 0.02$ (statistical errors estimated based on the differences for the three standard stars between the parameters found and the reference ones, as well as the values derived for HD 93521 using the two spectra). These results confirm the helium enrichment found by Lennon et al. (1991; $y = 0.20 \pm 0.05$) and Howarth & Smith (2001; $y = 0.18 \pm 0.03$). A comparison for HD 93521 between the observed and best-fitting He synthetic line profiles is shown in Fig. 5. No significant differences are found between the temperature and helium abundance yielded by the He I singlet and triplet transitions (see Najarro et al. 2006).

5.2.2. Metal abundances

This is the first time that the metal abundances are derived for this star. Determining its chemical composition could help establishing its birth place, as significantly subsolar abundances are expected if it was formed in situ far from the Galactic plane.

The high rotational velocity of HD 93521 makes a selection of useful metallic features excessively difficult. As done for the hydrogen and helium lines, a number of spectral domains were carefully chosen and selected on the basis that: (1) at most two species should significantly contribute to the blend; (2) all the lines with a significant strength should be theoretically modelled; (3) all the elemental abundances derived for the three reference stars (either using the observed spectrum or the one broadened to the $v \sin i$ of HD 93521) should reasonably match the reference values derived from the curve-of-growth analysis (the absolute difference is on average 0.09 dex and at most 0.23 dex). Only three spectral regions fulfilled these criteria: 4060–4082 Å (main contributors C III and O II), 4691–4709 Å (main contributor O II) and 4995–5011 Å (main contributor N II). Unfortunately, the abundances of the other metals (e.g., Mg, Si) could not be reliably investigated. The parameters in Table 3 have been used, such that any errors in $T_{\rm eff}$ and $\log g$ are propagated to the derived abundances. The results are shown in Table 3, while the observed and synthetic line profiles are shown in Fig. 6. Figure 7 shows an example of the variation of the fit quality in the region 4060–4082 Å for different combinations of the C and O abundances. Taking into account the differences for the three reference stars between the abundances found and the reference ones, the different values obtained for oxygen from the two different spectral domains (there is a good agreement with a difference of at most 0.16 dex), and finally the values derived for HD 93521 using the two spectra, the statistical errors on both the abundances and abundance ratios can be set at the ≈0.15 dex level.

Compared to the values derived for the three reference stars based on the spectra broadened with $v \sin i = 390$ km s^{-1}, the abundances of HD 93521 are on average lower by 0.69 dex for C, higher by 0.26 dex for N and lower by 0.27 dex for O. A nitrogen enrichment at the surface is expected given the high helium abundance and is indeed observed: the [N/C] and [N/O] abundance ratios are much higher than in 10 Lac and HD 57682, and also higher than in τ Sco which is the prototype of the class of slowly-rotating, main sequence B stars (unexpectedly) displaying a nitrogen excess (e.g., Morel et al. 2008). The quantitative behaviour of the [N/C] and [N/O] abundance ratios is within the errors what is expected for CNO-cycled material dredged up to the surface (Przybilla et al. 2010). Determinations of the CNO abundances for such fast rotators are very rare in the literature: Villamariz et al. (2002) found [N/C] > + 0.78 and [N/O] > + 0.12 dex for HD 191423 (O9 III:n; $v \sin i = 450$ km s^{-1}), while Villamariz & Herrero (2005) found [N/C] ≈ +0.48 and [N/O] ≈ −0.35 dex for ζ Oph (O9.5 Vnn; $v \sin i = 400$ km s^{-1}).

As the abundances of the three metals investigated are affected at different extent by nuclear CNO-processing, it is difficult to estimate the metallicity of HD 93521. However, oxygen is expected to be only slightly depleted at these levels of nitrogen enrichment and may be taken as a proxy for the global metal content. Assuming a depletion of oxygen of ≈0.1 dex (e.g., Heger & Langer 2000), there is thus some evidence for a lack of metals in HD 93521 compared to solar at the 0.2 dex level. It remains to be seen, however, if these low abundances are not an artifact of the data treatment: given the lack of true continuum regions, there may be a tendency to systematically place the continuum too low and therefore to underestimate the strength of the metal lines. To investigate this issue, we have redetermined the abundances of

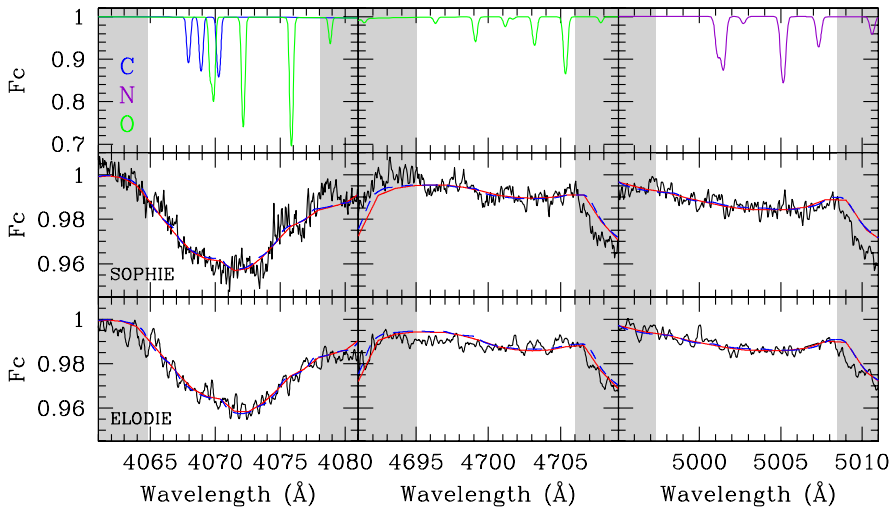

Fig. 6. Comparison for HD 93521 between the observed (black) and best-fitting synthetic metal line profiles under the assumption of a spherical star (red) and a gravity darkened rotationally flattened star (blue). The light grey-shaded areas delineate the regions where the quality of the fit has been evaluated. The top panels show the synthetic profiles computed for $T_{\rm eff}$ = 31 000 K, $\log g$ = 3.7 dex, ξ = 10 km s^{-1} and the abundances obtained using the ELODIE spectrum and assuming a spherical star.

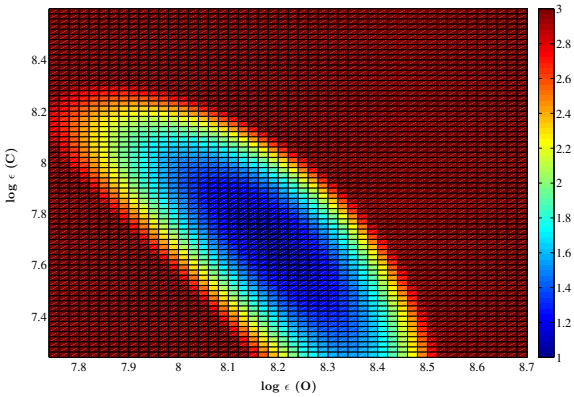

Fig. 7. Variation of the fit quality in the region 4060–4082 Å for different combinations of the C and O abundances (colour coded as a function of the reduced χ^2) in the case of the SOPHIE spectrum of HD 93521. The best fit is found for $\log \epsilon$(C) = 7.70 dex and $\log \epsilon$(O) = 8.20 dex.

HD 93521 after uniformly shifting the continuum level upwards by 0.5%. This leads to an upward revision of $T_{\rm eff}$ and $\log g$, as well as abundances that are typically 0.15 dex higher (this translates to ≈0.30 dex for a shift of 1%; Table 4). We therefore conclude that the uncertainties in the metal abundances (especially owing to the difficulties in the continuum placement) prevent a clear conclusion to be drawn solely based on chemical arguments regarding the birthplace of HD 93521 (either in or far from the Galactic plane). This is especially true when one considers that, although the differences are small, the assumption of a gravity darkened rotationally flattened star leads to systematically higher abundances (see Sect. 5.3). It should also be kept in mind that the microturbulent velocity is not constrained and has been fixed to ξ = 10 km s^{-1}; adopting a lower value would result in generally slightly higher abundances (see Table 4). Nevertheless, our conclusions regarding the He and N-rich status of HD 93521 appear robust against differences in continuum placement and choice of microturbulence (Table 4).

5.3. Assuming a gravity darkened rotationally flattened star

To refine the metal abundances, we have accounted for gravity darkening and rotational flattening using an approach similar to the one of Howarth & Smith (2001).

The stellar surface is assumed to be an equipotential surface of the Roche potential model. The latter can be written in spherical coordinates centred on the centre of a star of mass m_*.

$$\Omega = -\frac{G\,m_*}{r(\theta)} - \frac{\omega^2}{2} \times r^2 \sin^2\theta, \tag{1}$$

where r is the distance from the centre of the star, θ is the co-latitude, φ is the longitude and ω the (constant) angular rotation velocity.

The local gravity is then equal to the gradient of the Roche potential. We have also taken into account the inner radiation pressure following the approach of Howarth (1997).

$$\boldsymbol{g} = (1-\Gamma)\,\boldsymbol{\nabla}\Omega, \tag{2}$$

where $\Gamma = \frac{\sigma_{\rm Th}}{c}\sigma(T_{\rm eff}^{\rm p})^4 \frac{1}{\|g_{\rm pole}\|}$, $\sigma_{\rm Th}$ = 0.036 m^2 kg^{-1} is the Thomson scattering cross section, and σ the Stefan-Boltzmann constant.

The temperature is computed using the von Zeipel (1924) theorem

$$T_{\rm eff}^{\rm local} = T_{\rm eff}^{\rm p}\left(\frac{\|\nabla\Omega_{\rm local}\|}{\|\nabla\Omega_{\rm pole}\|}\right)^{0.25\,\alpha} \tag{3}$$

where α is traditionally taken equal to 1 for massive stars. Recent interferometric observations of rapidly rotating B stars (e.g. Kraus et al. 2012), as well as theoretical work (Espinosa Lara & Rieutord 2011) suggest however that this might not be

Table 4. Sensitivity of the results to differences in continuum placement and choice of microturbulence.

	Continuum shifted upwards by		Microturbulence changed from 10 to 5 km s^{-1}
	0.5%	1%	
$\Delta T_{\rm eff}$ [K]	+490	+1040	...
$\Delta \log g$	+0.10	+0.24	...
Δy	+0.007	+0.015	...
$\Delta \log \epsilon$(C)	+0.10	+0.14	–0.03
$\Delta \log \epsilon$(N)	+0.14	+0.41	+0.05
$\Delta \log \epsilon$(O)	+0.13	+0.36	+0.12
Δ[N/C]	+0.04	+0.27	+0.08
Δ[N/O]	+0.01	+0.05	–0.07

Notes. For the results with a different continuum location, the abundances have been estimated using the revised parameters.

totally appropriate. Observations are better fitted by a value of $\alpha \approx 0.75$, whilst the theoretical results suggest a more complex law with a dependence of the best-fit α parameter on the actual flattening of the star. In the following, we have adopted $\alpha = 0.75$. This value of the gravity darkening exponent reduces the temperature contrast between the pole and the equator compared to the traditional von Zeipel law.

The stellar surface is discretized into 240 × 60 (longitude × colatitude) constantly spaced points. In each surface point, the local temperature and gravity are known, thus, we can compute a local contribution to the spectrum by linear interpolation between four spectra of a grid of synthetic spectra computed with the non-LTE line-formation code DETAIL/SURFACE coupled with the LTE Kurucz models. The spectra of the grid are spaced by 1000 K in $T_{\rm eff}$ and 0.1 dex in $\log g$. The appropriate Doppler shift is then applied to the local spectra accounting for the rotational velocity and these spectra are also multiplied by the area of the surface element projected along the line of sight towards the observer. The last corrective factor applied to the local contribution to the spectrum is the limb-darkening. The limb-darkening coefficient is based on the tabulation of Al-Naimiy (1978) for a linear limb-darkening law[9]. The total spectrum is then computed by summing the incremental contributions of each surface point. We assume that there is no cross-talk between the different surface elements.

This model was then used to generate a grid of synthetic spectra for different metal abundances. To limit the number of free parameters, several parameters were frozen. This is the case of the stellar mass (15 $M_\odot$), the effective temperature at the poles ($T_{\rm eff}^{\rm p}$ = 34 737 K), the polar radius (6.49 $R_\odot$), the projected equatorial rotational velocity ($v \sin i$ = 390 km s^{-1}), the inclination of the rotation axis (i = 90°) and the von Zeipel coefficient (α = 0.75). The polar temperature and radius are chosen in such a way that the average effective temperature and $\log g$ of the star as seen by the observer correspond to 30 918 K and 3.67 respectively, i.e. agree with the numbers inferred in Sect. 5.2.1. This grid of models was then used in the same manner as the pure plane-parallel models of Sect. 5.2.2 to adjust the three spectral regions (see Fig. 6) by varying the CNO abundances. The resulting CNO abundances are listed in the bottom part of Table 3. As can be seen from this table, the differences between the abundances derived assuming either a spherical star or a rotationally flattened star are very small and the results of this section therefore fully confirm the conclusions of Sect. 5.2.2. This good agreement between the CNO abundances stems from the fact that in the rotationally flattened model we have chosen the average (area weighted) $T_{\rm eff}$ and $\log g$ to match the best-fit parameters of the pure plane-parallel model.

Finally, we have tested the sensitivity of the synthetic spectra computed from our rotationally flattened models to some of the frozen parameters. For this purpose, we have varied the mass to 8 and 20 $M_\odot$, the inclination to 70° and the von Zeipel coefficient to 0.50 and 1.0. In each case, the other parameters were adapted in such a way as to recover the mean surface temperature and gravity. The resulting differences in the synthetic spectra over the three spectral regions adopted for the CNO diagnostics, with respect to the best-fit model, were always found to be negligible.

[9] We have compared the synthetic spectra with those simulated using more recent tabulations of the limb-darkening coefficients of Claret & Bloemen (2011). The differences between the normalized synthetic spectra are of the order 3×10^{-4} continuum units, i.e. negligible in view of other uncertainties.

6. Discussion

6.1. Could HD 93521 be a hot subdwarf?

Ebbets & Savage (1982) suggested that HD 93521 could be a low-mass Population II star. Lennon et al. (1991) argued that this is unlikely because of the strength of the metal lines that would be at odds with a low metal abundance expected for a Population II star. However, subdwarf O (sdO) and subdwarf B (sdB) stars are evolved low-mass objects (post red-giant branch, post horizontal branch or post asymptotic giant branch) which display a wide range of helium abundances and, in some cases, a strong enrichment of iron group elements (Heber et al. 2006, 2009). Thus the situation appears less clear cut than previously assumed. Therefore, it is worth to critically consider whether HD 93521 could be a subdwarf OB star.

The distinction between sdB and sdO stars stems from the presence of He II lines in the spectra of the latter and their absence in the former. Since HD 93521 displays weak but definite He II lines in its spectrum, we have to compare its properties mostly with those of sdO stars, although the effective temperature of HD 93521 that we infer from our model atmosphere fits would actually be more typical of an sdB star.

Let us first consider the abundances. Most sdO stars display spectra that point at an He enrichment (up to a factor 10^4 with respect to solar, e.g. Heber et al. 2006) which is usually correlated with enhanced C and/or N abundances (Heber 2009, and references therein). In the spectrum of HD 93521, we find indeed a moderate enhancement of helium and nitrogen (Sect. 5), but at a less extreme level (for helium) than in typical sdOs. The abundance pattern of HD 93521 could instead be the result of strong rotational mixing in a normal O-type star. Actually, the projected rotational velocity of 390 km s^{-1} is much larger than what is observed in hot subdwarfs. Indeed, with the exception of one object, single sdB stars are slow rotators with $v \sin i \leq 10$ km s^{-1} (Geier et al. 2012). The exception is EC 22081-1916 which displays $v \sin i$ = 163 km s^{-1} and could be the outcome of a merger event (see Geier et al. 2012). Hot subdwarfs in very close binaries could be spun up by tidal forces, but the binary fraction among He-enriched sdOs is rather low (a few percent), much lower than in sdBs (Napiwotzki et al. 2004). It seems very unlikely also that HD 93521 could be in a close binary system: its large $v \sin i$ indicates that such a system would be seen under an inclination near $i \approx 90°$ and should hence display short-term radial velocity variations that would have been clearly detected in previous intensive spectroscopic monitoring campaigns (Rauw et al. 2008; see also Sect. 6.2).

Hot ($T_{\rm eff} \geq 30\,000$ K) subdwarfs of the sdB category are known to display short period (a few minutes) pressure mode non-radial pulsations. Much longer periods (45 min to 2 h) attributed to gravity modes were also observed in somewhat cooler sdBs ($T_{\rm eff} \leq 30\,000$ K; Woudt et al. 2007; see also Fontaine et al. 2008, and references therein). There is only one known example of a pulsating sdO in the field (Woudt et al. 2007) which has very fast pulsations (periods of 1–2 min). The non-radial pulsations detected in HD 93521 have periods of 1.75 and 2.89 h (Rauw et al. 2008) much longer than the p-mode oscillations seen in hot sdBs. Although they are comparable to the periods of slowly pulsating sdB stars, the effective temperature and gravity place HD 93521 clearly outside the range of this category (see Fig. 1 of Fontaine et al. 2008). Our model atmosphere fits (Sect. 5) yield an averaged $\log g = 3.67$, much smaller than for typical sdOs ($\log g$ in the range 4.6 to 6.7, see Fig. 2 of Heber et al. 2006).

HD 93521 has an apparent magnitude of $V = 7.06$. Its Hipparcos parallax, $(0.85 \pm 0.49) \times 10^{-3}$ arcsec (van Leeuwen 2007), indicates a distance that is significantly larger than for most other sdOs of comparable apparent magnitude (e.g. BD+75° 325, $V = 9.44$, $\Pi = (7.39 \pm 0.95) \times 10^{-3}$ arcsec, sdO5; HD 49798, $V = 8.18$, $\Pi = (1.20 \pm 0.50) \times 10^{-3}$ arcsec, sdO5.5), although the error on the parallax of HD 93521 and HD 49798 are admittedly quite large. The luminosities of sdOs actually span two orders of magnitude (Heber 2009) and part of this wide range is due to their wide range of temperatures (36 000–78 000 K, Heber et al. 2006). Our determination of the surface temperature would place HD 93521 towards the border between sdO and sdB stars. This means that we have to compare the parallax of HD 93521 with that of late-type and hence probably intrinsically fainter sdOs, thereby enhancing the disagreement.

As an additional criterion for the sdO scenario we can consider the stellar wind features. The winds of sdOs are weak in comparison to those of normal O-stars (see e.g. Hamann et al. 1981) and the associated UV spectral features are thus also generally weaker. IUE and HST spectra of HD 93521 around the relevant wind lines are shown by Massa (1995), Howarth & Reid (1993) and Bjorkman et al. (1994). There is a rather prominent P-Cygni feature in the C IV $\lambda\lambda$ 1548, 1551 doublet which contrasts with the narrow, symmetric absorptions seen in the sdO star HD 49798 (Hamann et al. 1981). However, the profiles of the wind lines (including the C IV doublet) of HD 93521 are rather peculiar for O-type stars. These peculiarities have been interpreted as the signature of an axisymmetric wind structure with a density contrast of about 60 between the equatorial and polar wind (Bjorkman et al. 1994). The determination of the global mass-loss rate of HD 93521 is thus not straightforward (spherically symmetric wind models obviously fail in this context). Using their axisymmetric model, Bjorkman et al. (1994) quote the best-fit values of the product of the polar mass-loss rate times the ionization fraction for C IV, Si IV and N V. These values range between $10^{-10.5}$ and $10^{-9.0}$ $M_\odot$ yr^{-1}, which, if the ionization fractions were close to unity, would be quite comparable to the mass-loss rates of the sdOs studied by Hamann et al. (1981). However, Bjorkman et al. (1994) argue that the ionization fractions are significantly less than unity and that their result would be consistent with $\dot{M} = 10^{-7.2}$ $M_\odot$ yr^{-1}. On the other hand, the four sdOs studied by Hamann et al. (1981) are much hotter than HD 93521 and a comparison with late sdO or sdB stars might be better. So far, observational evidence for winds in this category of subdwarfs is scarce and the few cases with a positive detection of wind emission in the Hα line are consistent with mass loss rates of 10^{-11} to 10^{-10} $M_\odot$ yr^{-1} (Unglaub 2008). Therefore, our present knowledge of the wind of HD 93521 does not allow us to draw a firm conclusion about the comparison of its mass-loss rate with that of hot subdwarfs.

Finally, we need to address the issue of the X-ray emission. Little is known about the X-ray emission of hot subdwarfs. An exception are two compact binary systems, HD 49798 and BD+37° 442, which host a white dwarf or neutron star accreting material from the sdO component (Tiengo et al. 2004; Mereghetti et al. 2009, 2011; La Palombara et al. 2012). The X-ray spectra of these objects are rather soft and are well fitted by a model consisting of a black-body component ($kT \approx 40$ eV) along with a power-law ($\Gamma \approx 2$). Both objects show pulsations of the X-ray flux with periods of 13.2 and 19.2 s. As we have shown in Sect. 4, our X-ray data are not well described by this spectral model and do not display any signature of pulsations with periods between 1.0 and 1000 s. This excludes the possibility that HD 93521 could be an sdO with a compact companion.

During the eclipse of the white dwarf in HD 49798, Mereghetti et al. (2011) detected an X-ray luminosity of 2×10^{30} erg s^{-1}, corresponding to $L_{\rm X}/L_{\rm bol} = 7 \times 10^{-8}$ which they attribute to the intrinsic X-ray emission of the sdO component. Whilst this $L_{\rm X}/L_{\rm bol}$ ratio is very similar to that of HD 93521, and of normal O-type stars in general, overall the various arguments presented in this section are definitely at odds with an sdO or sdOB nature of HD 93521.

6.2. The runaway status

We have measured the radial velocity of HD 93521 on our mean ELODIE spectrum. As this spectrum results from the combination of many individual spectra taken at various NRP phases, one expects it a priori to provide line profiles that should be rather free of the NRP signatures. We have only measured lines that are expected to be relatively free of strong blends and have a rather symmetric shape. Our line list is composed of Hγ, Hβ, He I $\lambda\lambda$ 4471, 4922 and He II $\lambda\lambda$ 4200, 4686, 5412. In this way, we infer a heliocentric radial velocity of 9.5 ± 6.3 km s^{-1}, which, using the formalism of Moffat et al. (1998) and Nazé (2004), translates into a peculiar radial velocity of 10.0 ± 6.3 km s^{-1}, well below the conventional 30 km s^{-1} threshold (Cruz-González et al. 1974) for runaway stars.

Using radial velocities compiled from the literature, Gies (1987) found a heliocentric radial velocity of -13.9 km s^{-1} corresponding to a peculiar radial velocity of -12.5 km s^{-1}. Whilst this result is still below the threshold for a runaway status, it is actually quite different from our result. This prompted us to check the RVs on the average He I line profiles in the data used for the analysis of the NRPs (Rauw et al. 2008). The latter yield heliocentric RVs of -16.2 and -2.9 km s^{-1} for the He I λ 5876 line respectively in February 2006 and April 2007, as well as 35.6 and 3.8 km s^{-1} for the He I λ 6678 line respectively in February 1997 and May 2005. Finally, measuring the same lines as for the mean ELODIE spectrum on our SOPHIE spectrum yields a heliocentric RV of 21.4 ± 11.1 km s^{-1}. Whilst these differences could be due to orbital motion in a (most likely) long-period (years) binary system, an alternative explanation could be the NRPs. Rzaev & Panchuk (2006) studied the bisector radial velocities of a number of He I lines in the spectrum of HD 93521 over a time span of 2.7 h. They found apparent variations of the radial velocities with amplitudes of tens of km s^{-1}. Therefore, the radial velocities of HD 93521 could strongly depend on the specific phase of the NRPs or the sampling of the latter. This means that the true heliocentric RV is difficult to assess. Nonetheless, in view of the above results, it seems unlikely

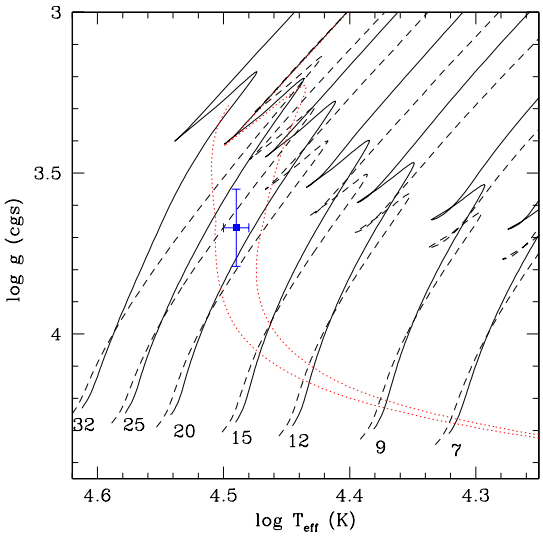

Fig. 8. Location of HD 93521 in the ($\log T_{\rm eff}$, $\log g$) diagram (blue dot with error bars) as inferred from our model atmosphere fit (Sect. 5.2.1). The main-sequence parts of the Geneva evolutionary tracks from Ekström et al. (2012) are shown by the solid lines for stars initially rotating at 40% of the critical velocity. The initial mass of the star is given in $M_\odot$ by the label at the bottom of the track. The dashed lines yield the same tracks for zero rotational velocity. The isochrones for ages of 6.3 and 7.9 Myr are shown by the dotted red lines.

that the true peculiar velocity of HD 93521 could be significantly larger than the 30 km s^{-1} threshold.

The Hipparcos catalogue based on the revised reduction (van Leeuwen 2007) lists a parallax of $\Pi = (0.85 \pm 049) \times 10^{-3}$ arcsec and proper motions of $\mu_\alpha \cos\delta = (0.32 \pm 0.40) \times 10^{-3}$ and $\mu_\delta = (2.44 \pm 0.37) \times 10^{-3}$ arcsec yr^{-1}. We have used these numbers to estimate a peculiar tangential velocity of HD 93521 of $v_{\rm t} = 26.8 \pm 9.2$ km s^{-1}. Adopting the criterion of Moffat et al. (1998), this number is well below the threshold for considering HD 93521 as a runaway star.

Based on its kinematic properties, HD 93521 can thus not unambiguously be classified as a runaway star. However, de Wit et al. (2005) argue that stars located more than 500 pc above the Galactic plane must de facto be runaways, as there is currently no evidence for star formation in the halo. Indeed, in their study of a sample of 10 high Galactic latitude B-type stars with masses between 5 and 13 $M_\odot$, Ramspeck et al. (2001) did not find a conclusive candidate for a star formed in the halo. Although they were lacking kinematic data for some of their targets, they found that the evolutionary time scales were sufficiently long for the stars to have travelled to their current location if their ejection velocity reaches values up to 440 km s^{-1}.

To estimate the evolutionary age of HD 93521, we have plotted the star in a ($\log T_{\rm eff}$, $\log g$) diagram against the evolutionary tracks and isochrones of Ekström et al. (2012). The result is shown in Fig. 8. HD 93521 falls between the evolutionary tracks of initial mass 20 and 25 $M_\odot$ and close to the 6 Myr isochrone. Note that this estimate might actually be a lower limit of the true age, if the evolution of the star was affected by binary effects, such as mass transfer during a Roche lobe overflow phase or a merger event (following ejection through dynamical interactions in a dense cluster)[10] leading to a blue straggler star (de Mink et al. 2010).

Dynamical interactions in dense clusters can produce very high maximum ejection velocities of up to 700 km s^{-1} for a 60 $M_\odot$ O-star and even up to 1400 km s^{-1} for low-mass stars (Leonard 1991), whilst the supernova ejection scenario generally predicts maximum ejection velocities of $\leq$300 km s^{-1} (Portegies-Zwart 2000). However, Przybilla et al. (2008) proposed that an ejection velocity of about 400 km s^{-1} could result from a supernova explosion in a tight Wolf-Rayet + B-star binary. From a sample of 96 likely OB runaway stars, Silva & Napiwotzki (2011) found evidence for a bi-modal distribution of the ejection velocities with two populations with velocities $\leq$300 km s^{-1} and around 400–500 km s^{-1} respectively. Therefore, assuming an ejection velocity of 400 km s^{-1}, the minimum time requested to reach the star's present location, 1 kpc above the Galactic plane, would be about 2.4 Myr, which is well below the estimated evolutionary age. Therefore, in light of our current results, we cannot rule out the possibility that HD 93521 could be a runaway star, probably observed near the apex of its orbit.

7. Summary and conclusions

Our analysis of the X-ray and optical data of HD 93521 provides new clues about the nature and origin of this star. We found no evidence of a stellar cluster or other tracers of star formation activity which makes it unlikely that the star has formed at its current position. The X-ray data did not reveal any evidence for a compact companion that could have been produced in a supernova explosion. The stellar parameters inferred from an analysis of the optical and X-ray spectrum are consistent with an "ordinary" Population I late O-type star and reject an interpretation of the star as a low-mass subdwarf. The He and N surface abundances are enhanced, as expected for a fast rotating evolved main-sequence O-type star (Meynet & Maeder 2000). The X-ray spectra can be represented by a two-temperature optically thin thermal plasma model with a dominant component with $kT \approx 0.3$ keV and a rather hot secondary plasma component with $kT \approx 3$ keV. At first sight, the subsolar metallicity inferred from fitting the X-ray spectrum could be somewhat of a surprise. However, it is not uncommon to derive subsolar metallicities from the fit of CCD X-ray spectra of O-type stars. A prominent example of this situation is the population of OB stars in M 17 (Broos et al. 2007) which has a metallicity of $\approx$0.3 $Z_\odot$.

Whilst the runaway status of the star remains ambiguous, the most likely explanation seems nevertheless that the star has not formed in the Galactic halo, but was rather ejected from the plane, either through dynamical interactions in a dense cluster or an unstable multiple system, or as a result of a supernova explosion in a binary system. The rapid rotation of the star, if not due to mass and angular momentum transfer in a binary system, could be the result of the dynamical interaction, maybe associated with a merger event (e.g. de Mink et al. 2010) that would produce a blue straggler and could alleviate the flight time constraint. One open issue that remains with this scenario is how the star maintained its extreme rotational velocity well after the event that led to its ejection from the plane. A better knowledge of the proper motion and distance of the star, as will be provided

[10] In the dynamical interactions scenario, the ejection of a close binary system is a rare event and should proceed at a comparatively low ejection velocity (Leonard & Duncan 1990).

by ESA's forthcoming *Gaia* mission will certainly be extremely beneficial to complete our understanding of this intriguing star.

Acknowledgements. We are most grateful to our amateur colleagues Gaston Dessy (Biesme) and Joël Bavais (Ath) who provided us with imaging observations of the field of HD 93521. We further wish to thank Drs. Valérie Van Grootel and Sandro Mereghetti for enlightening discussions respectively about the general properties of sdOs and their X-ray emission in particular. We thank an anonymous referee for his/her constructive report. T.M. acknowledges financial support from Belspo for contract PRODEX-*Gaia* DPAC. G.R. and M.P. acknowledge support through the XMM/INTEGRAL PRODEX contract as well as by the Communauté Française de Belgique – Action de recherche concertée – Académie Wallonie – Europe. We would like to thank K. Butler for making the NLTE line-formation codes DETAIL/SURFACE available to us.

References

Al-Naimiy, H. M. 1978, Ap&SS, 53, 181
Arnaud, K. A. 1996, in Astronomical Data Analysis Software and Systems V, eds. G. Jacoby, & J. Barnes (San Francisco: ASP), 101, 17
Asplund, M., Grevesse, N., Sauval, A. J., & Scott, P. 2009, ARA&A, 47, 481
Baranne, A., Queloz, D., Mayor, M., et al. 1996, A&AS, 119, 373
Bjorkman, J. E., Ignace, R., Tripp, T. M., & Cassinelli, J. P. 1994, ApJ, 435, 416
Bohlin, R. C., Savage, B. D., & Drake, J. F. 1978, ApJ, 224, 132
Bonnell, I. A., Vine, S. G., & Bate, M. R. 2004, MNRAS, 349, 735
Bressert, E., Bastian, N., Evans, C. J., et al. 2012, A&A, 542, A49
Broos, P. S., Feigelson, E. D., Townsley, L. K., et al. 2007, ApJS, 169, 353
Butler, K., & Giddings, J. R. 1985, in Newsletter of Analysis of Astronomical Spectra, No. 9 (Univ. London)
Claret, A., & Bloemen, S. 2011, A&A, 529, A75
Cruz-González, C., Recillas-Cruz, E., Costero, R., Peimbert, M., & Torres-Peimbert, S. 1974, RMxAA, 1, 211
Damiani, F., Prisinzano, L., Micela, G., & Sciortino, S. 2006, A&A, 459, 477
de Mink, S. E., Langer, N., & Izzard, R. G. 2010, in Active OB stars: structure, evolution, mass-loss and critical limits, eds. C. Neiner, G. Wade, G. Meynet, & G. Peters (Cambridge: Cambridge University Press), IAU Symp., 272, 531
de Wit, W. J., Testi, L., Palla, F., & Zinnecker, H. 2005, A&A, 437, 247
Ebbets, D. C., & Savage, B. D. 1982, ApJ, 262, 234
Ekström, S., Georgy, C., Eggenberger, P., et al. 2012, A&A, 537, A146
Espinosa Lara, F., & Rieutord, M. 2011, A&A, 533, A43
Fontaine, G., Brassard, P., Charpinet, S., et al. 2008, in Hot Subdwarf Stars and Related Objects, eds. U. Heber, S. Jeffery, & R. Napiwotzki (San Francisco: ASP), ASP Conf., 392, 231
Geier, S., Heber, U., Edelmann, H., Napiwotzki, R., & Morales-Rueda, L. 2012, in Fifth Meeting on Hot Subdwarf Stars and Related Objects, eds. D. Kilkenny, C. S. Jeffery, & C. Koen (San Francisco: ASP), ASP Conf., 452, 81
Giacconi, R., Rosati, P., Tozzi, P., et al. 2001, ApJ, 551, 624
Giddings, J. R. 1981, Ph.D. Thesis, University of London
Gies, D. R. 1987, ApJS, 64, 545
Hamann, W.-R., Gruschinske, J., Kudritzki, R. P., & Simon, K. P. 1981, A&A, 104, 249
Heber, U. 2009, ARA&A, 47, 211
Heber, U., Hirsch, H., Ströer, A., et al. 2006, Baltic Astron., 15, 91
Heger, A., & Langer, N. 2000, ApJ, 544, 1016
Howarth, I. D. 1997, Observatory, 117, 335
Howarth, I. D., & Reid, A. H. N. 1993, A&A, 279, 148
Howarth, I. D., & Smith, K. C. 2001, MNRAS, 327, 353
Howarth, I. D., Siebert, K. W., Hussein, G. A. J., & Prinja, R. K. 1997, MNRAS, 284, 265
Hubrig, S., Briquet, M., Morel, T., et al. 2008, A&A, 488, 287
Irvine, N. J. 1989, ApJ, 337, L33
Jansen, F., Lumb, D., Altieri, B., et al. 2001, A&A, 365, L1
Kraus, S., Monnier, J. D., Che, X., et al. 2012, ApJ, 744, 19
Krumholz, M. R., Klein, R. I., McKee, C. F., Offner, S. S. R., & Cunningham, A. J. 2009, Science, 323, 754
Lamb, J. B., Oey, M. S., Werk, J. K., & Ingleby, L. D. 2010, ApJ, 725, 1886
La Palombara, N., Mereghetti, S., Tiengo, A., & Esposito, P. 2012, ApJ 750, L34
Lennon, D. J., Dufton, P. L., Keenan, F. P., & Holmgren, D. E. 1991, A&A, 246, 175
Leonard, P. J. T. 1991, AJ, 101, 562
Leonard, P. J. T., & Duncan, M. J. 1990, ApJ, 353, 486
Massa, D. 1995, ApJ, 438, 376
Massaro, E., Giommi, P., Leto, C., et al. 2009, A&A, 495, 691
Mereghetti, S., Tiengo, A., Esposito, P., et al. 2009, Science, 325, 1222
Mereghetti, S., La Palombara, N., Tiengo, A., et al. 2011, ApJ, 737, 51
Meynet, G., & Maeder, A. 2000, A&A, 361, 101
Moffat, A. F. J., Marchenko, S. V., Seggewiss, W., et al. 1998, A&A, 331, 949
Morel, T. 2011, Bull. Soc. Roy. Sci. Liège, 80, 405
Morel, T., Hubrig, S., & Briquet, M. 2008, A&A, 481, 453
Mucciarelli, P., Preibisch, T., & Zinnecker, H. 2011, A&A, 533, A121
Najarro, F., Hillier, D. J., Puls, J., Lanz, T., & Martins, F. 2006, A&A, 456, 659
Napiwotzki, R., Karl, C. A., Lisker, T., et al. 2004, Ap&SS, 291, 321
Nazé, Y. 2004, Ph.D. Thesis, Liège University
Nazé, Y. 2009, A&A, 506, 1055
Nazé, Y., Rauw, G., Vreux, J.-M., & De Becker, M. 2004, A&A, 417, 667
Nieva, M. F., & Przybilla, N. 2007, A&A, 467, 295
Okazaki, A. T., & Negueruela, I. 2001, A&A, 377, 161
Perruchot, S., Kohler, D., Bouchy, F., et al. 2008, in Ground-based and Airborne Instrumentation for Astronomy II, eds. I. S. McLean, & M. M. Casali, Proc. SPIE, 7014, 70140
Preibisch, T., & Feigelson, E. D. 2005, ApJS, 160, 390
Portegies-Zwart, S. F. 2000, ApJ, 544, 437
Przybilla, N., Nieva, M. F., Heber, U., & Butler, K. 2008, ApJ, 684, L103
Przybilla, N., Firnstein, M., Nieva, M. F., Meynet, G., & Maeder, A. 2010, A&A, 517, A38
Przybilla, N., Nieva, M. F., & Butler, K. 2011, JPhCS, 328, 012015
Rakowski, C. E., Schulz, N. S., Wolk, S. J., & Testa, P. 2006, ApJ, 649, L111
Ramspeck, M., Heber, U., & Moehler, S. 2001, A&A, 378, 907
Rauw, G. 2011, A&A, 536, A31
Rauw, G., De Becker, M., Gosset, E., Pittard, J. M., & Stevens, I. R. 2003, A&A, 408, 171
Rauw, G., De Becker, M., van Winkel, H., et al. 2008, A&A, 487, 659
Rzaev, A. K., & Panchuk, V. E. 2006, Astron. Rep., 50, 31
Sana, H., Rauw, G., Sung, H., Gosset, E., & Vreux, J.-M. 2007, MNRAS, 377, 945
Selier, R., Heydari-Malayeri, M., & Gouliermis, D. A. 2011, A&A, 529, A40
Silva, M. D. V., & Napiwotzki, R. 2011, MNRAS, 411, 2596
Smith, R. K., Brickhouse, N. S., Liedahl, D. A., & Raymond, J. C. 2001, ApJ, 556, L91
Smith, M. A., Cohen, D. H., Gu, M. F., et al. 2004, ApJ, 600, 972
Strüder, L., Briel, U., Dennerl, K., et al. 2001, A&A, 365, L18
Tiengo, A., Mereghetti, S., Israel, G. L., & Stella, L. 2004, Nucl. Phys. B, Proc. Suppl., 132, 705
Torres-Dodgen, A. V., Tapia, M., & Carroll, M. 1991, MNRAS, 249, 1
Turner, M. J. L., Abbey, A., Arnaud, M., et al. 2001, A&A, 365, L27
Unglaub, K. 2008, in Hot Subdwarf Stars and Related Objects, eds. U. Heber, S. Jeffery, & R. Napiwotzki (San Francisco: ASP), ASP Conf., 392, 95
van Leeuwen, F. 2007, A&A, 474, 653
Villamariz, M. R., Herrero, A., Becker, S. R., & Butler, K. 2002, A&A, 388, 940
Villamariz, M. R., & Herrero, A. 2005, A&A, 442, 263
von Zeipel, H., 1924, MNRAS, 84, 665
Vrancken, M., Hensberge, H., David, M., & Verschueren, W. 1997, A&A, 320, 878
Weidner, C., Kroupa, P., & Bonnell, I. A. D. 2010, MNRAS, 401, 275
Woudt, P. A., Warner, B., & Kilkenny, D. 2007, in 15th European Workshop on White Dwarfs, eds. R. Napiwotzki, & M. R. Burleigh (San Francisco: ASP), ASP Conf., 372, 619

Revista Mexicana de Astronomía y Astrofísica, **50**, 67–76 (2014)

EPOCH-DEPENDENT ABSORPTION LINE PROFILE VARIABILITY IN λ CEP

J. M. Uuh-Sonda,[1] G. Rauw,[2] P. Eenens,[1] L. Mahy,[2] M. Palate,[2] E. Gosset,[2,3] and C. A. Flores[1]

Received 2013 September 30; accepted 2013 December 2

RESUMEN

Reportamos el análisis de una campaña de monitoreo espectroscópico multi-época de la estrella O6 Ief λ Cep. Observaciones previas habían reportado la existencia de dos modos de pulsaciones no-radiales en esta estrella. Nuestros datos revelan una situación considerablemente más compleja. Las frequencias contenidas en el espectro de potencia cambian considerablemente de una época a otra. No encontramos ninguna frecuencia estable que pueda ser atribuida inequívocamente a pulsaciones. La dependencia temporal de las frequencias y los patrones de variabilidad son similares a los observados en las líneas de emisión del viento en esta y otras estrellas Oef, lo cual sugiere que ambos fenómenos tienen probablemente el mismo origen, aunque éste siga todavía sin conocerse.

ABSTRACT

We present the analysis of a multi-epoch spectroscopic monitoring campaign of the O6 Ief star λ Cep. Previous observations reported the existence of two modes of non-radial pulsations in this star. Our data reveal a much more complex situation. The frequency content of the power spectrum considerably changes from one epoch to the other. We find no stable frequency that can unambiguously be attributed to pulsations. The epoch-dependence of the frequencies and variability patterns are similar to what is seen in the wind emission lines of this and other Oef stars, suggesting that both phenomena likely have the same, currently still unknown, origin.

Key Words: stars: early-type — stars: individual (λ Cep) — stars: oscillations — stars: variables: general

1. INTRODUCTION

Line profile variability is a widespread phenomenon among O-type stars, and even more so among O supergiants (Fullerton, Gies, & Bolton 1996). For single stars, this variability is usually attributed to pulsations, rotational modulations, magnetic fields, structures in the stellar wind, or a mix of these phenomena. The variability of absorption lines, if due to stellar pulsations, can be used to constrain theoretical models of the stellar interior (e.g. Briquet et al. 2011; Godart et al. 2012). Until recent years, the most robust evidence for pulsations in O-type stars was found in the two O9.5 V stars ζ Oph (Kambe et al. 1997) and HD 93521 (Rauw et al. 2008, and references therein). Thanks to the high-precision photometry from the *CoRoT* mission, β Cep-like pulsations have been found in the O9 V star HD 46202 (Briquet et al. 2011), and probable non-radial pulsations were detected in Plaskett's Star (= HD 47129, O8 III/I + O7.5 V/III, Mahy et al. 2011). However, these *CoRoT* data also revealed a more complex situation as far as earlier main-sequence O-stars are concerned. Indeed, Blomme et al. (2011) found that the Fourier spectra of the O4 V((f$^+$)) star HD 46223, the O5.5 V((f)) star HD 46150 and the O8 V star HD 46966 are dominated by so-called red noise, i.e. stochastic variations whose power increases towards lower frequencies. For these objects, the presence of genuine pulsations could thus not be firmly established. This suggests that the instability that causes the late O-type stars to pulsate does not extend to the earliest spectral types, at least not on the main-sequence.

[1]Departamento de Astronomía, Universidad de Guanajuato, Guanajuato, Mexico.
[2]Institut d'Astrophysique et de Géophysique, Université de Liège, Belgium.
[3]Senior Research Associate F.R.S.-FNRS.

TABLE 1

SUMMARY OF THE TIME SAMPLING OF OUR OBSERVING CAMPAIGNS

Campaign	Starting and ending dates (JD-2450000)	n	$<$S/N$>$	ΔT (days)	$<\Delta t>$ (days)	$\Delta\nu_{\rm nat}$ (day^{-1})	$\nu_{\rm max}$ (day^{-1})
OHP 12/2009	5174.293 – 5179.385	57	280	5.092	1.12×10^{-2}	0.197	44.52
OHP 06/2010	5369.406 – 5375.605	100	405	6.199	1.40×10^{-2}	0.161	35.60
SPM 06/2010	5370.853 – 5375.980	76	250	5.127	1.31×10^{-2}	0.195	38.12
OHP 12/2010	5539.270 – 5543.433	51	210	4.163	1.40×10^{-2}	0.240	35.63
SPM 09/2011	5812.788 – 5820.899	95	265	8.110	1.53×10^{-2}	0.123	32.68
OHP 09/2011	5825.333 – 5830.651	116	340	5.318	1.40×10^{-2}	0.188	35.63

In this context, the bright O6 Ief supergiant λ Cep (= HD 210839) is a very interesting target. To start, it is a bright ($V = 5.08$) and most probably single object (Gies 1987). λ Cep is one out of a handful of so-called Oef stars in our Galaxy. These objects (including another bright O-star, ζ Pup) are characterized by a double-peaked He II λ 4686 emission line in their spectrum (Conti & Leep 1974). The variability of this line in the spectrum of λ Cep has been documented by a number of authors (Conti & Frost 1974; Leep & Conti 1979; Grady, Snow, & Timothy 1983; McCandliss 1988; Henrichs, Kaper, & Zwarthoed 1988; Henrichs 1991; Kaper et al. 1997, 1999). In the context of the present work, we concentrate mostly on the variability of the absorption lines. Indeed, a previous study of λ Cep's optical absorption line spectrum revealed the likely presence of low-order non-radial pulsations (NRPs) with periods of 12.3 ($l = 3$) and 6.6 hrs ($l = 5$) (de Jong et al. 1999). However, this result was based on a single line (He I λ 4713) observed during a single five-night multi-site campaign. Since other Oef stars have been found to display a strong epoch-dependence in their variability (Rauw, De Becker, & Vreux 2003; De Becker & Rauw 2004) the results of de Jong et al. (1999) needed confirmation. We have thus set up a multi-epoch, multi-site spectroscopic monitoring to re-investigate the absorption line profile variability of λ Cep.

2. OBSERVATION AND DATA REDUCTION

Spectroscopic observations of λ Cep were collected during six observing campaigns resulting in a total of 495 spectra. Four campaigns (December 2009, June 2010, December 2010 and September 2011) were performed at the Observatoire de Haute Provence (OHP, France) using the Aurélie spectrograph fed by the 1.52 m telescope. The OHP data were taken with a 1200 lines mm^{-1} grating blazed at 5000 Å. This set-up covered the wavelength domain from 4460 to 4670 Å with a resolving power of 20000. The detector was a CCD EEV42-20 with 2048×1024 pixels of 13.5 μm^2. Typical exposure times were 10 – 15 minutes. To achieve the most accurate wavelength calibration, Th-Ar lamp exposures were taken regularly over each observing night (typically once per hour). The other two campaigns (June 2010 and September 2011) were performed at the Observatorio Astrónomico Nacional de San Pedro Mártir (SPM, Mexico) using the echelle spectrograph mounted on the 2.1 m telescope. The spectral coverage is about 3800–7300 Å with a resolving power of 18000 at 5000 Å. The detector used for the June 2010 observations was a Thomson TH7398M CCD with 2048×2048 pixels of 14 μm^2, whereas the September 2011 observations were taken with a Marconi 2 CCD with 2048×2048 pixels of 13.5 μm^2. Th-Ar lamp exposures were taken about every hour and a half.

The data were reduced using the MIDAS software provided by ESO. The wavelength calibration was done using the Th-Ar lamp exposures. For the Aurélie data, the rms error on the wavelength solutions was found to be around 0.0025 Å, whilst it is about 0.0080 Å for the SPM data. A very critical step was the normalization of the spectra. Whilst the Aurélie data could be normalized self-consistently over their full wavelength range using a series of continuum windows, this turned out to be much more challenging for the data collected with the echelle spectrograph of SPM. Indeed, because of the strongly peaked blaze of the latter instrument, normalization had to be done on specific orders covering the two lines He I λ 4471 and He II λ 4542.

Table 1 provides a summary of our observing campaigns and the characteristics of the sampling. For each campaign, n provides the total number of spectra that were collected, whilst $<$S/N$>$ indicates the mean signal-to-noise ratio of the spectra. ΔT indicates the total time between the first and last

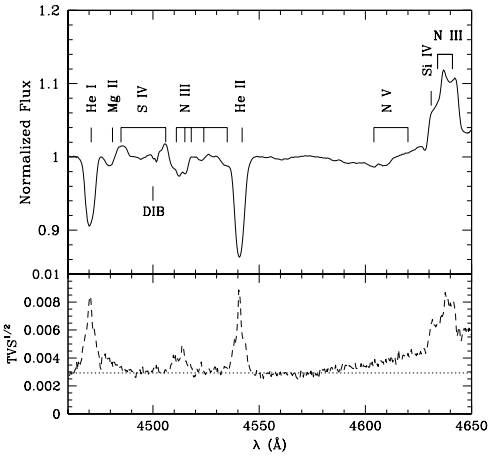

Fig. 1. Upper panel: mean spectrum of λ Cep as obtained from the full set of 324 Aurélie spectra. The most important spectral features are labelled: stellar lines are identified above the spectrum, whereas the diffuse interstellar band (DIB) near 4500 Å is indicated below. Lower panel: square root of the temporal variance spectrum of the full set of Aurélie spectra. The dotted line yields the 1% significance level computed according to the mean S/N of the data.

observations, whereas $<\Delta t>$ provides the average time interval between two consecutive exposures of a same night. Finally, Table 1 provides some information in view of the forthcoming Fourier analyses. The last two columns indicate the natural width of the peaks in the periodogram $\Delta\nu_{\rm nat} = (\Delta T)^{-1}$ as well as $\nu_{\rm max} = (2 <\Delta t>)^{-1}$ which provides a rough indication of the highest frequency that can possibly be sampled with our time series.

3. ANALYSIS

To analyze our dataset, we make use of the tools used by Rauw et al. (2008) in their investigation of the variability of HD 93521. The first step involves computation of the temporal variance spectrum (TVS, Fullerton et al. 1996) to identify those parts of the spectrum that display significant variability. We then apply a 2D-Fourier analysis on a wavelength-by-wavelength basis over the part of the spectrum where variability is detected (see Rauw et al. 2008). For this purpose, we use the Fourier technique for time series with an uneven sampling designed by Heck, Manfroid, & Mersch (1985) and amended by Gosset et al. (2001). Whenever a significant frequency is found, we prewhiten the data for the corresponding variations, and we then repeat our Fourier analysis on the prewhitened time series. Due to aliasing and the contribution of power at low frequency from a potential red noise component, the choice of the 'right' frequency is sometimes non-trivial. This process is performed for up to three frequencies[4], and allows us to build diagrams showing the amplitude and phase associated to the various frequencies as a function of wavelength. Finally, to evaluate the error bars on the semiamplitudes and phases of the various Fourier components, we have used Monte Carlo simulations assuming that the uncertainties on the normalized flux at a given wavelength and a given time are equal to the noise level of the corresponding spectrum evaluated over a nearby continuum window.

Figure 1 illustrates the mean spectrum and the TVS as computed from the full set of our OHP observations. This figure shows that significant variability is present in the strong absorption lines (He I λ 4471, He II λ 4542) as well as in the N III λλ 4634-4642 emission complex. Weaker absorption lines, such as the group of N III transitions at λλ 4509-4522 are also weakly detected in the TVS, whilst the weak S IV emission lines are not detected as variable.

As an example, Figure 2 illustrates the variability of the He I λ 4471 and He II λ 4542 lines in the June 2010 OHP data. The variability is clearly seen, as its peak-to-peak amplitude is about 3%. At first sight, the variations could be consistent with NRPs. Indeed, they mostly consist of red-wards moving substructures similar to what is commonly seen in the line profiles of non-radial pulsators. The variability pattern is not fully constant though, as the widths and strengths of these substructures vary from night to night. Figures 1 and 2 show that, although the variability extends over the full width of the line, the most prominent variations actually occur in the core of the line.

For each subset of our data, we have computed periodograms up to a frequency of 15 d^{-1} for the He I λ 4471 and He II λ 4542 lines respectively, over the wavelength domains 4465−4477 and 4535−4546 Å. For the OHP data, we have also analyzed the variations of the N III λλ 4634−42 emission over the 4628−4646 wavelength range[5]. This emission triplet is produced in the photosphere, although its strength is dependent on the conditions in the innermost ac-

[4] As we show below, three frequencies are usually sufficient to account for the power in the Fourier spectrum.

[5] Due to the strongly peaked blaze of the SPM echelle spectrograph, we were not able to normalize the SPM data of this emission complex with sufficient accuracy.

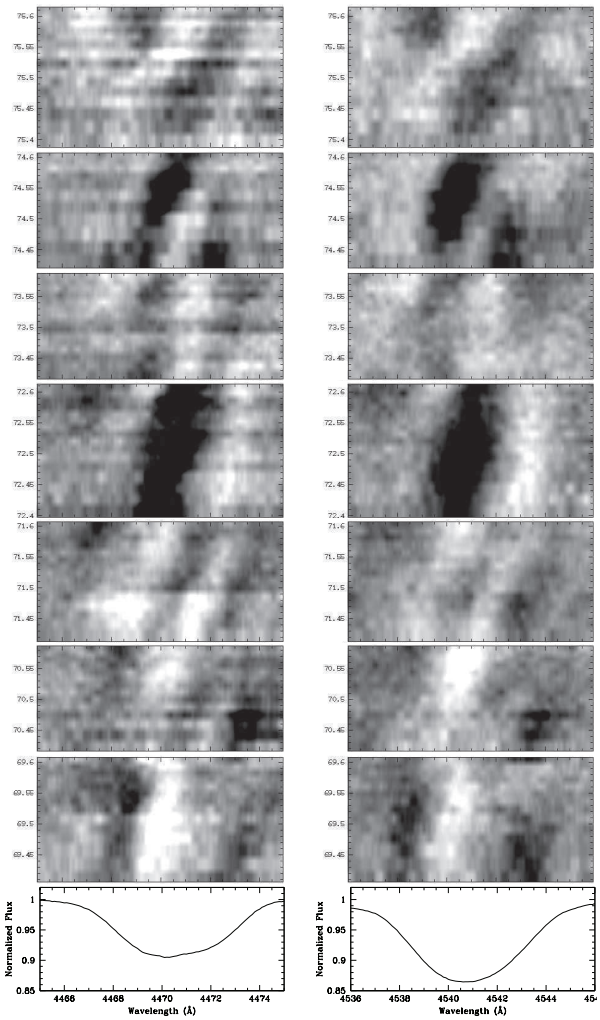

Fig. 2. Greyscale images illustrating the residuals of individual He I λ 4471 (left) and He II λ 4542 (right) line profiles with respect to the mean profiles (shown by the lower panels) for the June 2010 OHP data. The labels on the vertical axes of the greyscales yield the date of the observation expressed as HJD-2455300.

celerating part of the stellar wind (Rivero González, Puls, & Najarro 2011). Therefore the variability of this complex could reflect both the changing conditions in the photosphere (due e.g. to pulsations) and at the very base of the wind. The interpretation of its variability is however complicated by the blend with other species such as Si IV λ 4631 and C III $\lambda\lambda$ 4647−50.

Below we summarize the results obtained in our analyses. Figure 3 illustrates the output of our method for the specific case of the June 2010 OHP data set.

For some of the individual observing campaigns (e.g., December 2009, December 2010), the power spectra after prewhitening the dominant frequency are characterized by power at low frequencies which

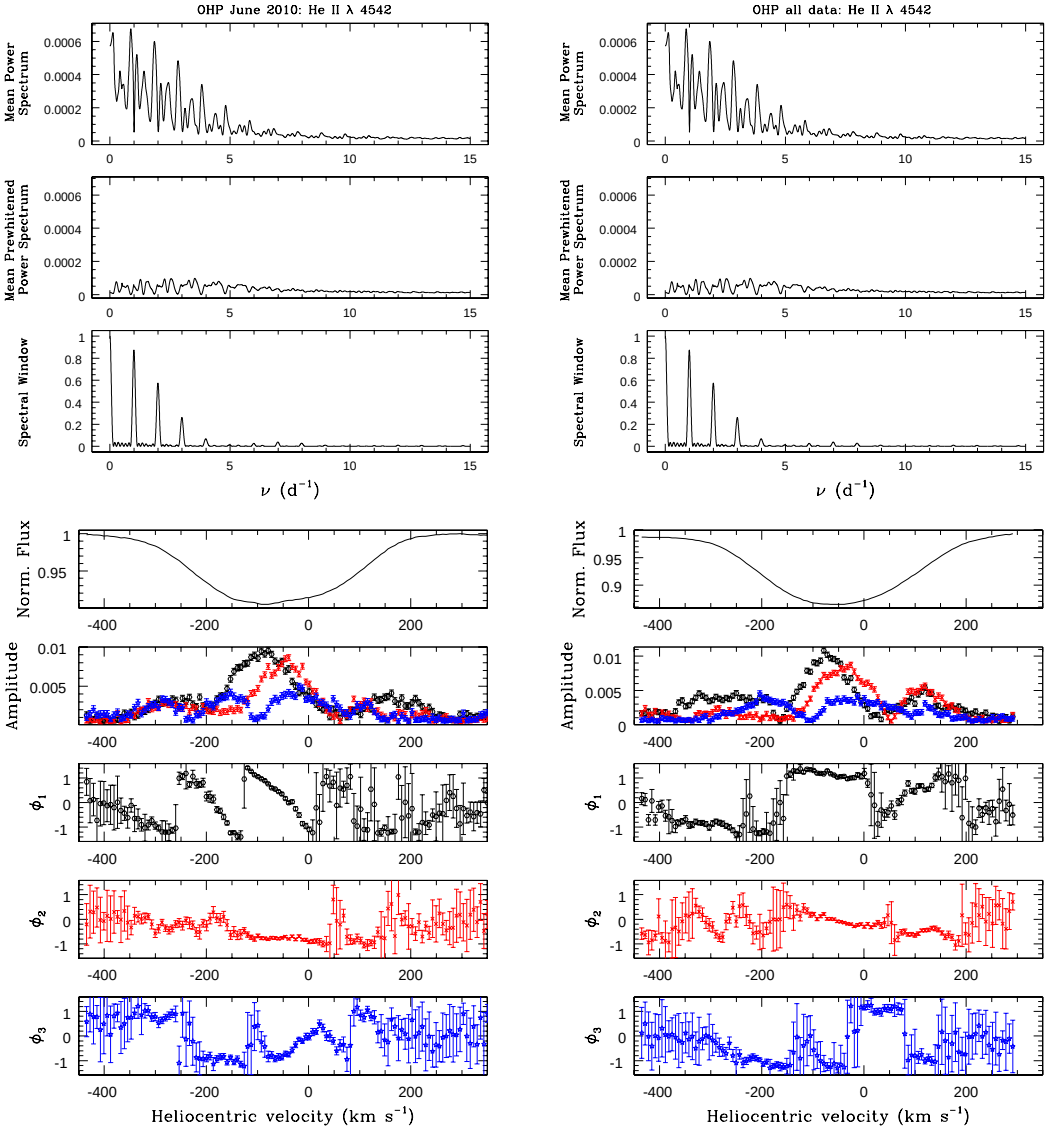

Fig. 3. Illustration of the output of our Fourier and prewhitening analysis in the case of the June 2010 OHP data set. The figures on the left correspond to the He I λ 4471 line, whilst those on the right are relative to the He II λ 4542 line. The top three panels illustrate for each line, the original periodogram, the periodogram after prewhitening of the three frequencies quoted in Table 2 and the spectral window (from top to bottom), as a function of frequency. The lower five panels provide the mean normalized line profile, the amplitude of the variations associated with the different frequencies (black hexagone, red crosses and blue stars correspond to ν_1, ν_2 and ν_3 respectively), as well as their phases modulo π, as a function of radial velocity across the line profile. The error bars on the amplitude and phase were evaluated via Monte Carlo simulations (see text). The color figure can be viewed online.

TABLE 2

FREQUENCIES OF THE STRONGEST PEAKS IN THE POWER SPECTRA

Campaign	He I λ 4471			He II λ 4542			N III $\lambda\lambda$ 4634-42		
	ν_1	ν_2	ν_3	ν_1	ν_2	ν_3	ν_1	ν_2	ν_3
	(d^{-1})			(d^{-1})			(d^{-1})		
OHP 12/2009	2.21	–	–	2.15	–	–	2.32	–	–
OHP 06/2010	0.87	1.41	2.12	0.87	1.40	3.80	0.56	0.85	0.30
SPM 06/2010	2.22	2.86	1.60	2.24	0.63	2.90	–	–	–
OHP 12/2010	0.75	5.58	–	0.76	–	–	2.10	0.47:	7.19
SPM 09/2011	1.00:	4.17	0.55	0.66	–	–	–	–	–
OHP 09/2011	0.31	3.00	0.54:	0.29	1.61	3.41	0.38	–	–

A colon behind the value of the frequency means that our time series provides a poor phase coverage of the corresponding cycle.

cannot be explained by a simple combination of individual peaks and their aliases. This situation is reminiscent of red noise. In case there is a significant contribution of red noise, it can bias the choice of the right frequency amongst the various aliases. Indeed, the addition of red noise will apparently enhance the strength of the aliases in the lower frequency domain. Moreover, in this case, the prewhitening of a specific frequency overcorrects the effect of this frequency (and overestimates the associated amplitude), as it pumps some power which actually belongs to the red noise.

When all the OHP data are combined, the power spectrum cannot be explained by the combination of a small number of frequencies. Indeed, the actual structures in the power spectrum are broader than expected from the sampling of the data set and prewhitening leaves a substantial power around the prewhitened frequencies that cannot be attributed to their aliases. This result has important implications as far as the stability of the variations is concerned (see § 4.1 below).

Table 2 provides an overview of the frequencies that we have detected in our spectroscopic time series of λ Cep. We have checked whether or not our data correctly sample the corresponding cycles. In most cases, the sampling is either very good or even excellent. There are however a few cases where the sampling is poor. These are mostly frequencies near 0.5 or 1 d^{-1} which are notoriously problematic in single-site ground-based observing campaigns. These frequencies are identified by a colon in Table 2.

The OHP and SPM campaigns in June 2010 were performed simultaneously, allowing in principle a better coverage of the variations of λ Cep, as the time coverage achieved from both observatories is about 60% during five consecutive days. Unfortunately, because of the difficulties with the normalization of the SPM data and despite several attempts, it turned out to be impossible to normalize the data from both observatories in a fully consistent way. Therefore, if we combine the time series from OHP and SPM into a single time series, we are dominated by frequencies near 1 and 0.1 d^{-1}, which reflect the artificial variations introduced by the different normalizations. What we can do though, is to compare the frequencies found from the individual observatories. The agreement is quite reasonable: data from both observatories indicate a frequency between 2.12 and 2.24 d^{-1}, as well as a variation with a frequency of 0.87 d^{-1} or its alias at 2.86 d^{-1} (either of these frequencies yield good results during the prewhitening process).

The normalization problems with the SPM data of the September 2011 campaign lead to a periodogram of the He I λ 4471 line dominated by 1 d^{-1}. This is clearly an artefact which impacts our analysis for this spectral line during this specific campaign.

4. DISCUSSION

4.1. *The long-term stability of the variability of λ Cep*

Although there are a few higher frequencies, the majority of the strongest peaks are located below 3 d^{-1} (see Table 2). The most obvious candidate for a stable periodicity that emerges from our analysis corresponds to a frequency near 2 d^{-1} (actually in the range 2.10−2.32 d^{-1}). We note however that, even for this frequency, its visibility in the individual observing campaigns is strongly variable from one epoch to the other. This epoch-dependence can

TABLE 3

PROPERTIES OF NRP CANDIDATES

ν (d^{-1})	Line	Campaign	$\frac{\lvert\Delta\phi\rvert}{\pi}$	l
0.29	He II λ 4542	OHP 09/2011	$\sim$1.7	2
0.31	He I λ 4471	OHP 09/2011	$\sim$1.7	2
0.54	He I λ 4471	OHP 09/2011	$\sim$2.0	2–3
0.66	He II λ 4542	SPM 09/2011	$\sim$1.0	–
0.87	He I λ 4471	OHP 06/2010	$\sim$2.5	3
1.60	He I λ 4471	SPM 06/2010	$\sim$0.5	–
2.15	He II λ 4542	OHP 12/2009	$\sim$2.5	3
2.21	He I λ 4471	OHP 12/2009	$\sim$2.7	3
2.22	He I λ 4471	SPM 06/2010	$\sim$0.8	–
2.24	He II λ 4542	SPM 06/2010	$\sim$1.0	–
2.86	He I λ 4471	SPM 06/2010	$\sim$3.5	4
2.90	He II λ 4542	SPM 06/2010	$\sim$3.5	4
3.00	He I λ 4471	OHP 09/2011	$\sim$2.5	3
3.41	He II λ 4542	OHP 09/2011	$\sim$1.5	2

either be genuine, or it can be the result of the sampling of the time series. The latter situation is well illustrated by the June 2010 data. In the SPM time series, the 2.2 d^{-1} frequency makes up the strongest peak in the periodogram of both helium lines, whilst in the OHP data, it appears only in third position in the power spectrum of the He I λ 4471 line and is missing among the three most important frequencies of the He II λ 4542 line.

de Jong et al. (1999) analyzed 169 spectra of λ Cep having a S/N similar to our data, and reported two frequencies, at 1.95 and 3.6 d^{-1} that they attributed to non-radial pulsations. On the one hand, our data seem to confirm the existence (and long-term stability) of a period near 12 hours, although the practical problems in correctly sampling this period make it difficult to establish its actual value. Assuming that all detections in Table 2 in the range 2.10–2.32 d^{-1} refer to the same frequency[6], we estimate a value of (2.19 ± 0.08) d^{-1}, corresponding to a period of (10.9 ± 0.4) hr. When considering this frequency as a candidate non-radial pulsation, we note however that the degree l seems to differ from one epoch to the other (see § 4.2). This casts serious doubt on the stability of the period. On the other hand, our data show no evidence of the 3.6 d^{-1} frequency reported by de Jong et al. (1999), although such a frequency would be well sampled by our time series. This frequency thus probably reflects a transient phenomenon.

[6]If we restrict ourselves to those occurrences that show a behaviour of the phase constant consistent with NRPs (see Table 3), the frequency would be (2.21 ± 0.04) d^{-1} for an associated period of (10.9 ± 0.2) hr.

Kholtygin et al. (2011) analyzed two series of spectroscopic observations of λ Cep obtained in 1997 (3 nights) and 2007 (4 nights). They found line profile variability at the 2–3% level in many He I, He II and H I lines. Unfortunately, only one of the nights of the 1997 campaign was actually suitable for a Fourier analysis which indicated variations of the He II λ 5412 line with a frequency near 3 – 4 d^{-1}. The 2007 time series was less densely sampled than the 1997 time series, but Kholtygin et al. (2011) nevertheless derived a list of 13 different frequencies. A first series of 6 frequencies (0.3, 0.6, 0.7, 0.9, 1.4, 1.6 d^{-1}) was attributed to rotational modulation, whilst the remaining frequencies (2.2, 2.3, 2.5, 2.6, 4.1, 4.5, and 6.9 d^{-1}) were interpreted as non-radial pulsations[7]. Many of these frequencies also emerge at least once from our analysis.

4.2. *Non-radial pulsations?*

Establishing the presence of a periodicity in the line profile variability of λ Cep does not necessarily imply that it is due to non-radial pulsations. To check which of the periodicities detected in our analysis are good candidates for NRPs, we have inspected the amplitude and phase diagrams obtained in the course of the prewhitening process.

Non-radial pulsations are expected to produce a pattern of alternating absorption excesses and deficits that cross the line profile from blue to red as the star rotates. This results in a progressive variation of the phase of the modulation across the line profile. In our data, only a subset of the frequencies identified in Table 2 yields a monotonic progression of the phase constant ϕ across those parts of the line profile where the amplitude of the variation is large (see, e.g., the ν_1 frequency of the He I λ 4471 line in Figure 3), whilst other frequencies do not show a coherent trend (e.g., the ν_3 frequency of the He II λ 4542 line in Figure 3).

Telting & Schrijvers (1997) and Schrijvers & Telting (1999) presented linear relations between the observed phase difference between the blue and red line wings and the degree l, as well as between the blue-to-red phase difference of the variations in the first harmonics and the absolute value of the azimuthal order $|m|$. These relations were shown to work to first order for spheroidal and toroidal, sectoral and tesseral pulsation modes with $l \leq 15$ and $|m| \geq 2$ (Telting & Schrijvers 1997). In our data, we have no detection of the first harmonics, thus preventing us

[7]It has to be stressed though that some of these frequencies were apparently only detected over a very narrow wavelength range.

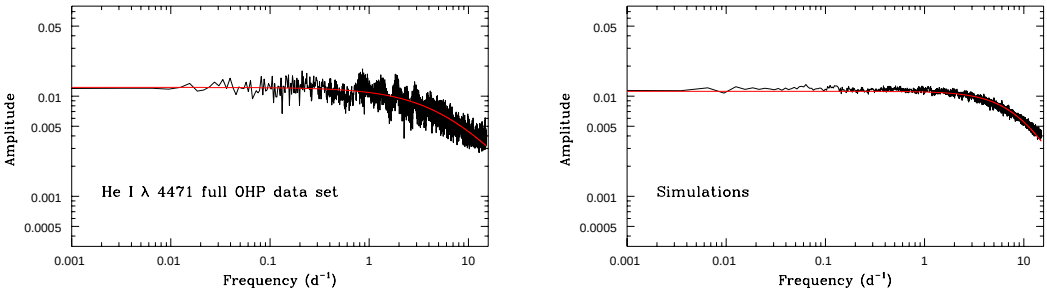

Fig. 4. Left: log-log plot of the amplitude spectrum of the full OHP time series of the He I $\lambda\,4471$ line. The red line shows the best-fit red-noise relation with $A_0 = 0.012$, $\gamma = 1.15$ and $\tau = 0.026$ day. Right: same, but for simulated data, where all the variations are assumed to arise from red noise. See text for details of the simulations. The color figure can be viewed online.

from determining the value of $|m|$. But, we can still attempt to determine l using the relations quoted by Schrijvers & Telting (1999). The results are listed in Table 3. Note that we do not quote values of $l < 2$, as such values are outside the conditions of applicability of the Schrijvers & Telting (1999) relations.

The fact that a frequency appears in Table 3 does not necessarily imply that it is truly associated with non-radial pulsations. Indeed, some of the frequencies behave differently for different epochs or lines. For instance, no clear trend is seen in the phase of the $0.63\,\mathrm{d}^{-1}$ frequency in the June 2010 SPM data, although the same frequency shows a trend in the SPM data of September 2011. In a similar way, we note a stepwise variation of the phase constant for the $2.24\,\mathrm{d}^{-1}$ frequency in the He II $\lambda\,4542$ SPM June 2010 data, whereas the variation is much more progressive for the $2.22\,\mathrm{d}^{-1}$ frequency in the He I $\lambda\,4471$ data of the same campaign. In both cases, $|\Delta\phi| \leq \pi$. This behaviour strongly contrasts with the clear monotonic progression of the phase constant over $2.5-2.7\,\pi$ observed for the $2.15-2.21\,\mathrm{d}^{-1}$ frequency in the OHP December 2009 data. We have checked that this difference in behaviour is robust against the number of frequencies that we prewhiten in a given data set and hence does not arise from interference between the different modes. This result suggests that, after all, we might not be observing the same mode at different epochs. Finally, the phase variation of the $0.87\,\mathrm{d}^{-1}$ frequency in the June 2010 OHP data is different for the He I $\lambda\,4471$ and He II $\lambda\,4542$ lines (monotonic decrease in the former case against roughly constant phase in the latter case).

It appears thus that there is no evidence for persistent NRPs in λ Cep. Instead, the various modes seem to be transient if they are indeed associated with NRPs.

4.3. *Red noise?*

As pointed out in § 3, in some cases, prewhitening of a frequency leads to a power spectrum, dominated by low frequencies, but without a distinct individual frequency responsible for the observed power. This situation could indicate that the signal is actually due to a stochastic process, referred to as red noise. Blomme et al. (2011) reported the detection of such a red noise component in the power spectra of the *CoRoT* photometry of early-type O-stars on the main-sequence. These authors suggested that the red noise could come either from a sub-surface convection layer, granulation or wind inhomogeneities. Although speculative, these explanations, especially the first and the last one, could also be relevant for λ Cep.

Following, the approach of Blomme et al. (2011), which is based on the formalism of Stanishev et al. (2002), we have fitted an expression

$$A(\nu) = \frac{A_0}{1 + (2\,\pi\,\tau\,\nu)^{\gamma}} \ ,$$

to the amplitude spectra of λ Cep. Here $A(\nu)$ is the amplitude derived from the power spectrum, A_0 is a scaling factor, γ is the slope of the linear part (in a log-log plot) and τ (in days) is an indication of the mean duration of the dominant structures in the line profile variability. The fits were performed for the amplitude spectra computed between 5×10^{-4} and $15\,\mathrm{d}^{-1}$. Above this frequency, the amplitude spectra are mostly dominated by white noise. As an illustration, the left panel of Figure 4 shows a log-log plot of the amplitude spectrum of the He I $\lambda\,4471$ line in the full OHP time series.

The best-fit parameters of the red-noise model vary from epoch to epoch and between the various lines. On average, we find $\gamma = 1.22 \pm 0.19$ and $\tau = (0.028 \pm 0.013)$ day. The γ value is intermediate between the values (0.91 – 0.96) of the three early-type stars investigated by Blomme et al. (2011) and the value (2.3) of Plaskett's Star studied by Mahy et al. (2011). On the other hand, the τ value is significantly shorter than for any of the above cited stars (0.08 – 0.17 day, Blomme et al. 2011; Mahy et al. 2011). Thus, the mean lifetime of the red-noise components is shorter in our case than what is observed in the *CoRoT* photometry of O-type stars.

The left panel of Figure 4 reveals a rather low dispersion of the observed amplitude spectrum about the best-fit $A(\nu)$ relation. At first sight, this is at odds with a red-noise behaviour, where the standard deviation of the periodogram is expected to be equal to the mean of the periodogram (see e.g. Timmer & König 1995), and should thus be significantly larger. The dispersion found here is also much smaller than what was observed in the analysis of the *CoRoT* photometry of O-stars (Mahy et al. 2011; Blomme et al. 2011). To understand the origin of this difference, we need to recall the way our observed amplitude spectrum is obtained. In fact, the observed periodogram is the sum of the periodograms computed at each wavelength bin across the line. Each of the helium lines studied here includes between 110 and 120 wavelength steps. Hence the resulting power spectrum is the mean of 110−120 power spectra. Therefore, if the noise properties of the different wavelength bins are independent, the dispersion of the periodogram is reduced by a factor $\approx \sqrt{110} - \sqrt{120}$.

We have generated synthetic light curves dominated by red noise using the recipe of Timmer & König (1995) along with the above formalism for $A(\nu)$ and the average parameters derived above. For the purpose of these simulations, we adopted the same sampling as for the full OHP time series. We further averaged 120 independent power spectra, computed with the same sampling, the same $A(\nu)$ relation, but independent random variables for the Fourier transform of the red noise (see equation 9 of Timmer & König 1995). The latter step was done to mimic the way the observed power spectra are obtained. The resulting amplitude spectrum is shown in the right panel of Figure 4. As one can see, the simulated amplitude spectrum indeed has a dispersion that is even smaller than what we found in the observed amplitude spectrum. This implies that the intrinsic wavelength width of the red-noise structures in λ Cep is wider than the wavelength step that we have adopted in our analysis. Furthermore, the observed amplitude spectrum displays some excesses that stand out relatively clearly, such as the feature near 2.15−2.21 d^{-1}. The width of this feature in Figure 4 clearly exceeds the natural width of the entire OHP time series ($1.5 \times 10^{-3}\,d^{-1}$), indicating that the feature cannot be due to a single periodicity, but rather arises from a quasi-periodic phenomenon. If we assume, as we have done in Figure 4, that the bulk of the power is due to red noise, we find that red noise accounts for about half of the observed amplitude of variations at these frequencies. In summary, we conclude that red noise probably contributes to the variations of λ Cep, but additional power could come from a few groups of discrete frequencies.

4.4. *An alternative scenario?*

The lack of a stable period and/or pattern of variability, as well as the putative presence of a red-noise component suggest a stochastic, chaotic or quasiperiodic phenomenon. This situation likely extends into the variability of the wind lines of stars such as λ Cep. Indeed, Rauw et al. (2003) and De Becker & Rauw (2004) found substantial variability in the He II λ 4686 emission line of other Oef stars with apparent periodicities that exist only over the typical time scale of an observing campaign, but are not stable over the long term. Recently, Henrichs & Sudnik (2012, 2013) reached a similar conclusion for the variability of this line in the specific case of λ Cep. They suggested that this situation arises from the presence of numerous, short-lived, localized magnetic loops at the stellar surface, so-called stellar prominences, corotating with the star. These magnetic loops would be the footpoints of wind structures. This explanation could extend to the variability of the photospheric lines studied in this paper if these magnetic loops are associated with spots that rotate across the line of sight, and mimic the line profile variations usually attributed to NRPs. Henrichs & Sudnik (2013) suggest that the rotation period of λ Cep should be about 4 d. If the quasi-periodic variations on time scales of 10.9 hours detected in this paper are indeed due to such spots, one would need about 9 spots on the stellar surface.

To date, there has been no firm detection of a magnetic field in λ Cep: Kholtygin et al. (2011) inferred an upper limit of 1 kG on the longitudinal magnetic field. However, if the scenario proposed by Henrichs & Sudnik (2012, 2013) is right, the magnetic configuration would be considerably more complex than a dipole, rendering its detection much more challenging (see Kochukhov & Sudnik 2013).

5. CONCLUSION

The initial goal of our study was to get a deeper insight into the non-radial pulsations of λ Cep. However, our data revealed an unexpectedly complex situation, with no clear evidence for a single set of stable pulsation modes. This situation is very similar to what is observed for the emission lines of this star, as well as of other members of the Oef class, suggesting a common origin. The question as to what causes the observed line profile variability of λ Cep is thus still open. We have investigated the possibility that red noise might be responsible for this phenomenon, but this explanation does not seem to account for the full power. Additional variability likely arises from a large number of transient periodicities that might or might not be due to oscillations of the stellar surface. To make further progress in understanding the variability of this object, more stringent constraints on its magnetic field, regarding both its strength and its geometry, are needed.

This research is supported by a bilateral convention between Conacyt (Mexico) and F.R.S.-FNRS (Belgium), and an ARC grant for Concerted Research Actions, financed by the Federation Wallonia-Brussels. The Liège team further acknowledges additional support by the Communauté Française de Belgique for the OHP observing campaigns, as well as by Belspo through an XMM/INTEGRAL PRODEX contract.

REFERENCES

Blomme, R., et al. 2011, A&A, 533, A4
Briquet, M., et al. 2011, A&A, 527, A112
Conti, P. S., & Frost, S. A. 1974, ApJ, 190, L137
Conti, P. S., & Leep, E. M. 1974, ApJ, 193, 113
De Becker, M., & Rauw, G. 2004, A&A, 427, 995
de Jong, J. A., Henrichs, H. F., Schrijvers, C., Gies, D. R., Telting, J. H., Kaper, L., & Zwarthoed, G. A. A. 1999, A&A, 345, 172
Fullerton, A. W., Gies, D. R., & Bolton, C. T. 1996, ApJS, 103, 475
Gies, D. R. 1987, ApJS, 64, 545
Godart, M., Dupret, M.-A., Noels, A., Montalbán, J., & Ventura, P. 2012, in ASP Conf. Proc. 462, Progress in Solar/Stellar Physics with Helio- and Asteroseismology, ed. H. Shibahashi, M. Takata, & A. E. Lynas-Gray (San Francisco: ASP), 27
Gosset, E., Royer, P., Rauw, G., Manfroid, J., & Vreux, J.-M. 2001, MNRAS, 327, 435
Grady, C. A., Snow, T. P., Jr., & Timothy, J. G. 1983, ApJ, 271, 691
Heck, A., Manfroid, J., & Mersch, G. 1985, A&AS, 59, 63
Henrichs, H. F. 1991, in Proc. ESO Workshop 36, Rapid Variability of OB stars: Nature and Diagnostic Value, ed. D. Baade (Garching: ESO), 199
Henrichs, H. F., Kaper, L., & Zwarthoed, G. A. A. 1988, in ESA Proc. 281, Celebratory Symp. on a Decade of UV Astronomy with the IUE Satellite, Vol. 2, ed. N. Longdon & E. J. Rolfe (Noordwijk: ESA), 145
Henrichs, H. F., & Sudnik, N. P. 2012, 6th Mimes Workshop (CEA: Saclay, France)
_____. 2013, IAU Symp. 302, Magnetic fields throughout Stellar Evolution, ed. P. Petit, M. Jardine, & H. Spruit, in press (arXiv:1310.5264)
Kambe, E., et al. 1997, ApJ, 481, 406
Kaper, L., Henrichs, H. F., Nichols, J. S., & Telting, J. H. 1999, A&A, 344, 231
Kaper, L., et al. 1997, A&A, 327, 281
Kholtygin, A. F., Sudnik, N. P., Burlakova, T. E., & Valyavin, G. G. 2011, Astron. Rep., 55, 1105
Kochukhov, O., & Sudnik, N. 2013, A&A, 554, A93
Leep, E. M., & Conti, P. S. 1979, ApJ, 228, 224
Mahy, L., et al. 2011, A&A, 525, A101
McCandliss, S. R. 1988, PhD thesis, University of Colorado, Boulder, USA
Rauw, G., De Becker, M., & Vreux, J.-M. 2003, A&A, 399, 287
Rauw, G., et al. 2008, A&A, 487, 659
Rivero González, J. G., Puls, J., & Najarro, F. 2011, A&A, 536, A58
Schrijvers, C., & Telting, J. H. 1999, A&A, 342, 453
Stanishev, V., Kraicheva, Z., Boffin, H. M. J., & Genkov, V. 2002, A&A, 394, 625
Telting, J. H., & Schrijvers, C. 1997, A&A, 317, 723
Timmer, J., & König, M. 1995, A&A, 300, 707

Philippe Eenens, Carlos Arturo Flores, and Jorge Uuh-Sonda: Departamento de Astronomía, Universidad de Guanajuato, Apartado 144, 36000 Guanajuato, Guanajuato, Mexico.
Eric Gosset, Laurent Mahy, Matthieu Palate, and Gregor Rauw: Groupe d'Astrophysique des Hautes Energies, Institut d'Astrophysique et de Géophysique, Université de Liège, Allée du 6 Août, 4000 Liège, Belgium (gosset, mahy, palate, rauw@astro.ulg.ac.be).

Setting a New Standard in the Analysis of Binary Stars
K. Pavlovski, A. Tkachenko and G. Torres (eds)
EAS Publications Series, **64** *(2013) 229–236*

COMBISPEC: A NOVEL APPROACH IN THE MODELLING OF MASSIVE BINARIES

M. Palate[1]

Abstract. Spectral modelling and especially for massive stars is not a straightforward problem and over the past decades many advances have been made in this field. We now have sophisticated model atmosphere codes that allow to derive the stellar parameters. However, these codes are based on the assumption that the star is single and spherical which is no longer valid for the components of a binary system. On the other hand, observational studies indicate that binarity has an impact on the spectra. This is why we have developed a model called CoMBiSpeC (code of massive binary spectral computation) that specifically accounts for the impact of binarity on the spectra.

1 Introduction

(Massive) binary systems are crucial to improve our knowledge of the fundamental properties of (massive) stars. A common way to derive these properties is synthetic spectral modelling. However, the current stellar atmosphere models are designed for single spherical stars and therefore neglect interaction effects that occur in close binaries. In this context we have developed the CoMBiSpeC (code of massive binary spectral computation) model that accounts for the interactions between the components of a massive binary in the spectral computation. CoMBiSpeC computes the stellar surfaces for components of synchronous non-eccentric binary systems and then the gravity and temperature distributions as well as the spectra at several orbital phases. In the case of eccentric systems the TIDES (tidal interactions with dissipation of energy through shear) code (Moreno *et al.* 1999, 2005, 2011) is used for the surface and velocity field computation. Our model is presented in Section 2 and three examples of applications are described in Section 3.

[1] Institut d'Astrophysique et de Géophysique, Université de Liège, Bât. B5c, Allée du 6 Août 17, 4000 Liège, Belgium

DOI: 10.1051/eas/1364031

2 The model

For clarity, we divided the code CoMBiSpeC into two parts, one part involving the surface, gravity and temperature calculation, and a second the spectral computation. A full description of the model can be found in Palate & Rauw (2012) and Palate *et al.* (2013a).

2.1 Geometrical modelling

In the case of circular systems in synchronous rotation, the stellar surface is an equipotential of the Roche potential. In massive stars, the radiation pressure is however very important and acts on the shape of stars. We thus have modified the classical Roche potential by adding the internal radiation pressure (effect on each star's own surface) and the external radiation pressure (effect of the companion) effects. A more detailed description of the radiation pressure effect can be found in Palate *et al.* (2013a). Our approach is based on the works of Drechsel *et al.* (1995) and Phillips & Podsiadlowski (2002) for the treatment of the external radiation pressure and the Howarth (1997) approach for the inner radiation pressure. The effect of the external radiation pressure can be seen as a force that decreases the attraction of the companion. Its treatment therefore consists of scaling the mass of the companion in the Roche potential. The scale parameter $\delta = \frac{F_{\rm rad}}{F_{\rm grav}}$ is computed iteratively for each surface point in a similar way to the reflection effect treatment of Wilson (1990). The modified "Roche" potential can be written (for the primary)

$$\Omega = \frac{1}{r} + \frac{q(1-\delta(r,\varphi,\theta))}{\sqrt{r^2 - 2r\cos\varphi\sin\theta + 1}} + \frac{q+1}{2}\cdot r^2\sin^2\theta - qr\cos\varphi\sin\theta, \qquad (2.1)$$

where $r = \sqrt{x^2+y^2+z^2}$, $q = \frac{m_2}{m_1}$, $x = r\cos\varphi\sin\theta$, $y = r\sin\varphi\sin\theta$, and $z = r\cos\theta$. Here, θ and φ are, respectively, the colatitude and longitude angle in the spherical coordinates centered on the star under consideration.

According to Howarth (1997), the inner radiation pressure can be treated as a simple scaling of the Roche potential and thus, $\Omega_{\rm eff} = (1-\Gamma)\,\Omega$, with $\Gamma = \frac{\sigma_{\rm Th}}{m_{\rm H}c}\sigma T_{\rm pole}^4 \frac{1}{\|\vec{g}_{\rm pole}\|}$ and where $\frac{\sigma_{\rm Th}}{m_{\rm H}} \approx 0.036\,{\rm m^2\,kg^{-1}}$, $\sigma_{\rm Th}$ is the Thomson scattering cross section and σ the Stefan-Boltzmann constant. The stellar surfaces are represented with a discretised grid of 240×60 points (in φ and θ respectively). The local acceleration of gravity is given by the gradient of the Roche potential. The temperature is computed accounting for gravity darkening and following the von Zeipel (1924) theorem

$$T_{\rm local} = T_{\rm pole}\left(\frac{\|\underline{\nabla}\Omega_{\rm local}\|}{\|\underline{\nabla}\Omega_{\rm pole}\|}\right)^{0.25}, \qquad (2.2)$$

We also account for the reflection effects described by Wilson (1990) that leads to a local increase in temperature of the front part of the stars due to the illumination by the companion.

In the cases of eccentric binaries, we use the TIDES code (Moreno *et al.* 1999, 2005, 2011) for the surface and velocity field computation. The TIDES code calculation involves the solution of the equations of motion of the surface elements in the presence of gravitational, Coriolis, centrifugal, viscous and gas pressure forces. We then use CoMBiSpeC to complete the geometrical computation (*i.e.* the gravity and temperature computation).

2.2 Spectral modelling

The second part of the algorithm computes the spectrum of the binary by summing the incremental contributions of each surface point. non-LTE OB star spectral grids (TLUSTY OSTAR2002 and BSTAR2006 grid, Lanz & Hubeny 2003, 2007) are used to compute the integrated spectrum of the star at each orbital phase. The spectral grid is computed for solar metallicity. Each spectrum is defined by two parameters: gravity and temperature. As we know these parameters for each point at the stellar surfaces, we can compute the local contribution to the spectrum. The computation consists of a linear interpolation between the flux of the four nearest spectra in the grid. The appropriate Doppler shift is then applied to the spectrum accounting for the orbital and rotational velocity of the surface element. We multiply the spectrum by the area of the element projected along the line of sight towards the observer and by a limb-darkening coefficient based on the tabulation of Claret & Bloemen (2011). Finally, we sum the contribution to the total spectrum. It has to be stressed that we have assumed that there is no heat transfer between the different surface elements as far as the formation of the spectrum is concerned. In the case of circular orbit, phase zero corresponds to the "eclipse" of the primary by the secondary. Over the first half of the orbital cycle (phase $= [0, 0.5]$), the primary star has a negative radial velocity. For the eccentric orbit, phase zero corresponds to the periastron passage.

3 Examples of application

We present here three examples in which the CoMBiSpeC and TIDES (for the third example) codes have changed our interpretation of the spectra. A more extensive description of these examples can be found in Palate & Rauw (2012) and Palate *et al.* (2013a,b). The first two model calculations are based on the parameters of two real systems: HD 100213 and HD 165052 studied by Linder *et al.* (2007). The third example is based on the best parameters derived with the CoMBiSpeC and TIDES codes for the Spica system (Harrington *et al.* 2009; Palate *et al.* 2013b). The parameters of these systems can be found in Tables 1 and 2.

3.1 Temperature distribution effect

The model of HD 100213 leads to a contact configuration if radiation pressure is not accounted for, but when it is included, the system becomes slightly detached. A non-uniform surface temperature distribution in HD 100213 was reported by

Table 1. Parameters of the non-eccentric binary systems. Inclination in brackets stands for non-eclipsing system.

Parameters	HD 165052	HD 100213
Spectral type	O6.5V + O7V	O7.5V + O9.5V
Period (day)	2.95515	1.3872
Mass ratio	0.87	0.68
Semi-major axis ($R_\odot$)	31.25	17.34
Inclination (°)	(23)	77.8
Mass of primary ($M_\odot$)	25.15	21.7
Mass of secondary ($M_\odot$)	21.79	14.7
Primary polar temperature (K)	35500	35100
Secondary polar temperature (K)	34400	31500

Table 2. Spica parameters used for computation with the TIDES + CoMBiSpeC model. [(a)] Argument of periastron of the secondary. [(b)] The β_0 parameter is the ratio of the rotation and orbital angular velocities at periastron and can be expressed as: $\beta_0 = 0.02\frac{P}{R}\frac{v_{\rm rot}}{(1+e)^{1/2}}\frac{(1-e)^{3/2}}{(1+e)^{1/2}}$, where $v_{\rm rot}$ is the rigid body rotation velocity (in km s^{-1}), R is the equilibrium radius (in $R_\odot$), and e is the eccentricity. [(c)] 1 $R_\odot^2$ day^{-1} = 5.67×10^{16} cm^2 s^{-1}.

Parameters	Primary	Secondary
Common parameters		
Period (day)	4.01452	
Eccentricity	0.067	
$\omega^{(a)}$ (°)	255	
Inclination (°)	60	
CoMBiSpeC parameters		
Mass ($M_\odot$)	10.25	6.97
Polar temperature (K)	24000	19500
Polar radius ($R_\odot$)	6.84	3.64
$v_{\rm rot}$ (km s^{-1})	199	87
$\beta_0^{(b)}$	2.07	1.67
Microturbulent velocity (km s^{-1})	15	15
TIDES code parameters		
Viscosity, ν ($R_\odot^2$ day^{-1})[(c)]	0.028	0.028
Layer depth ($\Delta R/R$)	0.07	0.07
Polytropic index	1.5	1.5

Linder *et al.* (2007). This temperature distribution is observed through radial velocity measurements of the He II and He I lines (see Table 3) that are not formed over the same region of the stellar surfaces. The He II lines are preferentially formed over the hotter region of the stars whilst the He I lines are preferentially formed over the cooler regions. The radial velocity amplitude of the He II lines is

Table 3. Semi-amplitudes of the radial velocity curves (in $\mathrm{km\,s^{-1}}$) of the He lines in the HD 100213 model spectra. Columns 2 and 3 are the results obtained on our synthetic spectra (see Sect. 3.1) and the last two are the semi-amplitudes observed by Linder *et al.* (2007). The error on the observed semi-amplitudes is about $5\,\mathrm{km\,s^{-1}}$ except for the He 1 λ 5876 line where it is $\sim 10\,\mathrm{km\,s^{-1}}$.

Lines	K_1	K_2	$K_{1,\mathrm{obs}}$	$K_{2,\mathrm{obs}}$
He 1 λ 4026	245	362	247	364
He 1 λ 4471	246	361	245	372
He 1 λ 4686	241	344	251	355
He 1 λ 4921	257	363	246	373
He 11 λ 5412	239	339	240	351
He 11 λ 5876	245	358	270	389

observed to be smaller which indicates that the hotter regions have to correspond to the hemisphere facing the companion. The radial velocity amplitude of the He I lines is larger which indicates that the formation regions have to correspond to the hemisphere opposite to the companion. Without radiation pressure the front hemisphere is too cold to reproduce the observed temperature distribution, however, when radiation pressure is added, the stars are less deformed. This implies a moderate temperature increase of the facing hemispheres caused by the decreasing gravity darkening and a higher effectiveness of the reflection process. This temperature increase is, therefore, sufficient to explain the observations (within the error bar).

3.2 Struve-Sahade effect

The Struve-Sahade effect (hereafter S-S effect) was originally defined as the apparent strengthening of the secondary spectrum when the star is approaching the observer and its weakening as it moves away. A more general definition is the apparent variation of the line strengths of either of the binary components as a function of the orbital phase (Linder *et al.* 2007). This effect was reported by Linder *et al.* (2007) in HD 165052 (*e.g.*, in the He 1 λ 4026 line). Our simulations show that the S-S effect seems to be due to the combination of the spectra in which the lines have a non-Gaussian/non-Lorentzian and even asymmetric profile. For example, Figure 1 illustrates the He 1 λ 4026 line at two opposite phases. Our individual spectra reveal this line to be asymmetric with a steeper red wing for both stars. At phase 0.25, the blue wing of the secondary reinforces the core of the primary that thus appears to have a higher apparent equivalent width (EW) than its actual value. At the phase 0.75, the situation is reverted and the core of the secondary seems to be reinforced. When the combined binary spectra is fitted with two symmetric Gaussian profiles, the red-shifted component will be systematically assigned a lower flux, because the blue-shifted component will be apparently broader than the red one. Although the resulting fit can be of excellent quality, it will provide systematically larger EWs for the blue component and smaller EWs

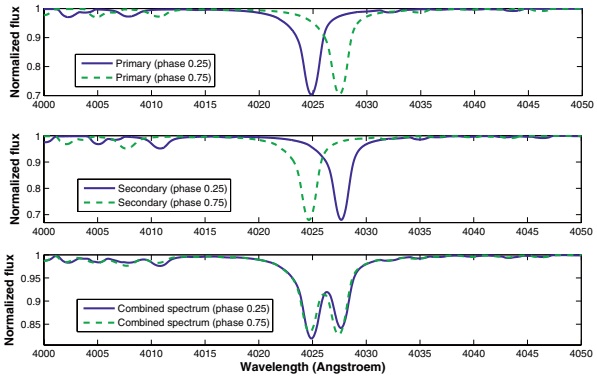

Fig. 1. He 1 λ 4026 line at phases 0.25 and 0.75 in the HD 165052 model. *Upper panel*: primary spectra. *Middle panel*: secondary spectra. *Lower panel*: combined spectra.

for the red. This situation therefore leads to an artificial S-S behaviour. This result hence leads to an alternative explanation of the S-S effect: in some binary systems and at least for some lines, this effect could simply be an artefact caused by the fitting of blended asymmetric lines with symmetric profiles. Therefore, the S-S effect does not stem from genuine physical processes, but rather reflects a bias in the measurement of the line profiles.

3.3 Line profile variations

Spica is a double-lined, short-period (∼4 days) spectroscopic binary in an eccentric orbit. The primary component is classified as B1.5 IV–V and the secondary component is classified as B3 V. The primary was believed to be a β Cephei-type star (Shobbrook *et al.* 1969, 1972) presenting spectroscopic line-profile variations that are commonly described in terms of travelling "waves" that migrate from the blue to the red wing of the weak photospheric absorption lines, but also include variations in the slope of the line wings.

Harrington *et al.* (2009) performed an *ab initio* calculation with the TIDES code of the line profiles at several orbital phases in order to study the variability that is caused by the response of the star to tidal perturbations. They were able to reproduce the general trends in the line-profile variability (migrating "bumps"). Harrington *et al.* (2009) describe these bumps as "tidal flows", a concept that differs from the non-radial pulsation interpretation in that the travelling waves on the stellar surface are a consequence entirely of the response of this surface to the forcing and restoring agents, the interior structure of the star playing no role. The primary star rotates super-synchronously, which significantly perturbs its

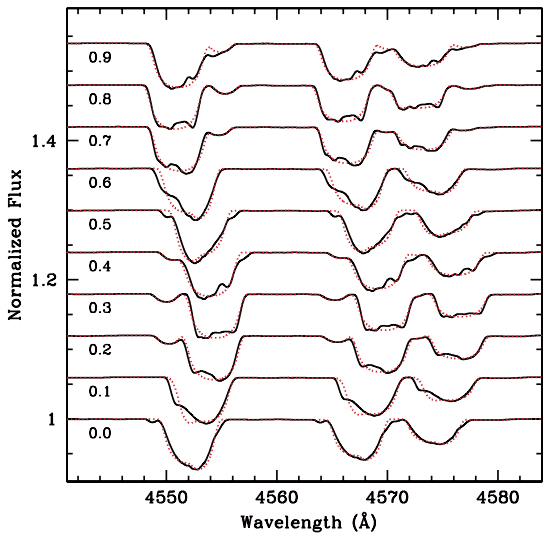

Fig. 2. The synthetic primary + secondary combined spectra of the Si III triplet are stacked in order of increasing orbital phase ($\phi = 0$ corresponds to periastron). The perturbed spectra are displayed with the dark tracing and the unperturbed spectra with dots. The "bumps" in the primary star's perturbed profiles are evident as is the difficulty they introduce in properly locating the contribution of the secondary except at $\phi \sim 0.3 \pm 0.05$ and 0.8 ± 0.05 when the contribution from the secondary is clearly resolved.

surface, leading to strong phase-dependent line profile variations. This super-synchronous rotation explains the presence of the tidal flows.

The study of Harrington *et al.* (2009) was limited to the analysis of line-profile variability alone, and no comparison of the effects on different lines (particularly those used for temperature and gravity diagnostics) was possible. These effect were modelled with CoMBiSpeC. Figure 2 shows the Si III triplet line profiles at 10 orbital phases in the perturbed and the unperturbed spectra[2]. The strong phase-dependent variations in the perturbed profiles due to tidal interaction are clearly seen and are similar to those present in the observational data. The same behaviour is present in numerous other photospheric absorptions without the need of any assumption regarding non-radial pulsations.

[2]Perturbed and unperturbed spectra stand respectively for models with and without tidal interaction.

4 Conclusions

CoMBiSpeC is a first step in the spectral modelling of massive binaries. This model includes various effects like reflection, radiation pressure, gravity darkening, limb-darkening that allow us to compute physical properties ($T_{\rm eff}$, $\log g$) at the stellar surface and, from there the spectra of binary systems. We have presented here two effects that are now explained in a rather simple way: the temperature distribution effect and the S-S effect. If we combine CoMBiSpeC and the TIDES code, we are able to compute the spectra of eccentric binaries. This 2-in-1 model has led us to propose a new explanation to the line profile variations of Spica in terms of the tidal response of the surface of the primary star. Several improvements could also be considered: extension to non-solar abundances, different turbulent velocity, lines affected by stellar winds, "cross-talk" (*i.e.*, heat transfer) between the surface elements, new treatment of the reflection effect, extension to low mass stars, ... However, despite these limitations and assumptions, our results are encouraging, making CoMBiSpeC a interesting tool for the analysis of massive binaries.

I would like to acknowledge Gregor Rauw for a careful reading of this paper and helpful comments. I also wish to express my gratitude to Gloria Koenigsberger for guidance in the use and implementation of the TIDES code. Finally, I acknowledge support through the XMM/INTEGRAL PRODEX contract (Belspo).

References

Claret, A., & Bloemen, S., 2011, A&A, 529, A75

Drechsel, H., Haas, S., Lorenz, R., & Gayler, S., 1995, A&A, 294, 723

Harrington, D.M., Koenigsberger, G., Moreno, E., & Kuhn, J., 2009, ApJ, 704, 813

Howarth, I.D., 1997, Observatory, 117, 335

Lanz, T., & Hubeny, I., 2003, ApJS, 146, 417

Lanz, T., & Hubeny, I., 2007, ApJS, 169, 83

Linder, N., Rauw, G., Sana, H., *et al.*, 2007, A&A, 474, 193

Moreno, E., & Koenigsberger, G., 1999, Rev. Mex. Astron. Astrofis., 35, 157

Moreno, E., Koenigsberger, G., & Toledano, O., 2005, A&A, 437, 641

Moreno, E., Koenigsberger, G., & Harrington, D.M., 2011, A&A, 528, A48

Palate, M., & Rauw, G., 2012, A&A, 537, A119

Palate, M., Rauw, G., Koenigsberger, G., & Moreno, E., 2013, A&A, 552, A39

Palate, M., Koenigsberger, G., Rauw, G., *et al.*, 2013, A&A, 556, A49

Phillips, S.N., & Podsiadlowski, Ph., 2002, MNRAS, 337, 431

Shobbrook, R.R., Herbison-Evans, D., Johnson, I.D. & Lomb, N.R., 1969, MNRAS, 145, 131

Shobbrook, R.R., Lomb, N.R., & Herbison-Evans, D., 1972, MNRAS, 156, 165

von Zeipel, H., 1924, MNRAS, 84, 665

Wilson, R.E., 1990, ApJ, 356, 613

A.4 Publications list

- **Massive binaries as seen with GAIA**
  Palate, M., Rauw, G., Gosset, E., & Nazé Y. 2010, Poster presented at the *39th Liège International Astrophysical Colloquium*, Liège, Belgique

- **Massive binaries as seen with GAIA**
  Palate, M., Rauw, G., Gosset, E., & Nazé Y. 2011, Bulletin de la Société Royale des Sciences de Liège, 80, 504-508

- **Spectral modelling of circular massive binary systems: Towards an understanding of the Struve-Sahade effect ?**
  Palate, M., Rauw, G. 2012, Astronomy & Astrophysics, 537, A119

- **The nature of the high Galactic latitude O-star HD 93521: new results from X-ray and optical spectroscopy**
  Rauw, G., Morel, T., & **Palate, M.** 2012, Astronomy & Astrophysics, 546, A77

- **Spectral modelling of massive binary systems**
  Palate, M., Rauw G., Koenigsberger G., & Moreno E. 2013, Astronomy & Astrophysics, 552, A39

- **Spectral modelling with interaction effects of the binary system Spica**
  Palate, M., Koenigsberger, G., Rauw, G., Harrington, D., & Moreno, E. 2013, Poster presented at the *Massive Stars from α to* Ω conference, Rhodes, Greece

- **Spectral modelling of the α Virginis (Spica) binary system**
  Palate, M., Koenigsberger, G., Rauw, G., Harrington, D., & Moreno, E. 2013, Astronomy & Astrophysics, 556, A49

- **Spectral modelling of massive binary systems: the example of LZ Cep**
  Palate, M., Rauw, G., & Mahy, L. 2013, Central European Astrophysical Bulletin, 37, 311-318

- **WR 138: new results from X-ray and optical spectroscopy**
  Palate, M., Rauw, G., De Becker, M., Nazé, Y., & Eenens, P. 2013, Astronomy & Astrophysics, 560, A27

- **Epoch-dependent absorption line profile variability in λ Cep**
  Uuh-Sonda, J.M., Rauw, G., Eenens, P., Mahy, L., **Palate, M.**, Gosset, E., Flores, C.A. 2014, Revista Mexicana de Astronomìa y Astrofìsica, 50, 67-76

- **CoMBiSpeC: a novel approach in the modelling of massive binaries**
  Palate, M., 2014, EAS Publications Series, 64, 229-236

- **Short-term spectroscopic variability of Plaskett's star**
  Palate, M., Rauw, G. 2014, submitted to Astronomy & Astrophysics

Appendix B

CoMBiSpeC information

B.1 Error messages

We give here the list of the error messages that can be displayed during the execution of the code.

- `Error in writing txt files in the Name routine.`
  This message is displayed if the code failed to write the output text files. *Name* corresponds to the name of the routine that tried to write its results. The origin of this error can be a deletion of the output folders before the end of the computation. The computation is stopped if the problem occurs in the surface computation but continues in the other cases.

- `Error in reading txt files in the Name routine.`
  If the text files needed for the computation are missing, this message appears. It can occur if we ask to compute spectra without computing the stellar surface. The code skips the routine and (generally) the computation stops.

- `Error in reading spectra files spec1 spec2 spec3 spec4.`
  At least one of the four spectra needed for the interpolation is missing while it is referenced in the grid. This can occur if we delete a spectrum in the grid or if the grid is missing (speci is the name of the spectra of the grid).

- `Missing spectrum, too large log(g), possible error, check point number: val.`
  The value of the $\log g$ seems too high and there exists no corresponding spectrum in the grid.

- `Error in phase computation.`
  This message only appears in the case of an eccentric orbit. It means that the computation of the phase from the *datos.propaz* file has failed.

- `Error in Newton-Raphson: value of r(phi,theta): val1. The error occurs at point number: val2.`
  In this case the Newton-Raphson has converged but the value of the radius is negative. The code stops.

- `Error of convergence for the primary: R = val1. The value of r(phi,theta) is: val2. The error occurs at point number: val3.`
  The Newton-Raphson search of the radius of the star has failed with a residual equal to *val1*, the value of the unconverged radius is *val2*, and the error concerns the point number *val3*. This error is rare in the case without radiation pressure but can appear in the case with radiation pressure. This is often due to a bad value of the equipotential of the surface. The code stops.

- `Error of convergence for Li val.`
  The code does not find the value of the (pseudo-)Lagrangian Li point. The *val* parameter is the value of the residual of the computation. In the case where the radiation pressure is added the computation of the pseudo-L1 point can be difficult.

- `No convergence in the computation of the stellar surface modified by the radiation pressure.`
  The code fails to converge to a solution for the surface computation of a circular system in which the radiation pressure effect is present. This can arise when the two stars are initially in contact.

- `Too many unconverged points in reflection: val1 val2.`
  The reflection process does not converge. The number of unconverged points for the primary and for the secondary are val1 and val2 (over a total of N/4 points where N is the total number of point of the stellar surface mesh). In this case, a second message appears:
  `No convergence in the reflection process, results will not be reliable, would you like to continue the computation? y/n.`
  If you continue the computation, the code will try to compute the temperature of the unconverged points. This temperature is the mean value of the two (or three) previous temperatures in the mesh. If there are more than

three unconverged temperatures one after the other, the program displays `Error in the Reflection routine (j): val1 val2` where j is P or S for the primary or the secondary, val1 is the value of the residual of the reflection coefficient iteration, and val2 is the unconverged temperature. In the latter case, the program stops.

- `The orbit of this model is eccentric. If the 'Binary_info.txt' file is missing, it means that the reflection process has failed and the temperature files contain the temperature without reflection.`
  This warning occurs in the case of eccentric binaries in which the assumptions of the reflection effect are not completely fulfilled. It is therefore possible that the treatment of the reflection process failed. In this case, the temperatures saved in the text file are the ones without reflection. The code continues with these values of the temperature.

- `Error in interpolation(i) for val1 wavelengths at point val2.`
  Indication of the under-sampling problem discussed in chapter 2. val1 indicates the number of problematic wavelengths and val2 the point of the mesh for which the problem occurs.

B.2 Physical constants

The values of the physical constants used in CoMBiSpeC are given in Table B.1.

Table B.1: Values of the physical constants used in CoMBiSpeC. Notice that 1 $\mathrm{W} = 1\,\mathrm{J\,s^{-1}} = 1\,\mathrm{N\,m\,s^{-1}} = 1\,\mathrm{kg\,m^2\,s^{-3}}$

Name	Symbol	Value	Units
Gravitational constant	G	$6.674\,10^{-11}$	$\mathrm{m^3\,kg^{-1}\,s^{-2}}$
Speed of light	c	$2.99792458\,10^{8}$	$\mathrm{m\,s^{-1}}$
Planck constant	h	$6.6260755\,10^{-34}$	$\mathrm{J\,s}$
Solar mass	$M_\odot$	$1.989\,10^{30}$	kg
Solar radius	$R_\odot$	$6.96\,10^{8}$	m
Stefan-Boltzmann constant	σ_{SB}	$5.6704\,10^{-8}$	$\mathrm{kg\,K^{-4}\,s^{-3}}$
Thomson scattering cross section	σ_{Th}	$6.65\,10^{-29}$	$\mathrm{m^2}$

B.3 Additional formulae

We give here the expression of the r-derivatives of the dimensionless Roche potential in spherical coordinates that are used in the surface and gravity computation.

1. r-derivative of the dimensionless Roche potential in spherical coordinates

$$\partial_r \Omega_1 = -\frac{1}{r^2} - q\frac{r-\zeta}{(r^2-2r\zeta+1)^{3/2}} + (q+1)r\sin^2\theta - q\zeta \tag{B.1}$$

$$\partial_r \Omega_2 = -\frac{q}{r^2} - \frac{r-\zeta}{(r^2-2r\zeta+1)^{3/2}} + (q+1)r\sin^2\theta - \zeta \tag{B.2}$$

where $r = \sqrt{x^2+y^2+z^2}$, $q = \frac{m_2}{m_1}$, $\zeta = \cos\varphi\sin\theta$, $x = r\cos\varphi\sin\theta$, $y = r\sin\varphi\sin\theta$, and $z = r\cos\theta$ and $\varphi \in [0, 2\pi]$, $\theta \in [0, \pi]$.

2. Second r-derivative of the dimensionless Roche potential in spherical coordinates

$$\partial^2_{rr}\Omega_1 = \frac{2}{r^3} - \frac{q}{(r^2-2r\zeta+1)^{3/2}}\left(1 - \frac{3(r-\zeta)^2}{r^2-2r\zeta+1}\right) + (q+1)\sin^2\theta \tag{B.3}$$

$$\partial^2_{rr}\Omega_2 = \frac{2q}{r^3} - \frac{1}{(r^2-2r\zeta+1)^{3/2}}\left(1 - \frac{3(r-\zeta)^2}{r^2-2r\zeta+1}\right) + (q+1)\sin^2\theta \tag{B.4}$$

where $r = \sqrt{x^2+y^2+z^2}$, $q = \frac{m_2}{m_1}$, $\zeta = \cos\varphi\sin\theta$, $x = r\cos\varphi\sin\theta$, $y = r\sin\varphi\sin\theta$, and $z = r\cos\theta$ and $\varphi \in [0, 2\pi]$, $\theta \in [0, \pi]$.

B.4 Parameters of the systems presented in this thesis

Table B.2: Parameters of the circular binary systems simulated in this thesis. The real system from which the parameters were derived are given as an indication. The models A, B, and C are described in Palate & Rauw (2012) and model D is described in Palate et al. (2013c). Inclinations in brackets stand for non-eclipsing systems. 1 stands for the primary star and 2 for the secondary star.

Parameters	Model A	Model B	Model C	Model D
System	HD 159176	HD 100213	HD 165052	LZ Cep
Spectral type 1	O 7V	O 7.5V	O 7V	O 9III
Spectral type 2	O 7V	O 9.5V	O 7.5V	O 9.7V
Period (d)	3.36673	1.3872	2.95515	3.070507
Inclination (°)	(48)	77.8	(23)	(49)
M_1 ($M_\odot$)	33.8	21.7	25.15	16.9
M_2 ($M_\odot$)	32.41	14.7	21.79	6.7
$R_{1,\mathrm{pole}}$ ($R_\odot$)	9.37	6.74	9.10	10.0
$R_{2,\mathrm{pole}}$ ($R_\odot$)	8.94	5.62	8.47	7.1
$T_{1,\mathrm{pole}}$ (K)	38000	35100	35500	33500
$T_{2,\mathrm{pole}}$ (K)	38000	31500	34400	29500

Table B.3: Same as Table B.2 for models F and G (see Palate & Rauw 2012).

Parameters	Model F	Model G
System	CPD -41°7742	AO Cas
Spectral type 1	O 9V	O 9V
Spectral type 2	B 1V	O 9.5III
Period (d)	2.44070	3.52348
Inclination (°)	77	65.7
M_1 ($M_\odot$)	17.97	15.59
M_2 ($M_\odot$)	9.96	9.65
$R_{1,\mathrm{pole}}$ ($R_\odot$)	7.45	4.6
$R_{2,\mathrm{pole}}$ ($R_\odot$)	5.39	9.0
$T_{1,\mathrm{pole}}$ (K)	34000	33700
$T_{2,\mathrm{pole}}$ (K)	26260	30500

Table B.4: Same as Table B.2 for the eccentric systems Spica and model E (see Palate et al. 2013a;b).

Parameters	Model E	Spica
System	HD 152248	Spica
Spectral type 1	O 7III	B 1IV
Spectral type 2	O 7.5III	B 3V
Period (d)	5.8160	4.01452
Eccentricity	0.133	0.067
$\omega^{(a)}$ (°)	82	255
Inclination (°)	(67.2)	(60)
M_1 ($M_\odot$)	27.8	10.25
M_2 ($M_\odot$)	27.2	6.97
$R_{1,\mathrm{pole}}$ ($R_\odot$)	15.99	6.84
$R_{2,\mathrm{pole}}$ ($R_\odot$)	14.47	3.64
$T_{1,\mathrm{pole}}$ (K)	34350	24000
$T_{2,\mathrm{pole}}$ (K)	34000	19500
$\mathrm{v}_1 \sin i$ (km s^{-1})	135	172
$\mathrm{v}_2 \sin i$ (km s^{-1})	135	75
$\beta_{0,1}{}^{(b)}$	0.81	2.07
$\beta_{0,2}{}^{(b)}$	0.89	1.67
Viscosity, ν_1 ($R_\odot{}^2\mathrm{d}^{-1}$)	0.05	0.028
Viscosity, ν_2 ($R_\odot{}^2\mathrm{d}^{-1}$)	0.02	0.028
Layer depth ($\Delta R/R$)	0.1	0.07
Polytropic index	3	1.5

[(a)]Argument of periastron of the secondary. [(b)]Ratio of the rotation and orbital angular velocities at periastron, $\beta_0 = 0.02 \frac{P\ \mathrm{v}_{rot}}{R} \frac{(1-e)^{3/2}}{(1+e)^{1/2}}$, where v_{rot} is the rigid body rotation velocity (in km s^{-1}), R is the equilibrium radius (in $R_\odot$), and e is the eccentricity.

B.5 CoMBiSpeC flowchart

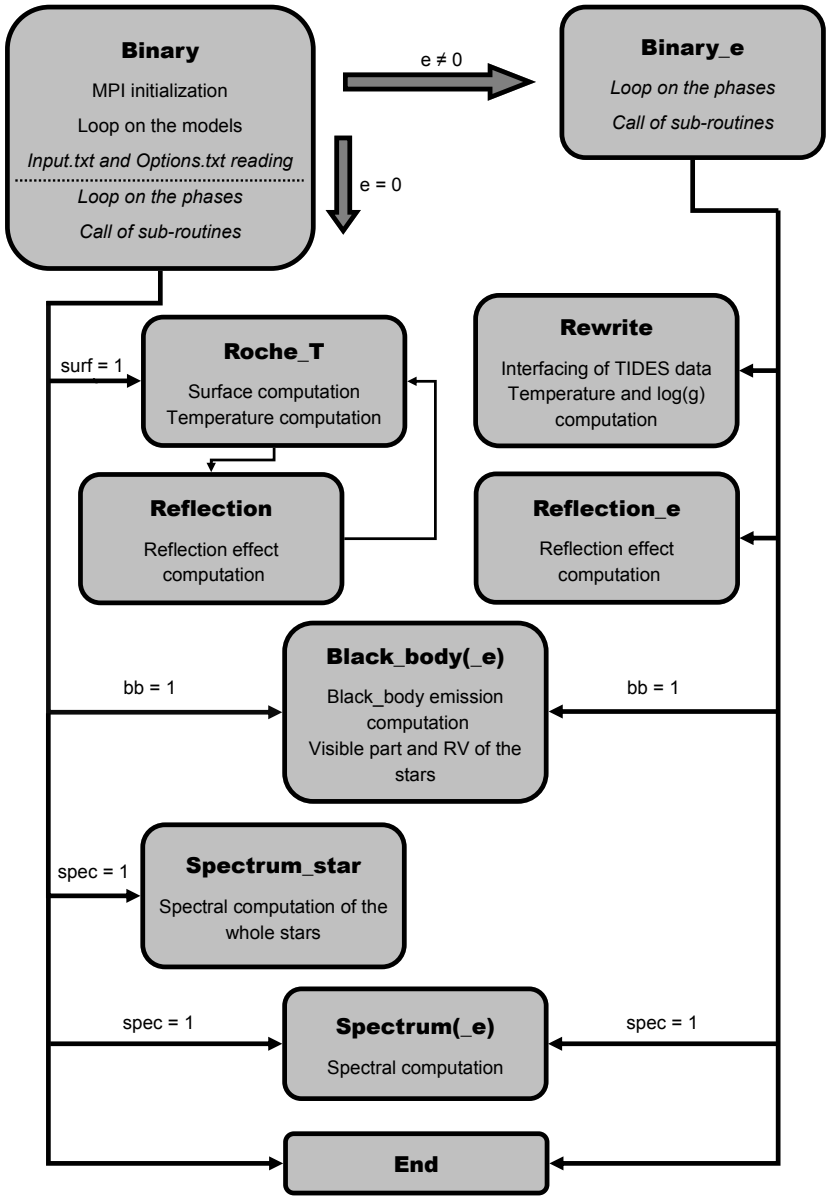

Bibliography

Aerts, C., Christensen-Dalsgaard, J., & Kurtz, D. W. 2010, Asteroseismology (Springer)

Al-Naimiy, H. M. 1978, Ap&SS, 53, 181

Annuk, K. 1990, Acta Astron., 40, 267

Brown, T. M. & Gilliland, R. L. 1994, ARA&A, 32, 37

Budaj, J. 2011, AJ, 141, 59

Castor, J. I., Abbott, D. C., & Klein, R. I. 1975, ApJ, 195, 157

Chiosi, C. & Maeder, A. 1986, ARA&A, 24, 329

Claret, A. & Bloemen, S. 2011, A&A, 529, A75

Conti, P. S. 1973, ApJ, 179, 161

Conti, P. S. & Alschuler, W. R. 1971, ApJ, 170, 325

Conti, P. S., Leep, E. M., & Lorre, J. J. 1977, ApJ, 214, 759

Crowther, P. A., Schnurr, O., Hirschi, R., et al. 2010, MNRAS, 408, 731

Dermine, T., Jorissen, A., Siess, L., & Frankowski, A. 2009, A&A, 507, 891

Diaz-Cordoves, J., Claret, A., & Gimenez, A. 1995, A&AS, 110, 329

Drechsel, H., Haas, S., Lorenz, R., & Gayler, S. 1995, A&A, 294, 723

Espinosa Lara, F. & Rieutord, M. 2011, A&A, 533, A43

Gayley, K. G. 2002, in Astronomical Society of the Pacific Conference Series, Vol. 260, Interacting Winds from Massive Stars, ed. A. F. J. Moffat & N. St-Louis, 583

Gayley, K. G., Townsend, R., Parsons, J., & Owocki, S. 2007, in Astronomical Society of the Pacific Conference Series, Vol. 367, Massive Stars in Interactive Binaries, ed. N. St.-Louis & A. F. J. Moffat, 393

Gies, D. R., Bagnuolo, Jr., W. G., & Penny, L. R. 1997, ApJ, 479, 408

Gies, D. R., Penny, L. R., Mayer, P., Drechsel, H., & Lorenz, R. 2002, ApJ, 574, 957

González, J. F. & Levato, H. 2006, A&A, 448, 283

Gräfener, G., Koesterke, L., & Hamann, W.-R. 2002, A&A, 387, 244

Gray, D. F. 2005, The Observation and Analysis of Stellar Photospheres (Cambridge University Press, Cambridge, UK)

Grunhut, J. H., Wade, G. A., Leutenegger, M., et al. 2013, MNRAS, 428, 1686

Hadrava, P. 1995, A&AS, 114, 393

Hamann, W.-R. & Gräfener, G. 2003, A&A, 410, 993

Harrington, D., Koenigsberger, G., Moreno, E., & Kuhn, J. 2009, ApJ, 704, 813

Hauschildt, P. H. & Baron, E. 1999, Journal of Computational and Applied Mathematics, 109, 41

Heger, A. & Langer, N. 2000, ApJ, 544, 1016

Hillier, D. J. & Miller, D. L. 1998, ApJ, 496, 407

Horne, K. 1991, in Fundamental Properties of Cataclysmic Variable Stars: 12th North American Workshop on Cataclysmic Variables and Low Mass X-ray Binaries (SDSU Press), ed. A. W. Shafter, 23

Howarth, I. D. 1997, The Observatory, 117, 335

Howarth, I. D., Siebert, K. W., Hussain, G. A. J., & Prinja, R. K. 1997, MNRAS, 284, 265

Hubeny, I. & Lanz, T. 1992, A&A, 262, 501

Karniadakis, G. E. & Kirby, II, R. M. 2003, Parallel Scientific Computing in C++ and MPI (Cambridge University Press, Cambridge, UK)

Kopal, Z. 1959, Close binary systems, in The International Astrophysics Series (Chapman & Hall Ltd., London)

Kurucz, R. L. 1970, SAO Special Report, 309

Lamontagne, R., Koenigsberger, G., Seggewiss, W., & Moffat, A. F. J. 1982, ApJ, 253, 230

Lanz, T. & Hubeny, I. 2003, ApJS, 146, 417

Lanz, T. & Hubeny, I. 2007, ApJS, 169, 83

Leão, M. R. M., de Gouveia Dal Pino, E. M., Falceta-Gonçalves, D., Melioli, C., & Geraissate, F. G. 2009, MNRAS, 394, 157

Linder, N. 2008, PhD thesis, University of Liège, Liège, Belgium

Linder, N., Rauw, G., Martins, F., et al. 2008, A&A, 489, 713

Linder, N., Rauw, G., Pollock, A. M. T., & Stevens, I. R. 2006, MNRAS, 370, 1623

Linder, N., Rauw, G., Sana, H., De Becker, M., & Gosset, E. 2007, A&A, 474, 193

Linnell, A. P., DeStefano, P., & Hubeny, I. 2012, PASP, 124, 885

Linnell, A. P. & Hubeny, I. 1994, ApJ, 434, 738

Lucy, L. B. 1968, ApJ, 153, 877

Machida, M. N., Tomisaka, K., Nakamura, F., & Fujimoto, M. Y. 2005, ApJ, 622, 39

Mahy, L. 2011, PhD thesis, University of Liège, Liège, Belgium

Mahy, L., Gosset, E., Baudin, F., et al. 2011a, A&A, 525, A101

Mahy, L., Martins, F., Machado, C., Donati, J.-F., & Bouret, J.-C. 2011b, A&A, 533, A9

Mahy, L., Nazé, Y., Rauw, G., et al. 2009, A&A, 502, 937

Marsh, T. R. & Horne, K. 1988, MNRAS, 235, 269

Martins, F., Schaerer, D., Hillier, D. J., et al. 2005, A&A, 441, 735

Massey, P. 1980, ApJ, 236, 526

Mathys, G. 1988, A&AS, 76, 427

Mathys, G. 1989, A&AS, 81, 237

Maury, A. C. 1921, Popular Astronomy, 29, 22

Milne, E. A. 1921, MNRAS, 81, 361

Moreno, E. & Koenigsberger, G. 1999, Rev. Mexicana Astron. Astrofis., 35, 157

Moreno, E., Koenigsberger, G., & Harrington, D. M. 2011, A&A, 528, A48

Moreno, E., Koenigsberger, G., & Toledano, O. 2005, A&A, 437, 641

Nazé, Y. 2006, Bulletin de la Societe Royale des Sciences de Liege, 75, 20

Oey, M. S. & Clarke, C. J. 2005, ApJ, 620, L43

Palate, M. 2013, in EAS Publications Series, Vol. 64, EAS Publications Series, 229–236

Palate, M., Koenigsberger, G., Rauw, G., Harrington, D., & Moreno, E. 2013a, A&A, 556, A49

Palate, M. & Rauw, G. 2012, A&A, 537, A119

Palate, M., Rauw, G., Koenigsberger, G., & Moreno, E. 2013b, A&A, 552, A39

Palate, M., Rauw, G., & Mahy, L. 2013c, Central European Astrophysical Bulletin, 37, 311

Pavlovski, K. & Hensberge, H. 2010, in Astronomical Society of the Pacific Conference Series, Vol. 435, Binaries - Key to Comprehension of the Universe, ed. A. Prša & M. Zejda, 207

Phillips, S. N. & Podsiadlowski, P. 2002, MNRAS, 337, 431

Pickering, E. C. & Bailey, S. I. 1896, ApJ, 4, 235

Rauw, G. 2009a, variable stars course

Rauw, G. 2009b, celestial mechanics course

Rauw, G., Crowther, P. A., De Becker, M., et al. 2005, A&A, 432, 985

Rauw, G., Crowther, P. A., Eenens, P. R. J., Manfroid, J., & Vreux, J.-M. 2002, A&A, 392, 563

Rauw, G., De Becker, M., Nazé, Y., Vreux, J.-M., & Williams, P., eds. 2011, Bulletin de la Société Royale des Sciences de Liège, Vol. 80, Proceedings of the 39th Liège Astrophysical Colloquium, held in Liège 12-16 July 2010

Rauw, G., Morel, T., & Palate, M. 2012, A&A, 546, A77

Russell, H. N. & Merrill, J. E. 1952, The determination of the elements of eclipsing binaries (Princeton University Observatory)

Sahade, J. 1959, PASP, 71, 151

Sana, H., Antokhina, E., Royer, P., et al. 2005, A&A, 441, 213

Sana, H. & Evans, C. J. 2011, in IAU Symposium, Vol. 272, IAU Symposium, ed. C. Neiner, G. Wade, G. Meynet, & G. Peters, 474–485

Santolaya-Rey, A. E., Puls, J., & Herrero, A. 1997, A&A, 323, 488

Schuerman, D. W. 1972, Ap&SS, 19, 351

Shobbrook, R. R., Herbison-Evans, D., Johnston, I. D., & Lomb, N. R. 1969, MNRAS, 145, 131

Shobbrook, R. R., Lomb, N. R., & Herbison-Evans, D. 1972, MNRAS, 156, 165

Simon, K. P. & Sturm, E. 1994, A&A, 281, 286

Simón-Díaz, S. & Herrero, A. 2007, A&A, 468, 1063

Smith, M. A. 1977, ApJ, 215, 574

Stickland, D. J. 1997, The Observatory, 117, 37

Struve, O. 1937, ApJ, 85, 41

Uuh-Sonda, J. M., Rauw, G., Eenens, P., et al. 2014, Rev. Mexicana Astron. Astrofis., 50, 67

Vanbeveren, D. 2009, New A Rev., 53, 27

Vink, J. S. 2008, New A Rev., 52, 419

Vogt, S. S. & Penrod, G. D. 1983, ApJ, 275, 661

von Zeipel, H. 1924, MNRAS, 84, 684

Walborn, N. R. & Fitzpatrick, E. L. 1990, PASP, 102, 379

Williamson, R. E. 1943, ApJ, 97, 51

Wilson, R. E. 1990, ApJ, 356, 613

Wilson, R. E. & Devinney, E. J. 1971, ApJ, 166, 605

Yorke, H. W. 2004, in IAU Symposium, Vol. 221, Star Formation at High Angular Resolution, ed. M. G. Burton, R. Jayawardhana, & T. L. Bourke, 141